Bio jet fuels production from lignocellulosic biomass : butyl levulinate a promising molecule towards the development of sustainable aviation fuels

Wenel Naudy Vásquez Salcedo

Normandie Université

INSA INSTITUT NATIONAL DES SCIENCES APPLIQUÉES ROUEN NORMANDIE

THÈSE

Pour obtenir le diplôme de doctorat

Spécialité **GENIE DES PROCEDES**

Préparée au sein de l'**INSA Rouen Normandie**

Bio Jet Fuels Production from Lignocellulosic Biomass: Butyl Levulinate a Promising Molecule Towards the Development of Sustainable Aviation Fuels.

Présentée et soutenue par

WENEL NAUDY VASQUEZ SALCEDO

Thèse soutenue le 05/07/2024

devant le jury composé de :

M. SEBASTIEN LEVENEUR	MAITRE DE CONFERENCES DES UNIVERSITES HDR - INSA Rouen Normandie	Directeur de thèse
M. GILLES CABOT	PROFESSEUR DES UNIVERSITÉS - Université de Rouen Normandie	Président du jury
M. BRUNO RENOU	PROFESSEUR DES UNIVERSITÉS - INSA de Rouen Normandie	Co-directeur de thèse
M. GUILLAUME DAYMA	PROFESSEUR DES UNIVERSITÉS - Institut de Combustion, Aérothermique, Réactivité et Environnement (ICARE), Orléans	Membre
M. GUILLAUME FAYET	DOCTEUR - INERIS, Verneuil-en-Halatte	Membre
MME FREDERIQUE BATTIN-LECLERC	DIRECTEUR DE RECHERCHE - Université de Lorraine	Rapporteur
M. YVES SCHUURMAN	DIRECTEUR DE RECHERCHE - IRCELYON, Villeurbanne	Rapporteur

Thèse dirigée par **SEBASTIEN LEVENEUR** (LABORATOIRE DE SECURITE DES PROCEDES CHIMIQUES) et **BRUNO RENOU** (COMPLEXE DE RECHERCHE INTERPROFESSIONNEL EN AEROTHERMOCHIMIE)

ED 591 PSIME

LSPC Laboratoire de sécurité des procédés chimiques

Normandie Université

DOCTORAL THESIS

To obtain the *Doctor of Philosophy* degree from Normandy University

Chemical Engineering Specialty

Prepared at the National Institute of Applied Sciences of Rouen Normandy

Doctoral School in Physics, Engineering Science, Materials and Energy

Biojet Fuels Production from Lignocellulosic Biomass: Butyl Levulinate a Promising Molecule Towards the Development of Sustainable Aviation Fuels

Prepared and Submitted by:

Wenel Naudy Vásquez Salcedo, M.Sc.

Thesis publicly defended on July 5^{th}, 2024 before the jury composed by:		
Mr. Sébastien Leveneur	Associate Professor / INSA Rouen	Thesis Director
Mr. Bruno Renou	Professor / INSA Rouen	Thesis Co-Director
Mr. Gilles Cabot	Professor / Rouen Normandie	Examiner
Mr. Guillaume Dayma	Professor / Orléans	Examiner
Mr. Guillaume Fayet	Ph.D. / INERIS	Examiner
Mrs. Frederique Battin-Leclerc	Research Director / CNRS LRGP	Rapporteur
Mr. Yves Schuurman	Research Director / CNRS IRCELYON	Rapporteur

Thesis directed by Sébastien Leveneur from the chemical process safety laboratory (LSPC) and Bruno Renou from the interprofessional research complex in aerothermochemistry (CORIA).

INSA INSTITUT NATIONAL DES SCIENCES APPLIQUÉES ROUEN NORMANDIE

MESCYT

ED 591 PSIME

LSPC Laboratoire de sécurité des procédés chimiques

CORIA UMR 6614

"How big would you dream if you knew you could not fail?"
Robert Schuller

Author Resume

Wenel Naudy Vásquez Salcedo
Born in 1994, Bonao
Dominican Republic

Education:

Oct 2021 - April 2024	**Ph.D. Candidate in Chemical Engineering** *LSPC and Coria Research Units* INSA Rouen Normandie, France
Sept 2019 - Sept 2021	**Master in Energy, Fluids and Environment** *Process Engineering Specialty* INSA Rouen Normandie, France
Sept 2011 - Oct 2017	**Bachelor degree in Chemical Engineering** *Magna Cum Laude* UASD, Dominican Republic
July 2009 - July 2011	**Electronics Technician** *High School degree* Bonao, Dominican Republic

Professional Experience:

Oct 2022 - Feb 2023	**INSA Rouen Normandy** *Practical Work Supervisor - Temporary Worker* France
Feb 2021 - Jul 2021	**LSPC - INSA Rouen Normandy** *Master Internship* France
Jul 2016 - Feb 2018	**PEPSICO - Frito Lay Dominicana** *R&D Platform Leader* Dominican Republic

Aug 2016 - Feb 2017	**Autonomous University of Santo Domingo** *Laboratory Assistant - Chemical Engineering department* Dominican Republic
Jun 2015 - Sept 2015	**GSA - Laboratory** *Environmental Analyst* Dominican Republic

Professional Training:

Uni Caen - 2023	**Machine Learning**
ITI - 2016	**Boilers selection, installation and maintenance**
EDX - 2016	**Introduction to Drinking Water Treatment**
EDX - 2016 - 2023	**Introduction to Urban Sewage Treatment**
INFOTEP - 2016	**Quality and Productivity**
INFOTEP - 2015	**Strategic Planning**
INFOTEP - 2015	**Modern Management Techniques**
Quality GB - 2014	**Integrated Management System of ISO 9001:2008, ISO 14001 and OHSAS 18001**
INFOTEP - 2014	**Project Implementation under ISO 9001:2008 standard**

Extra-curricular Activities:

Sep 2023 - Dec 2024	**Baseball Player** *Huskies Rouen - Regional Team DHR1* French Federation of Baseball and Softball
Sep 2023 - Dec 2024	**Softball Player** *Huskies Rouen - Second Division Team D2* French Federation of Baseball and Softball

List of Publications and Communications

Publications

1. Jose Delgado, **Wenel Naudy Vasquez Salcedo**, Giulia Bronzetti, Valeria Casson Moreno, Melanie Mignot, Julien Legros, Christoph Held, Henrik Grenman, Sebastien Leveneur. *Kinetic model assessment for the synthesis of γ-valerolactone from n-butyl levulinate and levulinic acid hydrogenation over the synergy effect of dual catalysts Ru/C and Amberlite IR-120.* Chemical Engineering Journal 430 (2022) 133053. `https://doi.org/10.1016/j.cej.2021.133053`

2. Jose Delgado, **Wenel Naudy Vasquez Salcedo**, Christine Devouge-Boyer, Jean-Pierre Hebert, Julien Legros, Bruno Renou, Christoph Held, Henrik Grenman, Sebastien Leveneur. *Reaction enthalpies for the hydrogenation of alkyl levulinates and levulinic acid on Ru/C – influence of experimental conditions and alkyl chain length.* Process Safety and Environmental Protection 171 (2023) 289–298. `https://doi.org/10.1016/j.psep.2023.01.025`

3. **Wenel Naudy Vasquez Salcedo**, Melanie Mignot, Bruno Renou, Sebastien Leveneur. *Assessment of kinetic models for the production of γ-valerolactone developed in isothermal, adiabatic and isoperibolic conditions.* Fuel 350 (2023) 128792. `https://doi.org/10.1016/j.fuel.2023.128792`

4. **Wenel Naudy Vasquez Salcedo**, Bruno Renou and Sebastien Leveneur. *Thermal Stability for the Continuous Production of γ-Valerolactone from the Hydrogenation of n-Butyl Levulinate in a CSTR.* Processes 2023, 11, 237. `https://doi.org/10.3390/pr11010237`

Communications

- **Wenel Naudy Vásquez Salcedo**, Bruno Renou, Sebastien Leveneur. *Gamma-valerolactone Production from Butyl Levulinate: Advance Kinetic Modeling and Thermal Risk Assessment.* **Oral presentation** at the Calorimetry and Thermal Analysis days, JCAT-52nd edition. June 15-17 2022 Colmar, France.

- **Wenel Naudy Vásquez Salcedo**, Jose Delgado, Henrik Grenman, Mohammad Kemal Agusta, Bruno Renou, Sebastien Leveneur. *Gamma-valerolactone: Promising Intermediate for Bio Jet Fuel.* **Oral presentation** at WasteEng2022, June 27-30 2022 Copenhagen, Denmark.

- Jose Emilio Delgado Liriano, **Wenel Naudy Vasquez Salcedo**, Jean-Pierre Hebert, Christoph Held, Henrik Grenman, Sebastien Leveneur. *Adiabatic Hydrogenation of Alkyl Levulinates.* **Oral Presentation** at the International Symposium on Green Chemistry (ISGC) 2022, La Rochelle, France.

- Jose Emilio Delgado Liriano, **Wenel Naudy Vasquez Salcedo**, Sebastien Leveneur. *Production of γ-Valerolactone: Reaction Enthalpies and Kinetic study.* **Oral Presentation** at JTACC+V4 Conference, June 20-23 2023, Balatonfured Hungary.

- S. Baco, **W. Vásquez**, M. Klinksiek, M. Mignot, J. Legros, C. Held, B. Renou, S. Leveneur. *Safe and Circular Biofuel Production from Lignocellulosic Biomass.* **Poster Presentation** at ECIU University, Research Conference, October 3-4 2023, Barcelona Spain.

Seminars

- **Calorimetry and Safety** Seminar at LSPC, May 11 2022: *γ-Valerolactone Production from Butyl Levulinate Hydrogenation.*
- **ARBRE project** Seminar at LSPC, October 21 2022: *Bio Jet Fuel Production from Lignocellulosic Biomass.*

Acknowledgments

First, I want to thank **God** for giving me the health, strength, and wisdom that have allowed me to reach this point in my life. I will always be grateful to my parents, **Francisco Vásquez Acosta** and **Digna Salcedo Rodríguez**, for always being by my side and giving me their unconditional support in all my projects. Having their support helped me to develop the confidence that characterizes me today. They taught me that all goals can be achieved by working correctly. I also want to thank my younger brother, **Draily Francisco Vásquez Salcedo**, for always believing in me. I want to thank all my family who always support me, trust me, and are always willing to help me.

I am grateful to my girlfriend, **Yamily Mateo Rosado**, for always being by my side and giving me her unconditional love and support. Being with her made the preparation of this thesis less difficult. Among all my close friends, this time I want to thank one of my best friends, **Patricia Ynes Batista Peguero**, who was always present during the development of this thesis, with whom I can always count on.

I thank my thesis supervisors, **Sébastein Leveneur** and **Bruno Renou**, for their guidance, support, and encouragement throughout this journey. Their expertise, patience, and constructive feedback have been instrumental in shaping this research. I would also like to thank the members of my individual supervision committee, **Alain Ledoux** and **Valeria Casson-Moreno**, for their involvement in developing this research.

I extend my appreciation to the **Ministry of Higher Education, Science, and Technology (MESCYT)** of the Dominican Republic for providing the main funding source during this research. I thank the **National Institute of Applied Sciences (INSA)**, the **Chemical Process Safety Laboratory (LSPC)**, and the **Interprofessional Research Complex in Aerothermochemistry (CORIA)** for providing the necessary workspace, resources, and facilities that made this research possible. Also, I thank to **MUST**, **ARBRE**, and **PROMETEE** projects for providing financial support to the research.

I want to thank the **CALIOPE** program and all the institutions involved in it for allowing me to come to France to do my doctorate. I am indebted to all **my colleagues** and **fellow researchers** for their camaraderie, stimulating discussions, and shared experiences, which have made this academic endeavor both rewarding and enjoyable.

I would also like to thank all the research, technical, and administrative staff of LSPC and CORIA for their involvement, participation, and support in this research. I would like to highlight the special contribution of **Maria Pereira** and **Jean-Pierre Herbert** from LSPC. Moreover, thank you for their support and assistance to **Alexis Vandel** and **Gilles Cabot** from CORIA. I am grateful to **Jose Delgado** and **Marie-Eve Clavel** for having received me and trained me in the use of the experimental facilities in the LSPC and CORIA research units, respectively.

This thesis would not have been the same without the collective contributions of all those mentioned above, and for that, I am sincerely grateful.

Wenel N. Vásquez S.
Rouen, France
July 2024

Abstract

In the context of the aviation sector, which poses significant challenges due to the complexity and stringent standards of fuel, our research proposal gains particular relevance. We aim to develop an integrated approach that fully valorizes lignocellulosic biomass into jet fuels, thereby contributing to the sustainable development of society.

Lignocellulosic biomass is a renewable resource that can be used as feedstock to produce high-value materials and chemicals, such as jet fuel. This type of biomass valorization includes many transformation steps, for which the kinetics and the thermal risk of the chemical reaction are not necessarily known. This work focuses on a specific compound: butyl levulinate (BL). This compound can be obtained from lignocellulosic biomass and can be transformed into gamma-valerolactone (GVL) via hydrogenation. The GVL is a vital platform molecule that can serve as a feedstock to produce substitutes for fossil fuels like gasoline, diesel, and jet fuels.

The main objectives of this research are:

1. To develop a robust and reliable kinetic model for BL hydrogenation to produce GVL. Here, we seek to develop a kinetic model experimentally in different thermal modes of operation, i.e., isothermal, isoperibolic, and adiabatic. This model type not only predicts kinetics and the corresponding heat-flow rate but also allows the assessment of the thermal risk related to the chemical reaction. The experiments for developing this kinetic model were performed in the calorimeter reactor Mettler-Toledo RC1.

2. The complete valorization of lignocellulosic biomass targets the industrial scale. Therefore, the continuous production of GVL from BL should be assessed. In that sense, we studied the thermal stability of the continuous production of GVL from BL in a CSTR reactor (continuous stirred tank reactor).

3. One of the intriguing aspects of our research is the potential use of butyl levulinate (BL) as a fuels additive. We have conducted a thorough assessment of the suitability of BL as a kerosene additive, aiming to understand how its addition affects the combustion efficiency and operating limits in a gas turbine combustion chamber.

The results obtained concerning the kinetic model showed that the Non-Competitive Langmuir-Hinshelwood models predict the experimental data of concentration and temperature for BL hydrogenation with good accuracy. The thermal risk analysis, linked to BL hydrogenation, showed that the energy released during the reaction is relatively low, $\mathbf{\Delta H_{hyd}} = -35.28\,kJ/mol \pm 1.00\,kJ/mol$, and subsequently the thermal stability study showed that for values of $\mathbf{Ua} > 1500\,W/m^3/K$ in a continuous reactor, the risk of thermal instabilities is low. The evaluation of BL as a kerosene additive showed that adding up to 20% of BL into Kerosene does not significantly change the physical properties, neither the combustion efficiency nor the operating limits in the operating conditions considered during the combustion assessment.

Résumé

Dans le contexte du secteur de l'aviation, qui pose des défis importants en raison de la complexité et des normes strictes en matière de carburant, notre proposition de recherche revêt une pertinence particulière. Nous visons à développer une approche intégrée qui valorise pleinement la biomasse lignocellulosique en carburéacteurs, contribuant ainsi au développement durable de la société.

La biomasse lignocellulosique est une ressource renouvelable qui peut être utilisée comme matière première pour produire des matériaux et des produits chimiques de grande valeur, tels que le kérosène. Ce type de valorisation de la biomasse comprend de nombreuses étapes de transformation, pour lesquelles la cinétique et le risque thermique de la réaction chimique ne sont pas forcément connus. Ce travail se concentre sur un composé spécifique : le lévulinate de butyle (BL). Ce composé peut être obtenu à partir de la biomasse lignocellulosique et peut être transformé en gamma-valérolactone (GVL) par hydrogénation. Le GVL est une molécule de plateforme vitale qui peut servir de matière première pour produire des substituts aux combustibles fossiles comme l'essence, le diesel et les carburéacteurs.

Les principaux objectifs de cette recherche sont les suivants :

1. Développer un modèle cinétique robuste et fiable pour l'hydrogénation BL afin de produire du GVL. Ici, nous cherchons à développer expérimentalement un modèle cinétique dans différents modes de fonctionnement thermiques, c'est-à-dire isotherme, isopéribolique et adiabatique. Ce type de modèle permet non seulement de prédire la cinétique et le débit de chaleur correspondant, mais aussi d'évaluer le risque thermique lié à la réaction chimique. Les expériences de développement de ce modèle cinétique ont été réalisées dans le réacteur calorimétrique Mettler-Toledo RC1.

2. La valorisation complète de la biomasse lignocellulosique vise l'échelle industrielle. Par conséquent, la production continue de GVL à partir de BL doit être évaluée. En ce sens, nous avons étudié la stabilité thermique de la production continue de GVL à partir de BL dans un réacteur CSTR (réacteur à cuve agitée continue).

3. L'un des aspects intrigants de notre recherche est l'utilisation potentielle du lévulinate de butyle (BL) comme additif pour carburants. Nous avons mené une évaluation approfondie de l'adéquation du BL en tant qu'additif de kérosène, dans le but de comprendre comment son ajout affecte le rendement de combustion et les limites de fonctionnement dans une chambre de combustion de turbine à gaz.

Les résultats obtenus concernant le modèle cinétique ont montré que les modèles non compétitifs de Langmuir-Hinshelwood prédisent les données expérimentales de concentration et de température pour l'hydrogénation des BL avec une bonne précision. L'analyse du risque thermique, liée à l'hydrogénation BL, a montré que l'énergie libérée lors de la réaction est relativement faible, $\mathbf{\Delta H_{hyd}} = -35.28\,kJ/mol \pm 1.00\,kJ/mol$, et par la suite l'étude de stabilité thermique a montré que pour des valeurs de $\mathbf{Ua} > 1500\,W/m^3/K$ dans un réacteur continu, le risque d'instabilités thermiques est faible. L'évaluation du BL en tant qu'additif de kérosène a montré que l'ajout de 20 % de BL dans le kérosène ne modifie pas de manière significative les propriétés physiques, ni l'efficacité de la combustion, ni les limites de fonctionnement dans les conditions de fonctionnement prises en compte lors de l'évaluation de la combustion.

Resumen

En el contexto del sector de la aviación, que plantea importantes retos debido a la complejidad y a los estrictos estándares de combustible, nuestra propuesta de investigación cobra especial relevancia. Nuestro objetivo es desarrollar un enfoque integrado que valorice plenamente la biomasa lignocelulósica en combustibles para aviones, contribuyendo así al desarrollo sostenible de la sociedad.

La biomasa lignocelulósica es un recurso renovable que se puede utilizar como materia prima para producir materiales y productos químicos de alto valor, como el combustible para aviones. Este tipo de valorización de la biomasa incluye muchas etapas de transformación, para las cuales no necesariamente se conoce la cinética y el riesgo térmico de la reacción química. Este trabajo se centra en un compuesto específico: el levulinato de butilo (BL). Este compuesto se puede obtener a partir de biomasa lignocelulósica y se puede transformar en gamma-valerolactona (GVL) mediante hidrogenación. El GVL es una molécula plataforma vital que puede servir como materia prima para producir sustitutos de combustibles fósiles como la gasolina, el diésel y los combustibles para aviones.

Los principales objetivos de esta investigación son:

1. Desarrollar un modelo cinético robusto y fiable para la hidrogenación de BL para producir GVL. Aquí, buscamos desarrollar un modelo cinético experimentalmente en diferentes modos de operación térmica, es decir, isotérmico, isoperibólico y adiabático. Este tipo de modelo no solo predice la cinética y el flujo de calor correspondiente, sino que también permite evaluar el riesgo térmico relacionado con la reacción química. Los experimentos para el desarrollo de este modelo cinético se realizaron en el reactor calorímetro Mettler-Toledo RC1.

2. La valorización completa de la biomasa lignocelulósica se dirige a la escala industrial. Por lo tanto, debe evaluarse la producción continua de GVL a partir de BL. En ese sentido, estudiamos la estabilidad térmica de la producción continua de GVL a partir de BL en un reactor CSTR (reactor continuo de tanque agitado).

3. Uno de los aspectos intrigantes de nuestra investigación es el potencial uso del levulinato de butilo (BL) como aditivo de combustibles. Hemos llevado a cabo una evaluación exhaustiva de la idoneidad del BL como aditivo de queroseno, con el objetivo de comprender cómo su adición afecta la eficiencia de la combustión y los límites de funcionamiento en una cámara de combustión de turbina de gas.

Los resultados obtenidos en relación con el modelo cinético mostraron que los modelos no competitivos de Langmuir-Hinshelwood predicen los datos experimentales de concentración y temperatura para la hidrogenación de BL con buena precisión. El análisis de riesgo térmico, vinculado a la hidrogenación BL, mostró que la energía liberada durante la reacción es relativamente baja, $\mathbf{\Delta H_{hyd}} = -35.28\,kJ/mol \pm 1.00\,kJ/mol$, y posteriormente el estudio de estabilidad térmica mostró que para valores de $\mathbf{Ua} > 1500\,W/m^3/K$ en un reactor continuo, el riesgo de inestabilidades térmicas es bajo. La evaluación del BL como aditivo de queroseno mostró que la adición de hasta un 20% de BL al queroseno no cambia significativamente las propiedades físicas, ni la eficiencia de la combustión ni los límites de funcionamiento en las condiciones de funcionamiento consideradas durante la evaluación de la combustión.

Table of Contents

List of Figures

List of Tables

Nomenclature

Abbreviations

AIC	Akaike Information Criterion
ALs	Alkyl Levulinates
BHP	Butyl 4-hydroxy Pentanoate
BL	Butyl Levulinate
BPE	Bayesian Parameter Estimation
BtL	Biomass to Liquid
BuOH	Butanol
CAD	Computer-Aided Design
CAF	Conventional Aviation Fuels
CFD	Computational Fluid Dynamics
CORIA	Interprofessional Research Complex in Aerothermochemistry
CSTR	Continuous Stirrer-Tank Reactor
EL	Ethyl Levulinate
ER1	Eley-Rideal Kinetic Model
GCR	Global Chemical Reaction
GHG	Greenhouse gas
GVL	Gamma-valerolactone
HARTur	High Altitude Reignition for Gas Turbine Facility
HPD	Highest Probability Density
LA	Levulinic Acid
LCB	Lignocellulosic Biomass
LH1	Langmuir-Hinshelwood without hydrogen dissociation
LH2	Langmuir-Hinshelwood with hydrogen dissociation
LHV	Lower Heating Value
LSPC	Chemical Process Safety Laboratory
NCLH1	Non-Competitive Langmuir-Hinshelwood without hydrogen dissociation
NCLH2	Non-Competitive Langmuir-Hinshelwood with hydrogen dissociation
OP	Operating Conditions of Pressure and Temperature
PSA	Parametric Sensitivity Analysis
RMG	Reaction Mechanism Generator
RQL	Rich-Burn, Quick-Quench and Lean-Burn
Ru/C	Ruthenium over Activated Carbon
SAF	Sustainable Aviation Fuels

Notations

[**BHP**]	Butyl 4-hydroxy Pentanoate Concentration
[**BL**]	Butyl Levulinate Concentration
[**BuOH**]	Butanol Concentration
[**GVL**]	Gamma-valerolactone Concentration
[$\mathbf{H_2}$]	Hydrogen Concentration
$\mathbf{C_p}$	Heat Capacity
D	Stirrer Diameter
Ea	Activation Energy
Fr	Froude Number
He	Henry's Constant
J	Differential Equation System Jacobian Matrix
$\mathbf{K_eq}$	Catalyst Surface Equilibrium Constant
$\mathbf{K_g}$	Combustion Chamber Geometric Factor
$\mathbf{K_i}$	Equilibrium Adsorption Constant for specie i
N	Stirring Rate
P	Pressure
$\mathbf{P_{H_2}}$	Hydrogen Pressure
Q	Volumetric Flow Rate
$\mathbf{Q_{C80}}$	Reaction Energy Absorbed in the C80
$\mathbf{Q_{RC1}}$	Reaction Energy Released in the RC1
R	Ideal Gas Constant
$\mathbf{R_{cyc}}$	Cyclization Rate
$\mathbf{R_{hyd}}$	Hydrogenation Rate
Re	Reynolds Number
$\mathbf{S_n(y_i)}$	Normalized Sensitivity of Variable y_i
T	Temperature
$\mathbf{T_{amb}}$	Ambient Temperature
$\mathbf{T_{in}}$	Inlet Temperature
$\mathbf{T_j}$	Reactor Jacket Temperature
$\mathbf{T_r}$	Reaction Temperature
UA	Global Heat Transfer Coefficient
Ua	Global Heat Transfer Coefficient per units of volume
$\mathbf{V_r}$	Reaction Volume
We	Weber Number
$\mathbf{\Delta H_{cyc}}$	Cyclization Enthalpy
$\mathbf{\Delta H_{hyd}}$	Hydrogenation Enthalpy
$\mathbf{\Delta H_{sol}}$	Solution Enthalpy
$\dot{\mathbf{m}}$	Mass Flow Rate
$\dot{\mathbf{n}}$	Molar Flow Rate
$\mathbf{k_{cyc}}$	Cyclization Rate Constant
$\mathbf{k_{hyd}}$	Hydrogenation Rate Constant
$\mathbf{k_La}$	Volumetric Mass Transfer Coefficient
$\mathbf{q_{rem}}$	Removal Heat Flow
$\mathbf{q_{rex}}$	Reaction Heat Flow
t	Time

Greek Letters

α	Heat Loss Coefficient
δ	Atomization Spray Thickness
η	Combustion Efficiency
λ	Jacobian Matrix Eigenvalue
μ	Dynamic Viscosity
ν	Kinematic Viscosity
ω	Catalyst Loading
Π	Combustion Chamber Operating Variable
ϕ	Fuel-Air Equivalence Ratio
ρ	Density
σ	Surface Tension
τ	Residence Time
θ	Atomization Spray Angle

Subscripts and Superscripts

0	Initial Value
$_{adi}$	Adiabatic Conditions Value
$_{cat}$	Catalyst Value
$_{crit}$	Critical Value
$_{ext}$	Extinction Value
$_{f}$	Final Value
$_{in}$	Inlet Value
$_{ins}$	Inserted Elements Value
$_{liq}$	Liquid Phase Value
$_{mix}$	Mixture Value
$_{mod}$	Modified Value
$_{out}$	Outlet Value
$_{ref}$	Reference Value
*	Equilibrium Value
$_{eq}$	Equilibrium Value

Chapter 1
Introduction

This chapter aims to provide a comprehensive overview of the literature pertinent to the doctoral thesis topic, offering insights into the current state of research. It then delves into presenting the general context of the study, providing all necessary elements to understand the research justification and significance. Finally, the chapter outlines the objectives and structure of the thesis, providing readers with a roadmap for navigating the manuscript.

1.1 Background

The substantial dependence of modern society on fossil oil for energy and material production emphasizes a fundamental aspect of the contemporary societal framework. Fossil oil, derived from ancient organic matter, serves as a cornerstone resource driving industrial processes, transportation systems, and the production of a vast array of everyday materials. As of 2022, global energy consumption reached approximately 604.04 exajoules (EJ), with fossil oil accounting for around 31.5 % of this total [18]. Throughout the 20th century, the United States developed a significant reliance on fossil fuels across all sectors of its economy [19].In 2020, Cambridge Econometrics assessed the dependency level of the European Union on imported oil; data indicates that crude oil and petroleum products contribute to nearly half of the final energy consumption in the EU, with the transport sector accounting for the majority of this demand [20].

However, it is essential to emphasize that petroleum is a non-renewable resource, meaning its availability is finite and subject to depletion over time. This poses a significant challenge, especially considering the ongoing increase in society's consumption of petroleum, which is driven by factors like population growth, economic expansion, and technological advancements. Research indicates that access to reliable energy services is fundamental for well-being, human and countries development [21, 22]. Given the finite nature of petroleum reserves, there is an increasing urgency to transition towards sustainable energy sources and innovative material production methods that do not depend on petroleum. Lignocellulosic biomass (LCB) stands out as a promising renewable source of carbon, that can be used to produce fuels and materials. It is considered a better alternative to fossil oil because of its global availability, lower environmental impact, and low cost [23, 24, 25, 26, 27, 3]. However, the use of LCB should be carefully managed to avoid the ethical dilemma of food versus fuel. We have a moral obligation to ensure that our energy and material production methods are sustainable and do not compromise the availability of food for the world's population [28, 29, 30].

The valorization of lignocellulosic biomass into chemicals, fuels, and materials is essential to decrease society's dependency on petroleum, reduce CO_2 emissions, and favor circular economy [30, 31, 12]. The valorization of LCB involves several stages of physical and chemical transformations to enhance efficiency and mitigate the risk of thermal runaway in biorefineries. The knowledge of catalysis, kinetics, thermodynamics, and thermal stability are crucial for such

processes [32]. Biofuels derived from lignocellulosic biomass have garnered significant attention and recognition for their adherence to established standards and industrial processing protocols, i.e., bioethanol and biodiesel [33, 34, 26]. However, a notable gap exists in our understanding and expertise regarding the production of jet fuels from biomass sources. While the production of biofuels such as ethanol and biodiesel has been extensively researched and standardized, the complexities inherent in jet fuel production from biomass present unique challenges. Factors such as meeting the stringent performance requirements, ensuring compatibility with existing aircraft engines, and achieving cost competitiveness necessitate a deeper exploration and development of innovative technologies in this area. Addressing this knowledge gap holds immense promise not only for diversifying our fuel sources but also for reducing the aviation industry's carbon footprint, ultimately contributing to a more sustainable future.

1.2 Sustainable Aviation Fuels

Aviation is an indispensable element in contemporary society, fostering worldwide connectivity and economic prosperity. Nonetheless, the environmental repercussions of aviation, notably its contribution to greenhouse gas (GHG) emissions and air pollution, have prompted concerns regarding its sustainability. Aviation contributes around 2 to 3 % of global CO_2 emissions, exhibiting a growth rate faster than rail, road, or maritime transport in recent decades. Notably, fuel consumption alone accounts for 77 to 91 % of these emissions, with processing contributing from 8 to 12 % [10]. Consequently, future strategies aimed at decarbonization and mitigating GHG emissions involve transitioning from conventional fossil kerosene fuels to drop-in biofuels, hydrogen, or battery-powered alternatives.

To reduce CO_2 emissions within a relatively short timeframe, adopting sustainable aviation fuels (SAF) emerges as a highly appealing option [11]. SAF is the term used to describe aviation fuels that are derived from non-fossil resources, such as biofuels from biomass, organic-derived waste feedstocks, or synthetic fuels from carbon capture, in which the production energy comes from renewable sources. The aviation industry and many governments are setting ambitious goals to reduce the impact of aircraft emissions on climate change. Through the Air Transport Action Group (ATAG), the aviation industry is now targeting net zero CO_2 emission by 2050 [2]. The Aerospace Technology Institute (ATI) assessment towards net zero emissions shows that Sustainable Aviation Fuels (SAF) are crucial to achieve this target [1].

When a fuel is burned in a jet engine, it reacts with oxygen in the air to produce mainly carbon dioxide CO_2, and water vapor H_2O. This combustion process releases large amounts of thermal energy, which the jet engine uses to produce thrust. The only way to reduce the CO_2 produced by an aircraft that operates with conventional fuels (CAF) is by decreasing fuel consumption, and this is achieved by increasing the efficiency of the jet engines [1]. SAF allow the reduction of greenhouse gas emissions throughout their life cycle. SAF reduce emissions during production or through feedstock (CO_2 capture). Figure 1.2 is a representation of the life cycle of CAF and SAF.

SAF viability comes from their ability to match the quality and characteristics of conventional jet fuel, enabling their utilization in existing aircraft fleets. This aspect holds paramount significance as it circumvents the need for manufacturers to undertake engine or aircraft redesigns and eliminates the necessity for fuel suppliers and airports to construct new fuel supply infrastructure. Furthermore, the aviation sector benefits significantly from the technical feasibility of implementing drop-in biofuels, owing to the remarkable uniformity observed in existing aircraft,

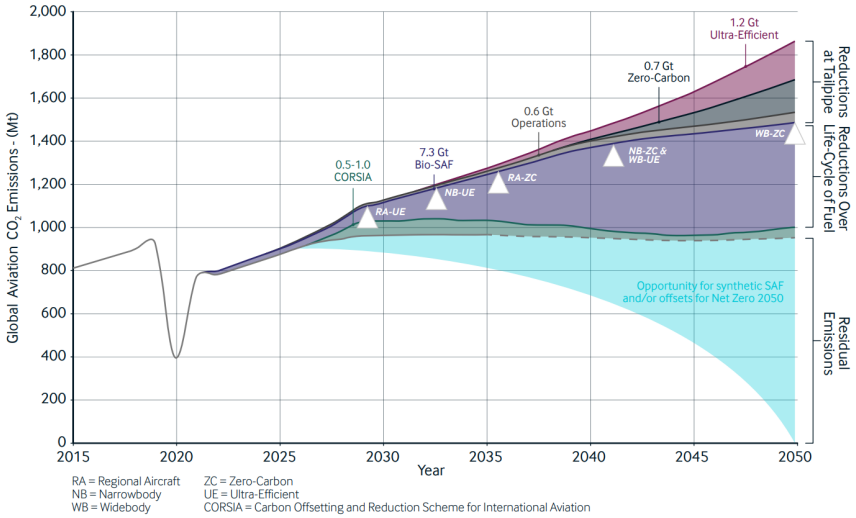

Figure 1.1 ATI's scenario for Net Zero global aviation emissions, taken from [1].

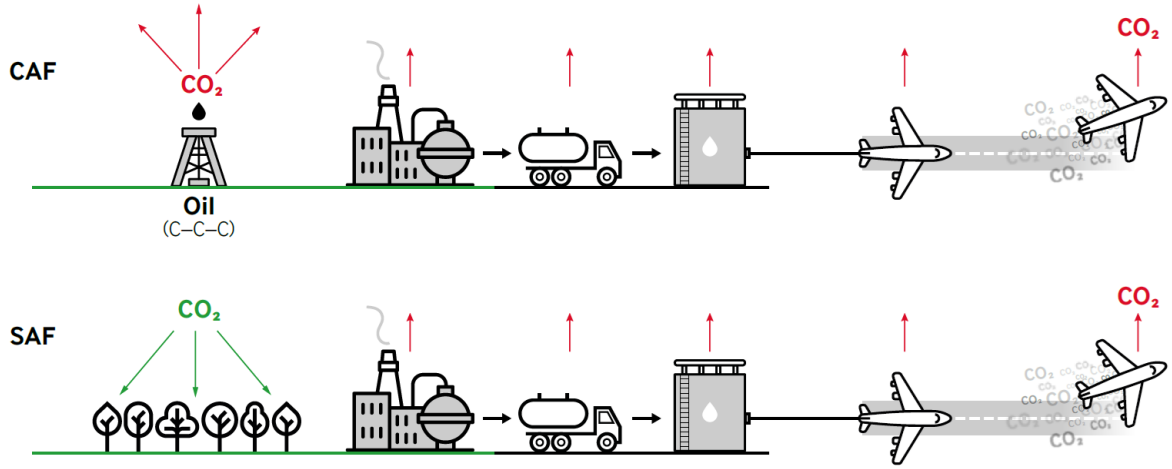

Figure 1.2 Life cycle emissions illustration of CAF and SAF, modified from [2].

engines, and fuel specifications [35]. As part of its long-term strategy, Europe has set a target for the aviation industry to incorporate a minimum of 40 % sustainable alternative fuels by the year 2050 [11, 36].

The global adoption of SAF could be faster today and focused only on some geographic regions. One of the main reasons limiting the use of 100% SAF is their lack of aromatic compounds. Current regulations state that the content of aromatic compounds of aviation fuel must be between 8-25% in order to comply with its secondary functions of lubrication and sealing [37]. For this reason, SAF must be blended with CAF up to a certain percentage to meet at least the minimum required of aromatic compounds. Conventional aviation fuels (CAF) are mixtures of hundreds of hydrocarbon compounds between 8 to 16 carbon atoms per molecule. It is usual to classify the hydrocarbons present in petroleum fuel into four main groups [38]:

- ***Paraffins***: These have the general formula C_nH_{2n+2}. They are the major constituents of CAF, and the percentage depends on the source of the crude oil and the distillation process. Paraffins generally have a higher energy content per unit of mass (MJ/kg) and lower density than other compounds with the same carbon atoms.

- ***Oleoffins***: They have the general formula C_nH_{2n}. They do not normally exist in crude oil but are produced by conversion processes in the refineries.
- ***Naphthenes***: Naphthenes, which have the general formula $(CH_2)_n$. They are saturated hydrocarbons in which the carbon atoms are linked to form rings instead of chains, like paraffin.
- ***Aromatics***: These ones contains at least one benzene ring. They have a higher density but lower energy content than other fuel hydrocarbons because they contain fewer hydrogen atoms.

In the aviation industry, the predominant fuel is kerosene (Jet A-1), derived from crude oil. The types of hydrocarbons found in kerosene are mainly n-paraffins, isoparaffins, naphthenes, and aromatic [2]. A promising avenue for sustainable aviation involves replacing kerosene with sustainable aviation fuels (SAF). Drop-in biofuels are fuels produced from biomass sources through biological, thermal, and chemical conversion processes. *Drop-in biofuels* can be blended with conventional fuels, requiring limited adaptations in existing infrastructure and equipment. Additionally, SAF may reduce oil dependency and create new job opportunities.

Table 1.1 Composition and properties of fuel Jet A-1 according to ASTM D1655, taken from [10].

		Value or range (best-worst)
Composition, wt. %:	n-alkanes	26 - 13
	iso-alkanes	37 - 19
	Monocyclic alkanes	19 - 30
	Bicyclic alkanes	3 - 17
	Sulfur max.	0.30
	Aromatics max.	25 % vol
Properties:	Hydrogen to carbon ratio (H/C)	2.01 - 1.90
	Specific energy (MJ/kg)	43.2 - 42.9
	Density at 15^{o}C (kg/m^3)	775.0 - 840.0
	Energy density (MJ/L)	33.7 - 35.5
	Net heat of combustion (MJ/kg)	42.8
	Avg. MW (g/mol)	152 - 166
	Kinematic viscosity (mm^2/s)	3.5 - 6.5
	Flash point (^{o}C)	42 - 60
	Freezing point (^{o}C)	Max. -47

1.2.1 Feedstocks for SAF

Sustainable aviation fuels (SAF) are fuels derived from carbon-containing renewable feedstocks. The origins of the carbon of the different feedstocks are outlined below; these definitions were taken from [2]:

1. *Biomass to Liquid (BtL)*: Carbon sources from naturally grown biomass, such as sugary or oily crops, agricultural and forestry residues, or even algae. In this case, the CO_2 is absorbed from the atmosphere by a plant that can be converted into fuel.

2. *Waste to Liquid (WtL)*: This is a subset of BtL, which comes from carbon sources from used cooking oil, animal fat, or organic matter in municipal solid waste. While the origin of the feedstocks is also biomass, in these cases, the CO_2 benefit if SAF comes from avoiding the release of carbon dioxide and other GHGs from organic waste into the atmosphere.

3. *Power to Liquid (PtL)*: This type of sustainable aviation fuel is produced using an innovative process. The energy input for PtL SAF comes from electric energy, which has to be produced from renewable sources. PtL SAF collects carbon from atmospheric or industrial flue gases. This carbon, in the form of CO_2, is converted to CO and is then combined with electrically produced hydrogen to produce a hydrocarbon fuel.

4. *Solar to Liquid (StL)*: This type of sustainable aviation fuel is produced using solar heat, which is a renewable energy source. By concentrating sunlight into a chemical reactor, CO_2 and water are converted into CO and hydrogen to produce a hydrocarbon fuel, just like in the PtL process. This highlights the importance of renewable energy in the production of sustainable aviation fuels.

1.2.2 Production Processes of SAF

Following the recognition of Sustainable Aviation Fuels (SAF) as a measure for mitigating emissions in international aviation, notable advancements have been achieved regarding production, certification, and commercial utilization. As of the year 2021, ASTM D7566 had approved seven conversion processes for SAF production, marking a significant milestone in the industry's journey towards sustainability:

1. Fischer-Tropsch hydro processed synthesized paraffinic kerosene (FT-SPK)

2. Synthesized paraffinic kerosene from hydro-processed esters and fatty acids (HEFA-SPK)

3. Synthesized iso-paraffins from hydro-processed fermented sugars (SIP)

4. Synthesized kerosene with aromatics derived by alkylation of light aromatics from non-petroleum sources (FT-SKA)

5. Alcohol to jet synthetic paraffinic kerosene (ATJ-SPK)

6. Catalytic hydro thermolysis jet (CHJ)

7. Synthesized paraffinic kerosene from hydrocarbon-hydro-processed esters and fatty acids (HC-HEFA-SPK)

Fischer-Tropsch

The Fischer-Tropsch (FT) process is a chemical process used to produce liquid hydrocarbons based on synthesis gas (CO and H_2). The final product obtained from this process depends on the type of reactor and catalyst used. FT synthesis can be described as a set of catalytic processes that comprises biomass gasification, cleaning, and conditioning of the produced synthesis gas and subsequent synthesis to obtain liquid biofuels.

[1]Fuel Readiness Level: It represents the fuel progress towards its commercialization.

Table 1.2 Conversion process, feedstocks, and Fuel Readiness Level of the production pathways certified by ASTM for use in commercial flights, modified from [11].

Conversion Process	Possible Feedstocks	Blending Ratio	FRL[1]
FT-SPK	Coal, natural gas, biomass	50 %	7
HEFA-SPK	Bio-oils, animal fat, recycled oils	50 %	9
HFS-SIP	Biomass used for sugar production	10 %	5-7
FT-SPK	Coal, natural gas, biomass	50 %	7
ATJ-SPK	Biomass from starch/sugar production	30 %	7
CHJ-SPK	Bio-oils	50 %	6-7
HC-HEFA-SPK	Hydrocarbons, esters and fatty acids	10 %	6

Hydroprocessed Esters and Fatty Acids

Hydroprocessed esters and fatty acids (HEFA) are processed by animal fats, vegetable oils, and algae oils. Triglycerides are the main building blocks of fats and oil. The transformation process involved catalytic reactions in the presence of hydrogen. Due to the presence of oxygen and unsaturated carbon bonds, it is necessary to perform deoxygenation and hydrogenation steps to produce saturated fuels. Most of the SAF available today comes from the HEFA process from WtL origin [2].

Synthesized Iso-Paraffins

Synthesized Iso-Paraffins (SIP) are synthetic hydrocarbons produced by hydroprocessing and fractionating farnesene from sugar fermentation [11]. In the first step, the biomass is pre-treated by enzymatic hydrolysis, and the solubilized sugars are separated and concentrated to subsequently undergo a biological conversion and oligomerization to obtain the liquid fuel.

Alcohol-to-Jet

Alcohol-to-jet (ATJ) is a biochemical conversion process for the production of an aviation fuel mixture based on alcohol. Only when biomass is pre-treated and conditioned can the alcohols be produced via fermentation processes. ATJ obtained from ethanol or butanol intermediates is allowed to be mixed up to 30 % with kerosene.

1.3 Lignocellulosic Biomass

A promising feedstock for producing sustainable aviation fuels (SAF) is the lignocellulosic biomass (LCB), or biomass to liquid (BtL). Lignocellulosic biomass refers to plant-derived materials mainly composed of cellulose, hemicellulose, and lignin polymers [3]. Studies indicate that approximately 181.5 billion tons of lignocellulosic biomass are generated annually worldwide, with around 8.2 billion tons currently being utilized [26]. The feedstocks available for energy are mainly from agriculture, forest, and industry [12]. Table 1.3 lists some types of LCB and examples.

The composition of the Lignocellulosic biomass may vary according to the source. However, the average consists of 40-50 % cellulose, 20-30 % hemicellulose and 15-30 % of lignin with other minor components, such as minerals [25]. Cellulose, a linear polysaccharide composed of glucose units linked by β-1,4-glycosidic bonds, forms the rigid framework of plant cell walls, providing mechanical strength and stability. Hemicellulose, a heterogeneous group of polysaccharides

Table 1.3 Lignocellulosic Biomass feedstocks for Energy, adapted from [12].

Source	Type	Example
Agriculture	Lignocellulosic energy crops	Herbaceous crops
	Crop residues	Crop straw
	Oil, sugar and starch energy crops	Rape seed, Sugarcane, Corn
Forest	Dedicated forestry	Short rotation plantations
	Forestry by-products	Barks, Wood blocks, etc.
Industry	Lignocellulosic agro-industrial residues	Rice husk, Sugarcane bagase
	Wood industry residues	Industrial waste wood
Other	Lignocellulosic waste	Residues from parks and gardens

comprising various sugar units, contributes to the amorphous regions of the cell wall, enhancing flexibility and cohesion. Lignin, a complex aromatic polymer derived from phenylpropanoid units, acts as a binding matrix between cellulose and hemicellulose, imparting rigidity, hydrophobicity, and resistance to microbial degradation.

Together, these three components constitute the structural integrity of lignocellulosic biomass, offering immense potential for applications in renewable energy, bioproducts, and sustainable materials [26, 39]. Figure 1.3 shows the general structure of lignocellulosic biomass.

Lignocellulosic biomass can be converted into valuable products using various methods, including thermochemical, physicochemical, or biological approaches such as pyrolysis, hydrolysis, and fermentation [27, 30, 40]. However, the effectiveness of these methods relies heavily on the quality of the pretreatment process. The physicochemical properties of biomass play a critical role in determining the most suitable pretreatment method for effective conversion [41]. Factors such as the biomass's composition, structure, and moisture content significantly influence the choice of pretreatment strategy [12].

Pretreatment is essential for breaking down the complex structure of biomass, making it easier to handle. These methods are classified into four primary categories: physical methods like extrusion and grinding; chemical methods including acid, base, ionic liquids, alkali, and transition metal salts; biological methods such as fungus and enzymes; and physicochemical methods like microwave-assisted chemical treatment and Ammonia Fiber Explosion (AFEX)[31]. The efficiency of separating and transforming lignocellulosic biomass's main components, i.e., cellulose, hemicellulose, and lignin, is often improved by combining pretreatment methods [39].

Chemical valorization offers a promising avenue for converting the key constituents of lignocellulosic biomass into **versatile platform compounds**, which serve as building blocks for a wide array of high-value chemicals, materials, and fuels. When starting from cellulose, the resulting products primarily consist of sugars, including notable compounds like 5-hydroxymethylfurfural (HMF), lactic acid, levulinic acid, alkyl levulinates, 1,2-ethylene glycol, sorbitol, 2,5-dihydroxy furan, formic acid, and glycolic acid [31, 42]. Upon the conversion of hemicellulose, the product spectrum shifts, with a focus on compounds such as xylose, furfural (FAL), alkyl levulinates, and γ-valerolactone (GVL) [31, 42]. Lignin constitutes the most abundant aromatic biopolymer on the planet from renewable resources. Therefore, it can be converted into high-value chemicals and fuels [43, 44]. This diverse spectrum of outputs underscores the potential for varied

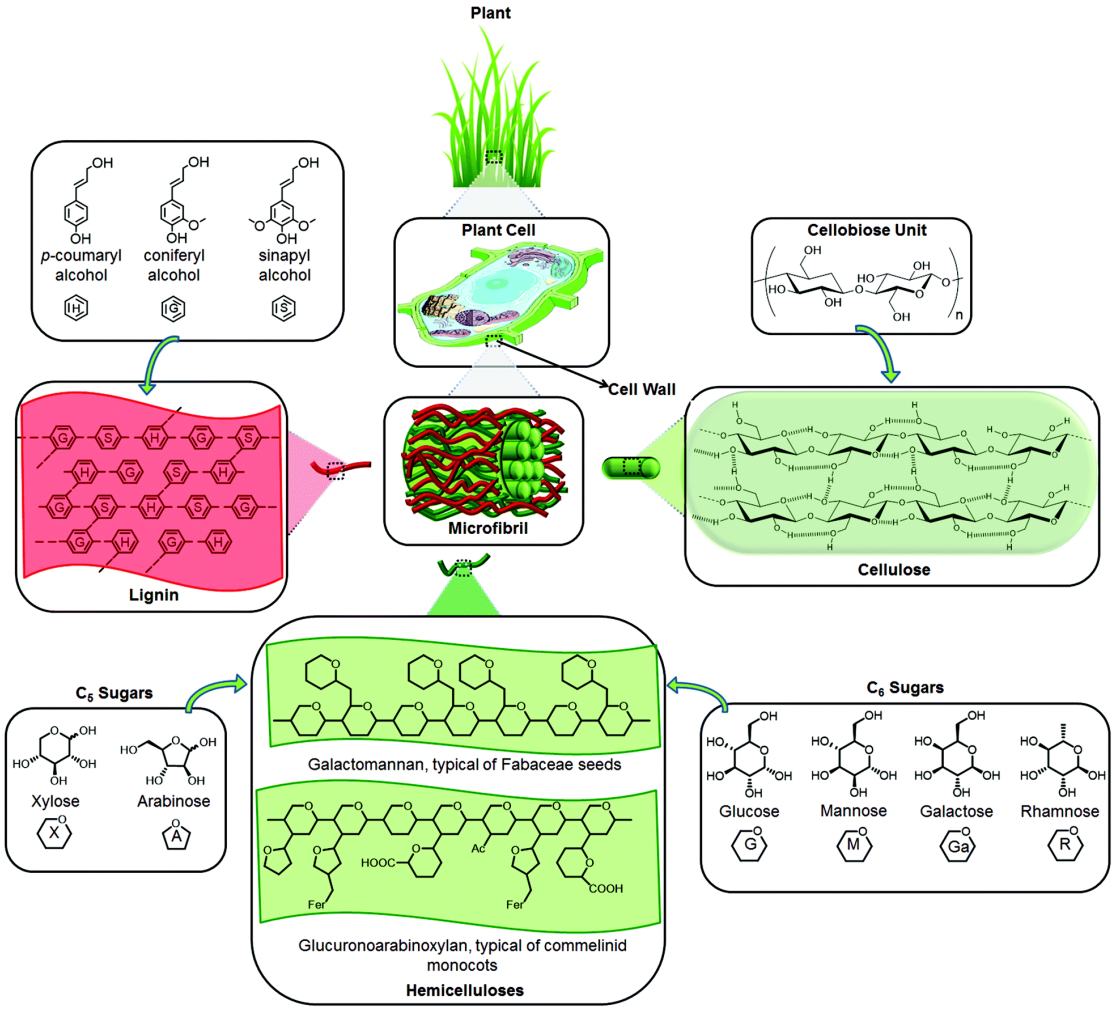

Figure 1.3 Main components and structure of Lignocellulosic Biomass, taken from [3].

downstream applications. This latter biomass compound can potentially address the limitation of 100% use of SAF due to its low content of aromatic compounds.

This work focuses mainly on alkyl levulinates, specifically butyl levulinate and gamma-valerolactone. Through these compounds, it is possible to establish a route of full valorization of the lignocellulosic biomass into a replacement of kerosene, i.e., SAF with a 100% blending percentage, and other high-value products. Figure 1.7 and Figure 1.10.

1.4 Alkyl Levulinates

Levulinic acid and alkyl levulinates are valuable compounds derived from biomass resources, offering various applications across various industries. Levulinic acid, a key platform chemical identified by the US Department of Energy as one of the 12 most valuable platform compounds, can be synthesized from renewable biomass feedstocks through various routes, including acid-catalyzed hydrolysis and dehydration of carbohydrates such as cellulose and hemicellulose [42]. Recent advancements in biocatalysis and enzymatic processes have enabled the sustainable production of levulinic acid from biomass-derived sugars. Alkyl levulinates, esters of levulinic acid, can be synthesized through esterification reactions between levulinic acid and alcohols, such as methanol, ethanol, or butanol, giving as main products methyl levulinate, ethyl levulinate,

and butyl levulinate, respectively [45]. Acid catalysts typically catalyze these reactions under controlled conditions. The choice of alcohol can influence the properties and applications of the resulting alkyl levulinate esters.

Synthesis of levulinic acid or alkyl levulinates from cellulose initiates with its hydrolysis, breaking down the cellulose monomers into glucose units. Subsequently, glucose undergoes isomerization to yield fructose, further dehydrated to form 5-HMF. Quereshi et al. [46] have proposed a mechanism for the synthesis of alkyl levulinates, consisting of two main reactions: first, the hydration of 5-HMF to form levulinic acid (LA), which is subsequently esterified into its corresponding ester based on the alcohol used for alcoholysis; second, 5-HMF is converted into alkyl levulinate via an HMF-ether intermediate, depending on the alcohol utilized, leading to the production of 5-ethoxymethylfurfural (EMF) for ethyl levulinate with ethanol or 5-butoxymethylfurfural (BMF) for butyl levulinate with butanol [42, 47].

When starting from hemicellulose to produce levulinic acid or alkyl levulinates, the process begins with hemicellulose undergoing hydrolysis facilitated by a Bronsted acid, forming a five-carbon sugar and xylose. Xylose subsequently undergoes a three-step continuous dehydration reaction to yield FAL (furfural). FAL is then subjected to a hydrogenation reaction, reducing FAL to furfuryl alcohol (FA). In the presence of a solid acid catalyst and the corresponding alcohol, a fraction of FA undergoes etherification to produce the corresponding furfuryl ether (FE). Additionally, the Bronsted acid facilitates the conversion of FA and FE into a mixture of levulinic acid (LA) and alkyl levulinates (AL) through a hydrolysis ring-opening reaction [42, 47].

Recent research efforts have focused on developing more sustainable and efficient synthesis routes for levulinic acid and alkyl levulinates, including biocatalytic and green chemistry approaches. Levulinic acid and alkyl levulinates represent important compounds in sustainable chemistry, offering diverse applications and significant potential in various industries. Among the alkyl levulinates, ethyl levulinate (EL) and butyl levulinate (BL) stand out as up-and-coming candidates for application as fuels due to their favorable properties and compatibility with conventional fuel systems. They exhibit high energy densities, favorable combustion characteristics, and compatibility with existing fuel infrastructure. These esters can be blended with diesel or gasoline in various proportions without requiring significant modifications to engines or fuel delivery systems [4, 48].

1.4.1 Butyl Levulinate

Butyl levulinate, also known as 4-oxopentanoate, has emerged as a key compound in biomass valorization and sustainable chemistry, drawing considerable attention for its diverse applications such as solvent, additive, and chemical. Notably, its potential as a diesel additive is interesting, as it can be derived from various feedstocks such as levulinic acid, furfuryl alcohol, glucose, fructose, xylose, cellulose, and lignocellulosic biomass. Ahmad et al. [4] conducted a comprehensive review outlining several pathways for butyl levulinate synthesis from different feedstocks, including production from levulinic acid via both biological and chemical methods, furfural and furfuryl alcohol, monosaccharides, and polysaccharides and raw biomass. The conversion and the yield of BL will depend on the feedstock, catalysts, and operating conditions used [4, 49]. Figure 1.5 shows the different pathways used to obtain butyl levulinate.

In recent years, researchers have intensified their efforts to explore various facets of butyl levulinate production and its applications, aiming to enhance both its synthesis and utility. One significant area of investigation has focused on understanding the role of solvents in the syn-

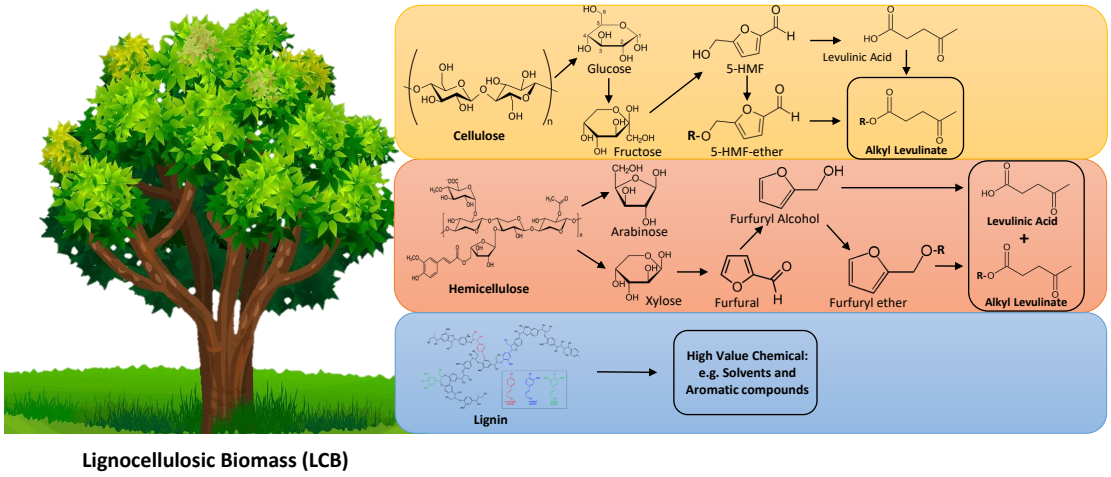

Figure 1.4 Reaction pathways to produce Alkyl Levulinates from lignocellulosic Biomass.

thesis process [17]. Different solvents can influence reaction kinetics, product yields, and the selectivity of the desired compound. Additionally, there has been a growing interest in employing heterogeneous catalysts for butyl levulinate production, offering advantages such as easier catalyst recovery and recycling [50, 51, 52]. Moreover, the development of continuous reactors has garnered attention due to their potential to streamline the production process, improve efficiency, and facilitate scalability [53].

Table 1.4 Physicochemical properties of EL and BL, adapted from [13, 14].

Property	Units	EL Value	BL Value
Chemical formula		$C_7H_{12}O_3$	$C_9H_{16}O_3$
CAS number		539-88-8	2052-15-5
Density (20 ^{o}C)	[g/mL]	1.016	0.974
Viscosity (20 ^{o}C)	[mm^2/s]	2.1	2.8
Flash Point	[^{o}C]	90	110
Boiling Point	[^{o}C]	206	232
Melting Point	[^{o}C]	<-60	<-60
Lower Heating Value	[MJ/kg]	25.2	28.0
KF water	[ppm]	778	234
Solubility of water in ester	[wt %]	8.5	2.6
Solubility of ester in water	[wt %]	15.2	1.3

Due to its properties, Table 1.4, Butyl Levulinate (BL) stands as a better alternative as a fuel additive compared with Ethyl Levulinate (EL) [54, 55]. Both levulinates increase lubricity and conductivity and reduce particulate emissions in diesel blends. These alkyl levulinates show a reduction of 25% (BL) and 31% (EL) in the energy content per unit of volume compared to conventional diesel. BL has a lower water solubility, and for blends of 20% (v/v) with diesel, EL was found to form a separate liquid phase from diesel at 283 K, while BL remained constant miscible in diesel even at the diesel cloud point that is 247 K [14].

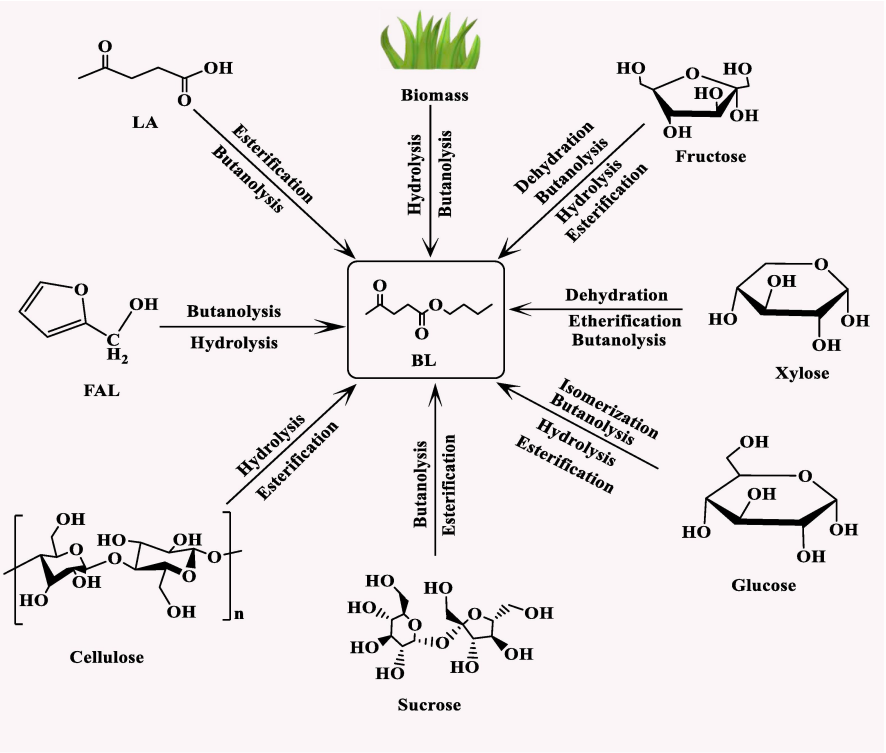

Figure 1.5 Feedstocks for the production of Butyl Levulinate, taken from [4].

Environmental concerns, rising costs, and the shortage of fossil fuels motivate the research and development of alternative aviation fuels. However, any potential alternative must be characterized and tested and meet certain characteristics; these include energy density, good atomization, rapid evaporation, the capability to relight in altitude conditions, low explosive risk on the ground, suitable viscosity, low freezing point, good chemical stability and reasonably nontoxic. For instance, Chuck et al. [56] investigated the compatibility with aviation kerosene of nine potential biofuels derived from sustainable sources, among which the BL was included. They found that BL reduced the energy density, but in all other aspects, this one seemed a reasonable substitute for aviation kerosene; they also warned that BL is not miscible at low temperatures but did not specify the limit.

1.5 Gamma Valerolactone

Over the past decade, gamma-valerolactone (GVL) has garnered significant interest as a valuable chemical synthesized from renewable feedstocks, such as biomass waste and food waste [57]. This attention stems from its unique physicochemical properties and its array of potential applications [5]. GVL is a C_5-cyclic ester belonging to the lactone family. It is a biobased platform molecule found in nature, e.g., fruits [15]. GVL is a clear and colorless liquid with a fruity odor under standard conditions.

GVL is often used as a food additive and sustainable starting chemical to produce energy and other products such as adipic acid and nylon precursor. Thanks to its low melting point, high boiling point, high flash point, and low vapor pressure, the ignition hazard is minimized, allowing it to be stored and transported to distant places safely. GVL does not react with water at temperatures lower than 333.15 K for four weeks [15]; therefore, GVL can be considered a stable molecule, and appropriate catalysts are required for GVL thermal decomposition [58].

Table 1.5 lists the most relevant physicochemical properties of GVL.

Table 1.5 Physicochemical properties of GVL, adapted from [15, 16].

Property	Value
Molecular Formula	$C_5H_8O_2$
CAS Number	108-29-2
Molecular Weight (g/mol)	100.112
Refractive Index (n20/D)	1.432
Density (kg/m^3)	1050
Flash Point (K)	369.15
Melting Point (K)	242.15
Boiling Point (K)	480.15-481.15
Solubility in Water (%)	100
LD_{50}, oral for rat (mg/kg)	8800
ΔH_{evap} (kJ/mol)	54.8 ± 0.4
$\Delta H^0_{c,liq}$ (kJ/mol)	-2649.6 ± 0.8
$\Delta H^0_{f,298}$ (kJ/mol)	-461.3
Cetane Number	<10
Vapor Pressure (kPa)	3.5 at 353.15 K
Lower Heating Value (MJ/kg)	25

1.5.1 Applications of Gamma Valerolactone

GVL as Solvent

Gamma-valerolactone has been recognized to be a green and non-toxic solvent because it has valuable polarity properties and low toxicity [5], and even more considering GVL's physicochemical properties make it a suitable solvent for different applications. GVL shows a better score in terms of safety compared to tetrahydrofuran (THF) [15], a popular solvent for chemical conversion. GVL is an excellent solvent for biomass and fuel transformation. Wettstein et al. [59] showed that GVL increases the yield of cellulose deconstruction to form levulinic acid and furfuryl alcohol. Di Bucchianico et al. [17] showed that using GVL as a solvent improves the fructose transformation into alkyl levulinates. Wang et al. [60] showed that GVL is a suitable solvent during the hydrogenation of levulinic acid and alkyl levulinates to produce GVL.Figure 1.6 and Table 1.6 show some of the chemicals and reactions that can be obtained/performed from lignocellulosic biomass using GVL as a solvent, respectively.

GVL and its Products as Fuel

GVL can be used as an additive to current petroleum fuels similar to ethanol because their lower heating values are similar, LHV_{GVL} = 25.0 MJ/kg versus LHV_{EtOH}= 29.7 MJ/kg. Horvath et al. [61] studied the effects of GVL on gasoline; they compared mixtures of 90 % vol of conventional gasoline and 10 % of GVL or ethanol. They observed that the blend containing GVL had a higher energy content and lower vapor pressure, reducing the emissions of volatile organic compounds (VOC). Bereczky et al. [62] observed that adding 7.1 % of GVL in fossil diesel led to a slight decrease in engine performance compared to fossil diesel since the cetane number is lower for the blend containing GVL. Nevertheless, blending GVL with fossil diesel significantly reduces the CO, total hydrocarbon, and smoke emissions, i.e., 47 %; this highlights the potential of GVL to reduce air pollution.

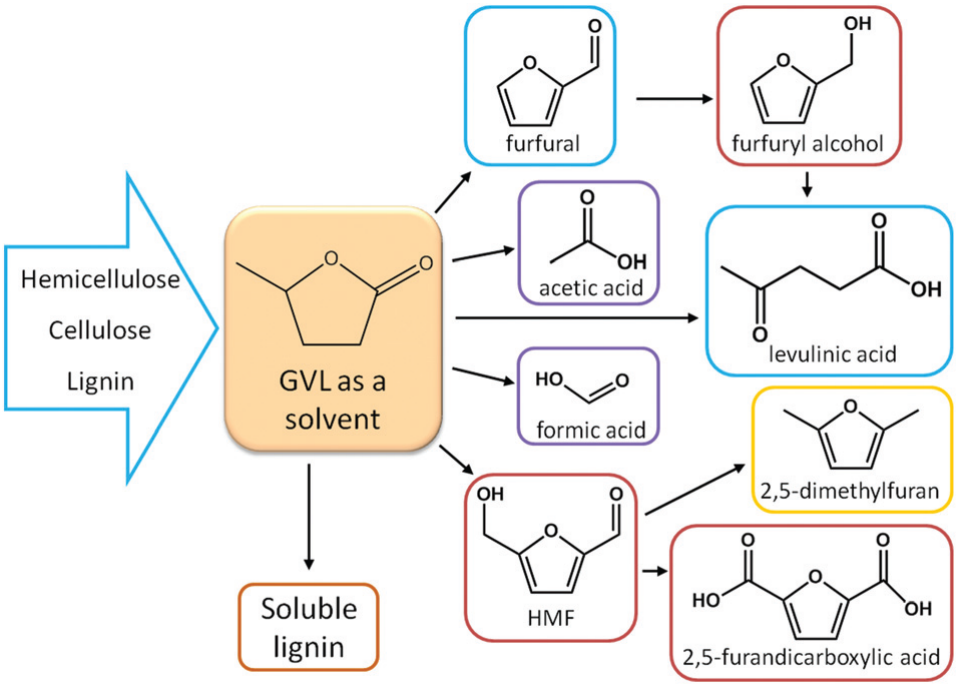

Figure 1.6 Lignocellulosic biomass-derived products using GVL as solvent, taken from [5].

Table 1.6 Chemical reactions conducted using GVL as solvent, adapted from [15, 17].

Reaction	Catalyst	Solvent	Yield
Cellulose to LA and FA	HCl_{aq}	GVL	70 %
Carbohydrates from corn stover and wood	H_2SO_4	GVL	70-90 %
Fructose, glucose and sucrose to HMF	H_2SO_4	GVL	75 %
CO_2 to amines	GVL	GVL	84 %
Bread waste to HMF	$SnCl_4$	GVL	20 %
Corn stover to LA and FA	Pt/SiO_2	GVL	70 %
Glucose to HMF	Amberlyst 70	GVL	59 %
Hemicellulose to furfural	H-Modernite	GVL	80 %
Xylose to furfural	H_2SO_4	GVL	75 %
Fructose and HMF to Butyl Levulinate	Amberlite	GVL/BuOH	>30 %

Due to the high water solubility, smaller cetane number, and relatively lower energy density than fossil-based fuels, GVL can not be implemented directly as fuel. However, to overcome these constraints, GVL can be upgraded into drop-in liquid fuels through catalytic transformation processes. One promising biofuel derived from GVL is methyl tetrahydrofuran (MTHF), which can be obtained via GVL hydrogenation [5, 63]. MTHF exhibits favorable properties for blending with gasoline, allowing up to 70 % blends. Furthermore, MTHF has a significantly higher cetane number of 87, surpassing that of GVL, thereby enhancing its suitability for diesel applications [16]. Additionally, GVL is a promising precursor for generating aromatic compounds and liquid alkanes through ring-opening reactions and subsequent conversion of the resulting intermediates. These aromatic and liquid alkanes, ranging from C_8 to C_{27}, possess immediate utility as constituents in gasoline, diesel, and jet fuel [58, 64, 65].

Additional applications of GVL

GVL presents an opportunity not only for producing renewable fuels but also for synthesizing interesting monomers capable of yielding polymers similar to those derived from petroleum but with different chemical properties. Manzer et al. [66] investigated the production of α-methylene-γ-valerolactone from GVL, which is similar to methyl methacrylate, but the incorporation of the lactone structure enhances the thermal stability. Lange et al. [67] studied the synthesis of methyl pentanoate through the ring-opening of GVL in methanol using acid catalysts, offering routes for its conversion into nylon precursors such as caprolactone, caprolactam, or adipic acid [5].

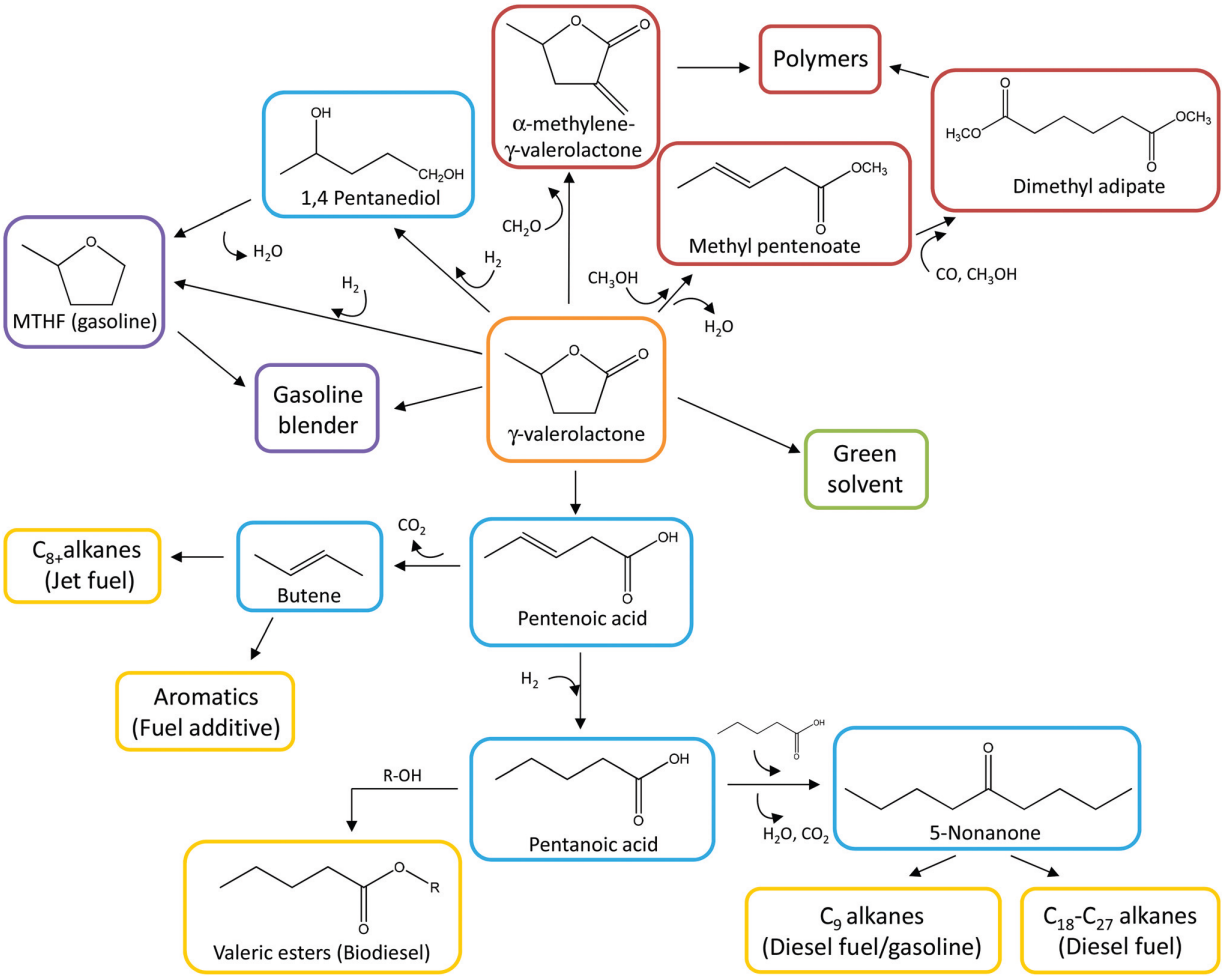

Figure 1.7 Reaction pathways to transform GVL into fuels, fuel additives and chemicals, tanken from [5].

1.5.2 Synthesis of Gamma Valerolactone

GVL synthesis from Levulinic Acid

Currently, the synthesis of gamma valerolactone (GVL) mainly relies on levulinic acid (LA) and its esters (alkyl levulinates) as feedstocks. The catalytic pathways in this process, which have traditionally been regarded as critical in biomass conversion systems, are now relatively well understood. The two possible reaction pathways to produce GVL from LA are illustrated in Figure 1.8.

Pathway 1 involves the hydrogenation of LA's ketone group, resulting in the formation of an unstable intermediate, 4-hydroxy pentanoic acid, followed by dehydration and intramolecular esterification, leading to ring closure and the production of GVL. *Pathway 2* corresponds to the dehydration of LA to α-angelica lactone followed by its hydrogenation to form GVL. The efficiency of the hydrogenation step in both pathways depends on the metal catalyst's activity, while the system's acidic conditions influence the dehydration and ring closure [15]. It has been observed that pathway 1 tends to occur in liquid-phase reactions [68, 69], whereas pathway number 2 is favored in gas-phase reactions [70, 71].

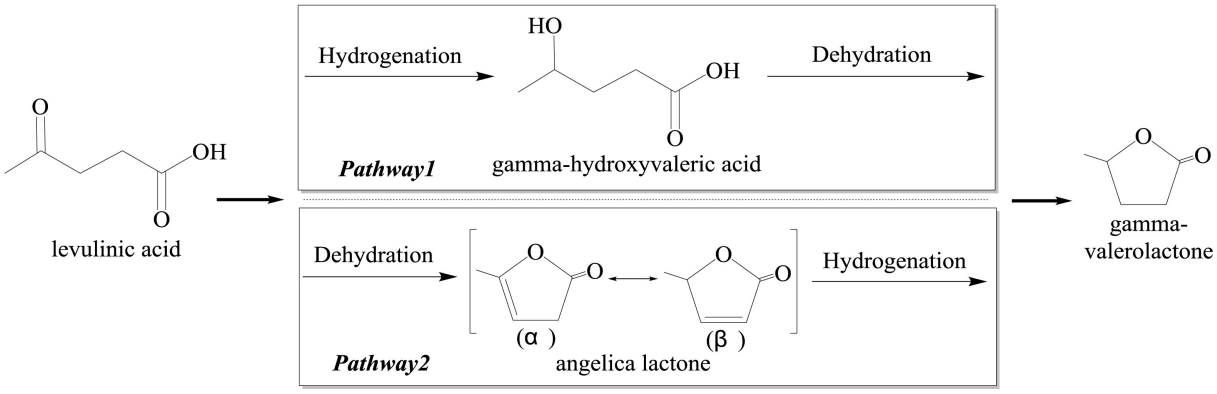

Figure 1.8 Reaction mechanism for GVL synthesis from LA, modified from [6].

1. *Homogeneous catalytic system*: In the process of synthesizing GVL from LA, several studies have demonstrated that using homogeneous catalysts can provide high yields of GVL under relatively mild and controllable reaction conditions [72, 73]. Notably, the combination of precious metal-based complexes (Ru or Ir) with chelating agent phosphine ligands is considered to be effective in promoting the efficiency of the kinetics, wherein the homogeneous catalysts with better catalytic activity are precious metal Ru-chelating tridentate phosphine complexes [6, 74].

2. *Heterogeneous catalytic system*: Homogeneous catalysts provide enough contact between the substrate and the catalyst to achieve a high catalytic efficiency. However, using precious metals and ligands has led to complex catalyst synthesis processes and high catalyst manufacturing costs, and the catalysts cannot be recycled. The recyclability of heterogeneous catalysts and the low cost following the introduction of non-noble metals will cause the gradual replacement of homogeneous catalysts by heterogeneous catalysts for industrial production. To satisfy the conditions for hydrogenation and acid catalysis, a metal that promotes hydrogenation is generally combined with various carriers to provide an acidic site needed to form a solid acid catalyst.

   Among the precious metal catalysts used for the hydrogenation of LA to prepare GVL, Ru, Rh, Pd, Pt, Au, and Re are prominently employed. Ru-based catalysts, in particular, exhibit high catalytic selectivity due to their excellent hydrogenation activity towards aliphatic carbonyl compounds. For instance, Manzer et al. [66] utilized activated carbon as a carrier to support 5% of precious metals Ru, Ir, Rh, Re, Pd, and Pt for LA hydrogenation to GVL, with their results highlighting the superior catalytic selectivity of the 5 % Ru/C catalyst.

3. *Bifunctional catalytic system*: In addition to metal hydrogenation, optimizing the acidity of the carrier is recognized as a vital approach to further improve the efficiency of LA conversion to GVL. A recent development involved the creation of ruthenium nanoparticles (RuNP) supported on a sulfonic acid ion-exchange resin (Ru@DOWEX) [75] for GVL synthesis from LA in the liquid phase. Impressively, this catalyst achieved a remarkable 99.8 % LA conversion and GVL selectivity exceeding 99 % at 70 °C and 5 bar H_2. The excellent performance can be attributed to the synergistic combination of the resin's acidity and Ru's hydrogenation sites. Moreover, the catalyst's mild reaction conditions significantly mitigated the issue of coke accumulation.

GVL synthesis from Alkyl Levulinates

Alkyl levulinates (ALs) stand out as one of the most important basic raw materials for the efficient synthesis of GVL. These molecules could be efficiently obtained from biomass-based derivatives. The synthesis route to synthesize GVL from AL is similar to that of GVL synthesis from LA, as shown in Figure 1.9. When LA is used, the intermediate product γ-hydroxyvaleric acid is produced by the hydrogenation of LA, then GVL is formed through intramolecular dehydration. The synthesis of GVL from ALs has a similar reaction pathway; the intermediate alkyl-3-hydroxyvalerate is produced by hydrogenation of the AL, and this intermediate is finally esterified and cyclized to obtain GVL. Additionally, kinetic experiments on the synthesis of GVL from AL indicated that AL with shorter alkyl groups are more likely to promote the synthesis of GVL [6].

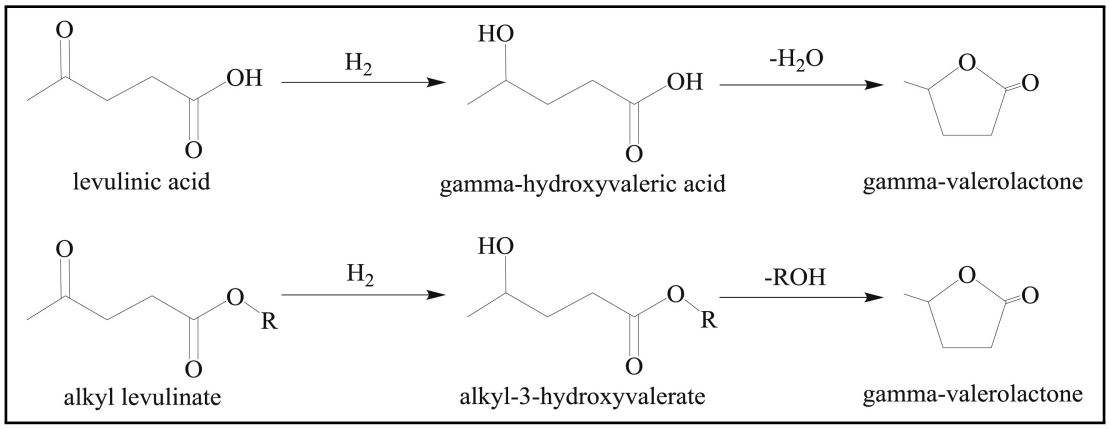

Figure 1.9 Reaction pathways for GVL synthesis from LA and ALs, taken from [6].

1. *Precious metal catalytic system*: Within precious metal catalyst systems, Ru-based catalysts are renowned for their high efficiency in preparing GVL from LA [76]. Moreover, these catalysts demonstrate exceptional catalytic performance in synthesizing GVL from alkyl levulinates. Numerous studies have investigated the production of GVL from ALs utilizing ruthenium as the catalyst. For instance, Wang et al. [60] examined the thermal risks associated with the hydrogenation of methyl and butyl levulinates, Zhao et al. [77] investigated the continuous conversion of methyl levulinate to GVL and Capecci et al. [78] focused on the hydrogenation of butyl levulinate to find the most probable kinetic models.

2. *Nonprecious metal catalytic system*: The catalytic transfer hydrogenation (CTH) is a promising strategy to drive down the cost of synthesizing GVL from ALs. Specifically, employing alcohols as hydrogen sources in hydrogenation can decrease reliance on zero-valent metal catalysts, particularly precious metals, typically utilized in traditional reaction pathways. This shift is facilitated by the highly selective reduction of carbonyl groups to alcoholic hydroxyl groups through the Meerwein-Ponndorf-Verley reaction. Catalysts based on Ni, Cu, Fe, Co, Zr, and Sn have exhibited favorable conversion rates and selectivities in this context [6, 15, 79, 80].

1.5.3 SAF Production from GVL

Gamma-valerolactone (GVL) has proven to be a suitable additive for gasoline and diesel fuels. However, its use as a jet fuel additive is limited by factors such as its lower heating value compared to kerosene, 25 vs 43 MJ/kg, and its water solubility. GVL can be utilized as a platform molecule and undergo further transformations to overcome these challenges to produce better-suited additives and the actual jet fuel [65]. GVL becomes feasible to synthesize essential components of jet fuels, including paraffins, olefins, and aromatic compounds. Significant utilization of GVL lies in the production of butene isomers via ring-opening and decarboxylation reactions facilitated by solid acid catalysts [81]. Consequently, these butenes serve as crucial raw materials for generating branched alkenes within the C_8-C_{24} range via oligomerization [58].

These alkenes, also known as jet fuel alkenes (JFA), hold significance in various engine applications [82]. Bond et al. [58] conducted a study on the catalytic conversion of GVL to liquid alkenes using a two-reactor system. In their research, an aqueous solution of GVL was introduced into an up-flow fixed bed reactor. Through ring-opening and decarboxylation reactions catalyzed by SiO_2/Al_2O_3 at 36 bar of pressure (with inert gas He) and temperatures ranging from 648 K to 673 K, butene isomers were produced, with reported yields of up to 90 %. Subsequently, the effluent from the first reactor underwent separation in a high-pressure vapor-liquid separator, separating liquid water, unreacted GVL, and other by-products from vapor phase products (butene and carbon dioxide). The butene oligomerization process was conducted in a down-flow fixed bed reactor using Amberlyst-70 catalyst at 36 bar and 443 K. The distribution of carbon in the branched alkene products was found to be primarily dependent on butene conversion.

Zhao et al. [83] implemented a similar approach to synthesize aromatic hydrocarbons from GVL. Employing zeolite catalysts like MCM-41 and HZSM-5, they converted GVL into aromatics, including benzene, toluene, and xylene, within a single reactor at a temperature of 773 K. GVL was probably transformed into a mixture comprising butene, CO, and CO_2. Consequently, under elevated temperatures, butene underwent isomerization and aromatization reactions, leading to the formation of aromatic compounds [84].

1.6 Objectives and Structure

The general objective of this research is to establish a feasible route for the full valorization of the lignocellulosic biomass (LCB) into sustainable aviation fuels (SAF); this valorization route is based on the discussion of this chapter. This valorization route mainly focuses on the production of sustainable aviation fuel (SAF) that is capable of replacing at 100% the conventional aviation fuel, i.e., kerosene.

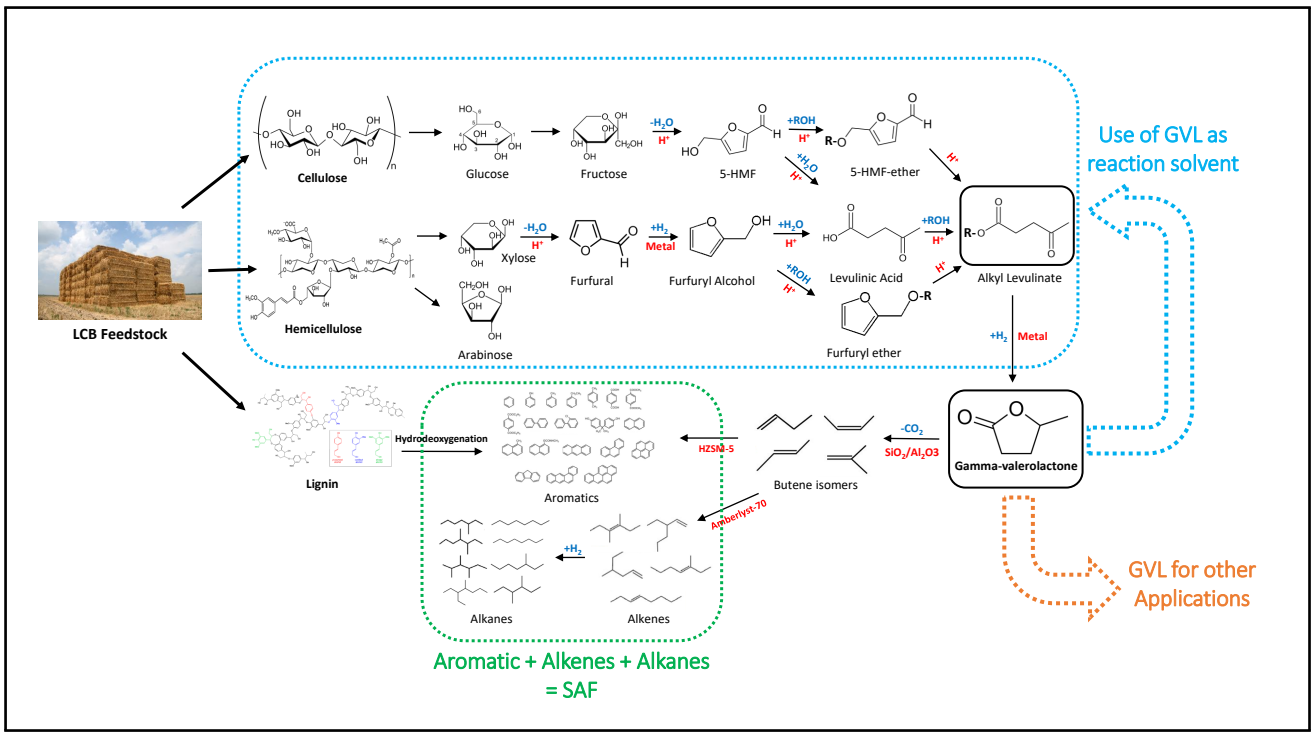

Figure 1.10 A promising route to full valorization LCB into SAF.

Figure 1.10 shows the steps required to valorize lignocellulosic biomass elements into SAF. In this figure, we can realize that alkyl levulinates and gamma-valerolactone serve as a connection between the stages: *i)* LCB decomposition into its different derivatives, stage marked in blue, and *ii)* the stage corresponding to SAF productions from GVL. In addition to serving as a connection for producing SAF from LCB, GVL has other potential applications, such as solvent during LCB decomposition and as a raw material to produce a wide variety of high-value compounds. This latter significantly increases the importance of this valorization route since it allows the production of SAF and covers other needs of modern society.

Given that gamma-valerolactone (GVL) serves as a fundamental building block for the production of Sustainable Aviation Fuel (SAF) and other materials derived from lignocellulosic biomass, one of the focus of this research is to study the hydrogenation of butyl levulinate (BL) in order to produce GVL. Kinetic models are usually developed in isothermal conditions for process optimization. The validity of such models in non-isothermal conditions could be an issue for pinch analysis and thermal risk assessment. We studied this reaction considering isothermal, isoperibolic, and adiabatic conditions. Such analysis establishes reliable and robust kinetic models, facilitating optimization of energy recovery, thermal risk assessment, and conversion yield.

The hydrogenation of butyl levulinate will be studied in a heterogeneous system, where BL is in the liquid phase, hydrogen is in the gas phase, GVL is a solvent, and ruthenium over activated carbon (Ru/C) is a solid catalyst. Thus, this study will provide valuable insight into the kinetic and thermal risk for the industrial implementation of this step in the valorization route of LCB into SAF. It is essential to highlight that the scope of our research is limited to the production of GVL from BL in the valorization route of LCB.

By this point, we have noticed the potential of lignocellulosic biomass (LCB) to produce SAF that can replace conventional aviation fuels. Nevertheless, we have also realized that one of the most important challenges in this valorization route is the large number of transformation steps that this feedstock requires to achieve its mission. These steps' development and industrial-scale implementation are not possible in the short term. Given the short-term goals set by different institutions regarding greenhouse gas emissions from the aviation sector, it is worth exploring the potential of intermediary compounds as possible additives that help to contribute to reducing greenhouse gas emissions. As we discussed earlier, butyl levulinate stands out as a potential drop-in additive to kerosene, but so far, there has yet to be a conclusive study about the limitations of BL in terms of jet engines' operability. The advantage of a drop-in additive is that there is no need to modify current infrastructure in place or jet engines in aircraft.

As butyl levulinate (BL) emerges as a potential jet fuel additive, a significant aspect of our research is to assess its suitability as a kerosene additive. Our approach involves evaluating the combustion dynamics of different blends of Kerosene/BL within a gas turbine combustion chamber equipped with an RQL (Rich-Burn, Quick-Quench, Lean-Burn) injection system. Here, we seek to understand how the addition of BL will affect the performance and the operability limits of kerosene inside a gas turbine engine operated under the real-world conditions under which aircraft engines operate, i.e., low pressure and low temperature. The performance (thrust or power, fuel consumption, temperatures, shaft speeds, etc.) and operating limits of a gas turbine engine are crucially dependent upon its inlet and exit conditions. The most important are pressure and temperature, which are determined by the ambient conditions, flight altitude, and flight speed.

1.6.1 Specific Objectives

Our specific objectives are divided into two main groups. Those concerning the production of GVL from BL and those concerning the evaluation of BL as a kerosene additive. These specific objectives are defined below:

GVL Production from BL

1. To assess the internal and external mass transfer limitation for the heterogeneous system. The chemical reaction in consideration is the hydrogenation of butyl levulinate (BL) to produce gamma-valerolactone (GVL) via hydrogenation in the presence of the solid catalyst ruthenium over activated carbon (Ru/C).

2. To study the energy released during the hydrogenation of butyl levulinate (BL). This means measuring the enthalpy of the reaction and its dependence on operating and initial conditions. This study is fundamental to evaluating the thermal risk of the chemical reaction.

3. To develop a robust and reliable kinetic model for the hydrogenation of butyl levulinate, integrating isothermal, isoperibolic, and adiabatic experiments to determine the kinetic parameters. To achieve this objective, it is necessary to know the mass transfer limitation and the enthalpy of the reaction in advance in order to solve the material and energy balance.

4. To assess the stationary thermal stability applying Van Heerden criterion and steady-state bifurcation for the continuous production of GVL in a continuous stirred tank reactor (CSTR). In order to determine the limit value of the global heat transfer coefficient (**Ua**) that will minimize the risk of thermal runaway.

5. To assess the dynamic thermal stability of continuous stirred tank reactor (CSTR) for butyl levulinate (BL) hydrogenation. This study seeks to understand or predict how our reactor will evolve, thermally speaking, when any process variable is perturbed.

6. To carry out a parametric sensitivity analysis (PSA) for butyl levulinate (BL) hydrogenation in a continuous stirred tank reactor (CSTR). This analysis helps determine which operating parameters can have a higher impact on the reactor operation.

BL as Kerosene Additive

7. To measure the lower heating value (LHV), density, viscosity, and surface tension for kerosene, butyl levulinate, and blends kerosene/BL at different temperatures and proportions. Moreover, the corresponding mixing rule that allows the evaluation of such properties for different ratios of Kerosene/BL at different temperatures will be established.

8. To define a methodology to measure the combustion efficiency in a gas turbine engine for the different blends of Kerosene/Butyl Levulinate. To measure the combustion efficiency of the blends, we focused on the effect of low-pressure and low-temperature conditions in order to evaluate the effect of BL in terms of operability during the combustion process.

9. To measure and compare the pollutant emissions (CO, CO_2, and NO_x) for the different Kerosene/Butyl Levulinate blends. This is to understand if adding BL into kerosene reduces GHG emissions during combustion.

10. To compare the atomization spray and the flame structure during the combustion process for the different Kerosene/Butyl Levulinate blends. This analysis will help to understand the behavior of the combustion efficiency from a local point of view.

Structure

This research is divided into six chapters; each chapter addresses different aspects of the research to meet the specific objectives, which complement each other to meet the general objectives. The content of the chapters is outlined as follows:

- ***Chapter 1***: This chapter corresponds to the introduction of the research. This chapter provides all the elements needed to understand this research's relevance and general objectives.

- ***Chapter 2***: This chapter outlines the materials and equipment employed throughout the research. This chapter presents and describes the facilities used and the primary objective of each.

- ***Chapter 3***: This chapter is dedicated to the study of butyl levulinate (BL) hydrogenation to produce GVL in different thermal modes. This chapter explains how we developed an advanced kinetic model for this chemical reaction in isothermal, isoperibolic, and adiabatic conditions. This chapter shows how specific objectives 1, 2, and 3 are met.

- ***Chapter 4***: This chapter presents a thermal risk assessment for the continuous production of GVL via BL hydrogenation. The kinetic model and reaction enthalpy were taken from the previous chapter, Chapter 3, to do such analysis. Chapter 4 shows how specific objectives 4, 5, and 6 are met.

- ***Chapter 5***: This chapter assesses the suitability of butyl levulinate (BL) as a kerosene additive. Here is the discussion of how BL impacts the combustion dynamics of kerosene inside a gas turbine engine during the combustion process. This chapter shows how specific objectives 7, 8, 9, and 10 are met.
- ***Chapter 6***: This chapter corresponds to the general conclusions found during this work and the potential perspectives.

Chapter 2
Materials and Equipment

This chapter presents the materials, equipment, and facilities employed during the research and their primary objectives. The selection of appropriate materials and equipment is crucial for ensuring the integrity and reliability of experimental results and procedures.

2.1 Materials

We used different compounds and materials for different purposes during this research. The list of materials used is shown below; it should be noted that these materials were used without any further purification or additional treatment.

- ***Butyl levulinate (BL):*** This compound, which is a liquid under normal conditions of pressure and temperature, is the main compound of our work since it will be used as the main reagent for the production of gamma-valerolactone, and will also be the object of study to evaluate its potential use as a kerosene additive.
- ***Hydrogen:*** This one, in gas form (H_2), will be our secondary reagent during the hydrogenation of butyl levulinate (BL) to produce gamma-valerolactone.
- ***Gamma-valerolactone (GVL):*** This compound, which is a liquid under normal conditions of pressure and temperature, is our main product obtained from the hydrogenation of butyl levulinate (BL). In addition to being our main product, it is also used as a solvent for the reaction; thanks to its chemical and thermal stability, GVL allows the reaction to be carried out under different operating conditions.
- ***Ruthenium over activated carbon (Ru/C):*** Ruthenium, 5% on activated carbon powder, reduced, nominally 50% water wet is our solid catalyst for the production of gamma-valerolactone (GVL) from butyl levulinate (BL) via hydrogenation, Ru-based catalyst exhibit high catalytic selectivity for this chemical reaction.
- ***Butanol:*** This is the by-product obtained from butyl levulinate hydrogenation. We used this compound mainly for analytical detection and calibration curves for chemical quantification.
- ***Acetone:*** This compound was used as a solvent or diluting agent to prepare samples to be analyzed via gas chromatography.
- ***Keroseno jet fuel A1:*** This fuel plays a fundamental role in our research, as it is the current commercial fuel for aircraft and will serve as a reference to evaluate how the addition of butyl levulinate (BL) can affect its combustion dynamics and its performance during the combustion process inside a gas turbine engine.

Table 2.1 shows a summary of the materials, with additional information about their purity and provider.

Table 2.1 List of materials used during the research.

Material	Application	Purity	CAS Number	Provider
Ru/C	Catalyst	5% Ru	7440-18-8	Alfa-Aesar
Acetone	Dilution Solvent	99% wt	67-64-1	Carlo Erba
Butanol	Analytic Identification	99% wt	71-36-3	Lab Line
Butyl Levulinate	Reagent and Bio-Fuel	98% wt	2052-15-5	Alfa-Aesar
Hydrogen gas (H_2)	Reagent	99% v/v	1333-74-0	Linde
Gamma-Valerolactone	Reaction Solvent	99% wt	108-29-2	Sigma Aldrich
Kerosene Jet Fuel A1	Fuel	-	64742-81-0	TotalEnergies

2.2 Equipment

2.2.1 Physical and Thermal Properties

Knowing substances' physical and thermal properties is of great importance when carrying out either a kinetic model assessment or a combustion assessment. It is possible to obtain this information from the literature for most of the pure compounds in our research. However, for blends, Kerosene/BL, this information is not available. During this research, measuring the lower heating value, surface tension, dynamic viscosity, and density for the blends and pure compounds was necessary. To do so, the following instruments were used:

- ***Parr 1356 Oxygen Combustion Bomb Calorimeter***: The primary use of this instrument is to calculate the lower heating value (LHV) of a substance. This instrument has been designed to provide rapid and reliable heat of combustion values for solid and liquid fuels. It works in isoperibolic conditions; the calorimeter jacket is held at a constant temperature while heat from the burning sample, in the presence of pure oxygen O_2, causes the bomb and bucket temperature to rise. The small heat flow between the bucket and its surroundings during a test is monitored by a microprocessor in the calorimeter, which, based on the heat transfer and the initial mass of the fuels, calculates the heat of combustion. This instrument is shown in Figure 2.1a.

- ***LAUDA Drop Volume Tensiometer TVT 2***: This instrument measures the surface and interfacial tension of liquids. Its strengths lie in the high-precision determination of dynamic interfacial tension. TVT 2 uses the fact that the volume of a drop released from a needle in the air depends on its surface tension or its interfacial tension between the two phases if released into a second, immiscible phase (oil). With the TVT 2, this measuring principle has been brought by LAUDA Scientific into a measuring device that is easy to use simultaneously, thanks to precision engineering. This instrument is shown in Figure 2.1b.

- ***SVM 3000 Stabinger Viscometer***: The SVM 300 Stabinger viscometer is a rotational viscometer with a cylinder geometry that measures the dynamic viscosity and density of oils and fuels according to ASTM D7042. Rotational viscosity measurement is based on torque and speed measurement, and a rotating magnet produces an eddy current field with an exact speed-dependent brake torque. The SVM 3000 also has a density-measuring cell that employs the well-known oscillating U-tube principle. The density and viscosity measurement can be done at different temperatures by changing the instrument's set point. This instrument is shown in Figure 2.1c.

(a) Parr Bomb Calorimeter

(b) Tensiometer TVT 2

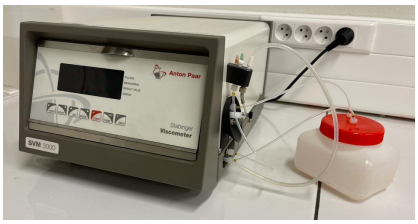

(c) Stabinger Viscometer

Figure 2.1 Illustration of the instruments employed to measure physical and thermal properties.

2.2.2 Kinetic Experiments

The experimental part for the development of the kinetic model for the hydrogenation of butyl levulinate (BL) to produce gamma-valerolactone (GVL) was developed in the ***Mettler Toledo RC1mx Calorimeter***. The development of this kinetic considers experiments performed under isothermal and non-isothermal conditions, i.e., isothermal, isoperibolic, and adiabatic conditions.

The RC1 consists of a Hastelloy C22 metal vessel with a 1.8 L capacity and a 100 bar pressure tolerance, and a stirrer suitable for gas-liquid transfer reactions. It is coupled with a high-precision sensor to measure the temperature of the reaction media at all times. It has a calibration heating rod that is used to evaluate the heat capacity (C_p), the overall heat transfer coefficient (UA). With these elements, the RC1 can calculate the heat exchange of the reaction media. The RC1 features independent heating and cooling loops, enabling rapid temperature regulation. Additionally, it is equipped with a PID automatic control system to regulate the pressure inside the reactor. These features enable precise monitoring and control of pressure, temperature, and heat exchange during a chemical reaction. All measurements are saved in an Excel file every two seconds. Figure 2.3 illustrates the RC1 calorimeter and the experimental setup.

All these features of the RC1 make it suitable to study the hydrogenation of butyl levulinate using hydrogen in the gas phase and ruthenium over activated carbon as a catalyst. Since the PID controller helps to keep the hydrogen pressure inside the reactor constant, this is of great importance since hydrogen is consumed throughout the reaction, and a reduction in hydrogen pressure could slow down the reaction rate.

The operation of the RC1 is adapted according to the thermal mode chosen for its operation and is defined as follows:

- *Isothermal mode*: The main characteristic of isothermal mode is that the temperature of the reactionary media T_r remains constant during the reaction. To ensure that T_r remains constant during the reaction, the temperature of the reactor jacket T_j is regulated by the independent heating and cooling loops. T_j increases when the reaction is endothermic and decreases when the reaction is exothermic.

- *Isoperibolic mode*: The main characteristic of the isoperibolic mode is that the temperature of the reactor jacket T_j remains constant throughout the reaction. In contrast, the temperature of the reactionary media T_r evolves according to the type of chemical reaction increases for exothermic reactions, and decreases for endothermic reactions.

- *Adiabatic mode*: The main characteristic of adiabatic mode is that ideally, all the energy that is released during an exothermic reaction is accumulated in the system, thus causing a significant increase in the temperature of the reactionary media T_r.

  This mode of operation is achieved in the RC1 by establishing the condition that the temperature of the reactor jacket T_j is equal to T_r, thus causing a kind of thermal insulation. This is possible thanks to the fast response of the RC1's independent heating and cooling loops. Figure 2.2 shows the graphical report of an adiabatic experiment; the chemical reaction took place while the stirring rate was equal to 1000 RPM.

Thanks to its versatility, this equipment was used to develop the kinetic model and measure the energy released during the hydrogenation of BL to produce GVL.

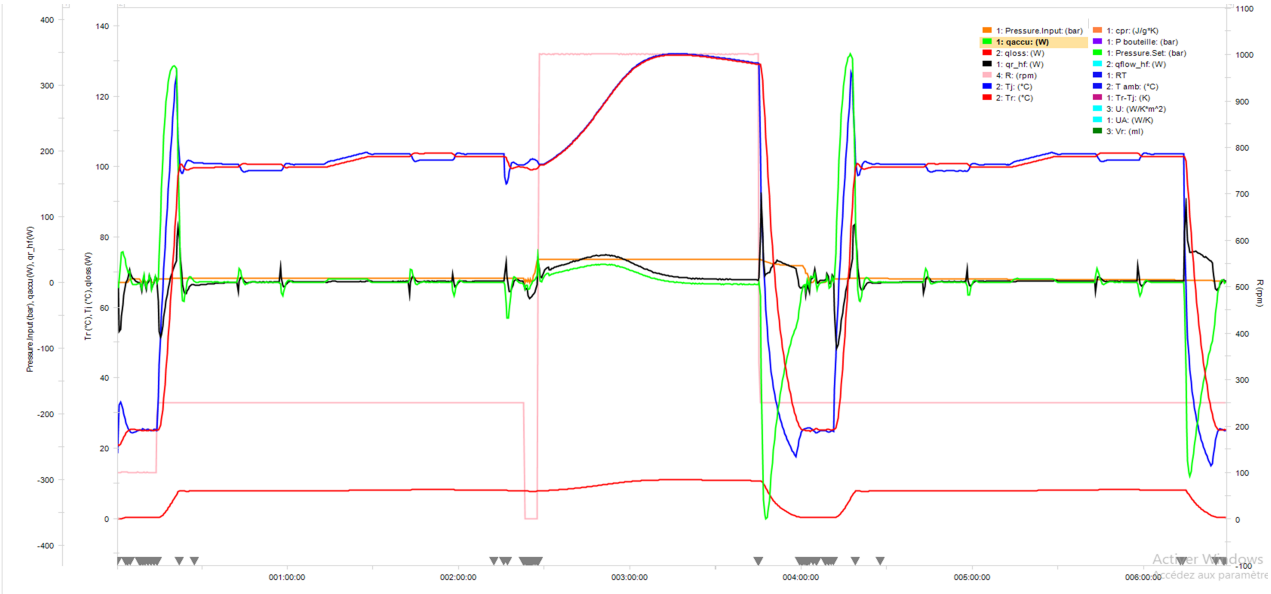

Figure 2.2 Graphical report of an adiabatic experiment performed in the RC1.

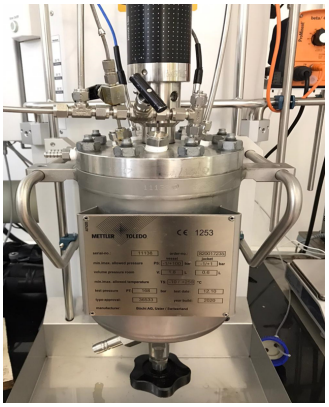

(a) Reactor tank

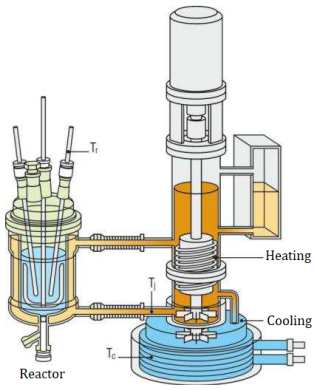

(b) Temperature control.

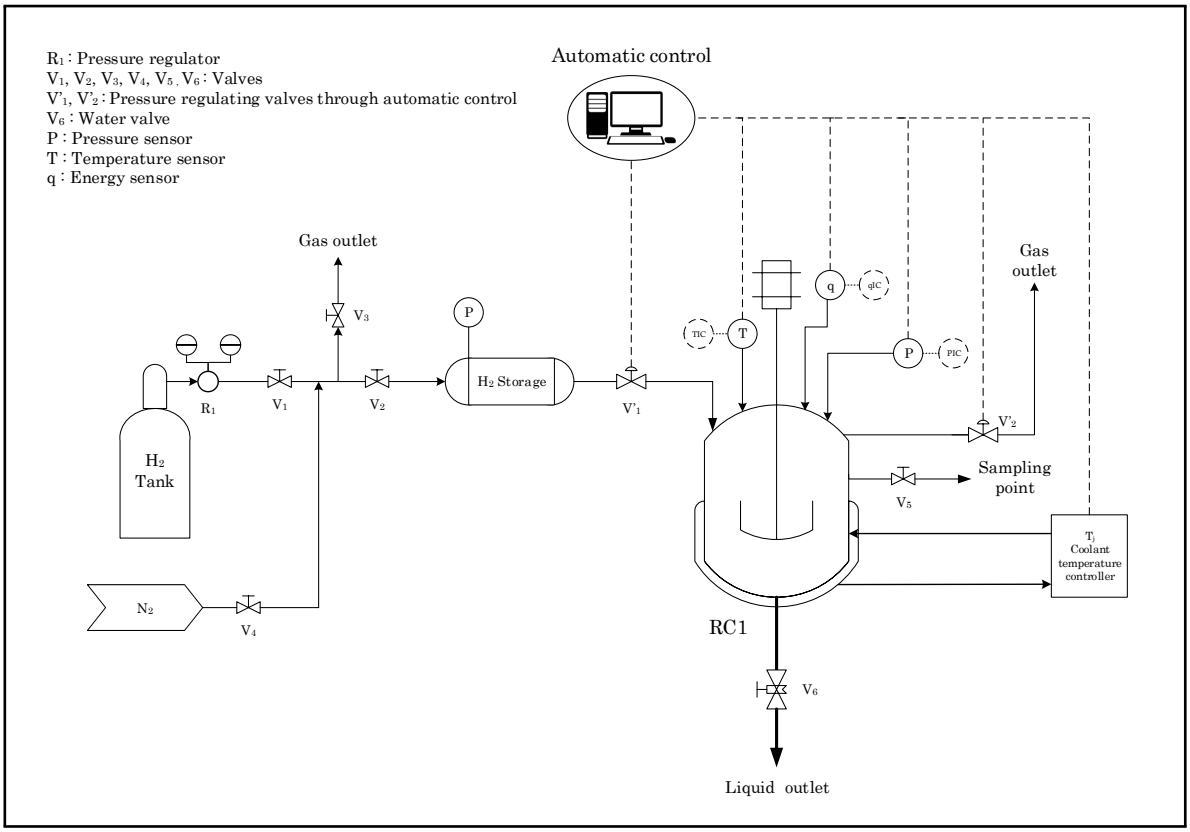

(c) Experimental setup

Figure 2.3 Mettler Toledo RC1mx Calorimeter.

2.2.3 Reaction Enthalpy

To complement the measurements of energy released during the hydrogenation of butyl levulinate, we have incorporated the ***Tian Calvet C80 Calorimeter***, Figure 2.4, it is suitable for isothermal calorimetry, mixing calorimetry and temperature programming calorimetry. It is designed for studies like physical transformation, thermal stability, mixing, evaporation, gas-solid, gas-liquid, liquid-liquid reaction, reaction under pressure, specific heat measurement, thermal conductivity, etc.

The C80 calorimeter features a three-dimensional transducer for maximum sensitivity, allowing high precision and reproducibility. This micro calorimeter can work up to a maximum temperature of 573 K, with a standard error of 0.1 K for temperature measurements and a standard error of 0.1% for enthalpy measurements. Inside this instrument are several energy flow detectors and the support for two experimental cells, i.e., the measurement cell and the reference cells, which are surrounded by thermocouples. The reference cell cancels out the effect of residual drifts in the temperature or any external disturbance. This compensation is adequate when experimental cells placed in the detectors are symmetrical in terms of physical and thermal properties. The cells used in our case are the turn-over mixing cells, Figure 2.4c.

(a) External view

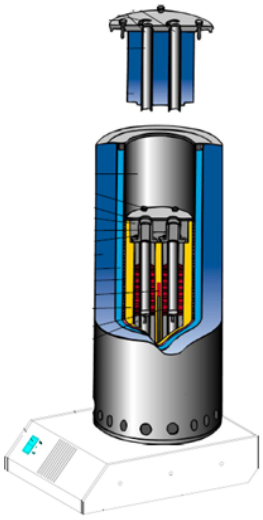

(b) Internal view

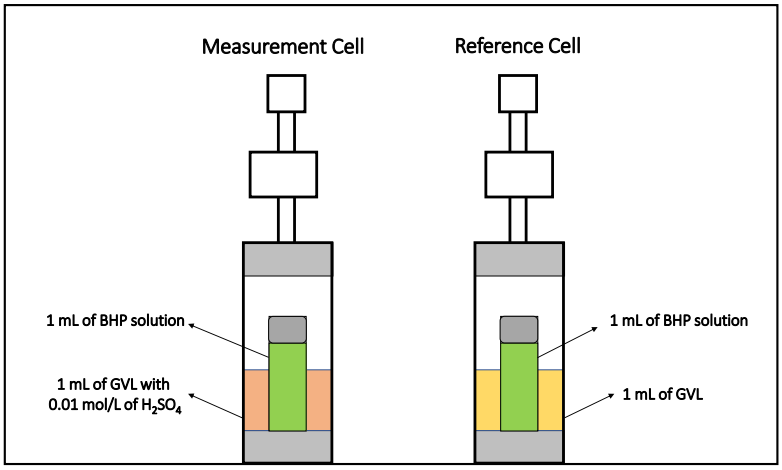

(c) Turn-over mixing cells

Figure 2.4 Tian Calvet C80 Calorimeter illustration.

2.2.4 Analytic Measurement

Gas chromatography coupled with a flame ionization detector, GC-FID, technique was applied to quantify the amount of chemicals in samples taken during the experiment. GC-FID instrument was from Scion Instruments supplier. This instrument was equipped with a low polarity column, Phenomenex ZB-5, composed of 95 % dimethyl siloxane, and 5 % of phenyl groups. Column dimensions: length: 30 3, internal diameter: 0.32 mm, coating width: 0.25 μm. Helium at 99.99 % was used as carrier gas at a constant flow rate of 1.2 mL/min. The injector's and the detector's temperature were set at 250 ^{o}C. The oven temperature ramp was set to 50 ^{o}C (1 min) - 20 ^{o}C/min - 200 ^{o}C (1 min). Samples were diluted in acetone to be analyzed; the injection volume was 1 μL, and the split ratio was 20:1.

2.2.5 Combustion Study

One of the most relevant aspects of this research is to assess the potential application of butyl levulinate (BL) as a kerosene additive. Therefore, it is necessary to study how adding BL impacts kerosene performance and combustion dynamics under actual operating conditions. For this reason, this study was conducted in the High Altitude Re-ignition for Gas Turbine facility, or ***HARTur facility***. The primary purpose of this facility is to enable the combustion dynamics assessment of fuel during the pull-away phase under high-altitude conditions, characterized by a decrease in operating pressure and temperature compared to the ground-level conditions.

HARTur facility was designed and built in the CORIA research center during Marie-Eve Clavel's doctoral thesis [7] for the experimental study of spray, flame, and turbulence interactions during pull-away at high altitude conditions. This thesis studied the pull-away under unfavorable conditions characterized by low pressure and low temperature in a combustion chamber with a RQL injection system. This work is the primary source of information linked to this facility; most of the technical information presented during our research about the HARTur facility comes from this reference.

Facilities of this type, which allow the study of aeronautical injection systems under low pressure and temperature conditions, are relatively difficult to build and implement, and only a few are available worldwide. Table 2.2 shows a comparison between the facilities that can be found in the literature and the HARTur facility.

Table 2.2 Facilities that allow the study of aeronautical injection systems under low pressure and temperature conditions [7].

Facility	Research Center	min P [kPa]	min T [K]
M1	ONERA	50	250
ATF[1]	Rolls Royce, UK	40	265
HARTF[2]	Cincinnati University	20	228
HARTur	Coria	30	248
MERCATO	ONERA	50	233

HARTur facility is illustrated in Figure 2.5, where the elements are labeled: the cooling units and the piping system, the combustion chamber, the afterburner with its cooling unit, and the pressure control system. These elements are described below:

[1] Altitude Test Facility
[2] High Altitude Relight Test Facility

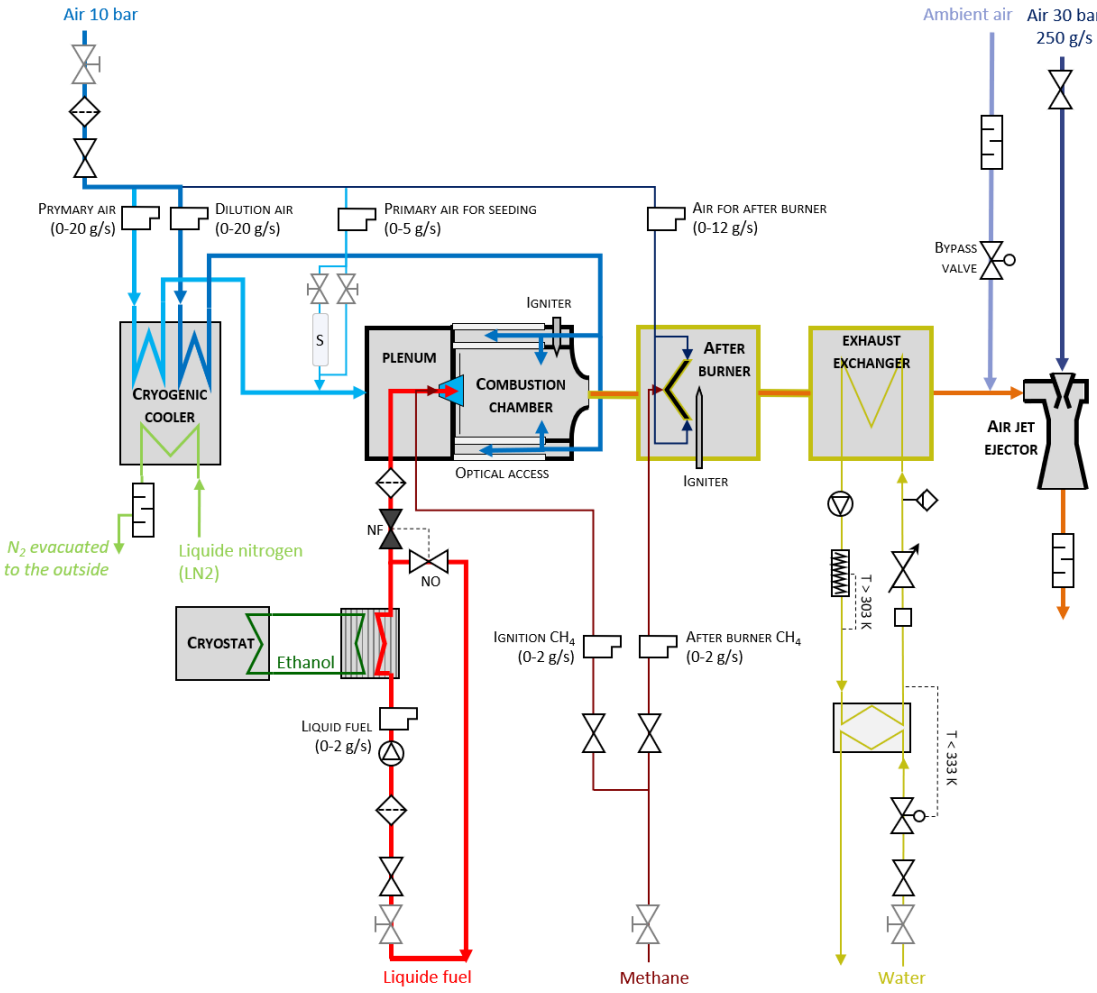

Figure 2.5 HARTut facility piping and instrumentation diagram, taken from [7].

Cooling units for air and fuel supply

To address the cooling issue, the HARTur facility is equipped with two independent cooling systems for fuel and air inlets. The air cooling system can lower the air temperature to 238 K. In this setup, the air undergoes cooling using liquid nitrogen (LN2) inside a cryogenic chiller. Two air flow meters regulate the flow of primary and dilution air,each with a capacity ranging from 0 to 72 kg/h, allowing for a combined maximum air capacity of 144 kg/h. Liquid nitrogen is stored in a pressurized vessel of 0.23 m^3 at 400 kPa, connected to the cryogenic chiller's inlet. Temperature control is achieved using an on-off pneumatic valve, regulating the flow of liquid nitrogen into the cryogenic chiller until the desired temperature is reached. The significant mass of aluminum within the cryogenic chiller ensures that the air temperature at the combustion chamber inlet fluctuates by a maximum of 2 K around the set temperature throughout 5 to 15 minutes.

The fuel temperature is controlled using a plate heat exchanger capable of cooling the fuel to 250 K. This cooling system employs ethanol as a heat transfer fluid, circulating between the heat exchanger and a Julabo FP55-SL cryostat. Kerosene is cooled separately from the air to avoid crystallization issues, as the temperature inside the cryogenic chiller is significantly lower than the freezing point of the kerosene.

Combustion chamber

The combustion chamber features a single-injector design with a square cross-section measuring 100 mm on each side and a length of 120 mm. Figure 2.6 shows a sectional view of the combustion chamber. It is made of stainless steel with an outer wall made of aluminum that is air-cooled by the dilution air. The four sides of the combustion chamber are equipped with high-purity fused silica windows, corning grade 7980-5F. The lateral windows, 85 mm × 40 mm, allow optical access to the flame; The windows placed at the top and at the bottom of the chamber, 85 mm × 10 mm, are in the vertical plane that cuts the injector at its center. These 4 windows facilitate the implementation of local analysis, enabling a detailed analysis of spray and flame structure.

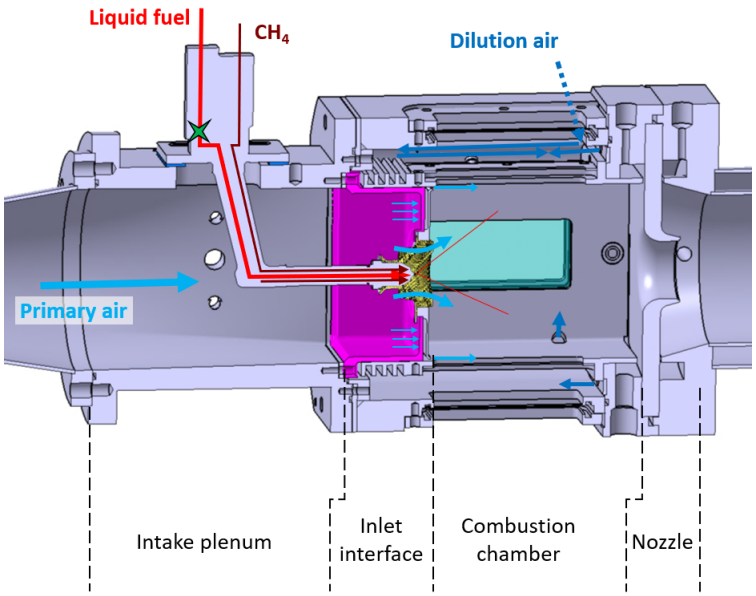

Figure 2.6 Combustion chamber's CAD: sectional view.

The region between the combustion chamber and the intake plenum is referred to as the inlet interface, which comprises several elements outlined below:

- *The fuel injector*, depicted in grey in Figure 2.6 with red lines indicating the fuel piping, provides fuel atomization inside the combustion chamber through the injection system. During the ignition phase and preheating of the combustion chamber, only the pilot circuit is used with methane to achieve a stable condition. Subsequently, as thermal stabilization is attained, methane is progressively replaced by fuel through the primary liquid fuel piping circuit. This methane ignition process also allows the windows to be less clogged by the soot produced by the flame under unfavorable conditions.

- *The injection system*, in yellow in Figure 2.6, surrounds the tip of the fuel injector. It aims to inject part of the primary air flow within the combustion chamber with a swirling motion over the fuel spray issuing from the fuel injector. This design facilitates the secondary atomization, evaporation, and mixing inside the combustion chamber.

- *A multi-perforated plate*, highlighted in pink in Figure 2.6, is coupled with a deflector, a thin wall positioned in front of the perforated plate. The injection system and the fuel injector are located in the center of this plate. This arrangement separates the primary air flow rate into two streams: passing through the injection system and the multi-perforated plate.

The number of holes in the perforated plate and their diameter (0.7 mm) have been optimized to cool the deflector efficiently while simultaneously creating an air boundary layer near the optical windows. The air film is a protective barrier, shielding the optical windows from fuel droplet impacts and thermal damage. The ratio between the air mass flow rate across the injection system and the total primary air flow rate is typically set at 0.5.

- *Combustion chamber nozzle*, Another element of the combustion chamber is the nozzle located at the end. This element is a device for measuring the average temperature of the burned gases coming from the combustion. The methodology used to calculate burned gases temperature is presented in Chapter 5.

This combustion chamber has been designed to implement an RQL injection system. Additional air, represented in dark blue in Figure 2.6, is subsequently injected through four 8 mm diameter holes on the lateral edges of the chamber at a distance of 80 mm from the injector. This dilution air (or secondary air) aims to approach the actual operating conditions of the RQL injectors that can be tested in this facility. Before entering the combustion chamber, the dilution air circulates in between the double walls of the combustion chamber; this has two advantages: *i)* it cools down the walls of the combustion chamber and *ii)* it reduces the thermal heat losses of the combustion chamber. Indeed, some energy transferred from the flame to the walls is absorbed by the dilution air and re-injected into the combustion chamber instead of being transmitted to the surroundings. Consequently, the combustion chamber operates with a quasiadiabatic mode.

Afterburner and burned-gases cooling unit

Burned gases from potentially incomplete combustion must be treated before being released into the environment. An afterburner and a burned-gases cooling unit have been designed and placed after the combustion chamber. The afterburner device stabilizes a methane/air flame downstream, a V-shaped flame-holder, and allows the post-combustion of incomplete burned gases from fuel/air flames. Then, these combustion products are cooled down through the burned-gases cooling unit. This heat exchanger operates with a closed-loop hydraulic circuit. This circuit also has an electrical heat load to maintain the water temperature above 303 K, which can be turned on during non-reactive and low-temperature conditions. The temperature of this circuit is controlled by a plate heat exchanger operating with domestic water.

Vacuum generation

The pressure inside the combustion chamber is controlled by an air-jet ejector system located downstream of the afterburner and the burned-gases cooling unit. This system is similar to that used by Paxton et al. [85]. The air-jet ejector system was designed and built by *Le Vide Industriel* company according to the following requirements. It can operate with any composition of gases, with a temperature range between 273 K and 373 K. The ejector is powered by 900 kg/h of air at 3000 kPa by an ATLAS COPCO compressor, dark blue lines in Figure 2.5. This compressor allows it to go down until 30 kPa over the air flow rate range, 0-144 kg/h. To control the pressure in the combustion chamber, a by-pass line is installed upstream of the air-jet ejector system, highlighted with a light blue line in Figure 2.5. The pressure can be controlled by adjusting the aperture of the by-pass valve without affecting either the combustion chamber's total air flow rate or the compressor's air flow rate.

Control and monitoring of the facility

Several devices are used to control and monitor the facility during operation. Air and fuel flow rates are maintained using Bronkhorst thermal and Coriolis mass flow controllers, respectively. Several K-type thermocouples are installed at different locations to monitor the temperature of fuel and air flows. The pressure in the combustion chamber is measured by a Keller pressure transducer (0-1.2 bar) and indicates the operating conditions during the pull-away. A pressure-gauge Rosemount records the pressure drop across the nozzle of the combustion chamber with a range of 0-3000 Pa. Finally, a Keller 0-30 bar is used to measure the pressure in the fuel stream after the cryostat to alert in case of icing at low temperatures.

Data acquisition and control of mass flow rates, pressures, and temperatures are carried out via LabView software. The program allows the control of the different flowmeters, the pneumatic valves, the by-pass valve that adjusts the pressure inside the combustion chamber, and the igniters at the combustion chamber and inside the afterburner. The temperatures are regulated separately on the cryostat for the fuel and via the cryogenic chiller for the primary and dilution air. The data acquisition is made at 10 Hz in real time. All the values are displayed continuously on the program interface and registered at a frequency of 1 Hz.

Figure 2.8 shows the data acquisition during an experiment in the HARtur facility. This figure shows the evolution of the mass flows of the fuel, the primary air, and the dilution air. We can also see the evolution of the temperature of the walls of the combustion chamber, among other variables.

Burned Gases Analysis

In addition, the HARTur facility allows the analysis of the composition of the burned gases coming from the combustion chamber, thanks to a sampling point located downstream of the chamber. The instrument used for this purpose was the **Gas Analyzer** HORIBA PG-250, Figure 2.7. This portable analyzer can measure with high precision and high consistency the concentrations of NO_x, SO_2, CO, CO_2, and O_2. It should be noted that gas analysis is not possible during low-pressure operation because the gas analyzer uses a suction pump to extract the sample of gases coming from the combustion chamber.

Figure 2.7 Illustration of the HORIBA PG-250 portable gas analyzer.

2.2.6 Optical Diagnostic

An important feature of the HARTur facility is the implementation of optical diagnostic; this is possible thanks to the optical access of the combustion chamber. This allows us to study the spray, flow, and flame from a local point of view. Two major campaigns will be carried out, laser tomography and chemiluminescence, to analyze the atomization spray and the flame structure in the combustion chamber, respectively.

Chemiluminescence was carried out with the ***intensified CCD camera PI-MAX 4*** from Princeton Instruments equipped with an optical filter Schott BG12 that transmits a light signal with a wavelength from 315-520 nm, and higher than 690 nm. During laser tomography tests, a laser beam passes through the vertical median plane of the chamber. Fuel drops in this plane reflect light by Mie scattering, and the signals are recorded into images by ***Photron Fastcam SA1.2*** at 5 kHz. A ***dual-cavity Nd:YLF laser*** (Darwin Dual, Quantronix) is used to illuminate fuel droplets in the combustion chamber. Each head delivers 2.5 kHz laser pulses with 20.5 W at 527 nm.

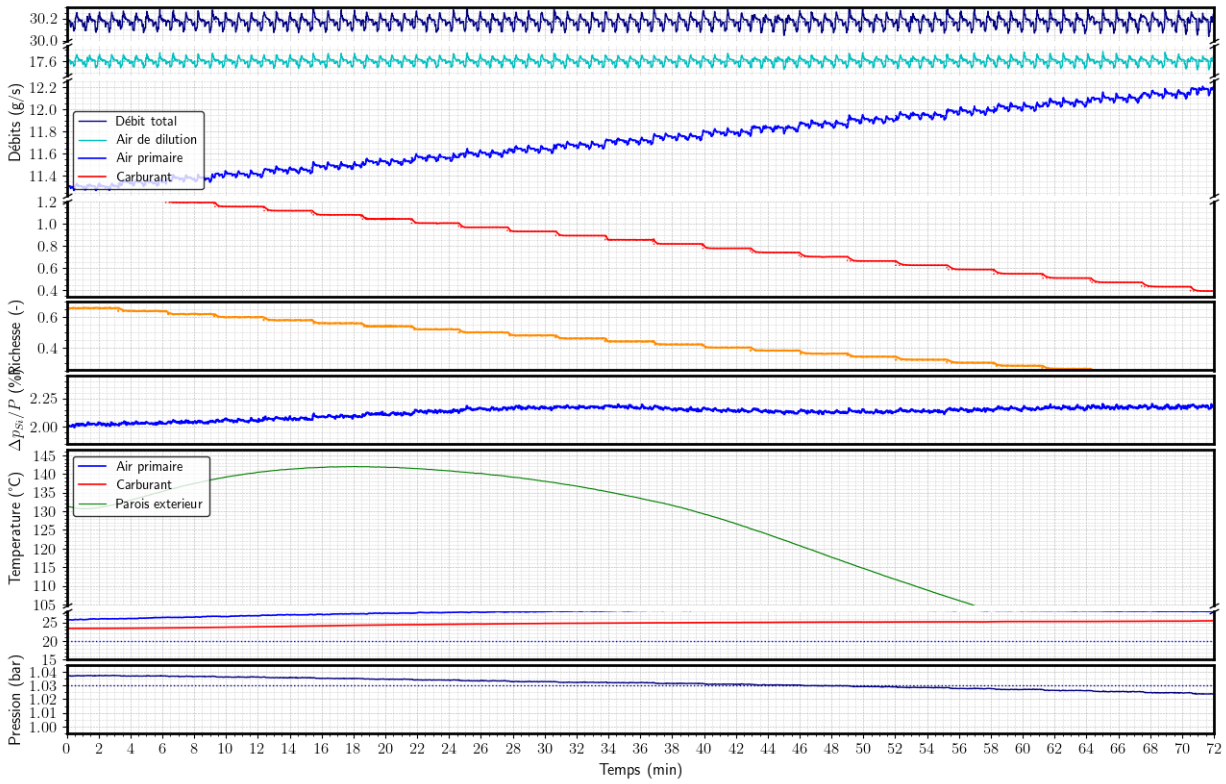

Figure 2.8 Graphical report of an experiment performed in HARTur facility.

Chapter 3
Butyl Levulinate Hydrogenation

This thesis chapter studies the hydrogenation of butyl levulinate (BL) to produce gamma-valerolactone (GVL). This chapter aims to develop an advanced kinetic model for this chemical reaction, considering isothermal, isoperibolic, and adiabatic conditions. Part of this chapter has been adapted from the following articles:

- Jose Delgado, **Wenel Naudy Vasquez Salcedo**, Christine Devouge-Boyer, Jean-Pierre Hebert, Julien Legros, Bruno Renou, Christoph Held, Henrik Grenman, Sebastien Leveneur. *Reaction enthalpies for the hydrogenation of alkyl levulinates and levulinic acid on Ru/C – influence of experimental conditions and alkyl chain length.* Process Safety and Environmental Protection 171 (2023) 289–298. `https://doi.org/10.1016/j.psep.2023.01.025`
- **Wenel Naudy Vasquez Salcedo**, Melanie Mignot, Bruno Renou, Sebastien Leveneur. *Assessment of kinetic models for the production of γ-valerolactone developed in isothermal, adiabatic and isoperibolic conditions.* Fuel 350 (2023) 128792. `https://doi.org/10.1016/j.fuel.2023.128792`

3.1 Chemical System

The production of gamma valerolactone (GVL) from alkyl levulinates (ALs) represents a fundamental step in the valorization route of lignocellulosic biomass (LCB) into sustainable aviation fuels (SAF). One of the main objectives of our research is to develop a kinetic model for producing GVL from butyl levulinate (BL) via hydrogenation. Kinetic models are fundamental tools for the optimal reactor design and industrial application of any chemical reaction. In addition, a robust and reliable kinetic model allows the maximization of energy recovery and the implementation of appropriate safety systems to minimize thermal risks when exothermic reactions are involved. To cover these aspects, our interest in this chapter is to develop a kinetic model that includes experiments performed under isothermal and non-isothermal conditions.

We chose butyl levulinate as a raw material because it has certain advantages over other alkyl levulinates and levulinic acid, such as lower thermal risk, potential application as a fuel additive, less corrosive, and butanol is obtained as a by-product; this latter has a particular interest from an industrial and commercial point of view. BL hydrogenation was studied in the RC1 calorimeter. The RC1 is a suitable autoclave reactor, coupled with a gas-liquid stirrer, that supports high pressure and can operate in isothermal, isoperibolic, and adiabatic conditions. The chemical system for this reaction comprises butyl levulinate in liquid form (reactant), hydrogen in gas form (reactant), ruthenium over activated carbon (solid catalyst), and gamma-valerolactone in liquid form (reaction solvent). For this heterogeneous system, the production of GVL via hydrogenation of BL occurs in a two-step serial reactions, i.e., hydrogenation and cyclization steps, as shown in Figure 3.1.

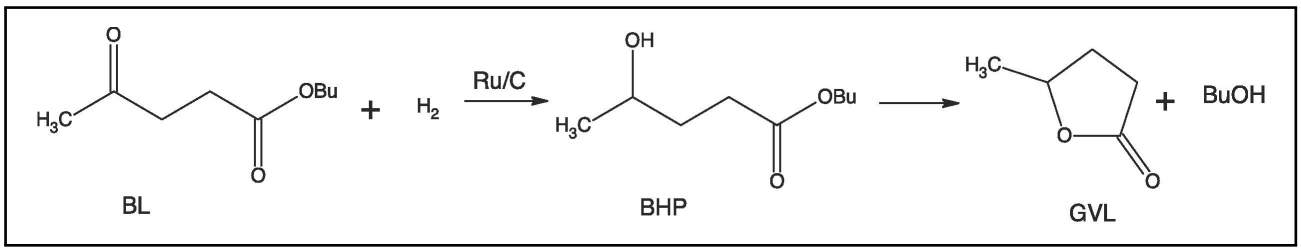

Figure 3.1 Reaction pathway for GVL production from BL hydrogenation over Ru/C.

The first step of the reaction is hydrogenation. It is produced when the double bond of the carbonyl group of the BL molecules is hydrogenated to produce the intermediate butyl 4-hydroxy pentanoate (BHP); this step reaction only occurs in the active sites of the catalyst, which in our case is the noble metal ruthenium over activated carbon. The second step is the cyclization of the intermediate BHP; during this step, the hydroxyl group of the intermediate reacts with the ester group to produce GVL as the main product and butanol as a by-product.

These two-step reactions occur sequentially in the liquid phase inside the RC1. The process involves loading butyl levulinate, gamma-valerolactone, and ruthenium into the RC1 to perform the experiments. Then, the temperature of the reaction mixture is increased until it reaches the set value. Following this, hydrogen is fed into the RC1 continuously via the automatic control (PID) to increase the pressure to the desired point; this hydrogen pressure is kept constant to ensure a constant hydrogen concentration during the reaction time. The stirring rate is set to 1000 RPM to start the reaction process. Figure 3.2 shows a representation of the chemical system.

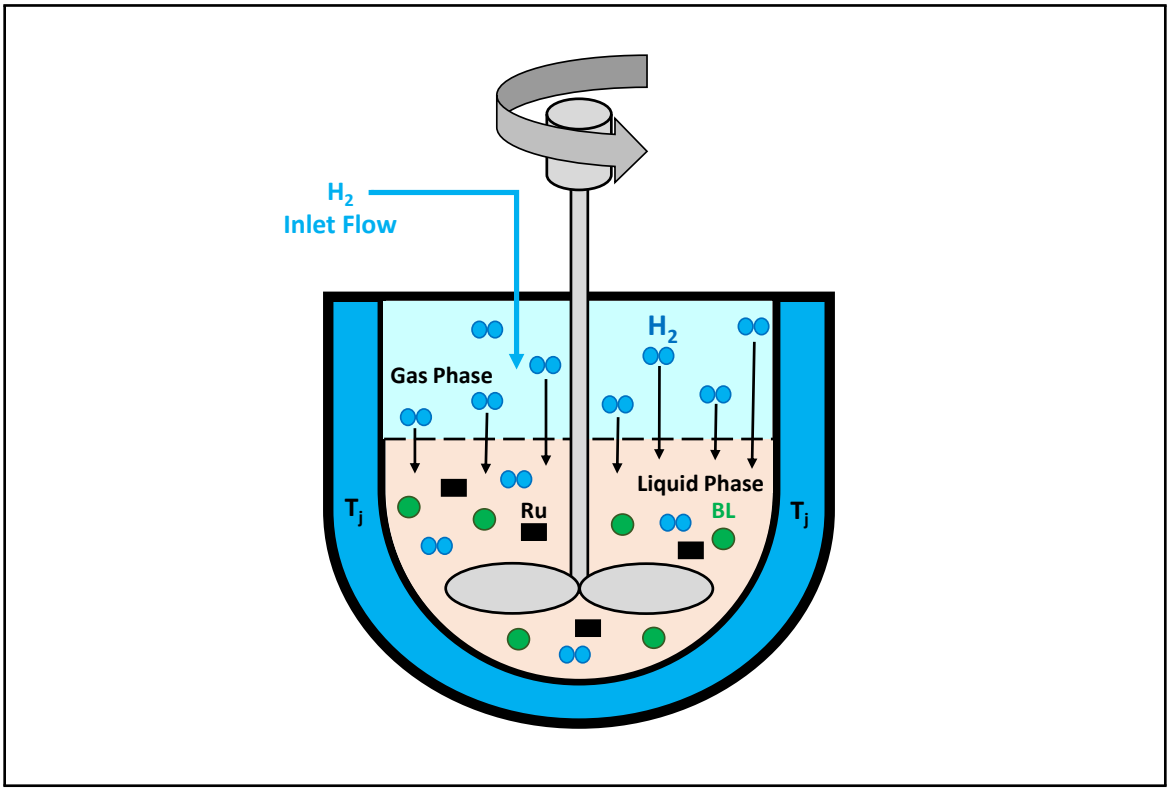

Figure 3.2 Representation of the chemical system in the RC1 during BL hydrogenation.

3.1.1 Material and Energy Balance

To establish the material and energy balance, it is necessary to identify the operation mode of the reactor. As we have already defined above, the reactants and the catalyst are loaded inside the reactor at the beginning, and only hydrogen is fed during the reaction to keep the pressure constant. Therefore, the RC1 operates in the semi-batch mode. In semi-batch reactors, the concentrations of chemical species are functions of time and are affected by the chemical reactions involving them. Except for the dosed species, these are affected by the chemical reactions and the dosing factor, in our case, hydrogen.

Inside the reactor, we can distinguish two main phases: the gas phase, made up of pure hydrogen, and the liquid phase, where all the reactants and the catalyst are located. The chemical reaction takes place in the liquid phase. The thermal contribution of hydrogen transfer was not considered to establish the energy balance. This consideration is possible because hydrogen is transferred from the gas phase, which is considered at the same temperature as the liquid phase. Therefore, the thermal contribution of the hydrogen to the liquid phase can be neglected. Thus, the material balance and the energy balance for our chemical system can be established as follows:

$$\frac{d[BL]}{dt} = -\mathbf{R_{hyd}} \tag{3.1}$$

$$\frac{d[BHP]}{dt} = +\mathbf{R_{hyd}} - \mathbf{R_{cyc}} \tag{3.2}$$

$$\frac{d[GVL]}{dt} = +\mathbf{R_{cyc}} \tag{3.3}$$

$$\frac{d[BuOH]}{dt} = +\mathbf{R_{cyc}} \tag{3.4}$$

$$\frac{d[H_2]_{liq}}{dt} = +\mathbf{k_L a}\left([H_2]^*_{liq} - [H_2]_{liq}\right) - \mathbf{R_{hyd}} \tag{3.5}$$

$$\frac{dT_r}{dt} = \frac{(-\mathbf{R_{hyd}}\cdot\mathbf{\Delta H_{hyd}} - \mathbf{R_{cyc}}\cdot\mathbf{\Delta H_{cyc}})V_r + \mathbf{UA}(T_j - T_r) + \alpha(T_{amb} - T_r)}{(mC_p)_{liq} + (mC_p)_{cat} + (mC_p)_{ins}} \tag{3.6}$$

From this system of differential equations, Equations 3.1 - 3.6, established from the mass and energy balance, we can note that the involved terms are:

- ***Hydrogenation rate***: This reaction rate, $\mathbf{R_{hyd}}$, represents the number of moles that are consumed or produced per unit of volume per unit of time of all chemical compounds affected by the hydrogenation step-reaction, in our case these compounds are the BL, hydrogen and the intermediate BHP.
- ***Cyclization rate***: This reaction rate, $\mathbf{R_{cyc}}$, represents the number of moles that are consumed or produced per unit of volume per unit of time of all chemical compounds affected by the cyclization step-reaction, in our case these compounds are the intermediate BHP, the main product GVL and the by-product butanol.
- ***Mass transfer Coefficient***: The hydrogen transfer rate from the gas phase to the liquid phase is calculated multiplying the volumetric mass transfer coefficient, $\mathbf{k_L a}$, by the difference between the hydrogen concentration at equilibrium, $[H_2]^*_{liq}$, and the hydrogen concentration in the liquid phase $[H_2]_{liq}$.

- ***Reaction Enthalpies***: The reaction enthalpy represents the energy released or absorbed during a chemical reaction. In our chemical system, there are two steps of the reaction, and there is a reaction enthalpy associated with each step one, i.e., hydrogenation enthalpy $\mathbf{\Delta H_{hyd}}$, and cyclization enthalpy $\mathbf{\Delta H_{cyc}}$.

- ***Heat Transfer Coefficient***: The heat-flow exchanged between the reaction mixture and the heat carrier fluid circulating in the jacket of the reactor is proportional to the product **UA**, where U is the global heat transfer coefficient and A the heat transfer area, and T_j is heat carrier fluid temperature located in the reactor jacket.

- ***Heat Loss Coefficient***: The heat losses from the reactor to the surroundings are proportional to the difference between the reaction mixture temperature T_r and the temperature of the surrounding T_{amb}, the temperature of the surrounding is measured during all experiments thanks to a thermocouple. The proportionality factor of heat losses in the RC1, α, is given by the manufacturer and equals 0.1 W/K.

- ***Thermal Heat Capacities***: The heat accumulation in the reactor depends on the heat capacity of all the elements inside the reactor. In our energy balance, we have included the reaction mixture heat capacity, $(mC_p)_{liq}$, that can be evaluated in the RC1 and also calculated from the literature [86]. The heat capacity of the solid catalyst, $(mC_p)_{cat}$, was obtained from the literature [87]. And the heat capacity of the inside elements of the RC1, $(mC_p)_{ins}$, such as the stirrer, thermocouple, calibration rod, etc. The manufacturer gives this value equal to 52 J/K.

3.2 Heat Transfer Analysis

The heat-flow exchange between the reaction mixture and the heat carrier fluid is defined by the global heat transfer coefficient U. The U coefficient represents the sum of five resistances to heat transfer in series, Equation 3.7 [88]. There are internal and external film resistances, internal and external fouling resistances, and wall conduction resistance. The fouling resistances are often assumed to be negligible. U coefficient is based on the heat transfer area A, internal and external diameters of the vessel d_i and d_o, the convective coefficients from reaction and jacket side h_r and h_j, the heat conductivity of the wall λ_w, and the height of the heat transfer area, L, which is likely to be affected by vortexing of the process fluid due to agitation as well as by the geometry of the system.

$$\frac{1}{\mathbf{UA}} = \frac{1}{h_r A} + R_r + \frac{\ln\left(d_i/d_o\right)}{2\pi L \lambda_w} + R_j + \frac{1}{h_j A} \tag{3.7}$$

Suppose the chemical reaction takes place at constant volume and constant operating conditions. In that case, only the convective coefficient from the reaction side, h_r, changes during the reaction, and the other terms can be combined into a constant term. The coefficient h_r depends directly on the properties of the reaction mixture (viscosity, heat conductivity, density, heat capacity) and the stirring efficiency (type of agitator, rotation speed, diameter of the reactor). These properties are related to h_r through the Nusselt correlation equations, which associates the dimensionless Nusselt number (Nu) to the Reynolds number (Re) and the Prandtl number (Pr), Equation 3.8. Figure 3.3 represents the two-film model for heat transfer.

$$Nu = \frac{h_r d_i}{\lambda_w} = C \cdot Re^a \cdot Pr^b \tag{3.8}$$

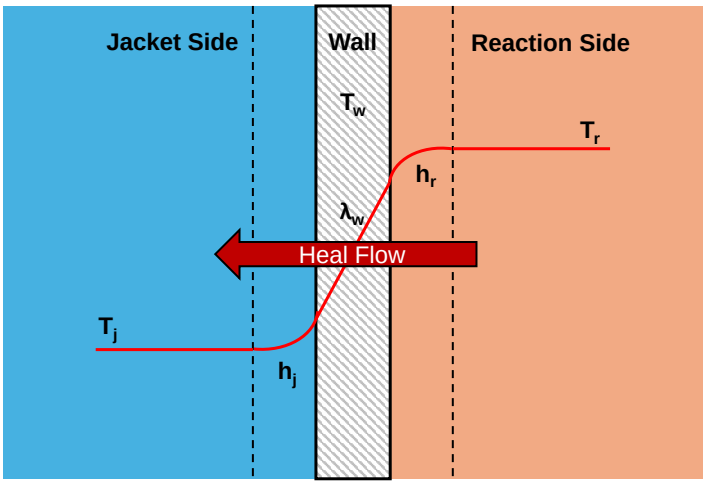

Figure 3.3 Two-film model representation for heat transfer from the reaction mixture to the jacket side.

3.2.1 Wilson Plot

The Wilson plot method is suitable for estimating the convection coefficients in various convective heat transfer processes. This method was developed by Wilson in 1915 to evaluate the convective coefficient in shell and tube condensers. It is based on separating the global thermal resistance into the reaction convective thermal resistance and the remaining thermal resistances participating in the heat transfer process [89], Equation 3.9.

$$\frac{1}{U} = \frac{1}{h_r} + \frac{1}{\phi_r} \tag{3.9}$$

Under isothermal conditions, the properties of the fluid and geometrical factors can be considered constant. This allows us to write h_r from Nusselt correlation as a function of the rotation speed of the stirrer, Equation 3.10 [90]. As we have seen, the convective coefficient h_r depends on several physical properties of the reaction mixture, such as density, viscosity, and thermal capacity. In our reaction system, the main species are BL and GVL; the contribution of the other chemical species in our reaction system is negligible compared to these two. Ariba et al. [86] developed mathematical equations to calculate these properties for various alkyl levulinates, alcohols, and GVL. Figure 3.4 shows these properties as a function of temperature; from these results, we can see that the difference between BL and GVL is insignificant.

$$h_r = C' N^a \tag{3.10}$$

To apply the Wilson plot method, we have used RC1 to calculate the **UA** value of pure BL at different temperatures and stirring rates (N); the experimental matrix and the results obtained are shown in Table 3.1. Figure 3.5a shows that there is a linear relationship between **UA** and $N^{-2/3}$, which means that a=2/3 in the Nusselt correlation. The latter proves that the two-film model describes the heat transfer process in the RC1.

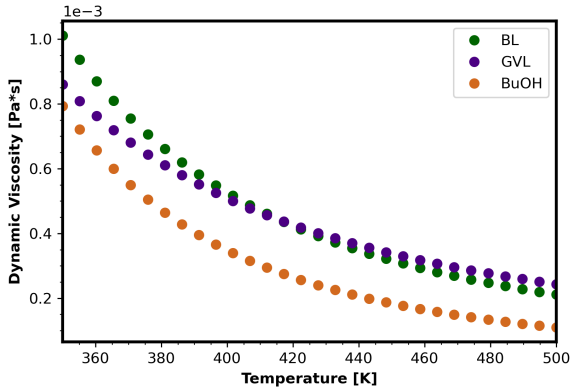

(a) Dynamic viscosity versus temperature.

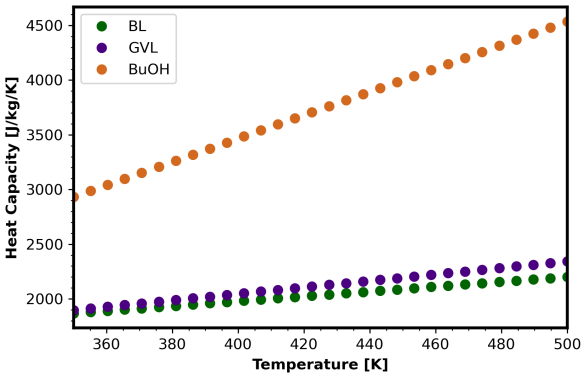

(b) Heat capacity versus temperature

Figure 3.4 Physical properties of BL, GVL, and BuOH as a function of the temperature.

Table 3.1 Experimental matrix for UA value determination in the RC1.

T [K]	N [RPM]	U [W/m2/K]	UA [W/K]
373	250	380.43	9.3262
	500	507.25	12.435
	750	580.19	14.223
	1000	593.66	15.261
	1200	647.39	15.871
393	250	415.02	10.174
	500	543.61	13.326
	750	622.64	15.264
	1000	677.05	16.598
	1200	707.00	17.332
413	250	435.33	10.672
	500	583.63	14.308
	750	674.37	16.532
	1000	730.75	17.914
	1200	769.84	18.872
433	250	475.26	11.651
	500	619.82	15.195
	750	719.95	17.650
	1000	780.86	19.143
	1200	810.70	19.874

The slope of the Wilson plot regression lines contains the information about h_r [91]. Using the slopes of the regression lines of all the Wilson plots, we can calculate the constant C' from Equation 3.10 and then the h_r for a given stirring rate. In our case, we seek to obtain mathematical equations that allow us to calculate **UA** as a function of the temperature for a given stirring rate. The experimental behavior of **UA** is shown in Figure 3.5b for the different stirring rates considered. Finally, Figure 3.5c shows the second-order polynomial fit for **UA** at 1000 RPM; this polynomial is the one used to calculate the evolution of **UA** during kinetic experiments.

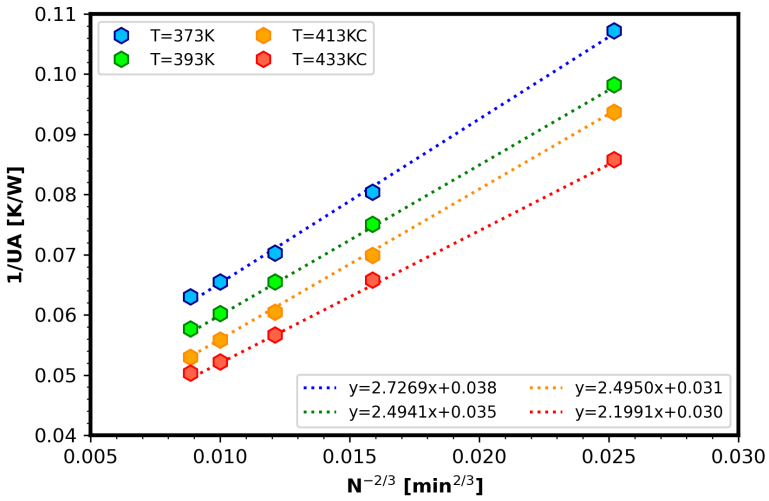

(a) $(UA)^{-1}$ versus $N^{-2/3}$.

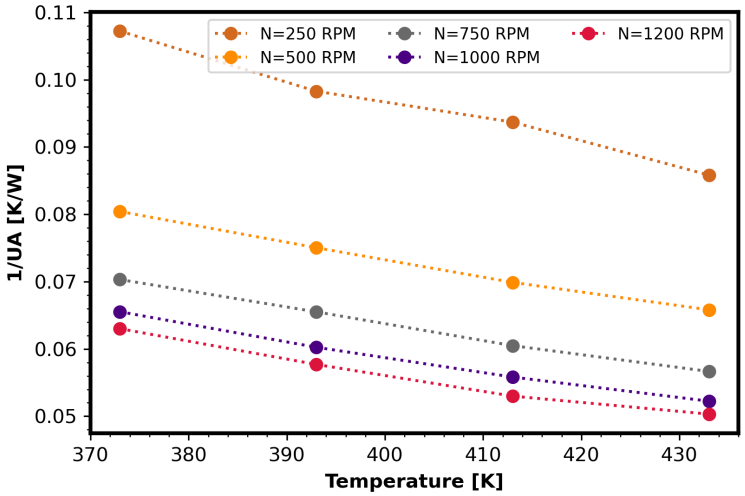

(b) $(UA)^{-1}$ versus temperature.

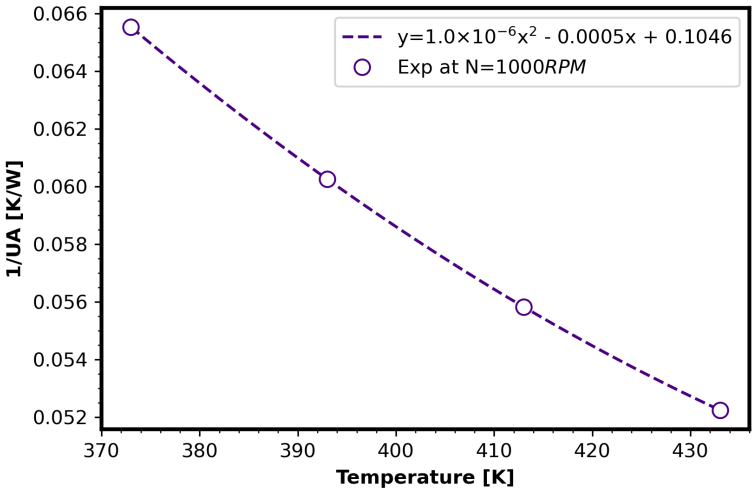

(c) $(UA)^{-1}$ versus T at 1000 RPM

Figure 3.5 Heat transfer analysis: Wilson Plot Results.

3.3 Mass Transfer Assessment

Heterogeneous systems are distinguished from homogeneous ones by the different phases present during the chemical reaction. In homogeneous systems, the catalysts are present in the same phase as reactants and products, usually in the liquid phase. Meanwhile, catalysts in heterogeneous systems are present in different phases, usually as solids. The main advantage of heterogeneous systems is that catalysts can be separated from the product stream relatively easily, which facilitates the creation of continuous chemical processes. A heterogeneous catalytic system involves the adsorption of reactants from a fluid phase into the catalyst, the reaction of the reactants absorbed in the catalyst, and the desorption of products into the fluid phase.

These mass transfer phenomena that characterize the heterogeneous system play a fundamental role in the chemical reaction rate since the reaction rate can be reduced if there is a mass transfer limitation of the reagents to the catalyst surface. Therefore, the limitations of mass transfer must be quantified to establish the optimal conditions for developing the chemical reaction.

In section 3.1, we have presented our chemical system, which is a heterogeneous system that has different phases inside the reactor: the gas phase in which there is pure hydrogen (reactant), the liquid phase in which the there is BL (central reactant) and the solid catalyst (Ru/C). For the chemical reaction to take place, the following steps must be carried out:

1. The hydrogen in the gas phase must pass into the liquid phase; this transfer process occurs via mass diffusion. Moreover, thanks to the mechanical help the stirrer provides that favors gas-liquid transfer.

2. The BL and hydrogen present in the liquid phase are adsorbed into the catalyst's surface; this adsorption process is determined by the adsorption constant of each species. It can also be favored by mechanical aid; a good stirring rate helps to have a good suspension and homogeneity of the catalyst in the liquid phase.

3. The reactants adsorbed into the catalyst via molecular diffusion are transported through the pores of the catalyst to the active sites where the reaction occurs. In our system, only adsorbed reactants can react.

These sequence of mass transfer steps are represented in Figure 3.6. These steps represent the mass transfer process during the chemical reaction, and each was evaluated and considered for developing our kinetic model.

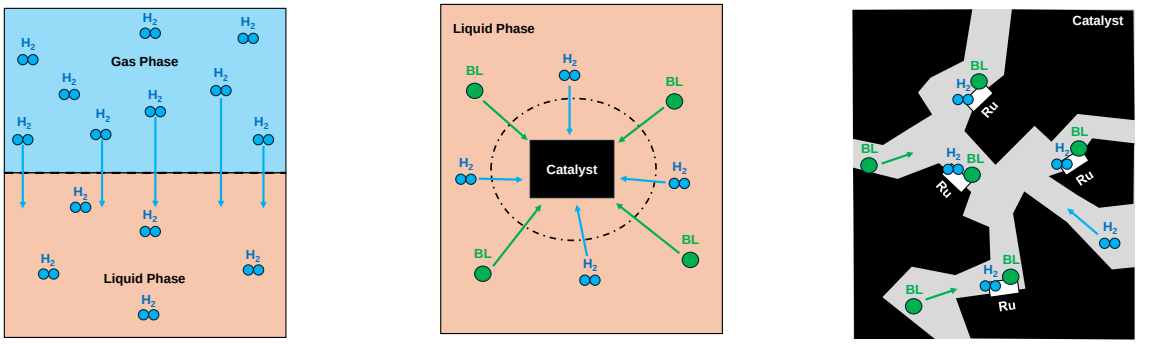

(a) Gas-liquid transfer. (b) Liquid-solid transfer. (c) Solid internal transfer.

Figure 3.6 Mass transfer sequence in our chemical system.

3.3.1 External Transfer

Our system has two external transfer processes: i) The gas-to-liquid transfer (hydrogen) mainly depends on the gas pressure and liquid physical properties. ii) The transfer from the liquid to the solid catalyst mainly depends on the adsorption constant and the appropriate distribution and suspension of the solid in the liquid phase.

Gas to Liquid Transfer

To determine the volumetric mass transfer coefficient ($\mathbf{k_La}$), which quantifies the hydrogen transfer from the gas phase to the liquid phase, we followed the methodology used by Wang et al. [92]. This methodology proposes to define $\mathbf{k_La}$ as a function that depends on a modified volumetric mass transfer coefficient $(k_La)_{mod}$ (which is considered to be constant), the temperature, density, and viscosity of the reactionary media, Equation 3.11.

$$\mathbf{k_La} = (k_La)_{mod} \cdot \left(\frac{T_{liq}}{\mu_{liq}}\right)^{0.5} \cdot \left(\frac{\rho_{liq}}{\mu_{liq}}\right)^{0.25} \tag{3.11}$$

Physical properties such as density and viscosity that are temperature dependent were calculated by Ariba et al. [86]. $(k_La)_{mod}$ was calculated experimentally, Table 3.2 show the experiments and the results obtained. These experiments were performed in the absence of a catalyst so that the reaction rates are equal to zero; thus, Equation 3.5 is simplified to:

$$\frac{d[H_2]_{liq}}{dt} = +\mathbf{k_La}\left([H_2]^*_{liq} - [H_2]_{liq}\right) \tag{3.12}$$

RC1 installation allows us to record the temperature and pressure evolution in the hydrogen reservoir. Knowing the volume, the temperature, and the pressure variation in the reservoir, we can apply the Redlich-Kwong-Mathias-Copeman (RKMC) state equation to calculate the hydrogen moles variation. According to Nasrifar [93], the RKMC equation is more accurate and robust for hydrogen. It was assumed that the number of moles of hydrogen disappearing in the reservoir corresponds to the hydrogen moles in the liquid phase. By integrating Equation 3.12, and using Equation 3.11, the $(k_La)_{mod}$ can be calculated as:

$$(k_La)_{mod} = \frac{1}{\Delta t \cdot \left(\frac{T_{liq}}{\mu_{liq}}\right)^{0.5} \cdot \left(\frac{\rho_{liq}}{\mu_{liq}}\right)^{0.25}} \cdot \ln\left(\frac{[H_2]^*_{liq} - [H_2]_0}{[H_2]^*_{liq} - [H_2]_f}\right) \tag{3.13}$$

Where Δt is the difference between the initial and final time during hydrogen transfer, T_{liq} is the liquid temperature, ρ_{liq} and μ_{liq} are the liquid density and viscosity, respectively. $[H_2]^*_{liq}$ is the hydrogen concentration at the gas-liquid interface defined as $He(T) = [H_2]^*_{liq}/P_{H_2}$, where $He(T)$ is Henry's constant. Henry's constant for BL and GVL was calculated with Equation 3.14, the parameters of this equation were obtained from the literature [92, 94].

$$He(T) = He(T_{ref}) \exp\left\{\frac{-\Delta H_{sol}}{R}\left(\frac{1}{T} - \frac{1}{T_{ref}}\right)\right\} \tag{3.14}$$

Table 3.2 Gas to liquid mass transfer experimental matrix and results.

Run	$\mathbf{m}_{BL}$	$\mathbf{T_r}$	$\mathbf{P}_{H_2}$	$\Delta\mathbf{t}$	$\Delta\mathbf{n}_{H_2}$	$(\mathbf{k_L a})_{\ mod}$
	$[kg]$	$[K]$	$[bar]$	$[s]$	$[mol]$	$[(Pa{\cdot}s{\cdot}K^{-1})^{0.5}(Pa{\cdot}s{\cdot}kg^{-1}{\cdot}m^{-3})^{0.25}s^{-1}]$
MT-1	0.520	373.15	25	38	0.0420	2.28×10^{-6}
MT-2	0.520	373.15	25	18	0.0286	2.10×10^{-6}
MT-3	0.520	413.15	25	16	0.0426	2.44×10^{-6}
MT-4	0.520	433.15	25	8	0.0322	2.21×10^{-6}

From the results, we can notice that the calculated value of $(k_L a)_{mod}$ for each run is very similar. The average value is $2.25 \times 10^{-6} Pa{\cdot}s{\cdot}K^{-1})^{0.5}(Pa{\cdot}s{\cdot}kg^{-1}{\cdot}m^{-3})^{0.25}s^{-1}$ and the standard deviation is equal to $0.14\,(Pa{\cdot}s{\cdot}K^{-1})^{0.5}(Pa{\cdot}s{\cdot}kg^{-1}{\cdot}m^{-3})^{0.25}s^{-1}$. This result is very similar to the one found by Wang et al. [92].

Liquid to Solid Transfer

For solid-catalyzed reactions to occur, the reactants must first diffuse through the stagnant boundary layer surrounding the catalyst particle. The adsorption constant and the mechanical stirring rate determine the liquid-solid transfer. The effect of the adsorption constant is considered during the derivation of the kinetic models.

Wang et al. [92] studied the mass transfer during the hydrogenation of different alkyl levulinates over Ru/C, the same heterogeneous system considered in this research. This study was carried out in a lab-scale reactor called a PARR reactor; they concluded that there was no limitation of mass transfer for a stirring rate of 1000 RPM. To reduce the liquid-solid mass transfer limitations in the RC1, we have addressed this as a scale-up problem using the PARR reactor as a reference. This aims to determine the optimal reaction volume and stirring rate configuration.

The scale-up criterion is usually given as an overall equation for mixing operations, Equation 3.15. N is the stirring rate, D_s is the stirrer diameter, and n is equal to 1 for equal liquid motion, 3/4 for equal solid suspension, and 2/3 for equal mass transfer rates.

$$ND_s^n = constant \tag{3.15}$$

Evaluating Equation 3.15, we have obtained that for a stirring rate equal to 746 RPM, we should have the same mass transfer and solid suspension as in the PARR reactor. Experiments in the RC1 were performed at 1000 RPM; this guarantees that there will be no liquid-solid mass transfer limitations in the RC1.

$$N_2 = N_1 \left(\frac{D_1}{D_2}\right)^{(2/3)} = (1000\,RMP)\left(\frac{2.9}{4.5}\right)^{(2/3)} = 746\,RPM \tag{3.16}$$

One way to compare the behavior of the liquid phase within both reactors is by comparing the following dimensionless numbers for both reactors:

- *Reynolds Number (Re)*, in fluid mechanics, is a measurement of the ratio of inertial force to viscous force. Defined as:

(a) PARR reactor.

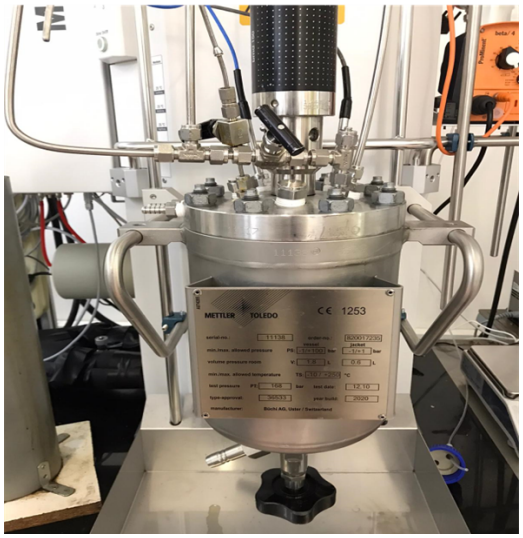

(b) RC1 calorimeter.

Figure 3.7 Image of the PARR reactor, vessel volume equal to 0.3 L, and the RC1 calorimeter, vessel volume equal to 1.8 L.

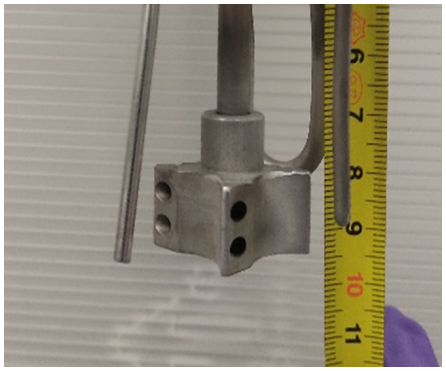

(a) PARR stirrer.

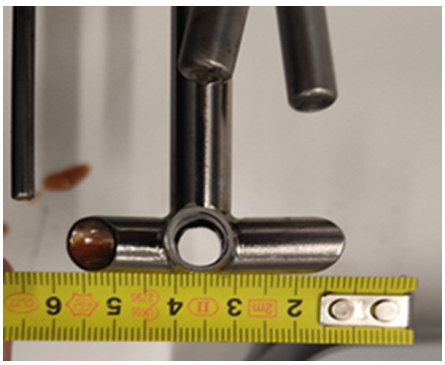

(b) RC1 stirrer.

Figure 3.8 Stirrer comparison between PARR, stirrer diameter equal to 2.9 cm, and RC1, stirer diameter equal to 4.5 cm.

$$Re = \frac{\rho N D_s^2}{\mu} \tag{3.17}$$

- *Froude Number (Fr)*, this dimensionless number is calculated using the ratio of inertial force to gravity. It is calculated as:

$$Fr = \frac{N^2 D_s}{g} \tag{3.18}$$

- Weber Number (We) represents the applied to surface tension forces ratio. Define as:

$$We = \frac{\rho N^2 D_s^2}{\sigma} \tag{3.19}$$

The evaluation of this dimensionless number for the PARR reactor and the RC1 calorimeter is shown in Table 3.3. Based on the results, there is no expected liquid-solid mass transfer limitation in the RC1 at 1000 RPM.

Table 3.3 Dimensionless numbers comparison between PARR and RC1 reactor at $N = 1000\,\text{RPM}$.

Number	PARR value	RC1 value	RC1/PARR
Reynolds Number	6751	16256	2.4
Froude Number	0.878	1.362	1.6
Weber Number	8176	19688	2.4

3.3.2 Internal Transfer

Another factor of great importance in solid-catalyzed reactions is the internal transfer of the reactants within the catalyst. Many solid catalysts have pores to increase the specific surface area available for adsorption and reaction, e.g., up to $10^3\,\text{m}^2/\text{g}$. Among the factors that most affect the transfer are the size of the pores of the catalyst and the size of the molecules that pass through the pores.

During our research, the solid catalyst used is ruthenium on activated carbon; according to some references, the particle size of this powder can be between 125-212 μm [95]. Internal mass transfer in the catalyst can be assessed through the mass diffusion coefficients of the chemical species through the catalyst pores. For such a study, it is necessary to characterize the structure of the catalyst, which is beyond our scope. In this work, we assume no internal mass transfer limitations in the catalyst. This latter is based on the particle size of the catalyst and its high activity in hydrogenation reactions. This is a strong assumption that may affect the results of the kinetic model and should be verified in future related works since in our case it could not be verified.

In this section, we have analyzed the mass transfer of our heterogeneous system theoretically and experimentally. As a result, we consider that our system has neither external nor internal limitations. To conclude this section, we performed two sets of experiments on the PARR and RC1 reactors under the same initial and operating conditions. The chosen conditions are where reaction rates are expected to be high, so any limitations that may reduce kinetics in the RC1 can be noted.

The conditions of these experiments are shown in Table 3.4, and the results obtained are presented in Figure 3.9; the results correspond to the evolution of the concentration of the different compounds during the chemical reaction. These results reinforce our previous conclusion that in the RC1 with the stirring rate equal to 1000 RPM, there will be no mass transfer limitations.

Table 3.4 Experimental matrix to compare PARR and RC1 kinetic evolution.

Run		Operating Conditions			Initial Conditions		
		T_r [K]	P_{H_2} [kPa]	N [RPM]	$[BL]_0$ [mol/m^3]	$[GVL]_0$ [mol/m^3]	ω_{cat} [kg/m^3]
1	Parr	373	1500	1000	1255	7434	8.00
	RC1	373	1500	1000	1255	7434	8.00
2	Parr	413	2000	1000	1206	7145	7.69
	RC1	413	2000	1000	1206	7145	7.69

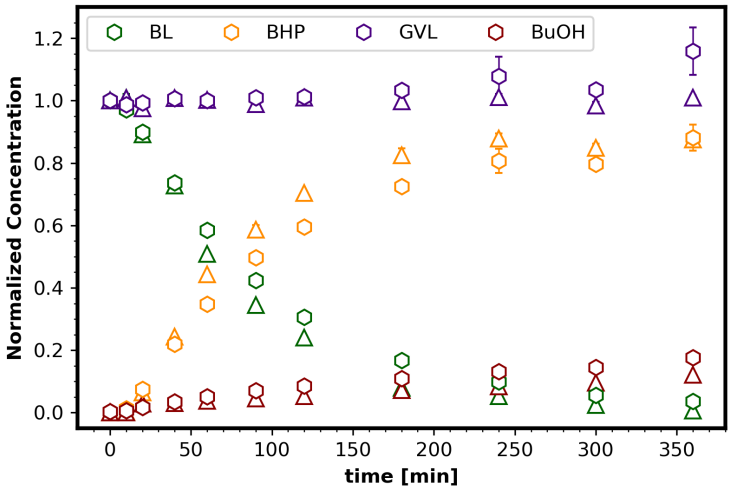

(a) Run #1: PARR vs RC1.

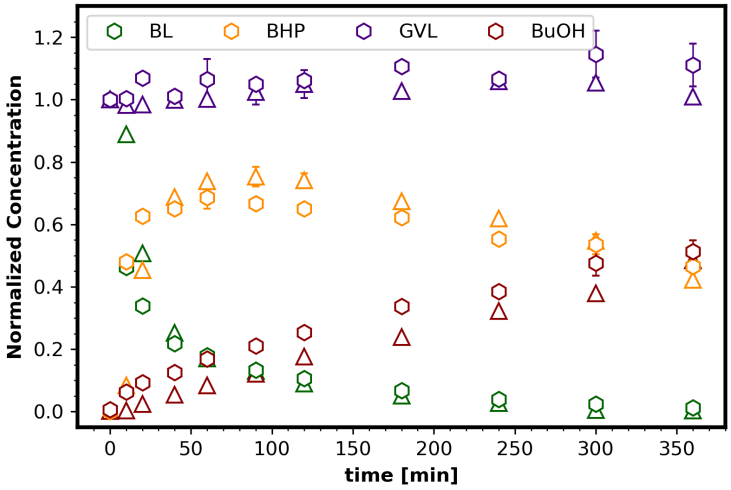

(b) Run #2: PARR vs RC1.

Figure 3.9 Mass transfer limitation: Kinetic comparison between PARR reactor and RC1 calorimeter. Triangles are for PARR, and hexagons for RC1.

3.4 Reaction Enthalpy

The reaction enthalpy, ΔH, is the heat energy absorbed or released during a chemical reaction at constant pressure. The reaction enthalpy is typically expressed in units of energy per amount of substance (such as joules per mole or kilojoules per mole) and can be positive or negative, indicating whether the reaction is endothermic (absorbs heat) or exothermic (releases heat), respectively.

As shown in Figure 3.1, the production of GVL via hydrogenation of BL over Ru/C occurs via two series reactions, i.e., hydrogenation and cyclization steps. Therefore, two reaction enthalpies are to be determined: the hydrogenation enthalpy of BL ($\mathbf{\Delta H_{hyd}}$) and the cyclization enthalpy of BHP ($\mathbf{\Delta H_{cyc}}$). To calculate these reaction enthalpies, experiments were performed in the RC1 and the C80 calorimeters under isothermal and isobaric conditions.

3.4.1 Hydrogenation Enthalpy

To calculate the hydrogenation enthalpy of BL ($\mathbf{\Delta H_{hyd}}$), this reaction was performed in the RC1 calorimeter at different operating temperatures and different initial concentrations as it is shown in Table 3.5. With this experimental matrix, we seek to verify the repeatability of the measurements and whether there is any influence of the initial concentration or temperature on the enthalpy values. The choice of the RC1 is because it is a suitable autoclave reactor to perform reactions at high pressure.

When hydrogenation is performed in the RC1, we have both step reactions as shown in the global chemical reaction (GCR). This is because the hydrogenation step takes place over the solid catalyst Ru/C to produce the intermediate. Then, the intermediate is catalyzed by temperature to produce GVL and butanol via the cyclization step.

$$\mathrm{BL} + \mathrm{H_2} \xrightarrow{H_{hyd}} \mathrm{BHP} \xrightarrow{H_{cyc}} \mathrm{GVL} + \mathrm{BuOH} \qquad \text{(GCR)}$$

The heat released during the reaction is calculated by integrating the heat flow rate during the reaction; the RC1 software does such integration. Applying a thermal balance and using the stoichiometry in the GCR, we can derivate the final expression to calculate the hydrogenation enthalpy:

$$\mathbf{\Delta H_{hyd}} = \frac{Q_{RC1} + \Delta n_{GVL} \cdot \mathbf{\Delta H_{cyc}}}{\Delta n_{BL}} \tag{3.20}$$

Where Q_{RC1} is the energy obtained from the RC1 by integrating the heat flow during the reaction, Δn_{BL} is the mole's variation of BL, and Δn_{GVL} is the mol variation of GVL. From Equation 3.20, we can notice that to calculate the hydrogenation enthalpy, we need to know the cyclization enthalpy; the calculation of the latter one is shown in the next subsection.

Table 3.5 Hydrogenation enthalpy: Experimental matrix and results, experiments were performed at P_{H_2}=3500 kPa, under isothermal and isobaric conditions.

Run	$\mathbf{m}_{BL0}$	$\mathbf{m}_{GVL0}$	**[Ru/C]**	$\mathbf{T_r}$	$\Delta\mathbf{n}_{BL}$	$\Delta\mathbf{n}_{GVL}$	$\mathbf{Q}_{released}$	$\mathbf{\Delta H_{hyd}}$
	$[kg]$	$[kg]$	$[kg/m^3]$	$[K]$	$[mol]$	$[mol]$	$[kJ]$	$[kJ/mol]$
Hyd-1	0.186	0.365	11.20	373.15	-1.173	0.755	36.72	-35.38
Hyd-2	0.186	0.365	11.20	373.15	-1.123	0.721	36.34	-36.43
Hyd-3	0.186	0.365	11.20	373.15	-1.132	0.371	36.03	-33.89
Hyd-4	0.186	0.365	10.87	403.15	-1.193	1.363	34.45	-36.11
Hyd-5	0.186	0.365	10.87	403.15	-1.173	0.893	35.30	-34.92
Hyd-6	0.100	0.452	10.85	403.15	-0.608	0.285	20.15	-36.09
Hyd-7	0.551	0.000	10.02	403.15	-3.576	1.347	113.62	-34.16

The hydrogenation enthalpy results are shown in Table 3 and Figure 3. These results show great consistency in terms of repeatability. We can notice that during the hydrogenation of BL, energy is released in the form of heat (Figure 3.10a), so we can affirm that the hydrogenation of BL is an exothermic reaction. We can also realize that we got practically the same enthalpy result for experiments performed at different initial concentrations and different operating temperatures, with the average value being: $\mathbf{\Delta H_{hyd}} = -35.28\,kJ/mol \pm 1.00\,kJ/mol$.

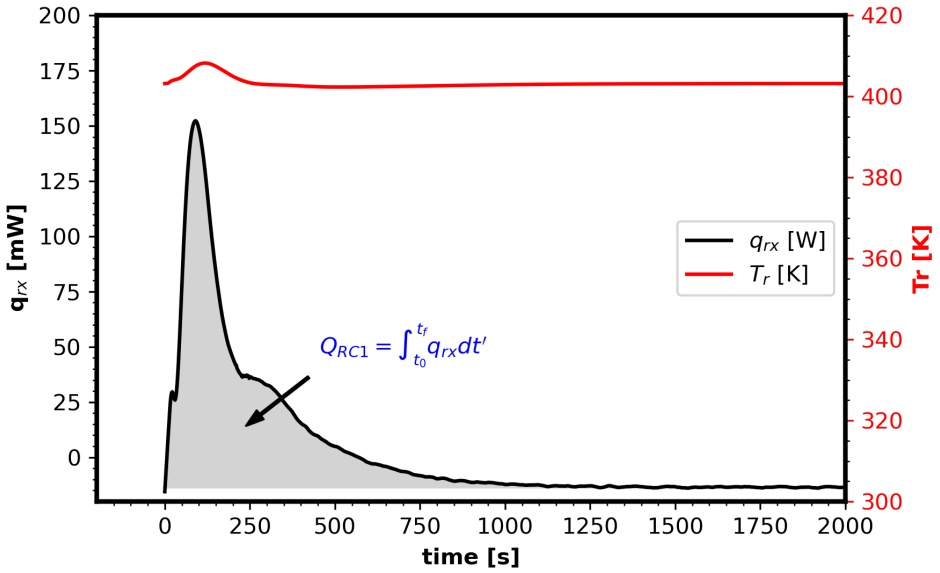

(a) Heat flow versus time during Hyd-4.

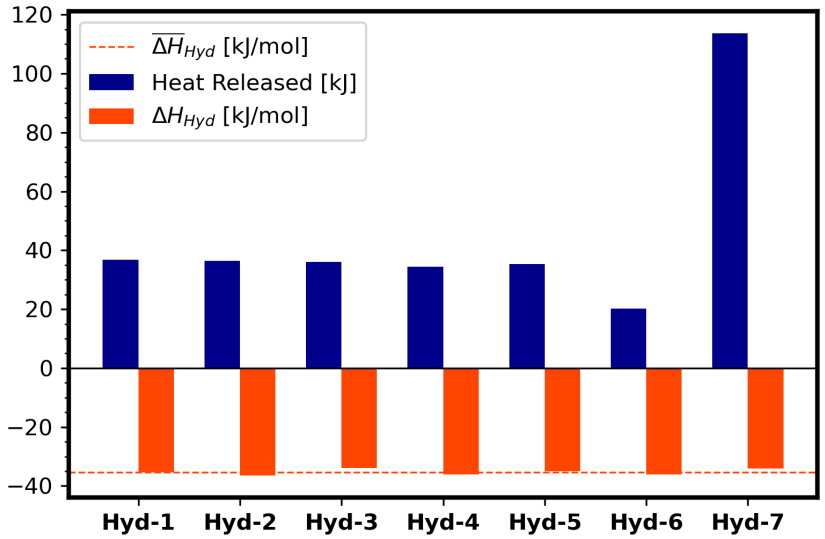

(b) Hydrogenation Enthalpy results.

Figure 3.10 Hydrogenation enthalpy results, (a) corresponds to the heat evolution during Run Hyd-4 and (b) Shows the heat released and enthalpy result for each Run.

3.4.2 Cyclization Enthalpy

In contrast to the hydrogenation enthalpy, which was calculated in RC1 since this is a reactor able to operate at high pressures, the determination of cyclization enthalpy ($\mathbf{\Delta H_{cyc}}$) does not require the presence of hydrogen at high pressure. The calculation of the cyclization enthalpy was carried out on the Tian Calvet C80 microcalorimeter. The C80 has the advantage of being an accurate microcalorimeter and only needs a few milligrams to carry out the measurements. Different BHP solutions were obtained from the RC1 hydrogenation experiments for use in the C80. The cyclization step reaction is shown in Equation Cyc.

$$\text{BHP} \xrightarrow{H_{cyc}} \text{GVL} + \text{BuOH} \tag{Cyc}$$

To carry out this reaction, it is necessary to prepare the C80 mixing cells as follows:

(i) In the measurement cell, 1 mL of BHP solution is placed in the internal compartment, and 1 mL of GVL with 0.01 mol/L of sulfuric acid is placed in the external compartment, which catalyzes the reaction.

(ii) The reference cell must be prepared in a symmetrical way to the measuring one; therefore, 1 mL of the BHP solution is placed in the internal compartment and 1mL of GVL in the external one, but without sulfuric acid so that, the reaction does not occur in the reference cell.

This preparation is shown in Figure 2.4c. This reaction was carried out at two different temperatures. Table 3.6 shows the experimental matrix and the results obtained. The heat of the reaction is calculated by integrating the heat flow during the reaction, as in the RC1; this integration is done by the C80 software. From the thermal balance applied to Equation Cyc, the cyclization enthalpy $\mathbf{\Delta H_{cyc}}$ can be calculated as follow:

$$\mathbf{\Delta H_{cyc}} = \frac{Q_{C80}}{\Delta n_{BHP}} \tag{3.21}$$

Q_{C80} is the heat obtained from the C80, and Δn_{BHP} is the mole's variation of BHP during the reaction. The latter one is calculated as:

$$\Delta n_{BHP} = \left([BHP]_f - [BHP]_0\right) V_r \tag{3.22}$$

Table 3.6 Cyclization enthalpy: Experimental matrix and results, under isothermal and isobaric conditions (101 kPa).

Run	$\mathbf{[BHP]_0}$	$\mathbf{[BHP]_f}$	$\mathbf{T_r}$	$\mathbf{\Delta n}_{BHP}$	$\mathbf{Q}_{absorbed}$	$\mathbf{\Delta H_{cyc}}$
	$[mol/m^3]$	$[mol/m^3]$	$[K]$	$[mol]$	$[J]$	$[kJ/mol]$
Cyc-1	1484	242	333.15	-2.483×10^{-3}	-14.10	5.68
Cyc-2	1336	254	333.15	-2.165×10^{-3}	-15.26	7.05
Cyc-3	1402	247	333.15	-2.310×10^{-3}	-14.97	6.48
Cyc-4	1407	307	363.15	-2.201×10^{-3}	-16.20	7.36
Cyc-5	276	34	363.15	-4.852×10^{-4}	-2.48	5.12

Table 3.6 and Figure 3.11 show the cyclization enthalpy results. These results show good consistency in terms of repeatability. Durgin, the cyclization of BHP heat was absorbed by the reactionary media (Figure 3.11a). Therefore, the cyclization of BHP is an endothermic reaction. We had a similar average value for both temperatures: $\mathbf{\Delta H_{cyc}} = 6.34\,kJ/mol \pm 0.93\,kJ/mol$.

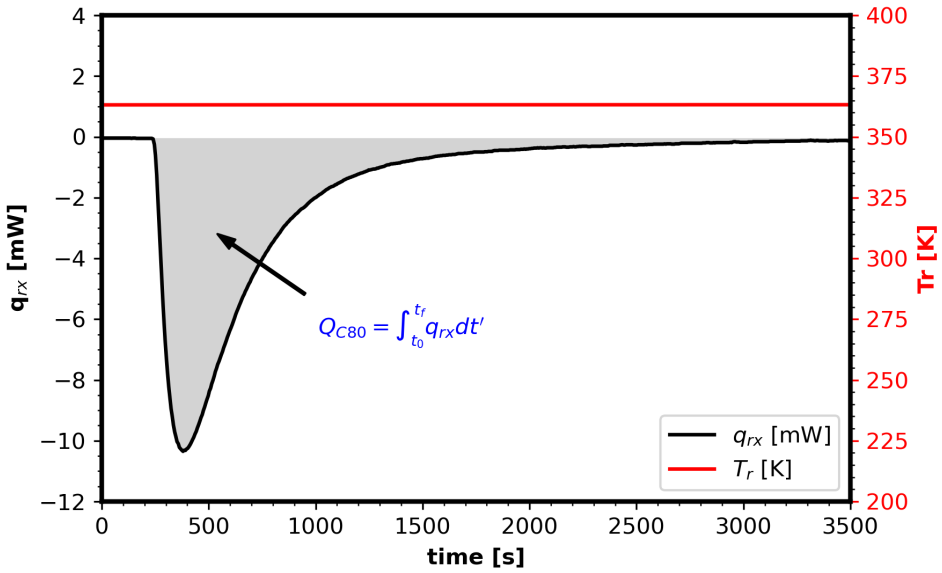

(a) Heat flow versus time during Cyc-4.

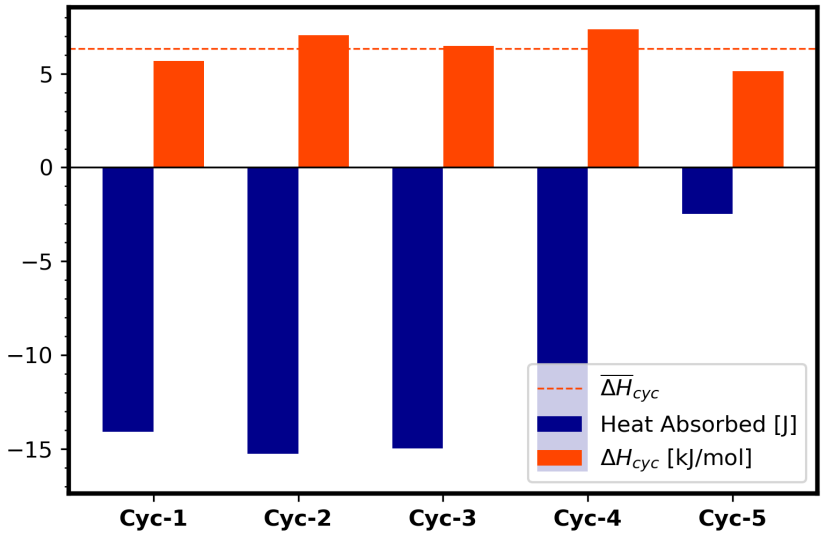

(b) Cyclization Enthalpy results

Figure 3.11 Cyclization enthalpy results, (a) corresponds to the heat evolution during Run Cyc-4 and (b) Shows the heat absorbed and the enthalpy result for each Run.

3.5 Kinetic Modeling

Kinetic modeling in heterogeneous systems is progressing to provide accurate predictions thanks to the advances in the physical and chemical representations of reaction phenomena. Kinetic models relate the physical and chemical state of a system (concentrations, pressure, temperature, etc.) to the rates of consumption/formation of the species. In general, kinetic models can be divided into: *i)* Phenomenological models that are based on the observed rates without considering the chemical or physical details, and *ii)* Elementary step models are based on the chemical and physical steps. The type of kinetic models considered in our research are the elementary ones.

The development of kinetic models is usually carried out under isothermal conditions, in which only the concentration of species is used as observable to estimate the kinetic parameters. The isothermal condition means that the temperature of the reaction media is kept constant during the reaction process. This type of kinetic model has certain limitations in terms of energy recovery optimization and thermal risk assessment since, during the estimation of kinetic parameters, temperature is not included as observable.

Kinetic models that integrate experiments performed under isothermal and non-isothermal conditions are uncommon in the literature. During non-isothermal conditions, one can only use the reaction temperature as an observable so as not to affect the thermal equilibrium of the reactionary media. This type of kinetic model, which includes both isothermal and non-isothermal conditions, is a great tool that enables the optimization of the reaction yield and, at the same enables the optimization of energy recovery and minimize thermal risk.

For the development of a robust and reliable kinetic model for the production of GVL from BL, a total of 17 experiments were performed in the RC1 calorimeter at different initial, operating, and thermal conditions, as shown in Table 3.7, these experiments were used during the regression stage to estimate the kinetic parameters. We have assessed five different kinetic models for heterogeneous reactions, described in the next Section. The developed models were validated to assess their reliability and select the most reliable ones; the experiments used for the validation stage are shown in Table 3.8.

The thermal conditions considered during the development of the kinetic model for GVL production were:

1. ***Isothermal Conditions:*** During isothermal mode operation, the temperature of the reactionary media T_r remains constant throughout the reaction process. This is achieved by controlling and adjusting the reactor jacket temperature T_j, which increases during endothermic reactions and decreases during exothermic reactions. During exothermic reactions, all heat released is transferred into the reactor jacket. It should be noted that this is the mode of operation where the thermal risk is lower since there is no heat accumulation in the system. In this mode, samples were taken at different times to track the evolution of the BL, BHP, and GVL concentrations. This concentration was used as an observable for the kinetic parameter estimation. Experiments in isothermal mode lasted at least 6 hours. Figure 3.12a and 3.12b show the experimental data collected from Run Isot-1.

2. ***Isoperibolic Conditions:*** During experiments in isoperibolic mode, the reactor jacket temperature T_j remains constant throughout the reaction, while the reaction media temperature T_r evolves depending on the type of reaction. T_r decreases for endothermic reactions and increases during exothermic reactions; after a certain time, T_r returns to values close to T_j. During exothermic reactions, part of the reaction's heat accumulates (causing the increase in T_r), and the other part is transferred to the reactor jacket. In this mode, samples were only taken before and after the reaction, but not during, to avoid affecting the thermal equilibrium inside the reactor. For this type of experiment, the reaction temperature T_r was tracked during the reaction and used as an observable for estimating the kinetic parameters. Figure 3.12c and 3.12d shows the experimental data collected from Run Isop-2. This mode of operation is interesting from an industrial point of view since it is not always possible to have a temperature control system for industrial reactors, and its implementation can be expensive.

3. ***Adiabatic Conditions:*** The absence of heat transfer characterizes this type of operation. During exothermic reactions, all the heat released is accumulated in the system, thus causing a significant increase in the reaction media temperature T_r. In order to achieve adiabatic conditions in RC1, the condition of $T_j = T_r$ was imposed on the temperature control system, thus minimizing the heat transfer from the reactionary media to the reactor jacket. Despite decreasing heat transfer to the reactor jacket, heat loss to the surroundings is still due to ambient temperature T_{amb}. As for the isoperibolic conditions, the samples were only taken before and after the chemical reaction. For this type of experiment, the reaction temperature T_r was tracked during the reaction and used as an observable for estimating the kinetic parameters. Figure 3.12e and 3.12f show the experimental data collected from Run Adi-6. It should be noted that this type of operation poses the most significant thermal risk since the total accumulation of heat can trigger decomposition reactions, uncontrollably increasing the pressure and temperature of the system.

Table 3.7 Experimental matrix for regression stage.

Run	$\mathbf{m}_{BL0}$	$\mathbf{m}_{GVL0}$	$\mathbf{m}_{Ru/C}$	$\mathbf{C}_{p_0}$	$\mathbf{UA}_0$	$\mathbf{P}_{H_2}$	$\mathbf{T}_{r_0}$	**Thermal Mode**
	$[kg]$	$[kg]$	$[kg]$	$[J/kg{\cdot}K]$	$[W/K]$	$[bar]$	$[K]$	
Isot-1	0.415	0.105	0.005	2736	17	35	393.15	Isothermal
Isot-2	0.500	0.000	0.007	2736	19	35	423.15	Isothermal
Isot-3	0.500	0.000	0.007	2736	19	35	432.15	Isothermal
Isot-4	0.117	0.402	0.004	2736	17	15	403.15	Isothermal
Isot-5	0.520	0.000	0.006	3131	17	20	394.15	Isothermal
Isop-1	0.500	0.000	0.005	2755	18	22	412.15	Isoperibolic
Isop-2	0.400	0.100	0.005	2773	17	30	392.15	Isoperibolic
Isop-3	0.420	0.100	0.005	2646	17	30	403.15	Isoperibolic
Isop-4	0.420	0.100	0.008	3131	17	35	393.15	Isoperibolic
Adi-1	0.520	0.000	0.006	2751	17	36	393.15	Adiabatic
Adi-2	0.520	0.000	0.006	2789	15	35	373.15	Adiabatic
Adi-3	0.520	0.000	0.005	2704	15	25	373.15	Adiabatic
Adi-4	0.420	0.100	0.007	2624	15	35	373.15	Adiabatic
Adi-5	0.520	0.000	0.006	2705	16	25	383.15	Adiabatic
Adi-6	0.350	0.170	0.008	2705	17	30	403.15	Adiabatic
Adi-7	0.400	0.120	0.005	3131	18	25	413.15	Adiabatic
Adi-8	0.520	0.000	0.004	3131	17	20	403.15	Adiabatic

Table 3.8 Experimental matrix for the validation stage.

Run	$\mathbf{m}_{BL0}$	$\mathbf{m}_{GVL0}$	$\mathbf{m}_{Ru/C}$	$\mathbf{C}_{p_0}$	$\mathbf{UA}_0$	$\mathbf{P}_{H_2}$	$\mathbf{T}_{r_0}$	**Thermal Mode**
	$[kg]$	$[kg]$	$[kg]$	$[J/kg{\cdot}K]$	$[W/K]$	$[bar]$	$[K]$	
Isot-6	0.415	0.105	0.005	2736	17	38	403.15	Isothermal
Isot-7	0.415	0.105	0.005	2736	15	35	373.15	Isothermal
Isot-8	0.520	0.000	0.006	2736	16	20	384.15	Isothermal
Isop-5	0.520	0.000	0.007	2788	15	35	373.15	Isoperibolic
Isop-6	0.420	0.100	0.008	2728	16	35	383.15	Isoperibolic

3.5.1 Kinetic Models

As discussed in Section 3.3, developing a kinetic model for a heterogeneous system must consider the mass transfer phenomena. In our reactionary system, the adsorption constant will be included in the mathematical equations that describe the hydrogenation rate reaction. This adsorption constant will be estimated during the regression stage based on experimental data, like this covering the liquid-to-solid mass transfer phenomena in the system.

As we have already seen, the global kinetics for the hydrogenation of BL is a two-step reaction, Figure 3.1. We have considered five different kinetic models for heterogeneous reactions to describe the hydrogenation step and determine the most reliable one. The derivation of the mathematical equations for the hydrogenation rate is based on the Langmuir-Hinshelwood adsorption theory. The following theory and demonstration were adapted and modified from the book "*Introduction to Chemical Engineering Kinetics and Reactor Design*" [96].

The Langmuir-Hinshelwood Adsorption:

The Langmuir isotherm corresponds to an idealized type of adsorption, and the analysis is predicated on the following key assumptions.

1. Molecules are adsorbed at discrete points of attachment on the surface, referred to as adsorption sites. Each site can accommodate only a single adsorbed species.
2. The energy of an adsorbed species is the same anywhere on the surface and is independent of the presence or absence of nearby adsorbed molecules. This assumption implies that the forces between adjacent adsorbed molecules are so small as to be negligible and that the probability of adsorption on an empty site is independent of whether or not an adjacent site is occupied. This assumption usually implies that the surface is uniform in an energetic sense. Suppose one prefers to use the concept of a non-uniform surface with a limited number of active centers that are the only points at which chemisorption occurs. In that case, this approach is permissible if it is assumed that all these active centers have the same activity for adsorption and that the rest of the surface has none.
3. The maximum amount of possible adsorption corresponds to a monolayer.
4. Adsorption is localized and occurs by collision of molecules with vacant sites.
5. The desorption rate depends only on the amount of material on the surface.

Derivation of the Langmuir-Hinshelwood Equations:

The kinetic approach to deriving a mathematical expression for the Langmuir isotherm assumes that the rate of adsorption on the surface is proportional to the product of the partial pressure P_i (or concentration C_i when the reaction occurs in liquid phases) of the adsorbate and the fraction of the catalyst surface that is bare. Adsorption may occur only when a molecule strikes an uncovered site. If the surface fraction covered by an adsorbed molecule A is denoted by θ_A, the bare fraction will be $\theta_* = (1 - \theta_A)$ if no other species are adsorbed. The rate of adsorption is given by:

For reactions in liquid phases:

$$r_{adsorption} = kC_A\theta_* = kC_A(1 - \theta_A) \tag{3.23}$$

k may be regarded as a “pseudo rate constant" for adsorption. The desorption rate depends only on the number of adsorbed molecules.

$$r_{desorption} = k'\theta_A \tag{3.24}$$

k' may be regarded as a ”pseudo rate constant" for desorption. At equilibrium, the rates of adsorption and desorption are equal.

$$kC_A(1-\theta_A) = k'\theta_A \tag{3.25}$$

The fraction of the sites occupied by species A is then.

$$\theta_A = \frac{kC_A}{k' + kC_A} \tag{3.26}$$

If one takes the ratio of the pseudo rate constant for adsorption to that for desorption as an equilibrium constant for adsorption $K = k/k'$, Equation 3.26 can be written as:

$$\theta_A = \frac{(k/k')C_A}{1 + (k/k')C_A} = \frac{KC_A}{1 + KC_A} \tag{3.27}$$

For situations where more than one species may adsorb, it is helpful to develop generalized Langmuir adsorption isotherms for multicomponent adsorption. Let us consider that θ_i represents the fraction of the sites occupied by species i and θ_* is the fraction of the vacant sites, then $\theta_* = [1 - \sum \theta_i]$, where the sum is taken over all species that can be adsorbed. The pseudo rate constants for adsorption and desorption may be expected to differ for each species so that they will be denoted by k_i and k_i', respectively. The adsorption and desorption rates of each species must be equal at equilibrium. Thus:

$$k_i C_i \left(1 - \sum_i \theta_i\right) = k_i'\theta_i \tag{3.28}$$

C_i is the concentration of the i^{th} species in the liquid phase. If Equation 3.28 is solved for the fractions occupied by specie i, we obtain:

$$\theta_i = \left(\frac{k_i}{k_i'}\right) C_i \left(1 - \sum_i \theta_i\right) = K_i C_i \left(1 - \sum_i \theta_i\right) \tag{3.29}$$

The adsorption equilibrium constant K_i has been substituted for the ratios of k_i to k_i'. Considering the summation of all the θ_i, thus, we arrived to:

$$\sum_i \theta_i = \left(\sum_i K_i C_i\right)\left(1 - \sum_i \theta_i\right) \tag{3.30}$$

Solving for $\sum_i \theta_i$ yields to:

$$\sum_i \theta_i = \frac{\sum_i K_i C_i}{1 + \sum_i K_i C_i} \tag{3.31}$$

or

$$\theta_* = 1 - \sum_i \theta_i = \frac{1}{1 + \sum_i K_i C_i} \tag{3.32}$$

Substituting Equation 3.32 in Equation 3.29, we obtain the main expression for the occupied sites by the species i:

$$\theta_i = \frac{K_i C_i}{1 + \sum_i K_i C_i} \tag{3.33}$$

1. Eley-Rideal Kinetic Model (ER1)

This kinetic model considers the possibility that the reaction occurs between an adsorbed species and a non-adsorbed one. In our case, the Eley-Rideal model considers that only BL is adsorbed into active sites of the catalyst. Then, molecular hydrogen collides directly with the adsorbed BL to react. Following this, the mechanism for the hydrogenation step reaction is:

Hydrogenation Step Mechanism

$$\begin{array}{ccc} BL + * & \rightleftharpoons & *BL \\ *BL + H_2 & \longrightarrow & *BHP \\ *BHP & \rightleftharpoons & BHP + * \end{array}$$

Where $*$ represents the vacant active sites of the catalyst, $*BL$ and $*BHP$ represent the adsorbed BL and BHP in the catalyst, respectively. Based on this mechanism, the hydrogenation rate can be expressed as:

$$\mathbf{R_{hyd}} = k_{hyd} \cdot \theta_{BL} \cdot C_{H_2} \cdot \omega_{cat} \tag{3.34}$$

Replacing Equation 3.33 into Equation 3.34, we obtain the ER1 mathematical equation for the hydrogenation rate:

$$\mathbf{R_{hyd}} = \frac{k_{hyd} \cdot K_{BL} \cdot [BL] \cdot [H_2] \cdot \omega_{cat}}{K_{BL} \cdot [BL] + K_{BHP} \cdot [BHP] + 1} \tag{ER1}$$

For the cyclization step, we have considered that only BHP that is not adsorbed reacts to produce GVL; this means that the BHP that is adsorbed into active sites of the catalyst must be desorbed before reacting. Based on this, the reaction mechanism for the cyclization step is:

Cyclization Step Mechanism

$$\begin{array}{ccc} BHP* & \longrightarrow & BHP + * \\ BHP & \longrightarrow & GVL + BuOH \end{array}$$

We have also considered that the cyclization rate can be defined by a first-order power law, Equation 3.35. All these considerations for the cyclization step will be the same for the other models and will lead to the same results. Therefore, Equation 3.35 will represent the cyclization rate for all the models considered in this work.

$$\mathbf{R_{cyc}} = k_{cyc} \cdot C_{BHP} \cdot \omega_{cat} + k_{non} C_{BHP} \tag{3.35}$$

2. Langmuir-Hinshelwood without hydrogen dissociation (LH1)

This kinetic model considers that all reactants, i.e., BL and H_2, are adsorbed into the catalyst's active sites without further dissociation. Furthermore, that the reaction takes place only between adsorbed species. Following this, the reaction mechanism for hydrogenation is:

Hydrogenation Step Mechanism

$$\begin{array}{ccc} BL + * & \rightleftharpoons & *BL \\ H_2 + * & \rightleftharpoons & *H_2 \\ *BL + *H_2 & \longrightarrow & *BHP + * \\ *BHP & \rightleftharpoons & BHP + * \end{array}$$

Where $*$ represents the vacant active sites of the catalyst. Thus, the hydrogenation rate can be defined as:

$$\mathbf{R_{hyd}} = k_{hyd} \cdot \theta_{BL} \cdot \theta_{H_2} \cdot \omega_{cat} \tag{3.36}$$

Replacing Equation 3.33 into Equation 3.36, we obtain the LH1 mathematical equation for the rate of hydrogenation:

$$\mathbf{R_{hyd}} = \frac{k_{hyd} \cdot K_{BL} \cdot [BL] \cdot K_{H_2} \cdot [H_2] \cdot \omega_{cat}}{\left(K_{BL} \cdot [BL] + K_{H_2} \cdot [H_2] + K_{BHP} \cdot [BHP] + 1\right)^2} \tag{LH1}$$

3. Langmuir-Hinshelwood with hydrogen dissociation (LH2)

Evidence shows that specific chemical adsorption processes dissociate the adsorbate to form two bonds with the adsorbent surface. On many metals, hydrogen is adsorbed in atomic form. For such situations, the kinetic approach to deriving the Langmuir-Hinshelwood equation requires that the process be regarded as a reaction between the dissociated molecule and two vacant active sites in the catalyst. Thus, the adsorption rate is written as:

$$r_{adsorption} = kC_A\theta_*^2 = kC_A(1-\theta_A)^2 \tag{3.37}$$

It is assumed that only species A is adsorbed and dissociated. The desorption process must involve a reaction between two adsorbed atoms to regenerate the original molecules. Consequently, it may be regarded as a second-order reaction between two adsorbed atoms:

$$r_{desorption} = k'\theta_A^2 \tag{3.38}$$

At equilibrium, we have:

$$kC_A(1-\theta_A)^2 = k'\theta_A^2 \tag{3.39}$$

or

$$\frac{\theta_A}{1-\theta_A} = \sqrt{\frac{kC_A}{k'}} = \sqrt{K_A C_A} \tag{3.40}$$

Solving for θ_A gives us

$$\theta_A = \frac{\sqrt{K_A C_A}}{1 + \sqrt{K_A C_A}} \tag{3.41}$$

When several species can be adsorbed into the catalyst but only one species is dissociated, species A in this demonstration. The active sites occupied by species A are given by Equation 3.42, and occupied sites by other species not dissociated by Equation 3.43.

$$\theta_A = \frac{\sqrt{K_A C_A}}{1 + \sqrt{K_A C_A} + \sum_{i \neq A} K_i C_i} \tag{3.42}$$

$$\theta_i = \frac{K_i C_i}{1 + \sqrt{K_A C_A} + \sum_{i \neq A} K_i C_i} \tag{3.43}$$

As in the LH1 model, this model LH2 considers that all the reactants are adsorbed into the active sites. However, molecular hydrogen (H_2) is dissociated to form elemental hydrogen (H). Then, adsorbed BL reacts with one elemental hydrogen to form the 'surface intermediate' BLH that reacts with another elemental hydrogen to produce the intermediate BHP. Based on this, the hydrogenation mechanism is as follows:

Hydrogenation Step Mechanism

$$\begin{array}{ccc} BL + * & \rightleftharpoons & *BL \\ H_2 + 2* & \rightleftharpoons & *H + *H \\ *BL + *H & \rightleftharpoons & *BLH + * \\ *BLH + *H & \longrightarrow & *BHP + * \\ *BHP & \rightleftharpoons & BHP + * \end{array}$$

Let us consider that BLH formation is fast, and BHP formation from BLH is the rate-determining step. We can introduce $K_{eq} = (\theta_{BLh} \cdot \theta_*)/(\theta_{BL} \cdot \theta_H)$ which is the equilibrium surface constant of BLH formation. Thus, the hydrogenation rate can be defined as:

$$\mathbf{R_{hyd}} = k_{hyd} \cdot \theta_{BLH} \cdot \theta_H \cdot \omega_{cat} \tag{3.44}$$

Replacing Equations 3.42, 3.43 and the equilibrium surface constant into 3.44, we obtain the LH2 mathematical equation for the rate of hydrogenation:

$$\mathbf{R_{hyd}} = \frac{k_{hyd} \cdot K_{BL} \cdot [BL] \cdot K_{eq} \cdot K_{H_2} \cdot [H_2] \cdot \omega_{cat}}{\left(K_{BL} \cdot [BL] + \sqrt{K_{H_2} \cdot [H_2]} + K_{BHP} \cdot [BHP] + K_{eq} \cdot K_{BL} \cdot [BL] \cdot \sqrt{K_{H_2} \cdot [H_2]} + 1\right)^2} \tag{LH2}$$

4. Non-Competitive Langmuir-Hinshelwood without hydrogen dissociation (NCLH1)

It is common to assume that a catalyst's active sites are identical, but this is not strictly correct. In some cases, due to size and shape, they can be grouped into different subgroups. In our case, for developing the NCLH1 model, we have considered two different types of active sites in the catalyst. Each reactant is adsorbed on only one active site, i.e., BL is adsorbed on a different type of active site than hydrogen. Therefore, there is no competition between the reactants for the catalyst's active sites. The reaction mechanism is similar to the one of LH1, but considering two types of active sites, it is as follows:

Hydrogenation Step Mechanism

$$\begin{array}{ccc} BL + * & \rightleftharpoons & *BL \\ H_2 + \diamond & \rightleftharpoons & \diamond H_2 \\ *BL + \diamond H_2 & \longrightarrow & *BHP + \diamond \\ *BHP & \rightleftharpoons & BHP + * \end{array}$$

Where $*$ and $\diamond$ represent the vacant active sites where BL and H_2 are adsorbed, respectively. Thus, the hydrogenation rate can be defined as:

$$\mathbf{R_{hyd}} = k_{hyd} \cdot \theta_{*BL} \cdot \theta_{\diamond H_2} \cdot \omega_{cat} \tag{3.45}$$

Since we now consider two different types of active sites, Equation 3.33 must be applied separately to each subset of active sites in the catalyst. As a result, the NCLH1 mathematical equation for the hydrogenation rate:

$$\mathbf{R_{hyd}} = k_{hyd} \left(\frac{K_{BL} C_{BL}}{1 + K_{BL} C_{BL} + K_{BHP} C_{BHP}} \right) \left(\frac{K_{H_2} C_{H_2}}{1 + K_{H_2} C_{H_2}} \right) \omega_{cat} \tag{3.46}$$

$$\mathbf{R_{hyd}} = \frac{k_{hyd} \cdot K_{BL} \cdot [BL] \cdot K_{H_2} \cdot [H_2] \cdot \omega_{cat}}{\left(K_{H_2} \cdot [H_2] + 1\right) \left(K_{BL} \cdot [BL] + K_{BHP} \cdot [BHP] + 1\right)} \tag{NCLH1}$$

5. Non-Competitive Langmuir-Hinshelwood with hydrogen dissociation (NCLH2)

The NCLH2 mechanism is quite similar to NCLH1; the only difference is that we consider hydrogen dissociation during the reaction mechanism, as in LH2. This combined mechanism is as follows:

Hydrogenation Step Mechanism

$$\begin{array}{ccc} BL + * & \rightleftharpoons & *BL \\ H_2 + 2\diamond & \rightleftharpoons & \diamond H + \diamond H \\ *BL + \diamond H & \rightleftharpoons & *BLH + \diamond \\ *BLH + \diamond H & \longrightarrow & *BHP + \diamond \\ *BHP & \rightleftharpoons & BHP + * \end{array}$$

Where $*$ and $\diamond$ represent the vacant active sites where BL and H_2 are adsorbed, respectively. Thus, the hydrogenation rate can be defined as:

$$\mathbf{R_{hyd}} = k_{hyd} \cdot \theta_{*BLH} \cdot \theta_{\diamond H} \cdot \omega_{cat} \tag{3.47}$$

Replacing Equation 3.33, Equation 3.42 and the surface equilibrium constant K_{eq} in Equation 3.47, we arrive to the NCLH2 mathematical equation to calculate the hydrogenation rate:

$$\mathbf{R_{hyd}} = k_{hyd} \left(\frac{K_{BL} C_{BL}}{1 + K_{BL} C_{BL} + K_{BHP} C_{BHP}} \right) \left(\frac{K_{H_2} C_{H_2}}{1 + \sqrt{K_{H_2} C_{H_2}}} \right) \omega_{cat} \tag{3.48}$$

$$\mathbf{R_{hyd}} = \frac{k_{hyd} \cdot K_{BL} \cdot [BL] \cdot K_i \cdot K_{H_2} \cdot [H_2] \cdot \omega_{cat}}{\left(\sqrt{K_{H_2} \cdot [H_2]} + 1\right) \left(K_{BL} \cdot [BL] + K_{BHP} \cdot [BHP] + K_i \cdot K_{BL} \cdot [BL] \cdot \sqrt{K_{H_2} \cdot [H_2]} + 1\right)} \tag{NCLH2}$$

3.5.2 Results

Five models have been presented above; each proposes different mechanisms for the BL hydrogenation step reaction in a heterogeneous system. Such models consider the equilibrium adsorption constants, the reaction rates constant, and the surface equilibrium constant. For the reaction rate constants, a modified Arrhenius equation, Equation Mod-Arr, was used to decrease the correlation between the pre-exponential factor and the activation energy by linearizing the original Arrhenius equation.

$$k_i(T) = \exp\left[\ln(k_i(T_{ref})) + \frac{Ea_i}{R{\cdot}T_{ref}}\left(1 - \frac{T_{ref}}{T}\right)\right] \qquad \text{(Mod-Arr)}$$

The observables used for the parameter estimation were the concentration of BL, BHP, and GVL and the reactionary media temperature T_r. Two approaches address this multi-response problem: conventional parameter estimation (CPE) and Bayesian parameter estimation (BPE). CPE occurs by optimization of a fit (between experimental and simulated data) based on an objective function. BPE changes the focus to probabilistic: "What is the probability of certain parameter values being true given the evidence observed and our prior knowledge about the chemical-physical system?" [97]. Bayes theorem is shown in Equation 3.49.

$$P(\Theta/Y) = \frac{P(Y/\Theta) \cdot P(\Theta)}{P(Y)} \tag{3.49}$$

Y represents the observed data, and Θ represents a vector of all the parameters required to simulate experimental data. Bayes theorem allows the estimation of the kinetic parameters vector Θ, and the covariance matrix $v(\Theta)$ [98], using the data collected during the experiments carried out under different initial conditions, operation conditions, and thermal mode. BPE can be used to calculate the region of parameter space with the highest probability density (HDP).

$$\Theta = \{k_{hyd}, k_{cyc}, Ea_{hyd}, Ea_{cyc}, K_{BL}, K_{H_2}, K_{BHP}, K_{eq}\} \tag{3.50}$$

The general form of the multi-response parameter estimation problem is:

$$Y_{ui} = F_i(x_u, \Theta) + E_{ui} \qquad (u = 1, \ldots, n \text{ and } i = 1, \ldots, m) \tag{3.51}$$

Where $u = 1, \ldots, n$ denotes the independent events, $i = 1, \ldots, m$ are the different observable variables in the model. Y_{ui} and $F_i(x_u, \Theta)$ are the experimental value and the expectation value for the observable i at the experimental design point x_u, respectively, and E_{ui} is the error of the model. Parameter estimation, simulation, and curve fitting were performed using the commercial software Athena Visual Studio V.14.2. This software can use the Bayesian framework that is more suitable for multi-response parameter estimation than the classical nonlinear least squares method [98, 99]. Indeed, Bayesian inference requires calculating the determinant criterion [100].

The differential equation system, obtained from the material and energy balance in Section 3.1.1, was integrated by the DDAPLUS solver with a modified Newton algorithm [101]. The GREGPLUS subroutine package was used to minimize the objective function OF(Θ), Equation 3.52, and to calculate the highest probability density HPD of the estimated parameters and the normalized covariance matrix. GREGPLUS uses successive quadratic programming starting from our initial guess values to minimize OF(Θ) [102].

$$\mathrm{OF}(\Theta) = (n + m + 1)\cdot \ln |\upsilon(\Theta)| \tag{3.52}$$

Where n is the number of events in response, m is the number of observables, and $|\upsilon(\Theta)|$ is the determinant of the covariance matrix of the responses. Each element of the covariance matrix of the responses is:

$$\upsilon_{ij}(\Theta) = \sum_{u=1}^{n} [Y_{ui} - F_i(x_u, \Theta)]\cdot[Y_{uj} - F_j(x_u, \Theta)] \tag{3.53}$$

This methodology was applied to all the kinetic models developed in Section 3.5.1 to estimate the kinetic parameters of each one. Then, the Akaike information criterion (AIC) was used to evaluate the most reliable models based on the expectation values of each model. This one penalizes models with too many parameters to estimate, and it was calculated as:

$$\mathrm{AIC} = n\cdot \ln \left(\frac{\sum_{u=1}^{n} [Y_{ui} - F_i(x_u, \Theta)]^2}{n} \right) + 2\cdot \mathrm{length}\{\Theta\} \tag{3.54}$$

Regression Stage

The regression stage consists of estimating the kinetic parameters of all the models, i.e., ER1, LH1, LH2, NCLH1, and NCLH2, using the data collected during the experimental matrix experiments, Table 3.7. Then, for each model, we calculate the Akaike criterion (AIC). The results are shown in Table 3.9; this table shows that NCLH1 and NCLH2 models present a good compromise between the lowest AIC values for Tr and medium AIC values for BL, BHP, and GVL.

Table 3.9 Akaike criterion (AIC) values for each observable and kinetic model.

Model	AIC value				Number of parameters
	BL	BHP	GVL	Tr	
ER1	2529	2010	2151	36	6
LH1	2498	2008	2131	117	7
LH2	2500	2010	2133	118	8
NCLH1	2520	1993	2139	54	7
NCLH2	2508	2056	2161	38	8

To maintain clarity and avoid confusion, we only show the results for the non-competitive Langmuir-Hinshelwood without hydrogen dissociation (NCLH1) model in this chapter. The parameter estimation results of the other models can be found in the Appendix A.1. Table 3.10 shows the values of the estimated parameters and the HPD for a 95% confidence for the NCLH1 model. The methodology used to estimate the kinetic parameters provided results with low credible intervals for the parameters, which is good. However, it is challenging to estimate the HPD for the equilibrium adsorption constants.

Table 3.10 Estimated values at T_{ref}=398.15 K with statistical data for NCLH1.

Parameter	Units	Value	HPD	HPD %
$\ln(k_{hyd}(T_{ref}))$	$mol/kg/s$	5.34	0.1160	2.17
$\ln(k_{cyc}(T_{ref}))$	$1/s$	-10.20	0.0289	0.28
$Ea_{hyd}/R/T_{ref}$	J/mol	9.25	0.7330	7.92
$Ea_{cyc}/R/T_{ref}$	J/mol	8.09	0.5885	7.27
$\ln(K_{BL})$	m^3/mol	0.011	-	-
$\ln(K_{H_2})$	m^3/mol	-2.91	0.2600	8.93
$\ln(K_{BHP})$	m^3/mol	7.96	-	-

Correlation between most of the estimated parameters is lower than 0.90 in absolute value, Table 3.11, so we can consider that the estimated parameters are not correlated [103]. This absence of correlation shows that the parameters are well-identified. The parameter $k_{hyd}(T_{ref})$ and K_{H_2} are strongly correlated due to the difficulty of estimating the adsorption constant of the other reactants.

Table 3.11 Normalized parameter covariance matrix for NCLH1.

	$\ln(k_{hyd}(T_{ref}))$	$\ln(k_{cyc}(T_{ref}))$	$Ea_{hyd}/R/T_{ref}$	$Ea_{cyc}/R/T_{ref}$	$\ln(K_{H_2})$
$\ln(k_{hyd}(T_{ref}))$	1				
$\ln(k_{cyc}(T_{ref}))$	0.070	1			
$Ea_{hyd}/R/T_{ref}$	-0.163	-0.047	1		
$Ea_{cyc}/R/T_{ref}$	-0.086	-0.671	-0.059	1	
$\ln(K_{H_2})$	-0.981	-0.071	0.123	0.081	1

Figure 3.12 shows the fit of the NCLH1 model with the Run Iso-1, Pun Isop-2, and Run Adi-6 experiments. We can see that the model is a good fit for both concentration and temperature in different thermal modes. The model's fit over all the experimental data can be assessed via the parity plots, Figure 3.13. The parity plots are obtained by plotting the expected values against the experimental values; a good fit of the model will be evidenced with a linear trend of the graphed data, as is our case.

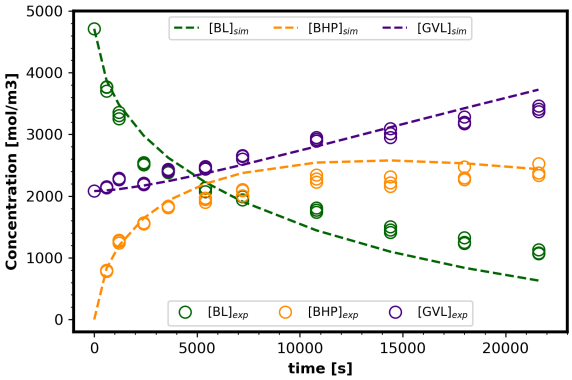

(a) Run Isot-1: Concentration Evolution.

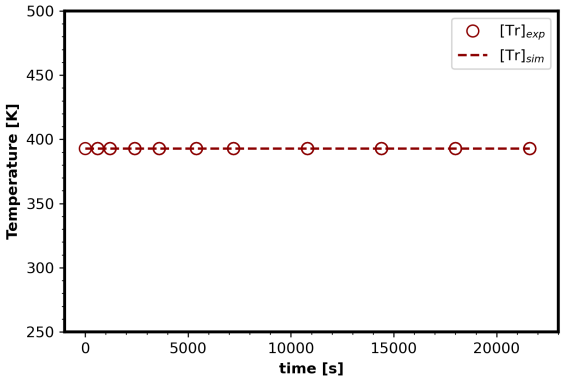

(b) Run Isot-1: Temperature Evolution.

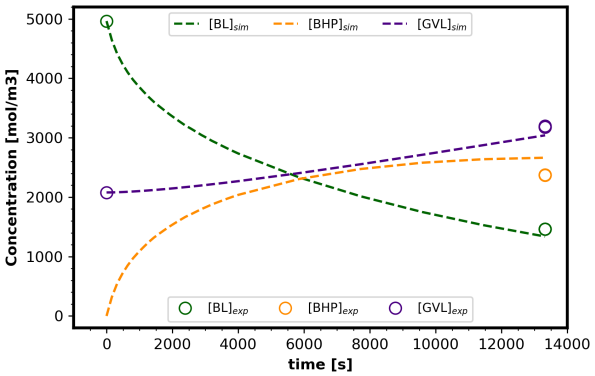

(c) Run Isop-2: Concentration Evolution.

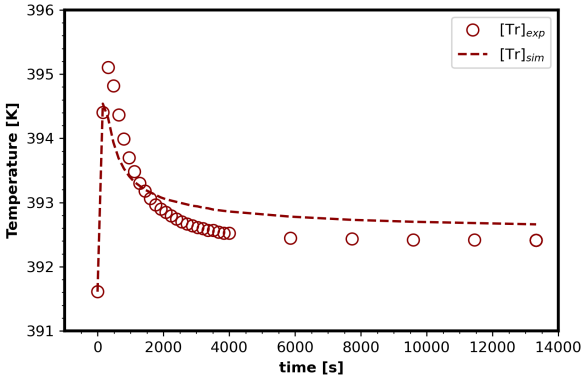

(d) Run Isop-2: Temperature Evolution.

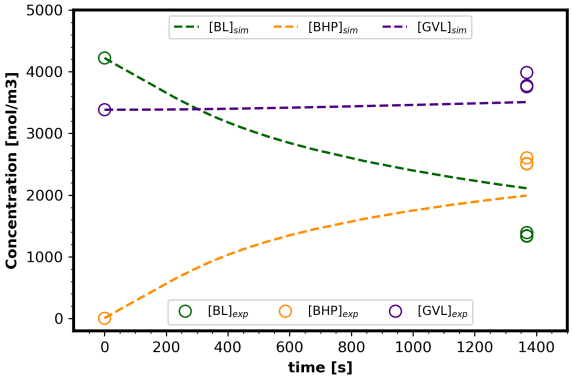

(e) Run Adi-6: Concentration Evolution.

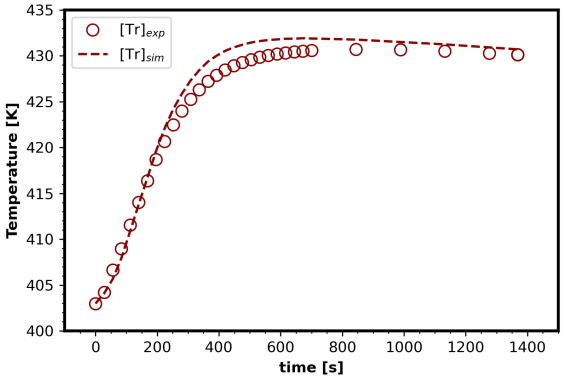

(f) Run Adi-6: Temperature Evolution.

Figure 3.12 Fit of the NCLH1 model to experimental data in isothermal, isoperibolic, and adiabatic conditions.

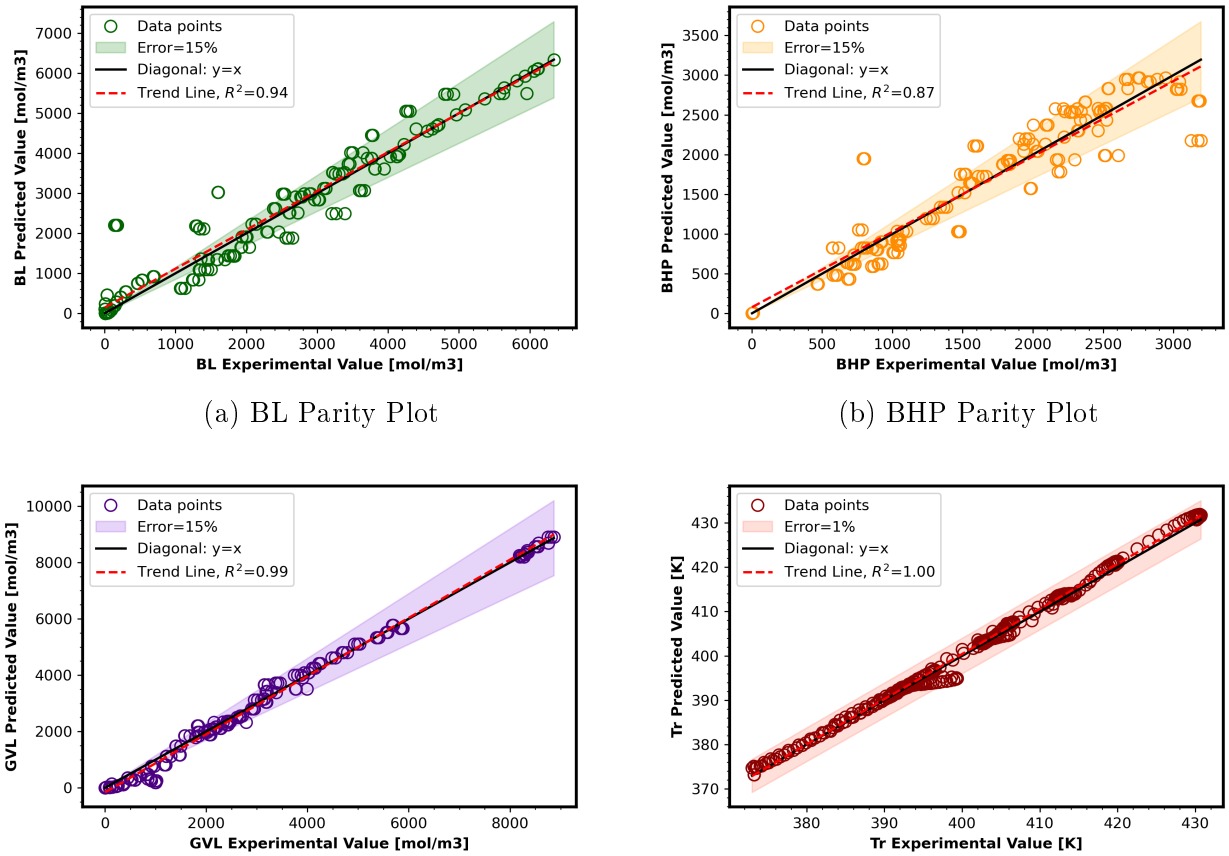

(a) BL Parity Plot

(b) BHP Parity Plot

(c) GVL Parity Plot

(d) Tr Parity Plot

Figure 3.13 Regression Stage Parity Plot, NCLH1 kinetic model.

Validation Stage

A holdout validation method was used for the validation. The validation stage evaluates the kinetic model against experiments not used during the regression stage. This is to validate that the kinetic model can predict situations not considered during its parameter estimation. Here, the kinetic parameters and adsorption constants obtained from the regression stage were used to predict the experimental data obtained from the validation experimental matrix, Table 3.8; for those experiments, we have predicted the concentration and temperature profiles at different operating, initial and thermal conditions.

Figure 3.14 shows the parity plots of NCLH1 model considering validation experiments. The results obtained during the validation stage show that our model can accurately predict the evolution of GVL concentration and reaction temperature during isothermal and non-isothermal conditions. However, our model presents drawbacks predicting the evolution of BL and BHP. Being the BHP concentration the one that presents serious deviations.

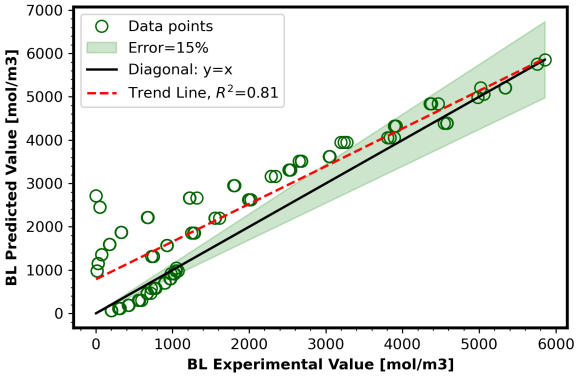

(a) BL Parity Plot

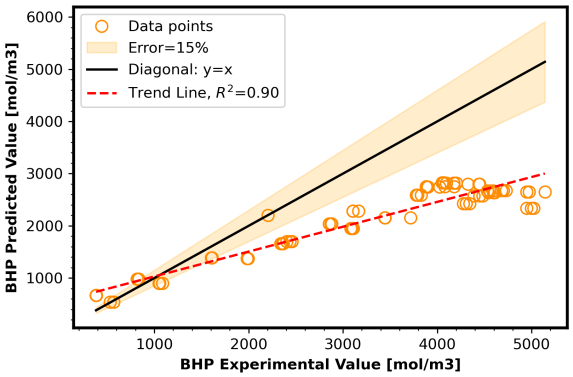

(b) BHP Parity Plot

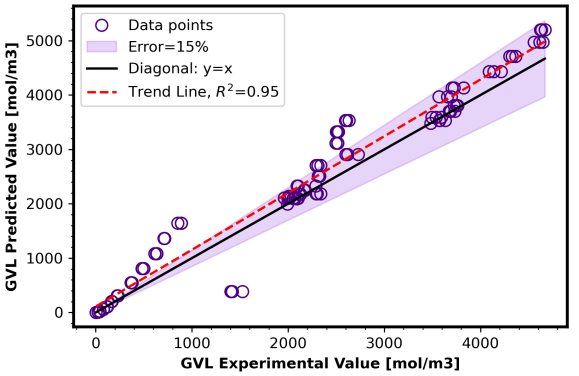

(c) GVL Parity Plot

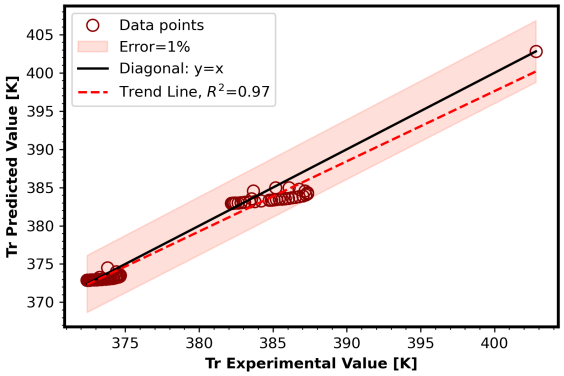

(d) Tr Parity Plot

Figure 3.14 Validation Stage Parity Plot, NCLH1 kinetic model.

3.6 Conclusions

As noted throughout this chapter, developing a kinetic model that integrates isothermal and non-isothermal operating conditions is difficult, even less so when heterogeneous systems are involved. In this type of reactionary system, heat and mass transfer aspects must be considered. In the first part of this chapter, we focused on properly defining our reaction system and establishing the material and energy balance, from which we would rely on the development of the kinetic model.

Our study case corresponds to the hydrogenation of BL over Ru/C to produce GVL; our first focus was heat transfer analysis, which is a fundamental aspect of non-isothermal operating conditions. This analysis focused on establishing mathematical expressions that would allow us to calculate the heat transfer coefficient **UA** as a function of the stirring rate N and the temperature of the reactionary media T_r; this was achieved by applying Wilson's plot methodology and the two-film heat transfer model. This heat transfer analysis occurs between the reactor jacket and the reactionary media.

For heterogeneous reaction systems, one of the factors that can negatively affect the reaction rate is the mass transfer limitations. In this sense, we have analyzed our reaction system's gas-liquid, liquid-solid, and internal solid transfers. For gas-liquid mass transfer of hydrogen, we have defined a mathematical equation that allows us to evaluate the volumetric mass transfer coefficient k_La in RC1 as a function that depends on the temperature, density, viscosity of the reactionary media, and a reference coefficient $(k_La)_{mod} = 2.25 \times 10^{-6} Pa{\cdot}s{\cdot}K^{-1})^{0.5}(Pa{\cdot}s{\cdot}kg^{-1}{\cdot}m^{-3})^{0.25}s^{-1}$. For liquid-solid mass transfer, we have determined that for a stirring speed of 1000 ,RPM, the catalyst suspension and homogeneity are good enough to minimize this type of limitation.

Another important aspect of developing kinetic models and assessing thermal risk is determining the energy released during the chemical reaction. As we have already seen, the hydrogenation reaction of BL in Ru/C to produce GVL occurs in two steps, i.e., hydrogenation and cyclization. Therefore, two enthalpies of the reaction must be measured. The enthalpy of hydrogenation was measured in the RC1 and was found to be equal to $\mathbf{\Delta H_{hyd}} = -35.28\,kJ/mol \pm 1.00\,kJ/mol$, which means that it is an exothermic reaction. On the other hand, the cyclization enthalpy of the BHP was measured in the calorimeter C80, and it was found to be equal to $\mathbf{\Delta H_{cyc}} = 6.34\,kJ/mol \pm 0.93\,kJ/mol$, which means that it is an endothermic reaction.

Finally, the development of the kinetic models for our reaction was carried out in the RC1 calorimeter; this reaction was carried out under different initial conditions, different operating conditions, and different thermal modes of operation, i.e., isothermal, isoperibolic, and adiabatic. For this heterogeneous reaction, we have developed 5 kinetic models that contemplate the equilibrium adsorption constants of the different compounds; this covers part of the mass transfer analysis.

The multi-response parameter estimation process was carried out using Bayesian statistics, and we also calculated the highest probability density (HPD) of the estimated parameters. Within the 5 models analyzed, it was determined through the Akaike information criterion (AIC) that the most robust and reliable are the non-competitive Langmuir-Hinshelwood models with and without hydrogen dissociation; the reliability of these models was confirmed through a validation stage, which contemplated experiments that were not used during the regression stage. Based on parity plots results, NCLH1 model presents a good fit with experimental data in the regression stage for all the observable, however, we realized that the model presents drawbacks during the validation stage for BL and BHP concentrations. The authors consider that this can be outcome by a deep study into internal mass transfer into the catalyst and a deep analysis of the adsorption constants of reagents over the catalyst.

This type of kinetic model, developed under isothermal and non-isothermal conditions, has the advantage that, in addition to optimizing process design, it serves to prevent thermal risks and energy recovery. It should be noted that the thermal risk for our chemical reaction is relatively low because the energy released during the reaction is moderate. Another positive point is that during the experiments carried out under adiabatic conditions, there was no evidence of decomposition reactions, which implies that the risk of thermal runaway is low.

Chapter 4
Continuous Production of GVL: Thermal Assessment

In this chapter, we have studied the risk of thermal runaway that would be present during the continuous production of GVL from BL hydrogenation over Ru/C in a continuous stirred-tank reactor (CSTR). We have assessed the risk of runaway via stability-based criteria and sensitivity-based analysis. Part of this chapter has been adapted from the following article:

- **Wenel Naudy Vasquez Salcedo**, Bruno Renou and Sebastien Leveneur. *Thermal Stability for the Continuous Production of γ-Valerolactone from the Hydrogenation of n-Butyl Levulinate in a CSTR.* Processes 2023, 11, 237. `https://doi.org/10.3390/pr11010237`

We have seen that gamma-valerolactone (GVL) can be a game-changer in the chemical industry because it could substitute fossil feedstocks in different fields. Among the different applications of GVL is its potential use as a raw material to produce SAF that can replace kerosene in the aviation industry. In order to meet the demand for materials and fuels, which increases over time, it is necessary to aim for the industrial-scale production of GVL, i.e., its production inside continuous reactors, which have a considerably higher volume than reactors at the laboratory scale.

In the previous chapter, we proved that producing GVL via hydrogenation of BL over Ru/C is an exothermic reaction. Despite the relatively low reaction enthalpy, $\mathbf{\Delta H_{hyd}} = -35.28\,kJ/mol \pm 1.00\,kJ/mol$, the thermal risk of this reaction is moderate but not zero. Despite having a moderate thermal risk, this chemical reaction should not be underestimated during its scale-up to an industrial level. At the industrial level, the reaction volume increases, which implies that the total energy released will be much greater.

The scale-up from the laboratory scale to the industrial scale implies an increase in volume. When the dimensions of a lab-scale reactor are proportionally increased to reach the industrial scale, the ratio between the reaction volume (V_r) and the surface of heat transfer (S) between the reactionary media and the reactor jacket is not necessarily kept constant. Thus reducing the heat transfer flow and increasing the thermal risk. For this reason, the heat transfer coefficient per unit volume, **Ua** [$W/m^3/K$], is a fundamental parameter during the design of industrial-scale reactors.

In this chapter, we assess the thermal risk of producing GVL via hydrogenation of BL over Ru/C in a continuous stirred-tank reactor (CSTR). We applied stability-based and sensitivity-based criteria to identify the safe operational conditions, i.e., the minimum value of **Ua**. This type of assessment is of great importance as it helps the design of reactors and allows the development of prevention systems. These prevention systems are necessary, and even more so for exothermic reactions involving hydrogen, which is a compound with a high risk of explosiveness.

Kummer and Varga [104] prepared an excellent review about reactors' thermal runaway. In this review, they explained that thermal runaway is responsible for 26.5% of the petrochemical accidents and responsible for 25% of the accidents in the French industry. Reactor thermal runaways are characterized by an uncontrolled increase in temperature and pressure due to the continuous increase of heat generation. This can cause explosions if it is not controlled because the heat generation rate increases exponentially with the temperature, and the heat removed by the jacket of the reaction increases linearly with temperature. They also explain that thermal runaway accidents occur due to the following:

1. A need for more basic understanding of the chemical system and thermochemistry, e.g., heat of reaction, mass transfer phenomena, secondary reactions, etc.
2. Inadequate engineering design for heat transfer.
3. Inadequate control systems and safety backup systems, e.g., loss of cooling fluid which is not monitored, wrong position of temperature sensors, etc.
4. Inadequate operational procedures and operator training, e.g., starting the reactor at low process temperature, mischarging of reacting, inadequate mixing, etc.

The work of this thesis allows us to cover the first two main causes of runaways. In the previous chapter, we described our reaction system in detail, and we studied its physical, chemical, and thermochemical characteristics in-depth, such as mass transfer phenomena and reaction enthalpy. We have provided several kinetic models capable of simulating isothermal and non-isothermal conditions. In this chapter, we are going to determine for which **Ua** values the risk of thermal runaway is minimal, thus covering the design part.

For the thermal assessment of the continuous production of GVL, we will consider the Non-competitive Langmuir Hinshelwood kinetic model (NCLH1) developed in the previous chapter. This is a suitable model for thermal assessment since its kinetic parameters were estimated considering isothermal, isoperibolic, and adiabatic conditions. The hydrogenation and cyclization rates are calculated with Equation 4.1 and 4.2, respectively. The kinetic rate constant were evaluated with Equation 4.3. The values for the kinetic parameters were presented in Table 3.10.

Hydrogenation Rate:

$$\mathbf{R_{hyd}} = \frac{k_{hyd}\cdot K_{BL}\cdot[BL]\cdot K_{H_2}\cdot[H_2]\cdot\omega_{cat}}{\left(K_{H_2}\cdot[H_2]+1\right)\left(K_{BL}\cdot[BL]+K_{BHP}\cdot[BHP]+1\right)} \tag{4.1}$$

Cyclization Rate:

$$\mathbf{R_{cyc}} = k_{cyc}\cdot[BHP] \tag{4.2}$$

Modified Arrhenius Equation:

$$\mathbf{k_i(T)} = \exp\left[\ln(k_i(T_{ref})) + \frac{Ea_i}{R\cdot T_{ref}}\left(1-\frac{T_{ref}}{T}\right)\right] \tag{4.3}$$

4.1 CSTR Material and Energy Balance

It is necessary to establish the material and energy balance for the thermal assessment, as was done in the previous chapter. However, in this case, the type of reactor is different. Here, our analysis focuses on a continuous reactor (CSTR), in which reactants and products are inlet and outlet flows, respectively. The CSTR reactor considered for the thermal assessment is shown in Figure 4.1.

To establish the material and energy balance, we have made the following considerations:

- The CSTR operates as an ideal reactor.
- There is no concentration gradient inside the reactor.
- There is no temperature gradient inside the reactor.
- The concentration in the outlet flow is the same as inside the reactor
- The temperature in the outlet flow is the same as inside the reactor (T_r).
- The reaction volume (V_r) is constant.
- The inlet flow is equal to the outlet flow, $Q_{in} = Q_{out} = Q$.

Following these considerations and remembering that the chemical reaction occurs in the liquid phase, the general form of the material balance for a compound j is:

$$\frac{dC_j}{dt} = \frac{C_{j_{in}} - C_{j_{out}}}{\tau} + \sum_i \nu_{j,i} \cdot R_i \tag{4.4}$$

Where C_j is the concentration of compound j, i represents the reaction index, $\tau = V_r/Q$ is the residence time, $\nu_{j,i}$ is the stoichiometry coefficient of compound j in reaction i, and R_i is the reaction rate. Apply Equation 4.4 for all the compounds in our chemical reaction we obtain:

$$\frac{d[BL]}{dt} = \frac{[BL]_{in} - [BL]_{out}}{\tau} - \mathbf{R_{hyd}} \tag{4.5}$$

$$\frac{d[H_2]}{dt} = \frac{[H_2]_{in} - [H_2]_{out}}{\tau} + \mathbf{k_L a}\left([H_2]^*_{liq} - [H_2]_{liq}\right) - \mathbf{R_{hyd}} \tag{4.6}$$

$$\frac{d[BHP]}{dt} = \frac{[BHP]_{in} - [BHP]_{out}}{\tau} + \mathbf{R_{hyd}} - \mathbf{R_{cyc}} \tag{4.7}$$

$$\frac{d[GVL]}{dt} = \frac{[GVL]_{in} - [GVL]_{out}}{\tau} + \mathbf{R_{cyc}} \tag{4.8}$$

$$\frac{d[BuOH]}{dt} = \frac{[BuOH]_{in} - [BuOH]_{out}}{\tau} + \mathbf{R_{cyc}} \tag{4.9}$$

The energy balance per unit of volume is:

$$\left[(\rho C_P)_{liq} + (\rho C_P)_{cat} + (\rho C_P)_{ins}\right] \frac{dT_r}{dt} = \frac{\sum C_{j_{in}} C_{P_j}}{\tau} (T_{in} - T_r) + \mathbf{Ua}\,(T_j - T_r) - \sum_i R_i \Delta H_i \tag{4.10}$$

Where Cp_j is the heat capacity of compound j, ρ is the density, T_{in} is the temperature of the inlet flow, T_j is the temperature of the heat-carrier fluid in the jacket and **Ua** is the global heat transfer coefficient per unit of volume. In some cases it is not possible to assume that T_j is constant, for such cases, the energy balance for the heat-carrier fluid in the jacket is as follows:

$$\rho_j C_{P_j} \frac{dT_j}{dt} = \frac{\rho_j C_{P_j}}{\tau_j} (T_{j_0} - T_j) + \mathbf{Ua} (T_r - T_j) \tag{4.11}$$

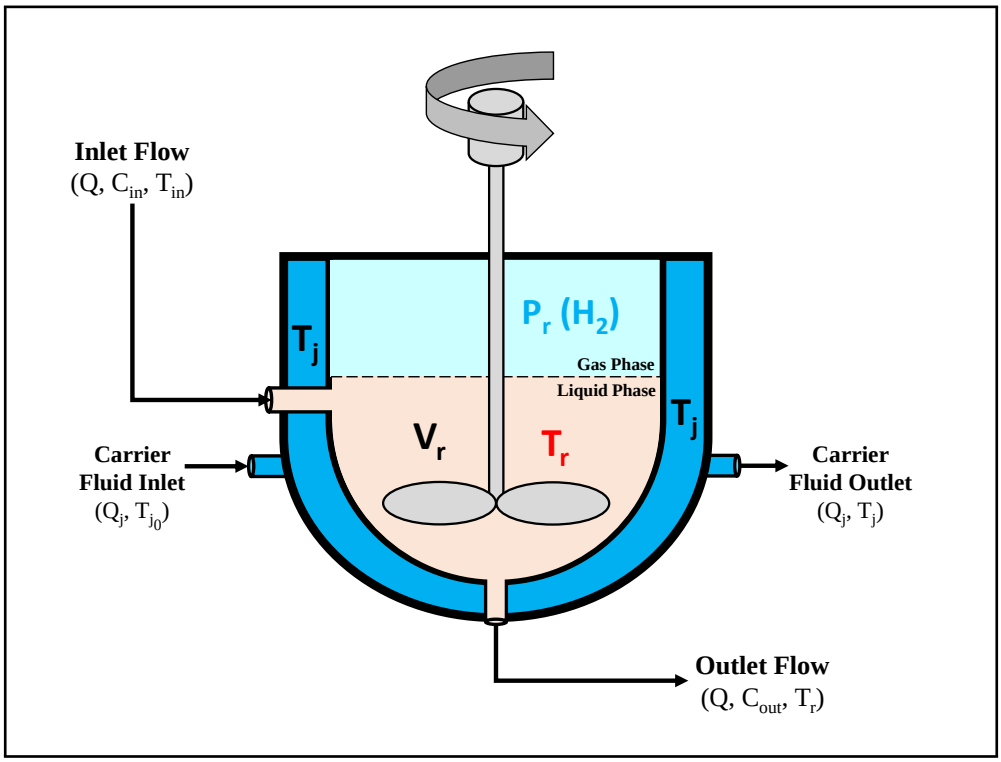

Figure 4.1 Representation of the CSTR considered for the thermal stability assessment.

4.1.1 CSTR Simulation

Thanks to the results obtained in the previous chapter and the material balance that we established, it is possible to simulate the operation of the CSTR reactor that we have described for the production of GVL from BL. In order not to increase the complexity of this study, the simulations, and the thermal assessment, the following considerations were made:

- The CRST operates in steady-state conditions, which means that $d/dt = 0$ for all variables.
- There are no mass transfer limitations in the CSTR.
- The hydrogen pressure inside the reactor is constant (isobaric conditions), and the hydrogen concentration is constant in the liquid phase. Therefore, hydrogen is not considered either in the simulation or thermal assessment.
- There is no gradient in the heat-carrier fluid temperature T_j. Thus, the energy balance in the jacket was not considered.
- The simulations and thermal assessment were done over the reaction temperature range 300-600 K. For the CSTR operating in isothermal conditions.

Since we did not have the experimental tools to validate our simulations experimentally, we have taken the RC1 calorimeter as a reference. Inlet concentrations, catalyst loading, and **Ua** are similar to the ones used to develop the kinetic model in the previous chapter. The initial and operating conditions chosen for our analysis are presented in Table 4.1.

Table 4.1 Operating conditions used during thermal stability assessment.

Inlet and Operating Conditions	Value	Units
$[BL]_{in}$	4840	mol/m^3
$[BHP]_{in}$	0	mol/m^3
$[GVL]_{in}$	2080	mol/m^3
$[BuOH]_{in}$	0	mol/m^3
ω_{cat}	10	kg/m^3
T_r	300 to 600	K
T_{in}	333	K
P_{H_2}	2500	kPa
τ	10000	s
Ua	17000	$W/m^3/K$

Our first approach is to compare the dominance of the steps-reaction, i.e., hydrogenation and cyclization rates. We aim to know which step reaction will dominate inside the reactor, whether exothermic (hydrogenation) or endothermic (cyclization). This comparison is made by evaluating the Modified Arrhenius Equation, Equation 4.3, for each reaction in the temperature range 300-600 K. The results of this comparison are shown in Figure 4.2. This figure shows that the hydrogenation rate constant k_{hyd} is much greater than the cyclization rate constant k_{cyc}, in the order of 10^6. This result is to be expected as the Ru/C catalyst is highly selective and greatly promotes hydrogenation.

On the other hand, cyclization is promoted only by temperature effects. Therefore, it is normal for it to be lower than hydrogenation. Our research group showed that the cyclization rate can be increased by using a second catalyst, an acid catalyst, such as Amberlite IR-120 [105].

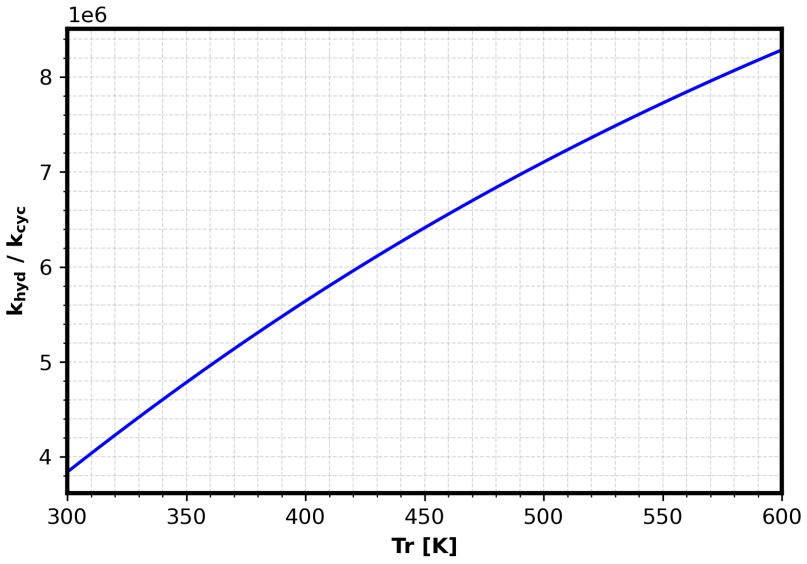

Figure 4.2 Steps reactions dominance: the ratio between hydrogenation and cyclization rates constant.

For the solution of the material and energy balance and the thermal assessment throughout this chapter, we have used the software MATLAB R2021b. In this section, we have simulated the concentrations at the reactor outlet and the corresponding energy released during the reaction. These results are presented in Figure 4.3, results are in the form of conversion and yield, Equations 4.12 - 4.14, and energy released due to the reaction per unit volume Equation 4.15. These results show how the reaction temperature (T_r) and the residence time (τ) affect the outlet concentrations and energy release.

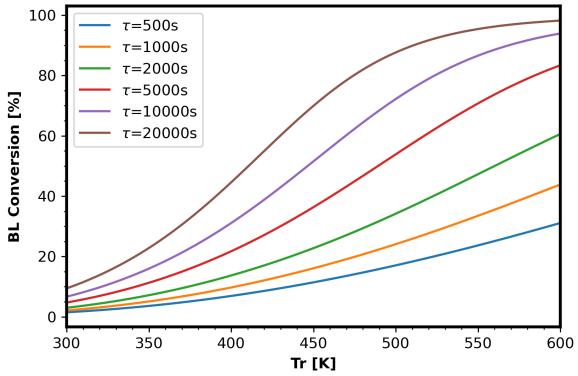

(a) BL Conversion.

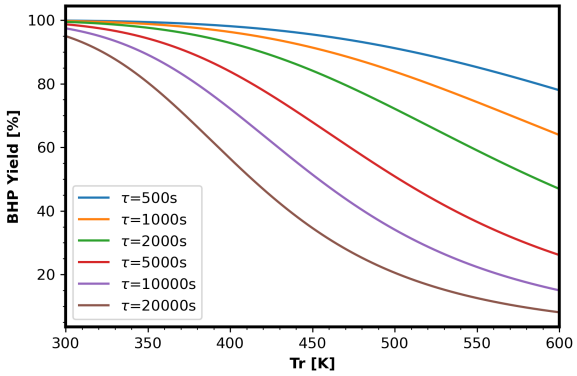

(b) BHP Yield.

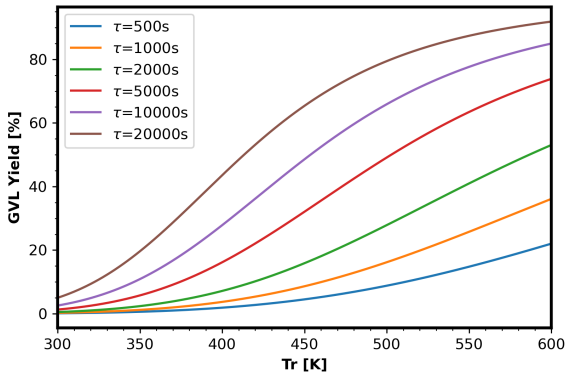

(c) GVL Yield.

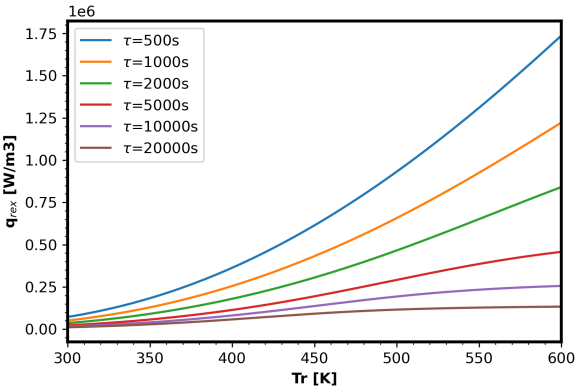

(d) Power per units of volume.

Figure 4.3 Effect of temperature and residence-time on (a) BL conversion, (b) BHP Yield, (c) GVL yield, and (d) Power generated by the chemical reaction.

$$\text{BL conversion } [\%] = \frac{[BL]_{in} - [BL]_{out}}{[BL]_{in}} * 100 \tag{4.12}$$

$$\text{BHP Yield } [\%] = \frac{[BHP]_{out} - [BHP]_{in}}{[BL]_{in} - [BL]_{out}} * 100 \tag{4.13}$$

$$\text{GVL Yield } [\%] = \frac{[GVL]_{out} - [GVL]_{in}}{[BL]_{in} - [BL]_{out}} * 100 \tag{4.14}$$

$$q_{rex} = R_{hyd}\Delta H_{hyd} - R_{cyc}\Delta H_{cyc} \tag{4.15}$$

$$q_{rem} = \mathbf{Ua}(T_j - T_r) \tag{4.16}$$

The results obtained from the simulation, Figure 4.3, clearly show that as the reaction temperature (T_r) and residence time (τ) increase, BL conversion and GVL production increase. Regarding the energy released by the reaction, we can see that it increases with temperature but decreases as the residence time increases. This behavior is expected since the longer the reactants last in the reactor, the longer the cyclization step occurs. As an endothermic reaction, the more it takes place, the higher the cooling effect on the system.

4.2 Van Heerden Criterion

The stability-based criteria state that a system can be considered stable if and only if *i)* after small perturbations, the system returns to its initial state and *ii)* if during dynamic behavior the system stays close to the initial state.

When a chemical reactor operates in a steady state, the heat produced by the reaction and the heat removed from the system are equal, thus keeping the reaction temperature (T_r) constant throughout the operation. Since the heat produced by the reaction increases exponentially with temperature, Equation 4.15, and the heat removed from the reactor increases proportionally, Equation 4.16, a variation in the operating temperature can lead to a runaway scenario.

The Van Heerden criterion, also called the "slope criterion", is a stability-based criterion. This criterion states that to satisfy steady-state thermal stability, the energy removed from the reactor must be greater than the energy produced by the reaction [104]. The mathematical form of this criterion is as follows:

$$\frac{dQ_{removed}}{dt} > \frac{dQ_{produced}}{dt} \tag{4.17}$$

Where $Q_{removed}$ is the heat removed from the reactor thanks to heat-carrier fluid in the reactor jacket, and $Q_{generated}$ is the heat produced by the chemical reaction. To start the BL hydrogenation, it is clear that energy is needed to increase the reactor temperature, but when the reaction starts, energy is produced, so part of the energy needs to be removed to maintain a constant temperature. The question we want to address in this section is: Given a situation of heat accumulation in the reactor, what is the minimum value of **Ua** for which the heat removed is greater than the heat produced considering that T_j=293 K? This question was formulated this way, considering that a common resource at the industrial level is water at ambient temperature.

Considering the operating conditions in Table 4.1, this question was addressed. For the choice of residence time, we based ourselves on the results obtained from the simulations of the balance of matter, Figure 4.3. From these results, we can realize that when $\tau = 10000\,s$, the reactor achieves good conversions and yields and moderate heat production.

To determine the minimum value **Ua**, we plotted the heat generated by the reaction, Equation 4.15, in the range of temperature 300-600 K. Then, we decreased the **Ua** value until we reached the value for which the heat removed, Equation 4.16, is less than the heat produced.
Figure 4.4 shows the results of applying the Van Heerden criterion. The results show that for **Ua**=800 W/m^3/K, the heat removed will be greater than the heat produced only in the temperature range of 330-430 K. For this **Ua** value, thermal stability conditions can be satisfied in the 300-600 K if and only if the T_j=255 K. Otherwise, **Ua** must be greater thant 800 W/m^3/K.

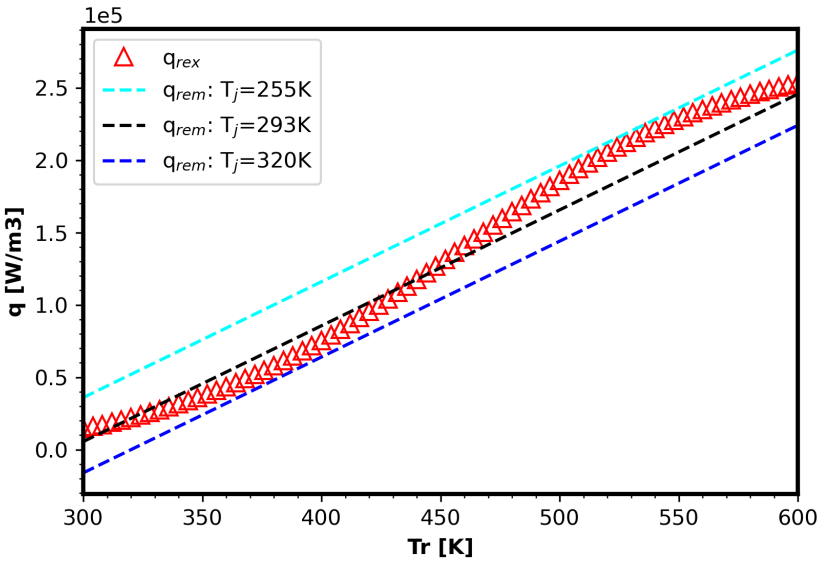

Figure 4.4 Van Heerden criterion results: Heat-flow produced versus heat-flow removed at different T_j for **Ua** = 800 W/m^3/K.

4.3 Steady States Bifurcation

We have previously explained that thermal risk comes from the fact that the heat produced in a reactor increases exponentially with temperature while the heat removed increases linearly. Bifurcation analysis is another criterion for stationary thermal stability that consists of determining the existence of a multiplicity of steady-states for fixed operating conditions.

Steady-state bifurcation analysis is commonly used to complement thermal risk assessments of chemical reactors. For example, Nguyen et al. [106] used this approach to determine the safest feed flow during the production of polystyrene in a CSTR. Rowena Ball [107] used this approach to complement a thermal oscillations study during the decomposition of organic peroxides.

This analysis determines the reactor jacket temperature T_j needed to maintain a given reactor temperature T_r during steady-state operation. It can be accomplished by solving the energy balance for T_j, Equation 4.10, at steady-state, which results in Equation 4.18.

$$T_j = T_r + \frac{1}{\mathbf{Ua}} \sum_i R_i \Delta H_i - \frac{\sum C_{j_{in}} C_{P_j}}{\tau \cdot \mathbf{Ua}} (T_{in} - T_r) \tag{4.18}$$

From Equation 4.18, we plotted T_r as a function of T_j for different values of **Ua**, Figure 4.5. Steady-state bifurcation occurs when more than one value of T_r is assigned to a single value of T_j. The set of all T_j values that have more than one T_r value assigned is designated as an unstable zone with a high thermal risk.

To better explain the latter, let us take the values T_r=400 K and **Ua**=800 W/m^3/K as examples. According to the energy balance in steady state, for T_r=400 K then T_j must be equal to 320 K, Figure 4.5, now let us imagine a hypothetical situation where the temperature T_j increases a few degrees due to any perturbation, this would cause a huge jump in T_r, taking it to values close to 560 K. According to Van Heerden's criterion for this value of T_r, reducing T_j to 293 K would not be enough to avoid accidents, explosions, or runaway scenarios. The results show, Figure 4.5, that the steady-state bifurcations start to disappear for **Ua** $\geq$ 1500 W/m^3/K.

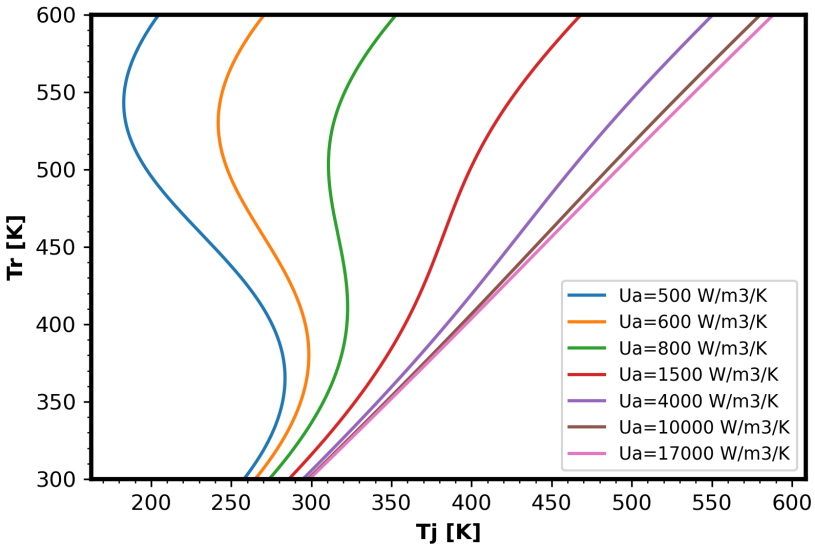

Figure 4.5 Steady-states bifurcation results.

It is important to note that the opposite case could occur, i.e., a sudden cooling of the reactor. If we take, for example, values of T_r=500 K and **Ua**=800 W/m^3/K, which correspond to T_j=305 K. A decrease in T_j due to any perturbation would cool the reactor to T_r=350 K. This abrupt cooling would affect the system's conversion, yield, and energy recovery. In conclusion, zones of a multiplicity of steady state due to bifurcations should be avoided since perturbations in the temperature T_j can produce the evolution of our system to new steady-state conditions that are very different from the initial ones in terms of temperature, conversion, yield, and thermal risk.

4.4 Dynamic Thermal Stability

A reactor's dynamic behavior differs from its stationary behavior, and its study can be more complex, as shown by Gómez García et al.[108]. It is well known that the Van Heerden criterion and the steady-state bifurcations must be verified to operate without stationary thermal risk. However, these conditions are insufficient to guarantee the reactor's dynamic thermal stability. Schweitzer et al. [109] explain that only dynamic analysis can provide an accurate answer concerning the safe operation of the reactor. Using the perturbations method, they analyzed the dynamic thermal stability of a three-phase reactor.

As Schweitzer et al. did, we applied the perturbations method to assess the thermal stability of a CSTR reactor during the GVL production from BL over Ru/C. If we consider the steady-state operation of the CSTR, the dynamic stability analysis consists of determining the dynamic evolution of our reactor after small perturbations in output variables, i.e., concentrations and temperature. Will the reactor return to its initial conditions? Or will it get into unstable conditions, where the final conditions differ from the initial ones? These are the questions that we want to address in this section.

Let us consider the general form of our dynamical model, Equations 4.5 - 4.11.

$$\frac{dy_i}{dt} = f_i(y_1, y_2, \ldots, y_n, \phi, t) \tag{4.19}$$

Where y_i represents the variables of the system, i.e., the concentration of BL, BHP, GVL, BuOH, T_r, and T_j, and ϕ represents the other parameters of the system. Let us define a small perturbation x_i on the whole set of variables around an operating point as follows:

$$x_i = y_i - y_{i,s} \longrightarrow y_i = y_{i,s} + x_i \tag{4.20}$$

Where $y_{i,s}$ is the value of the variable i at stationary conditions. Replacing Equation 4.20 in Equation 4.19, we can define the reactor dynamic model as:

$$\frac{d(y_{i,s} + x_i)}{dt} = f_i(y_{1,s} + x_1, y_{2,s} + x_2, \ldots, y_{n,s} + x_n, \phi, t) \tag{4.21}$$

If the perturbations are very small, we can apply the first-order Taylor expansion to linearize the model, Equation 4.21, around the operating point to obtain:

$$\frac{d(y_{i,s} + x_i)}{dt} = f_i(y_{1,s}, y_{2,s}, \ldots, y_{n,s}, \phi, t) + \left(\frac{\partial f_i}{\partial x_1}\right) x_1 + \left(\frac{\partial f_i}{\partial x_2}\right) x_2 + \ldots + \left(\frac{\partial f_i}{\partial x_n}\right) x_n \tag{4.22}$$

Under stationary conditions, we have:

$$\frac{dy_{i,s}}{dt} = 0 \tag{4.23}$$

$$f_i(y_{1,s}, y_{2,s}, \ldots, y_{n,s}, \phi, t) = 0 \tag{4.24}$$

Then, replacing Equations 4.23 and 4.24 in 4.22, we can obtain the model of perturbation, Equation 4.25.

$$\frac{dx_i}{dt} = \left(\frac{\partial f_i}{\partial x_1}\right) x_1 + \left(\frac{\partial f_i}{\partial x_2}\right) x_2 + \ldots + \left(\frac{\partial f_i}{\partial x_n}\right) x_n \tag{4.25}$$

Using a matrix notation, the model of perturbations becomes:

$$\dot{X} = \mathbf{J} \cdot X \tag{4.26}$$

with

$$\dot{X} = \begin{pmatrix} \frac{dx_1}{dt} \\ \vdots \\ \frac{dx_i}{dt} \\ \vdots \\ \frac{dx_n}{dt} \end{pmatrix}, \qquad \mathbf{J} = \begin{pmatrix} \frac{df_1}{dy_1} & \cdots & \frac{df_1}{dy_i} & \cdots & \frac{df_1}{dy_n} \\ \vdots & & \vdots & & \vdots \\ \frac{df_i}{dy_1} & \cdots & \frac{df_i}{dy_i} & \cdots & \frac{df_i}{dy_n} \\ \vdots & & \vdots & & \vdots \\ \frac{df_n}{dy_1} & \cdots & \frac{df_n}{dy_i} & \cdots & \frac{df_n}{dy_n} \end{pmatrix}, \qquad X = \begin{pmatrix} x_1 \\ \vdots \\ x_i \\ \vdots \\ x_n \end{pmatrix}$$

The solution of this linear first-order differential equation system allows us to know if the perturbation of at least one of the variables diverges with time and propagates it. This means that the reactor has reached an unstable state that will lead to a runaway. The solution of the Equation 4.25 is given by Equation 4.27 where $U_{i,m}$ is the eigenvector of the Jacobian matrix $\mathbf{J}$ associated to the eigenvalue λ_i.

$$x_i = \sum_{j}^{n} a_m \cdot U_{i,m} \cdot e^{\lambda_m t} \tag{4.27}$$

Based on the solution of the perturbation model, the condition for dynamic stability is that the real part of all the eigenvalues of the Jacobian matrix must be less than zero, Equation 4.28.

$$\forall i \ \lim_{t \to \infty} x_i = 0 \iff \forall i \ \mathbf{Re}(\lambda_i) < 0 \tag{4.28}$$

When eigenvalues are real numbers, and λ_i<0, perturbations are exponentially attenuated over time. However, if λ_i>0, then perturbations are exponentially amplified, and runaway conditions are achieved [110]. For complex eigenvalues, it is the same but with oscillatory behavior [107, 111].

As we did for the bifurcation analysis, we considered the operating conditions in Table 4.1. We have simulated the conditions in Table 4.1 but different **Ua** values. We considered the limit value of **Ua**=800 W/m^3/K, obtained from the Van Heerden criterion, and a value for which there is no stationary thermal risk **Ua**=5000 W/m^3/K. To assess the dynamic thermal stability, we defined the Jacobian matrix of the model in the range of temperature from 300 K to 600 K and calculated the eigenvalues of the matrix for each temperature.

The results obtained are shown in Figure 4.6. Figure 4.6a for **Ua**=800 W/m^3/K and Figure 4.6b for **Ua**=800 W/m^3/K. The results show that for these values, the real part of all eigenvalues is less than zero, $\mathbf{Re}(\lambda_i) < 0$. Therefore, we can conclude that there is no risk of thermal runaway due to dynamic instabilities. However, we can see that, in general, the dynamic instabilities will be attenuated faster for *Ua*=5000 W/m^3/K.

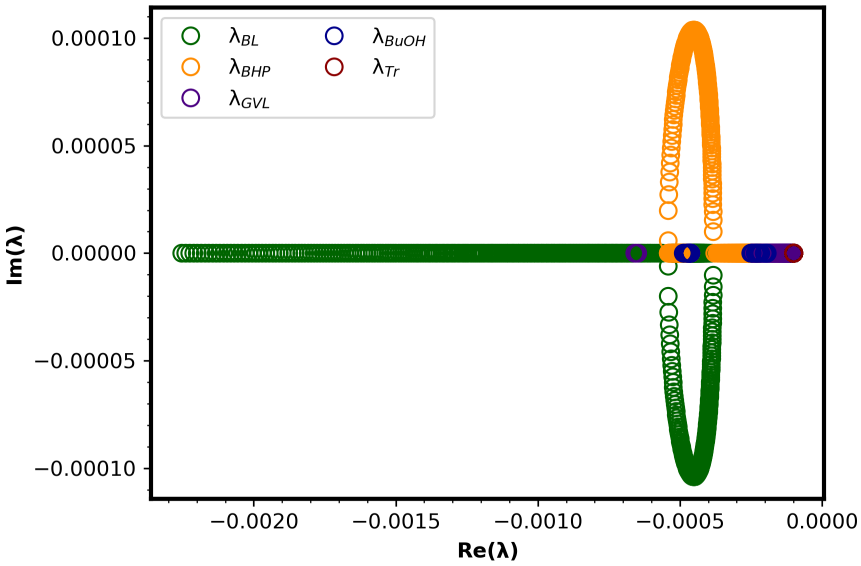

(a) Eigenvalues for Ua=800 W/m^3/K.

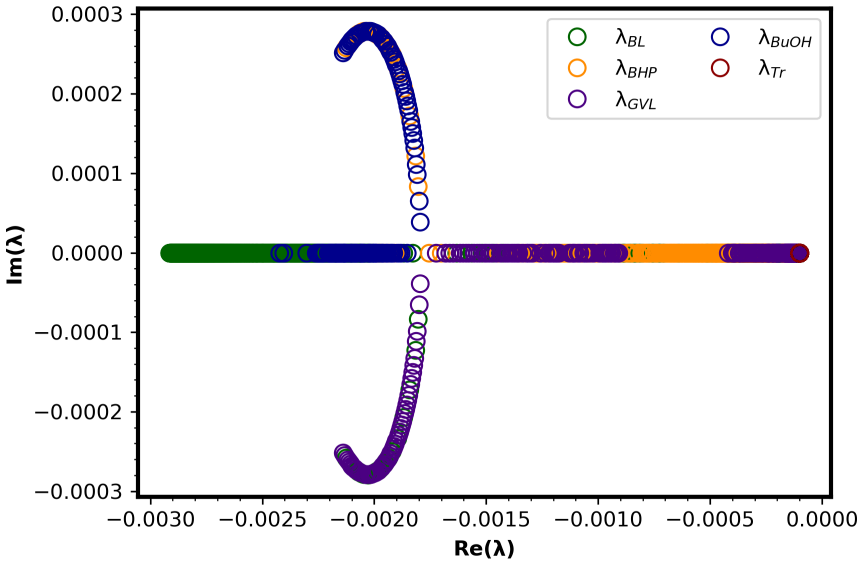

(b) Eigenvalues for Ua=5000 W/m^3/K.

Figure 4.6 Dynamic thermal stability results: Eigenvalues plot.

4.5 Parametric Sensitivity

Parametric sensitivity analysis (PSA) is crucial in chemical reaction systems. Because small changes in the critical operating parameter or initial conditions can result in a significant consequence in the system temperature or output variables [112]. A PSA is presented in this section to complement the thermal risk assessment. A one-factor-at-a-time PSA was done, similar to the one made by Zang et al. [113] for a semi-bath reactor. Kummer et al. [104] explain that near the runway (explosion) boundary, the system behavior becomes sensitive to small changes in some of the input or initial parameters.

As we did for the dynamic stability, we start from our chemical reaction model, Equation 4.19 in its vector form:

$$\frac{d\vec{y}}{dt} = \vec{f}(\vec{y}, \phi, t) \tag{4.29}$$

The first-order local sensitivity or absolute sensitivity of the dependent variable $\vec{y}$, concerning the input parameters ϕ, is calculated in the following form:

$$S(\vec{y}, \phi) = \frac{d\vec{y}}{d\phi} \tag{4.30}$$

Via differentiation of Equation 4.30, we obtain Equation 4.31.

$$\frac{S(\vec{y}, \phi)}{dt} = \mathbf{J} \cdot S(\vec{y}, \phi) + \frac{d\vec{f}}{d\phi} \tag{4.31}$$

Solving Equation 4.31 for $S(\vec{y}, \phi)$ in steady state, we obtain the main formula to calculate the sensitivity:

$$S(\vec{y}, \phi) = -\mathbf{J}^{-1} \cdot \frac{d\vec{f}}{d\phi} \tag{4.32}$$

With,

$$\frac{d\vec{f}}{d\phi} = \begin{pmatrix} \frac{df_1}{d\phi} \\ \vdots \\ \frac{df_n}{d\phi} \end{pmatrix} \tag{4.33}$$

To compare a variable's sensitivity according to different parameters, the normalized parametric sensitivity is defined by Equation 4.34. We have evaluated the parametric sensitivity of BL concentration in the outlet flow, GVL concentration in the outlet flow, and the reactor temperature (T_r).

$$S_n(y_i, \phi_j) = \frac{\phi_j}{y_i} \frac{dy_i}{d\phi_j} \tag{4.34}$$

We decided to focus on these three variables since they are the main reactant, the main product, and the variable linked to thermal risk. The parameters considered for this evaluation were: the concentration of BL in the inlet flow of the reactor $[BL]_{in}$, hydrogenation rate constant k_{hyd}, cyclization rate constant k_{cyc}, global heat transfer coefficient $\mathbf{Ua}$, residence time τ, catalyst loading in the reactor ω_{cat}, and the temperature of the inlet flow T_{in}.

The results obtained from the parametric sensitivity analysis are shown in Figure 4.7; these results were obtained for Ua=800 W/m^3/K and 5000 W/m^3/K. For **Ua**=800 W/m^3/K, we can see that the normalized sensitivity presents an abrupt jump for T_j values where there are thermal instabilities due to the multiplicity of steady states. We can see that the BL concentration in the outlet flow is more sensitive to the BL concentration in the inlet flow $[BL]_{in}$ and residence time τ. The sensitivity of the GVL concentration in the outlet flow, in addition to presenting a jump in the multiplicity zones, also suggests an oscillatory behavior for most of the parameters analyzed, Figure 4.7e, with the parameters that most affect the concentration of GVL being the initial concentration of BL $[BL]_{in}$, the residence time τ and the coefficient **Ua**. For the temperature of the reactor, we can only see an abrupt jump in the multiplicity zones, with the parameters that affect it the most being the temperature of the inlet flow T_{in}, the **Ua** coefficient and the residence time τ.

For **Ua**=5000 W/m^3/K, we can see that there are no jumps for any value of T_j, but rather than all sensitivities vary smoothly, thanks to the fact that there is no multiplicity of steady states. We can see that for this **Ua** value, the parameters that most affect the output variables are the same as for For **Ua**=800 W/m^3/K. For the concentration of GVL in the outlet flow, we can realize that there is a maximum sensitivity for almost all parameters for T_j near 450 K. We can also note that for **Ua**=5000 W/m^3/K the GVL concentration is more sensitive to the cyclization kinetic constant k_{cyc} than to the initial BL concentration $[BL]_{in}$ for $T_j \leq 430$ K.

4.6 Conclusions

This chapter focused on the thermal assessment of the continuous production of GVL via hydrogenation of BL over Ru/C in a CSTR reactor. This assessment used the NCLH1 kinetic model, developed in Chapter 3. With this kinetic model, we made simulations using the RC1 calorimeter reactor as a reference.

Initially, we established the material and energy balance for the system, and we determined for a temperature range of 300-600 K that the dominant reaction step is hydrogenation. Therefore, our system will exhibit exothermic behavior; for this reason, it is important to have a thermal assessment.

For the stationary thermal stability, we applied the Van Heerden criterion, with which we determined that for **Ua**=800 W/m^3/K it is not possible to prevent thermal accumulation in the system with a jacket temperature T_j=293 K. Then, applying the steady-state bifurcation analysis, we found that stationary instabilities due to steady-state multiplicities are reduced for **Ua** values greater than or equal to 1500 W/m^3/K. We then analyzed the dynamic stability of the CSTR reactor and concluded that there are no dynamic instabilities for **Ua**=800 W/m^3/K, in the temperature range of 300-600 K. This is an expected result, given that the energy released during BL hydrogenation is moderate and mitigated by the endothermic effect of the cyclization step reaction.

Finally, this chapter ends with a parametric sensitivity analysis (PSA), in which we analyze the sensitivity of the output variables BL concentration, GVL concentration, and reaction temperature with respect to the operating parameters of the system. From this analysis, we conclude that for **Ua**=800 W/m^3/K, the sensitivity zones of the system coincide with the stationary instabilities zones; in addition to this, we could also notice indications of oscillatory behaviors for the concentration of GVL in the outlet flow of the reactor.

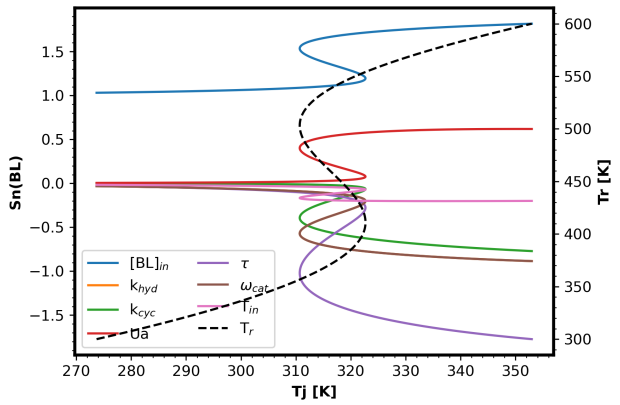

(a) BL PSA for **Ua**=800 W/m^3/K.

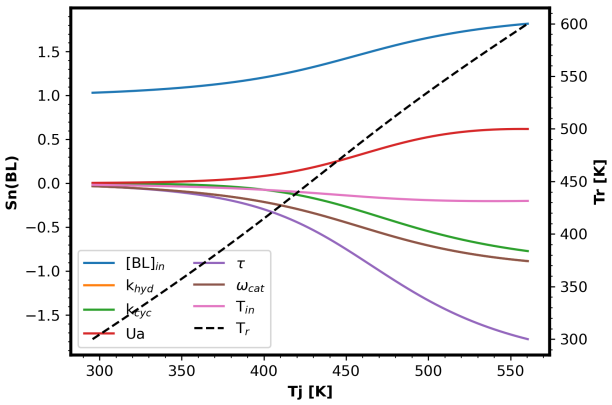

(b) BL PSA for **Ua**=5000 W/m^3/K.

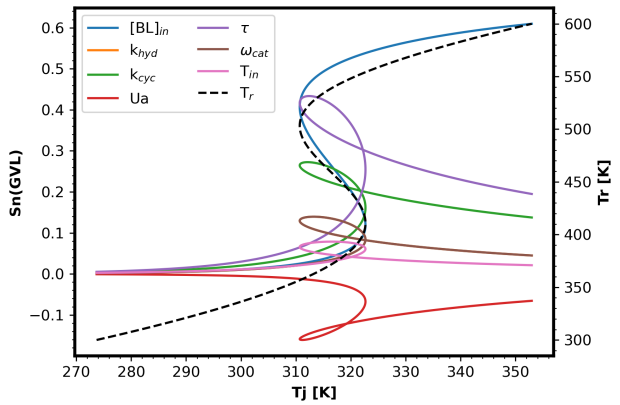

(c) GVL PSA for **Ua**=800 W/m^3/K.

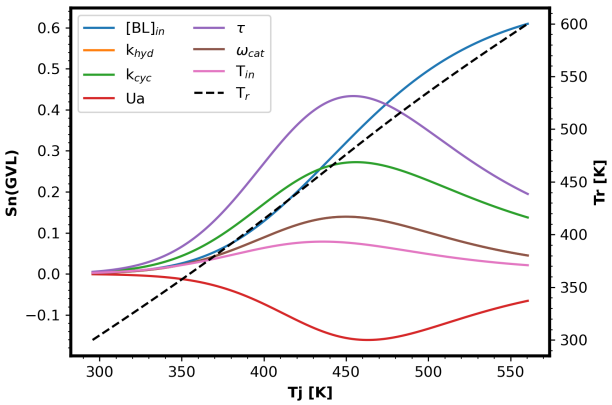

(d) GVL PSA for **Ua**=5000 W/m^3/K.

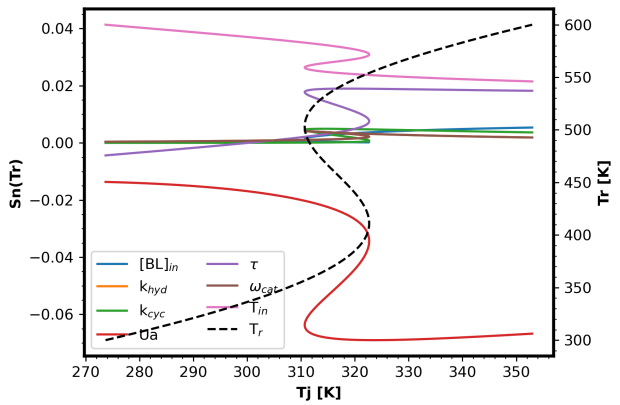

(e) Tr PSA for **Ua**=800 W/m^3/K.

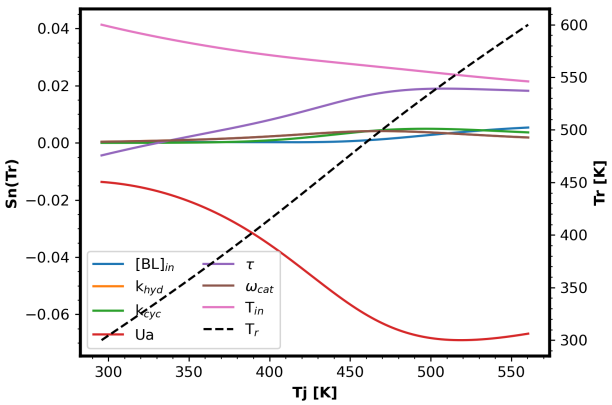

(f) Tr PSA for **Ua**=5000 W/m^3/K.

Figure 4.7 Parametric Sensitivity Analysis Results.

It should be noted that with the NCLH1 model developed under isothermal and non-isothermal conditions, more information concerning the thermal risk was obtained than with the kinetic model developed under isothermic conditions by Wang et al. [92]. A continuation of this work could be the experimental validation of the thermal assessment, the performance of the thermal assessment for a plug flow reactor (PFR), and the inclusion of the transient regime analysis for thermal stability.

Chapter 5
Combustion Assessment: BL as Kerosene Additive

This chapter aims to assess the suitability of BL as a kerosene additive. Here, we studied the drop-in effects of BL during the kerosene combustion process. The combustion efficiency of BL/kerosene mixtures is evaluated in a combustion chamber with an RQL injection system. This is complemented with optical diagnostics to understand the flame/spray behavior better. The results of this chapter are in the process of being published.

In Chapter 1, we showed that it is possible to replace kerosene with SAF produced from lignocellulosic biomass (LCB). However, due to the many transformation steps required by this feedstock, its commercial application will take longer. Nevertheless, to reach the environmental goals established by the different governments and institutions to reduce GHG emissions, it is worth exploring the potential applications as an additive of different intermediates in the transformation process of LCB into SAF. Butyl levulinate (BL), an LCB derivative, is potentially used as a drop-in additive to kerosene. The advantage of a drop-in additive is that there is no need to modify the current infrastructure for kerosene or the aircraft engine design. However, it is crucial to understand how the additive will affect the combustion process, e.g., the performance, operating limits, and pollutants emissions.

The performance of a gas turbine engine is crucially dependent upon the fuel and airflow conditions in the inlet. The most important are pressure and temperature, which are determined by the ambient conditions. When choosing fuels for aircraft gas turbines, it is crucial to consider the extensive pressure and temperature variations the fuel will encounter. At an altitude of 12 km, the ambient air pressure is merely a quarter of that at sea level, and air temperatures can drop as low as 193 K under extreme conditions. Also, fuel tank temperatures can become extremely high when an aircraft is exposed to tropical sunlight on the ground. Thus, studying the effects of pressure and temperature fuel properties is essential for gas turbine operation. The full range of inlet conditions that a given gas turbine could encounter is encompassed in the operational envelope.

In a gas turbine, the fuel must be injected, vaporized, and mixed with air before combustion occurs. The efficiency of these processes, and consequently the combustion itself, is heavily influenced by the physical properties of the fuel. Some of these properties are listed below:

- *Density*: The fuel density is important because it defines the energy content for a fixed volume, i.e., the aircraft fuel tank.
- *Vapor pressure*: The vapor pressure of a liquid is the pressure exerted by the vapor above its surface at a given temperature when the liquid and vapor are in dynamic equilibrium. A high vapor pressure is desirable because it guarantees a rapid evaporation of fuel. However, a low vapor pressure can reduce fuel losses and reduce fire hazards.

- *Viscosity*: The viscosity affects the power required to pump the fuel through the fuel system into the combustion chamber. Also, it has a marked effect on forming a well-atomized spray and, therefore, fuel evaporation and combustion rates.
- *Surface tension*: This property significantly affects the fuel atomization, hence the combustion efficiency.
- *Freezing Point*: Aircraft operate at high altitudes where ambient temperature can be as low as 193 K, and fuels may not form crystals during operation to avoid blocking.
- *Heat capacity*: Modern aircraft use the fuel as a heat sink to absorb heat from the engine. Thus, the heat capacity of the fuel is an important property.
- *Heating value*: The heating value, or energy content, of a fuel, is a measure of the energy released when the fuel is completely burned under standard conditions. For a gas turbine, the lower heating value (LHV) is the most relevant since it pertains to the complete combustion of the fuel to CO_2 and water vapor. The LHV of a fuel depends entirely on its chemical composition and, in particular, on the hydrogen-carbon ratio.

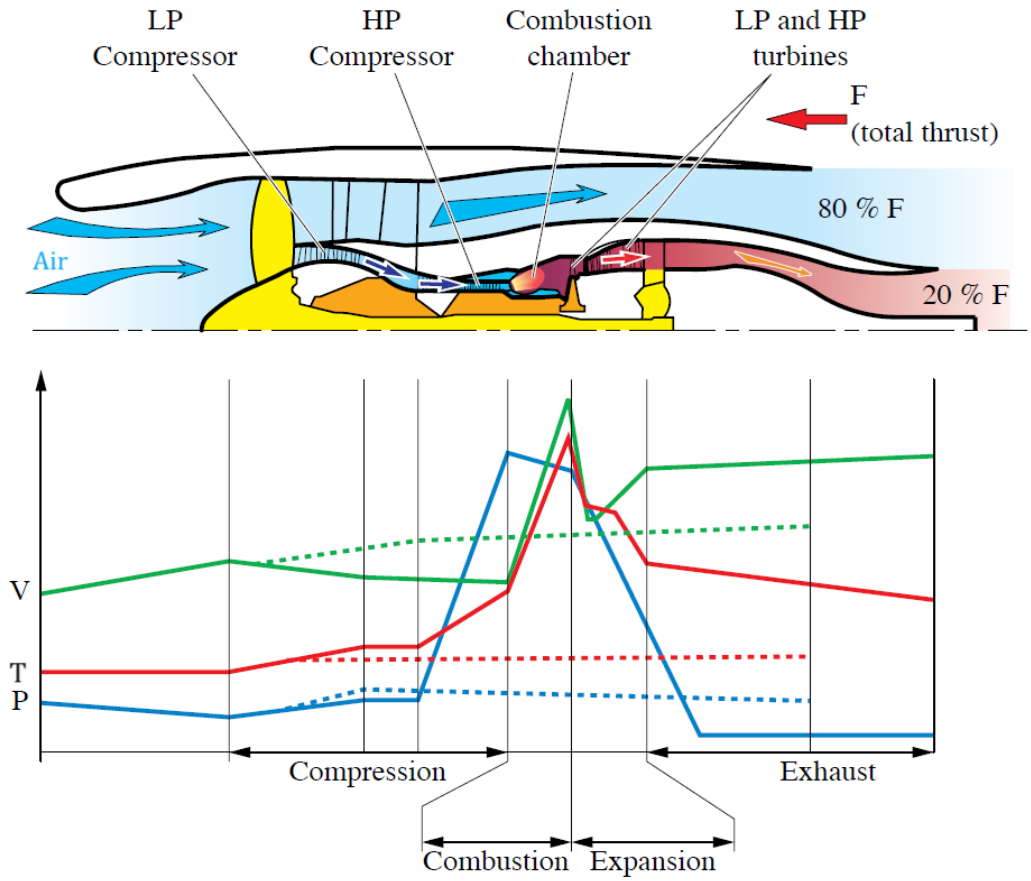

Figure 5.1 Diagram of the gas flow in a gas turbine engine, continuous lines represent the state of the flow that passes through the combustion chamber. Modified from [8].

Ignition and reignition processes are one of the most technically challenging aspects of gas turbine performance. The difference between ignition and reignition depends on the altitude and speed of the aircraft; ignition is when the aircraft is on the ground, and reignition is when it is in flight. During ignition, the engines need a starter component that rotates the high-pressure (HP) compressor, allowing air to enter the combustion chamber. While during reignition, the high-pressure (HP) compressor rotates fast enough under the action of the relative wind (auto-rotation).

Figure 5.1 represents a gas turbine engine. Usually, the total airflow captured by the aircraft engine is divided in two, where 80% prevents engine overheating. The remaining 20% passes through the low-pressure (LP) compressor into the combustion chamber. During reignition, due to environmental conditions, the temperature and pressure of the air are much lower than those at ground level. This figure shows a diagram of the behavior of pressure, temperature, and airflow volume in the different parts of the gas turbine. Solid lines represent the properties of 20% of the total air that passes through the combustion chamber, and dashed lines represent the properties of the remaining 80% of the air that does not pass through the combustion chamber.

Indeed, aeronautical engines reignition can be divided into different sub-processes:

1. Energy deposition (spark) and flame kernel formation.
2. Flame kernel propagation and spreading to the flame stabilization on a single injector.
3. Burner light-around. In this sub-process, the flame propagates from one injector to all the injectors in the annular combustion chamber.
4. Pull-away corresponds to the progressive increase of the engine rotation speed and fuel flow rate to reach idle conditions [114, 115].

During the ignition and reignition processes, even when the first three sub-processes are completed, there is a risk of flame extinction during the pull-away phase. This can happen because during the pull-away, the operational envelope of the combustion chamber (HP compressor) evolves in terms of rotational speed, airflow, pressure, temperature, etc. To guarantee the ignition and reignition, manufacturers must establish the fuel flow limits based on the operational envelope of the combustion chamber. This is known as the fuel dosing rule, which is fundamental for the correct operation of engines.

Indeed, if the fuel flow rate is very high during ignition, there is a risk of a sudden increase in pressure, destabilizing combustion during ignition. Once the engine is started, the fuel flow rate must be modified according to the operational envelope throughout the engine's pull-away (power-up) phase. The pull-away may be aborted if this fuel dosing rule is not well defined and adapted to the reactor (interaction between combustion chamber, turbine, and compressor). Figure 5.2 is a graphical representation of the fuel dosing rule. This establishes the fuel flow rate needed to start the ignition process (red star) and how it should vary during the pull-away as a function of the HP compressor operational envelope until the idle conditions are reached (green star).

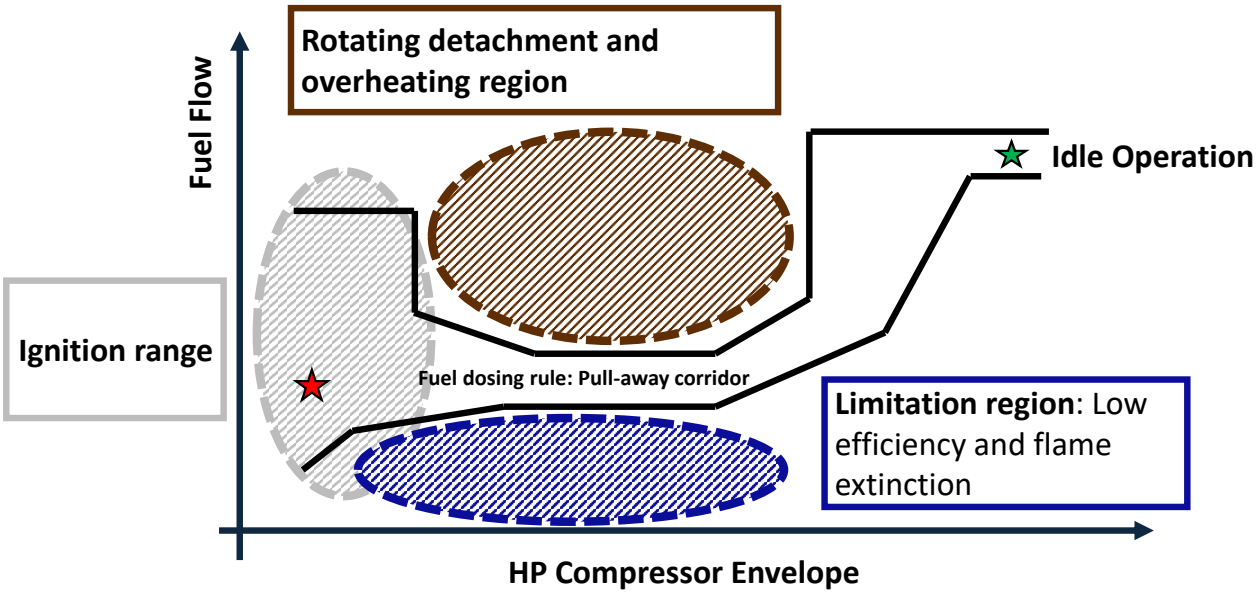

Figure 5.2 Dosing rule representation, and the main causes of pull-away failure.

The four main causes of pull-away failure, also shown in Figure 5.2, are:

1. *Rotating detachment*: The compressor enters its stall zone, the shaft stops accelerating, and the temperature rises rapidly.

2. *Overheating*: The temperature exceeds the limits set to prevent damage to parts downstream of the combustion chamber. This can occur if the mixture in the combustion chamber is near stoichiometry ratios.

3. *Stagnation*: It occurs when the compressor's rotation speed is stabilized below the idle one.

4. *Flame extinction*: This can occur due to several factors, including an incorrect fuel-air ratio in the combustion chamber (rich and lean extinction).

The combustion study during the pull-away phase is not very common, as there are few facilities available that allow the replication of the actual operational envelope to which the engines are subjected during flights, e.g., low pressure and low temperature. In this chapter, we assessed the effects of BL on the operability limits of kerosene during pull-away conditions. This means that the combustion process of blends of Kerosene/Butyl levulinate was studied in low-pressure and low-temperature conditions.

This study was performed in the HARTur facility at the CORIA research unit; globally, only a few facilities of this type are known to exist, allowing the study of combustion at low pressures and temperatures. Our study focuses on measuring the combustion efficiency and determining the operating limits of these blends during pull-away. With this assessment, we aim to evaluate the potential use of BL as a kerosene additive in real operating conditions in a gas turbine. This assessment is complemented by a local analysis of the spray and flame structure to evaluate the viscosity effects from a local point of view.

5.1 Atomization

Before combustion occurs inside a gas turbine, the fuel must be atomized and mixed with air. The atomization process involves separating the liquid fuel into small droplets to burn it in the combustion chamber effectively. The atomization process can be divided into two steps: *i)* primary atomization, in which the fuel is separated into ligaments, and *ii)* secondary atomization, in which the ligaments produced in primary atomization are separated into small droplets. In general, liquid fuel atomization is carried out by injecting the fuel through small orifices at high pressure or by mixing the fuel with high-pressure air or gas [38]. Depending on the situation, there are different types of injectors, some of which are better suited than others. Kang et al. [116] explained that pressure swirl injectors are extensively used in liquid rocket engines, gas turbine engines, internal combustion engines, and many other combustion applications. In these injectors, the pressurized liquid goes through tangential vanes into the swirling section to form an unstable and turbulent motion. Then, it is discharged in a cone shape through a hole into the combustion chamber. Figure 5.3 represents a pressure-swirl injector; in this figure, we can see how the atomization spray is generated in this type of injector.

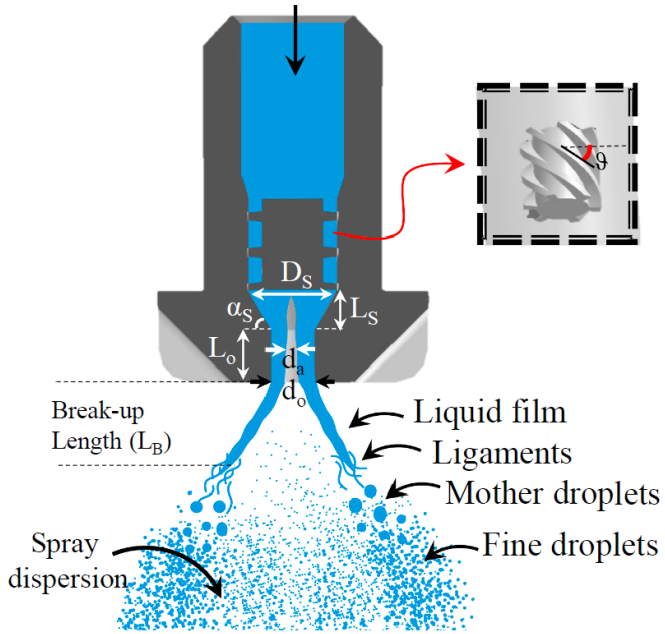

Figure 5.3 Atomization spray generation in a pressure-swirl nozzle, taken from [9].

The atomization process depends significantly on the cohesive forces of the liquid phase, determined by its viscosity and surface tension. The low-temperature conditions to which fuels are exposed before injection considerably influence their physical properties, such as viscosity, and consequently affect the atomization process. The influence of low temperature and high viscosity has always been a topic of study for the optimization of the atomization process during the ignition of a combustion engine [117, 118].

For example, Dafsari et al.[9] studied the effects of viscosity (driven by temperature) and pressure on the atomization spray that occurs in a pressure-swirl injector, they concluded that viscosity changes due to temperature changes have a big impact in the quality of atomization, one of their main results are shown in Figure 5.4. This figure shows how spray angle and breakup-length (L_B) change with pressure and low temperatures.

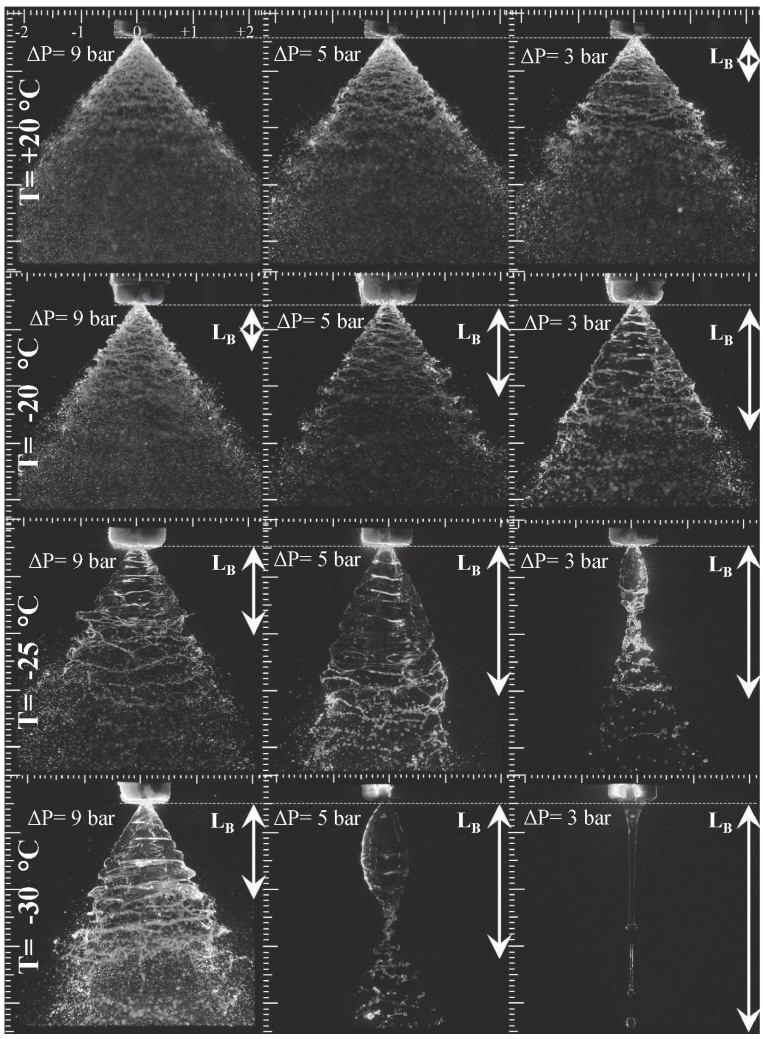

Figure 5.4 Effects of the temperature and pressure on the atomization spray, taken from [9].

5.1.1 Injection System

There are two main families of injectors: 1) *mechanical injectors*, in which the fuel is injected at high pressure through a small orifice that generates atomization, and 2) *Aerodynamic injectors*, in which a gas (usually air) at high speed collides with a liquid phase (at low speed) breaking the liquid ligaments into small droplets thanks to transfer of momentum.

Aeronautical injectors are a combination of mechanical and aerodynamic injectors. The fuel goes through a pressure-swirl nozzle injector, which allows a cone-shaped spray to be formed at the outlet. Atomization is immediately assisted by the aerodynamic effect of air injected via an injection system. Figure 5.5 shows a representation of the pressure-swirl nozzle injector and the air injection system in the HARTur facility.

The injection system used in the HARTur facility was designed and provided by *SAFRAN Aircraft Engines*; the details about this system are not provided for confidentiality reasons. During Marie-Eve Clavel's thesis [7], five different designs of injection systems were tested to study the operating limits and combustion dynamics of kerosene during pull-away conditions. These conditions are similar to those found during the pull-away phase of a gas turbine at high altitude, i.e., low pressure and low temperature.

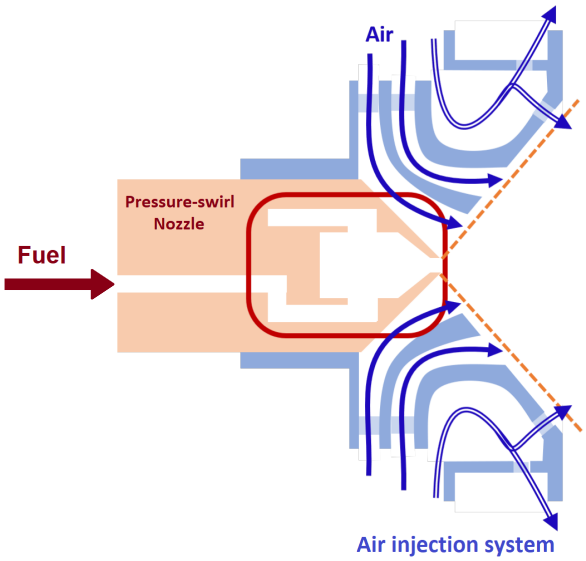

Figure 5.5 HARTur injection system assembly: Mechanical injector in red and Aerodynamic injector in blue. Modified from [7].

In general, each injection system was tested with kerosene at four different operating conditions (OP) in terms of pressure and temperature. The manufacturer has defined the fuel and air nominal mass flow rate for each operating condition in the injection system. For the injection system that we have used, these conditions are shown in Table 5.1. Where T corresponds to the temperature of the fuel and air in the intake plenum, Figure 5.11, P corresponds to the absolute pressure inside the combustion chamber, $\dot{m}_{fuel}$ in the nominal value of fuel flow rate, $\dot{m}_{air,1}$ and $\dot{m}_{air,2}$ are the primary and dilution air flow, respectively.

Table 5.1 HARTur facility: Operating conditions and nominal flow rate for kerosene.

	T [K]	**P [kPa]**	$\dot{\mathbf{m}}_{\mathbf{air,1}}$ **[kg/h]**	$\dot{\mathbf{m}}_{\mathbf{air,2}}$ **[kg/h]**	$\dot{\mathbf{m}}_{\mathbf{fuel}}$ **[kg/h]**
$\mathbf{OP_1}$	293	103	41.04	63.36	4.212
$\mathbf{OP_2}$	286	85	33.55	56.81	3.852
$\mathbf{OP_3}$	258	54	19.74	60.88	3.492
$\mathbf{OP_4}$	250	46	15.84	63.00	3.384

M. Clavel et al. aimed to study kerosene's flame structure and operating limits under these operating conditions (from OP_1 to OP_4) that come from an existing fuel dosing rule. This study makes it possible to determine the limits where the combustion efficiency will be the highest and to avoid flame extinction for a given operating condition of pressure and temperature. Figure 5.6 represents temperature versus pressure for each operating point (OP). In this figure, we can see how the pressure and temperature increase (from OP_4 to OP_1), representing the evolution of the operational envelope of the HP compressor during the pull-away phase at low-pressure and low-temperature conditions.

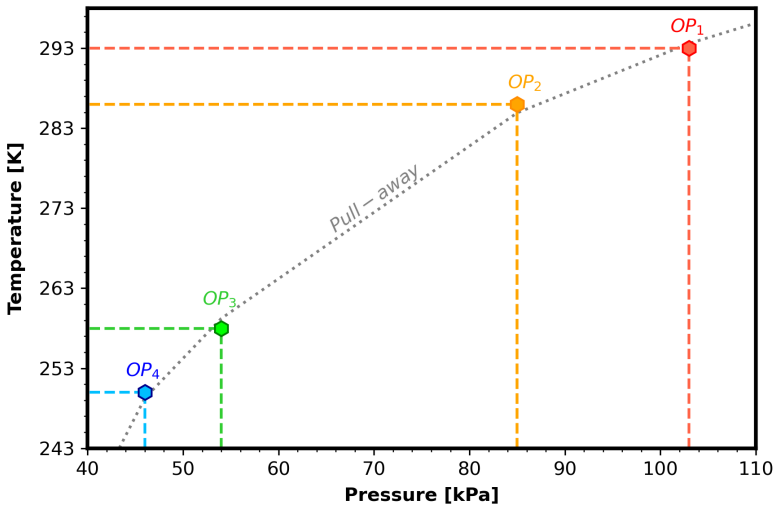

Figure 5.6 Graphical representation of the operating points in HARTur facility.

The methodology used to determine the operating limits is as follows: once the flame is established inside the combustion chamber, the air and fuel temperatures in the intake plenum are controlled according to the operating condition set point. Then, the pressure inside the combustion chamber is also adjusted according to its set point. Then, the mass flow rate for air and fuel are set to their nominal values; see Table 5.1 for kerosene. The next step is to progressively decrease the mass flow rate of the fuel, keeping the primary air and the dilution air flow rates constant.

Data is simultaneously acquired for subsequent exploitation during this progressive decrease in the fuel flow rate. Figure 2.8, shown in Chapter 2, shows data acquisition via LabView during kerosene combustion at OP_1 operating conditions. This process of decreasing the mass flow of the fuel is carried out until the flame extinction is reached. Figure 5.7 is a graphical representation of this process, where we have represented the different operating points.

The nominal mass flow rates presented in Table 5.1 correspond to the fuel-air ratios for kerosene that nominal combustion. However, since BL has a molecular structure different from kerosene, the fuel-air ratios for BL that provide the same combustion efficiency may differ. For this reason, instead of using mass flow rates for our assessments and comparisons, we will rely on the fuel-air equivalence ratio ϕ.

The equivalence ratio ϕ is the ratio between the oxygen content in the air supplied and the required for the complete stoichiometric combustion; it can be calculated by using Equation 5.1.

$$\phi = \frac{\text{fuel-to-air ratio}}{(\text{fuel-to-air ratio})_{st}} = \frac{\dot{m}_{fuel}/\dot{m}_{air}}{(\dot{m}_{fuel}/\dot{m}_{air})_{st}} = \frac{\dot{n}_{fuel}/\dot{n}_{air}}{(\dot{n}_{fuel}/\dot{n}_{air})_{st}} \tag{5.1}$$

Where $\dot{m}$ is the mass flow rate, $\dot{n}$ is the molar flow rate, and the subscript "st" stands for stoichiometric conditions. The advantage of using the equivalence ratio is that it considers both mass and molar values for the fuel and oxidizer.

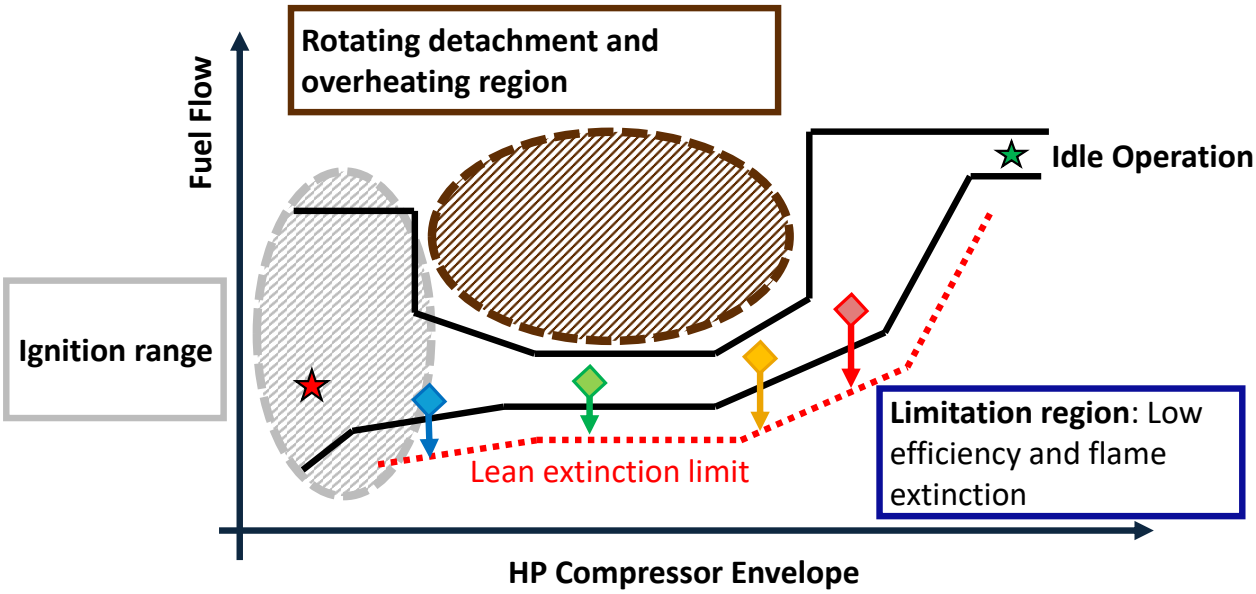

Figure 5.7 Representation of the dosing rule with operating points and extinction limit curve. Diamonds represent the operating conditions shown in Table 5.1

Then, our methodology to determine the operating limits for the different fuels (Kerosene and BL) will keep the primary and dilution air mass flow rates constant, as shown in Table 5.1 for the different operating conditions. However, instead of starting from a nominal fuel mass flow rate, we will start from a nominal equivalence ratio, from which the fuel mass flow rate will be defined. Thus, this nominal equivalence ratio progressively decreases until the flame extinction is reached.

The assessment of BL as a kerosene additive was performed at the operating conditions OP_1 (293 K and 103 kPa) and OP_3 (258 K and 54 kPa), for which the nominal equivalence ratio was set at 0.6 and 0.7, respectively. At these operating conditions, we determined the operating limits, analyzed the atomization spray, and analyzed the flame structure. All these are for different blend ratios of kerosene and butyl levulinate. The blends Kero/BL used for these analyses are described in the next section.

5.2 Physical Properties

As we already discussed, the performance of a gas turbine depends largely on the physical properties of the fuel, mainly the viscosity, which is driven by temperature and can affect the quality of the atomization. Our combustion assessment was done for different blends to assess butyl levulinate (BL) as a kerosene additive. These blends are 1) Pure kerosene, 2) 50% kerosene and 50% BL, 3) 80% kerosene and 20% BL, and 4) Pure BL.

Figure 5.8a shows that BL and kerosene are miscible at the different proportions considered and that, in all cases, they form a transparent solution at normal pressure and temperature conditions. In some cases, the physical properties depend on mass fractions or volume fractions. To pass from volume fraction to mass fraction and vice versa, we have used Equations 5.2 and 5.3, respectively.

$$x_i^{mass} = \frac{x_i^{vol} \cdot \rho_i}{\sum_i x_i^{vol} \cdot \rho_i} \tag{5.2}$$

$$x_i^{vol} = \frac{x_i^{mass}/\rho_i}{\sum_i x_i^{mass}/\rho_i} \tag{5.3}$$

Although most of the physical properties of kerosene and BL are available in the literature, more information is needed regarding the blends of these two compounds. In this section, we measured some properties that may affect the combustion process. We verified if we could predict the properties of the different blends by using the properties of the pure compounds and the corresponding mixing rule.

An important property of fuels, which is not physical, is the energy released during combustion, in other words, the lower heating value (LHV). To determine the lower heating value (LHV) of each blend, we have used the *Parr Bomb Calorimeter*. The results obtained are shown in Table A.11 and Figure 5.8. The first thing we can see is that the LHV of BL is 35% lower than kerosene and that the heating value of kerosene is reduced by 9% and 21% in the blends Kero/$BL_{80/20}$ and Kero/$BL_{50/50}$, respectively. From these results, we can also note that the mixing rule for LHV (Equation 5.4) predicts very well the experimental results.

$$LHV_{mix} = \sum_i x_i^{mass} \cdot LHV_i \tag{5.4}$$

Table 5.2 Lower Heating Values (LHV) of the Blends Kerosene/BL.

$\mathbf{x}_{Kero}^{vol}$	$\mathbf{x}_{BL}^{vol}$	$\mathbf{x}_{Kero}^{mass}$	$\mathbf{x}_{BL}^{mass}$	LHV_{exp} [MJ/kg]	STD	$LHV_{MixRule}$ [MJ/kg]
0.00	1.00	0.00	1.00	29.2	0.2	29.2
0.50	0.50	0.46	0.54	35.7	0.5	36.5
0.80	0.20	0.77	0.23	41.4	0.6	41.6
1.00	0.00	1.00	0.00	45.3	0.3	45.3

Other important properties are density, which helps to determine the energy content in the fuel tank, viscosity, and surface tension, which greatly influence the quality of atomization in the injection system. The density and viscosity of the different blends were measured in the *Stabinger Viscometer*. Due to the limitations of the equipment, these properties were measured in a temperature range between 263 K-293 K. On the other hand, the surface tension was measured in a temperature range between 273 K-293 K in the *Tensiometer TVT 2* equipment. We have applied the mixing rule for density, Equation 5.5, and the Arrhenius rules [119] for viscosity, Equations 5.6 and 5.7.

$$\rho_{mix} = \sum_i x_i^{vol} \cdot \rho_i \tag{5.5}$$

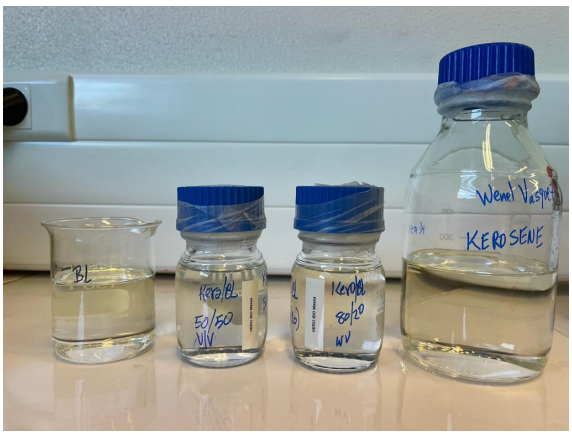

(a) Pure BL, Kero/$BL_{50/50}$, Kero/$BL_{80/20}$ and pure kerosene, respectively.

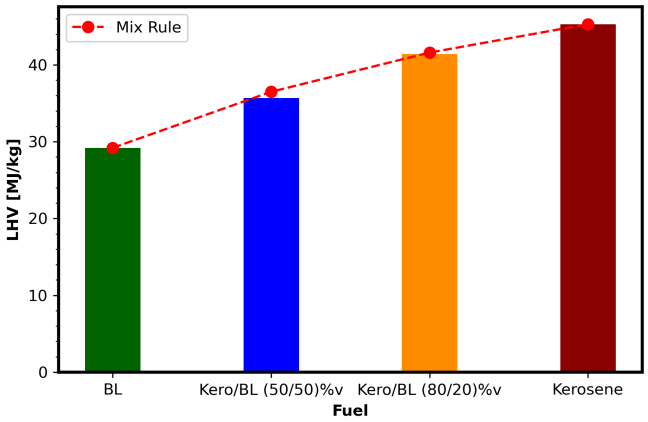

(b) LHV of the blends.

Figure 5.8 Blends for the combustion assessment and the corresponding lower heating value (LHV).

$$\ln(\mu_{mix}) = \sum_i x_i^{vol} \cdot \ln(\mu_i) \tag{5.6}$$

$$\ln(\nu_{mix}) = \sum_i x_i^{vol} \cdot \ln(\nu_i) \tag{5.7}$$

The results obtained from these measurements are shown in Figure 5.9, and the numerical values can be found in Appendix A.2. The first thing we can notice is that the mixing rules predict the physical properties in the temperature range analyzed with great accuracy. Regarding density, we realize a notable difference between the blends, with the lowest being the kerosene one and the highest being BL. This property is not significantly affected by temperature in any blend; based on this, we can assume that the volume of the blends does not vary significantly, and therefore, the volume fractions do not vary significantly either. Surface tension is another property that exhibits constant behavior in the study range.

On the other hand, regarding viscosity, Figure 5.9c and 5.9d, we can notice that there is a significant difference and that this difference becomes more important as the temperature decreases. We can see that pure BL has the highest viscosity of all the blends and that kerosene has the lowest. In general, we can realize that the Kero/$BL_{80/20}$ blend has the closest physical properties to kerosene and behaves similarly with the temperature. The significant increase in viscosity at low temperatures will negatively impact the atomization in the injection system and, consequently, the combustion efficiency. Therefore, it is expected that there will be notable differences in the combustion process for the different blends at low temperatures.

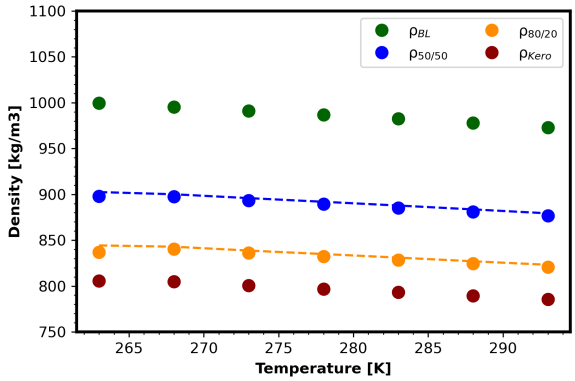

(a) Density vs Temperature.

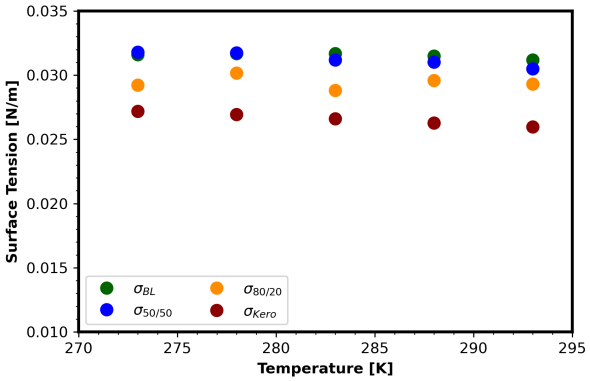

(b) Surface Tension vs Temperature.

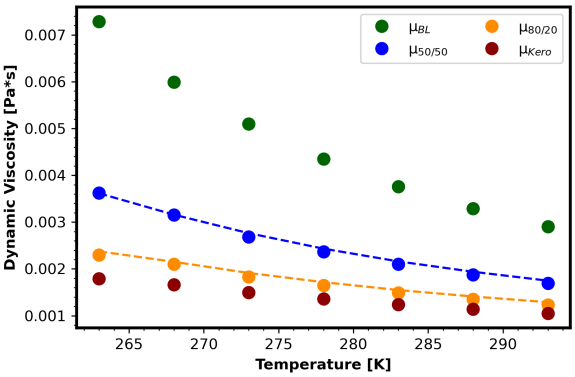

(c) Dynamic Viscosity vs Temperature.

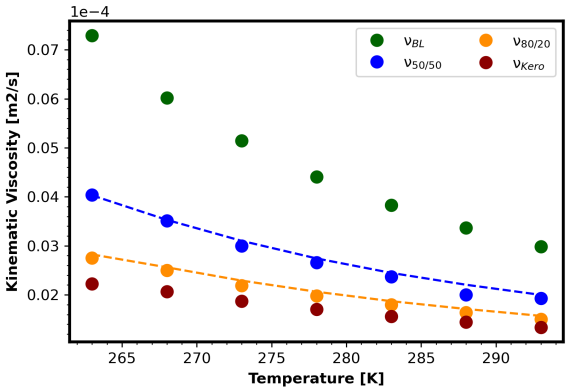

(d) Kinematic Viscosity vs Temperature.

Figure 5.9 Physical properties evolution with temperature for the different blends Kero/BL, dashed lines correspond to the mixing rules.

5.3 Combustion Efficiency

The combustion efficiency is a key parameter that can be used to assess the conversion of the chemical energy available in the fresh gases (reactants) into thermal energy in the burned gases. Let us consider a combustion process between a fuel and oxidizer that are initially at temperature T_0; the energy level of these reactants (h_R) is a temperature-dependent function. The burned gases issued from the combustion are at a final temperature T_f, and its energy level h_P is also a function that depends on the temperature. When combustion is complete, i.e., there are no unburned compounds, and chemical equilibrium is reached. The final temperature of the burned gases is the equilibrium temperature T_f^{eq}, and its energy level is represented by h_P^{eq}.

Figure 5.10 is a graphical representation that will help us understand the concept of combustion efficiency. This figure shows the energy level of the h_R reactants (in blue), the energy level of the products h_P (in purple), and the energy level of the products when combustion is complete, and equilibrium is reached h_P^{eq} (in red). Equation 5.8 gives any mixture of burned gases energy level. Where n_k is the number of moles of species k in the global chemical reaction, h_k^m is the molar enthalpy of species k, and h^m is the molar enthalpy of the gasses in units of energy per mole of fuel.

$$h^m = \sum_{k=1}^{N} n_k h_k^m \tag{5.8}$$

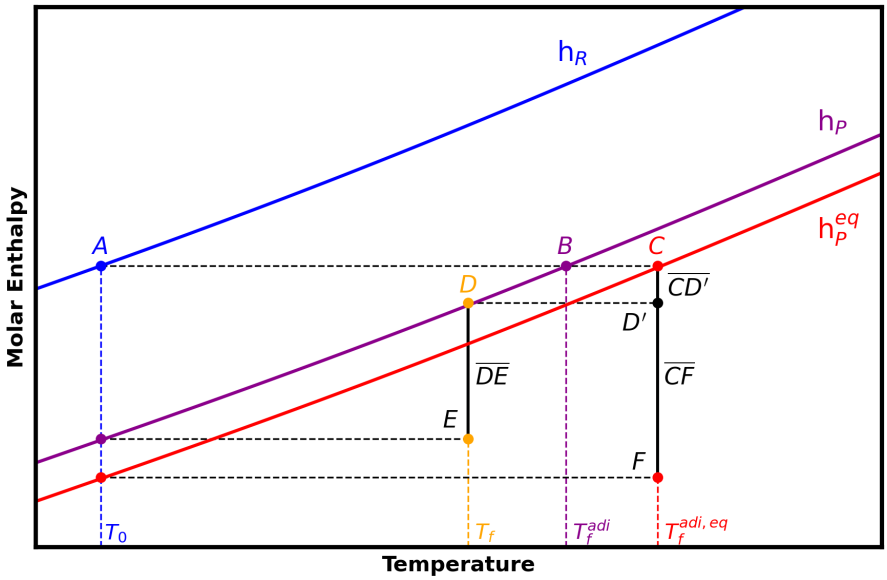

Figure 5.10 Representation of the molar enthalpy as a function of the temperature.

If we consider our combustion process following the different points marked in Figure 5.10, the initial state of the reactants at temperature T_0 is represented by point A. When the combustion process occurs under adiabatic conditions, i.e., there is no energy loss to the surroundings, the energy level of the burned gases at the temperature T_f^{adi} is represented by point B. If, in addition to adiabatic conditions, we have complete combustion and chemical equilibrium is reached, then the energy level of the burned gases is represented by point C. These gases are at the $T_f^{adi,eq}$ temperature, which is the maximum temperature that can be reached via the combustion of reactants at T_0. However, when there are neither adiabatic conditions, complete combustion, nor chemical equilibrium, the energy level of the burned gases is represented by point D, and these gases are at the final temperature T_f.

Based on the definition of combustion efficiency, it can be defined as the ratio between the thermal energy of the products, which is represented by the segment $\overline{DE}$, and the maximum energy that can be obtained during the combustion process, which is represented by the segment $\overline{CF}$). Equation 5.9 is the mathematical expression to calculate combustion efficiency. The segment $\overline{CD'}$ represents the energy losses during the non-adiabatic combustion process.

$$\eta_{comb} = \frac{\overline{DE}}{\overline{CF}} = \frac{h_P(T_f) - h_P(T_0)}{h_P^{eq}(T_f^{adi,eq}) - h_P(T_0)} \tag{5.9}$$

From these molar enthalpies of burned gases, the corresponding temperatures can be identified: the equilibrium temperature for adiabatic and complete combustion $T_f^{adi,eq}$, the temperature for non-complete but adiabatic combustion T_f^{adi}, and the temperature of burned gases for non-complete and non-adiabatic combustion T_f, this latter is measured downstream the combustion chamber in the nozzle section, Figure 5.11.

The experimental measurement of the molar enthalpy of fresh and burned gases is quite a complex task. For this reason, instead of using the molar enthalpies to calculate the combustion efficiency, we decided to approximate the combustion efficiency using the temperatures involved in the process. Equation 5.10 is the mathematical expression used to calculate combustion efficiency considering the temperatures. This approximation is possible because the heat capacity of the gas mixture is more or less constant since 70% of the mixture is nitrogen, $\Delta h = \int C_p dT \cong \overline{C_p}\Delta T$. Consequently, Equation 5.10 is not an absolute measurement of combustion efficiency but a valid relative approximation to compare different fuels and operating conditions.

$$\eta_{comb} \cong \frac{T_f - T_0}{T_f^{adi,eq} - T_0} \tag{5.10}$$

The inlet temperature of fresh gases T_0 is measured with a type K thermocouple. The equilibrium and adiabatic temperature of burned gases $T_f^{adi,eq}$, from now on, the equilibrium temperature, is calculated with Cantera library in Python from the inlet and operating conditions (pressure, temperature, and equivalence ratio). The burned gases temperature, T_f, cannot be well measured with a thermocouple due to the inhomogeneities (in terms of the temperature inside the combustion chamber), the two-phase medium, and the high temperature inside the combustion chamber. Therefore, the measurement of T_f relies on the use of a non-sonic nozzle placed downstream of the chamber. The pressure drop across the nozzle is measured, and the mean temperature of the burned gases crossing the nozzle can be reported. The details about this methodology are described in the Subsection 5.3.1.

To reduce the heat losses, the combustion chamber is surrounded by a double wall, through which dilution air circulates and is injected into the chamber. As a result, most of the heat escaping from the chamber is captured by the dilution air and thus reintroduced into the combustion chamber. Heat loss is estimated using a wall thermocouple placed on the outer surface of the combustion chamber. The temperature measured by this thermocouple never exceeds 200 °C. At this temperature, in steady-state operation, the heat loss through the walls due to radiation and natural convection is around -440 W [7]. Compared to the energy produced by the flame (40-50 kW), this value is less than 1%. Therefore, it is reasonable to assume that combustion occurs near adiabatic conditions.

5.3.1 Calibration Curve

The calibration curves aim to establish a mathematical relation between the pressure drop across the nozzle downstream of the combustion chamber and the average temperature of the burned gases passing through it. The following methodology was developed in the M. Clavel thesis [7] and is reminded here for the sake of clarity.

The mass flow rate $\dot{m}$, crossing the nozzle can be obtained from Bernoulli's theorem extended to weakly compressible fluids, Equation 5.11:

$$\dot{m} = \frac{C(\beta, Re_D)}{\sqrt{1-\beta^4}} \varepsilon(\gamma, \tau, \beta) \frac{\pi d^2}{4} \sqrt{2\Delta P \rho} \tag{5.11}$$

The quantities involved in Equation 5.11 are:

- The nozzle geometrical parameters: the nozzle outlet diameter d, the inlet diameter D and the opening ratio $\beta = d/D$.
- The properties of the flow: the density ρ, the pressure in the combustion chamber P and the Laplace coefficient γ of burned gases at T_f.
- The pressure drop across the nozzle ΔP.
- The expansion coefficient ε, that is a function of the Laplace coefficient γ, the pressure ration $\tau = (P - \Delta P)/P$ and β.
- The discharge coefficient C, that is a function of β and the Reynolds number Re_D. C is defined empirically in the European standards [120] for a given nozzle geometry and under certain conditions of Reynolds and pressure.

If assumptions of ideal gas behavior, stationary conditions, non-rotational and homogeneous flow, reversible adiabatic compression, and circular inlet section of the nozzle are made, the temperature of the burned gases T_f can be deduced from the pressure drop measurement across the nozzle with Equation 5.12.

$$T_f = 2C^2(\beta, Re_D) \cdot \varepsilon^2(\gamma, \tau, \beta) \cdot \frac{1}{r} \cdot \frac{\pi^2 d^4}{16(1-\beta^4)} \cdot \frac{\Delta P \cdot P}{\dot{m}^2} \tag{5.12}$$

Experimentally, all the assumptions made to obtain Equation 5.12 are not verified. Therefore, the coefficients $C^2(\beta, Re_D)$ and $\varepsilon^2(\gamma, \tau, \beta)$ cannot be directly calculated. This issue can be overcome by using an experimental calibration, where ΔP is measured under reactive operating conditions for which the temperature of the burned gases is known. From Equation 5.12, we can realize that T_f can be written as an explicit function of K_g and Π, where $K_g = \pi d^2/4\sqrt{1-\beta^4}$ is the geometrical factor of the combustion chamber and $\Pi = \Delta P \cdot P/\dot{m}^2$ is the operating variable. Consequently, the calibration curve of T_f can be fitted by following a second order polynomial, Equation 5.13, where the coefficients a_i were obtained experimentally for all the operating points, i.e., inlet temperature and pressure, that can be achieved in HARTur facility.

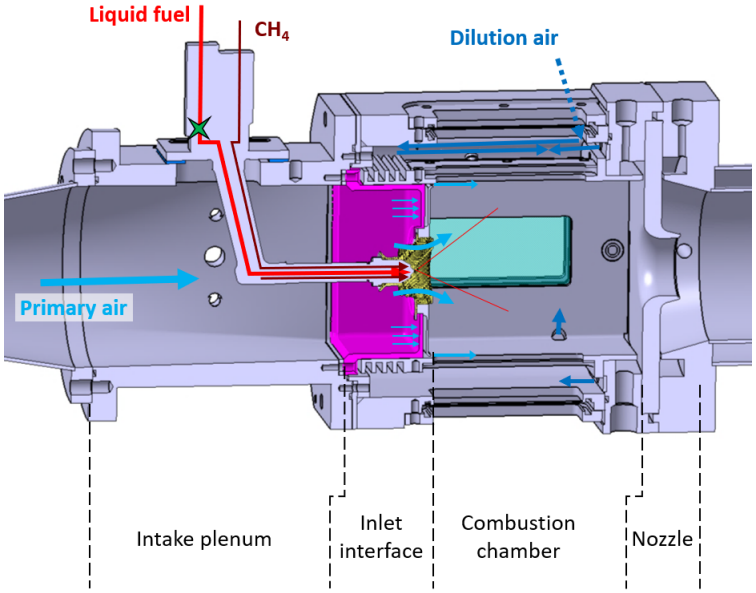

Figure 5.11 Combustion chamber's CAD: sectional view.

$$T_f = a_2(K_g^2 \cdot \Pi)^2 + a_1(K_g^2 \cdot \Pi) + a_0 \tag{5.13}$$

This calibration curve must be reported under conditions where the temperature of burned gases is known, and the same fuel injection system is used. To meet this constraint, n-heptane was used as fuel to report the calibration curves at the different operating points of pressure and temperature. N-heptane has a very high volatility compared to kerosene [121] and a similar Lower Heating Value (LHV=44.56 MJ/kg) [122].

For a standard inlet temperature T_0 and different pressure P in the combustion chamber, the combustion efficiency for n-heptane is expected to be near 1 and combustion to be complete. Thus, the temperature of burned gases T_f can be calculated from chemical equilibrium simulation with Cantera [123], using Polimi's detailed reaction mechanism for n-heptane oxidation, which includes 156 species and 3465 elementary reactions [124].

To verify these assumptions, Laser tomography imaging was performed to verify that the n-heptane drops were completely vaporized before the nozzle [7]; results showed that for all pressures and equivalence ratios, all the fuel droplets are evaporated in the first 3 cm of the chamber. In addition, *HORIBA PG-250* gas analyzer was used to measure the burned gas composition at the nozzle for ambient pressure to report the CO mole fraction. CO is an intermediate almost completely oxidized when chemical equilibrium is achieved in lean conditions. Therefore, it is a good indicator for determining when equilibrium is reached. The relation between the CO concentration and the temperature of the burned gases can be obtained from a 1D freely propagating flames analysis with Polimi's mechanism in Cantera.

Figure 5.12a shows the CO and the temperature evolution during the n-heptane oxidation; thus, based on the CO concentration, it is possible to determine how far is the burned gases temperature from the equilibrium one. For different equivalence ratio ϕ, CO concentration was measured and reported in Figure 5.12b, where the evolution of CO is plotted versus the difference between the temperature at which CO exists in a 1D premixed flame and the equilibrium temperature. The experimental values of CO concentration are below 1000 ppm, indicating that the difference between the burned gases temperature and the equilibrium temperature is less than 1% for n-heptane, Figure 5.12b. Thus, it is reasonable to calibrate the nozzle by using n-heptane and by assuming that $T_f = T_f^{adi,eq}$ which can be numerically obtained.

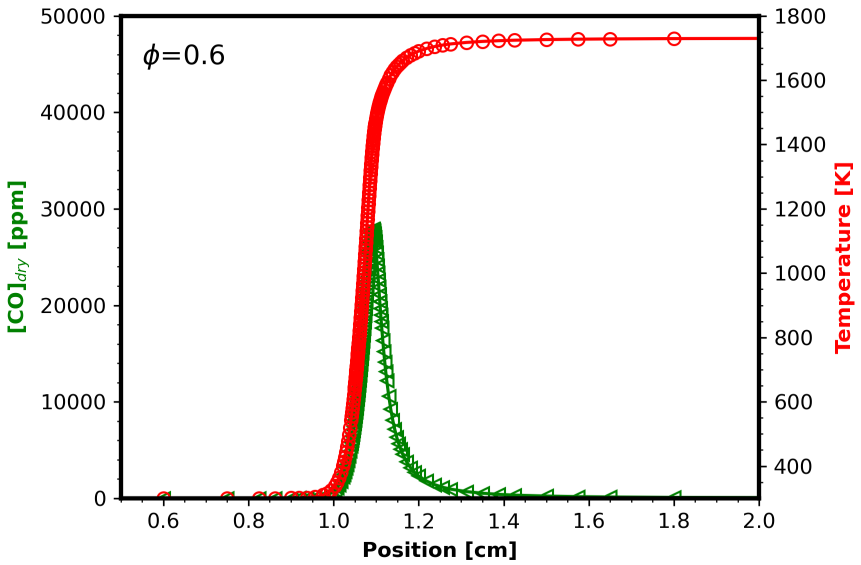

(a) 1D n-heptane computational flame for ϕ=0.6.

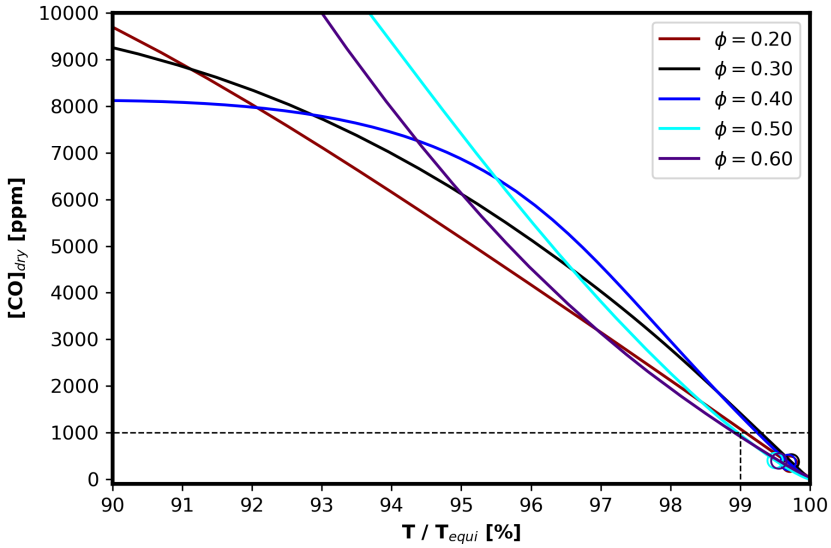

(b) CO concentration vs $T_f/T_f^{adi,eq}$.

Figure 5.12 1D freely propagating premixed flame of n-heptane: the relationship between CO concentration and burned gases equilibrium temperature.

Due to the limited pressure range of the pressure sensor placed to measure the pressure drop across the nozzle, ΔP_{max}=3000 Pa, two different nozzles were designed and built to optimize the sensibility of the measurements in the combustion chamber: *(i)* the nozzle N1 with d=33 mm, suitable for operating pressures near to the ambient pressure, 103 kPa and 85 kPa and *(ii)* the nozzle N2 with d=42 mm, suitable for low operating pressures, 54 kPa and 46 kPa. These nozzles were built according to the ISO 5167-3 standard specifications ISA 1932.

All the calibration curves were recalculated during this thesis; the results are reported in Figure 5.13. Nozzle N1 whith d=33 mm was used for OP_1=(103 kPa, 293 K) and OP_2=(85 kPa, 286 K), while N2 with d=42 mm was used for OP_3=(54 kPa, 258 K) and OP_4=(46 kPa, 250 K). The corresponding second-order polynomial for the operating conditions is presented in Equations 5.14 - 5.17.

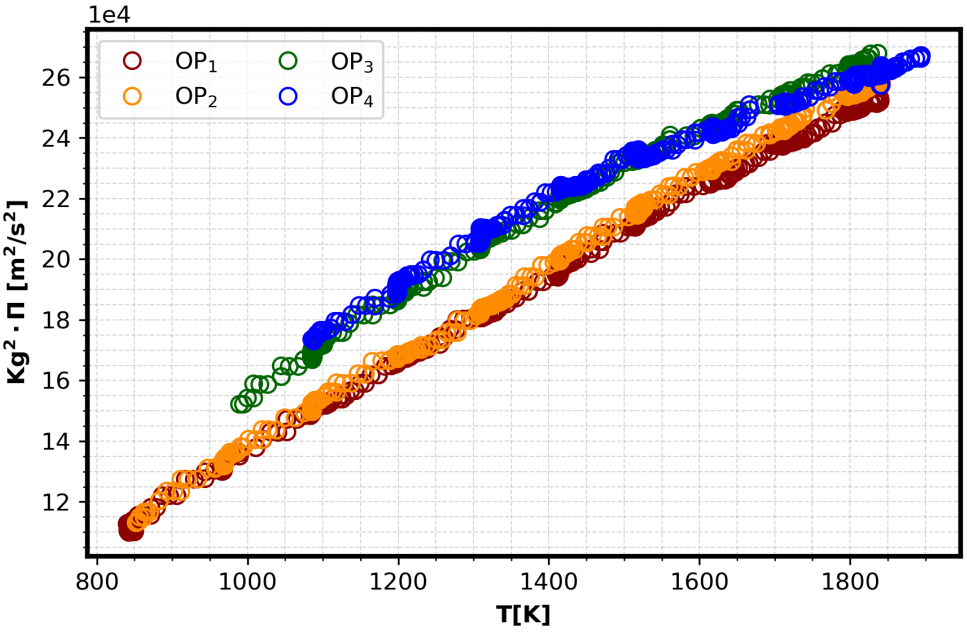

Figure 5.13 Calibration curves results.

$$T_f^{OP_1} = 5.0 \times 10^{-9}(K_g^2 \cdot \Pi)^2 + 0.0050(K_g^2 \cdot \Pi) + 217.45 \tag{5.14}$$

$$T_f^{OP_2} = 4.0 \times 10^{-9}(K_g^2 \cdot \Pi)^2 + 0.0053(K_g^2 \cdot \Pi) + 198.01 \tag{5.15}$$

$$T_f^{OP_3} = 3.0 \times 10^{-8}(K_g^2 \cdot \Pi)^2 - 0.0039(K_g^2 \cdot \Pi) + 988.54 \tag{5.16}$$

$$T_f^{OP_4} = 5.0 \times 10^{-8}(K_g^2 \cdot \Pi)^2 - 0.0133(K_g^2 \cdot \Pi) + 1939.5 \tag{5.17}$$

The uncertainty of the pressure gauge Rosemount used to measure the pressure drop across the nozzle in the combustion chamber is 3.0 Pa. In addition, for each calibration point of Nozzle N1, the fluctuation is on the order of 5.0 Pa; for Nozzle N2, fluctuations are close to 10.0 Pa. These pressure fluctuations reported in temperature fluctuations give a variation of 5.0 K for all the operating conditions.

5.3.2 Reaction Mechanism

We have already seen that to calculate the combustion efficiency η_{comb}; we need a way to determine the adiabatic temperature at equilibrium $T_f^{adi,eq}$. A reaction mechanism is a detailed process that shows the different transformation stages that reactants follow to be transformed into products. These mechanisms are based on experimental data like measurements of species profiles, measurement of the burned gases temperatures in 1D flames, measurements of 1D flame speed, measurements of auto-ignition delay time, etc.

Reaction mechanisms are valuable tools mainly used for computational fluid dynamics or CFD. However, we mainly focus on the equilibrium temperature. It should be noted that in our case, we focus on calculating the equilibrium temperature of burned gases. To do so, we used the Cantera library in Python with the corresponding reaction mechanism. The calculation of the equilibrium temperature is based on the second law of thermodynamics, i.e., minimizing the free Gibbs energy. Below, we explain how the Kerosene and BL reaction mechanisms were obtained.

Kerosene

The reaction mechanism for kerosene's combustion has been a case study for a long time. Thanks to this, several reaction mechanisms for its combustion are available in the literature. Kerosene is a mixture mainly of paraffin, iso-paraffins, naphthenes, and aromatic compounds, as shown in Table 1.1. Its proportions vary slightly depending on the source of the kerosene and its refining process. Dealing with the kinetics of each of the chemical compounds that make up kerosene is an arduous task. For that reason, to study the combustion kinetics of kerosene, a surrogate is usually used to represent all the compounds it contains.

An example of this is the mechanism developed by Dagaut et al. [125], which is a detailed reaction mechanism that considers that kerosene's composition is the following: 74% n-decane, 15% n-propylbenzene and 11% n-propylcyclohexane. Based on these three compounds, they developed a mechanism that consisted of 209 species and 1673 reversible reactions.

Another example is the reaction mechanism developed by Luche [126], who proposed a semi-detailed mechanism that accounts for 91 species and 991 reactions. This mechanism considers that kerosene can be represented as a n-decane molecule ($C_{10}H_{22}$). The overall reaction for Luche's surrogate is given by Equation 5.18.

$$C_{10}H_{22} + 15.5(O_2 + 3.76N_2) \rightarrow 10CO_2 + 11H_2O + 58.28N_2 \tag{5.18}$$

On the other hand, there are global mechanisms such as the one proposed by Franzelli et al. [127], which is a two-step global mechanism for the combustion of kerosene. This mechanism, also known as BFER, only includes two chemical reactions and assumes that kerosene can be represented by the chemical compound n-decene ($C_{10}H_{20}$). The two reactions of this mechanism are shown in Equations 5.19 and 5.20.

$$C_{10}H_{20} + 10O_2 \rightarrow 10CO + 10H_2O \tag{5.19}$$

$$CO + 0.5O_2 \leftrightarrow CO_2 \tag{5.20}$$

The reaction mechanisms mentioned before were used to calculate the equilibrium temperature $T_f^{adi,eq}$ for premixed fresh gases of kerosene and air at different equivalence ratios ϕ. The results obtained are shown in Figure 5.14. This figure shows that Dagaut's and Luche's mechanisms give the same result for all the values of ϕ. However, the two-step BFER mechanism gives the same value of equilibrium temperature for $\phi \leq 0.75$.

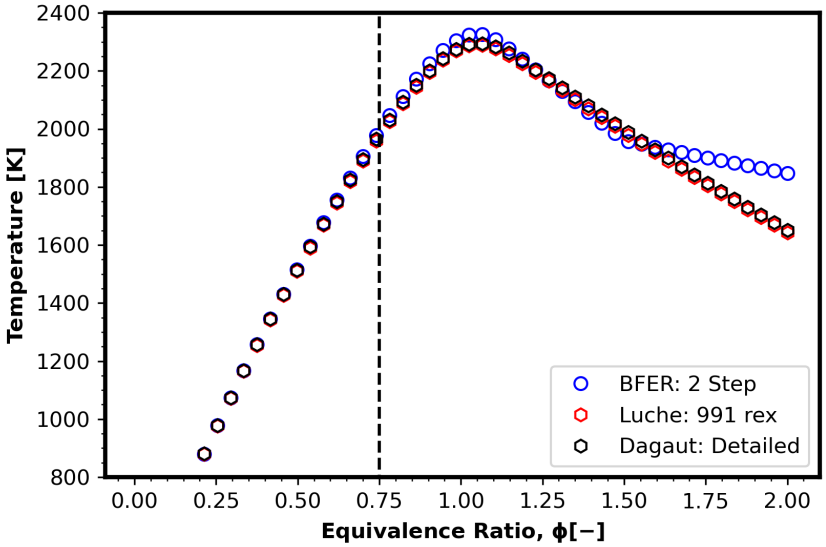

Figure 5.14 Kerosene equilibrium temperature versus equivalence ratio.

Butyl Levulinate

Currently, there is not much information available in the literature about the combustion of butyl levulinate. Therefore, it was not possible to obtain a reaction mechanism that has been validated experimentally. To calculate the equilibrium temperature of butyl levulinate, we have considered two approaches:

1. *1^{st} law of thermodynamics*: This principle consists of fixing the composition of burned gases and considering that all the energy coming from combustion is used to raise the temperature of the burned gases. Here, it is considered that the only products coming from combustion are CO_2 and H_2O; solving Equation 5.21, we can determine the temperature of the burned gases. The temperature obtained with this approach is the maximum temperature that could be obtained as a result of the combustion since there are no unoxidized species in the burned gases, such as CO.

$$\int_{T_0}^{T_f} \sum_k n_k C_{p_k} dT = \Delta H_{comb,T_0} = LHV_{fuel} \tag{5.21}$$

2. *2^{nd} law of thermodynamics*: This approach is based on the calculation of chemical equilibrium, which consists of determining the concentration of the burned gases for which the variation in the free Gibbs energy is cero ($\Delta G = 0$). Such calculation requires a reaction mechanism. In order to generate a reaction mechanism for the BL, we used the Reaction mechanism generator (RMG), which is an object-oriented program written in Python that constructs kinetic models composed of elementary chemical reaction steps using a general understanding of how molecules react [128].

   RMG can generate reaction mechanisms for species involving carbon, hydrogen, oxygen, sulfur, and nitrogen. Species thermo-chemistry is estimated through Benson group additivity, and reaction rate coefficients are estimated incorporating and extrapolating thermochemical and kinetic parameters from databases [129].

Ghosh et al. [130] studied the combustion kinetic of ethyl levulinate (EL), which is from the same family of levulinates as BL. They developed a reaction mechanism that describes the combustion process of EL with air, which involves 1426 species and 9867 reactions. We have used this mechanism to calculate the equilibrium temperature of EL for different equivalence ratios, and these results were used to validate the two approaches described above.

To develop reaction mechanisms for the combustion of EL and BL using the RMG program, we have incorporated the "*primaryThermoLibrary*" and "*GRI-Mech3.0*" databases. These databases contain the main elementary and intermediate reactions for molecules formed by carbon, hydrogen, and oxygen atoms. As a result, we obtained a reaction mechanism for EL that contains 85 species and 888 reactions, and for BL, we obtained a mechanism that involves 110 species and 1223 reactions.

It should be noted that the reaction mechanisms obtained were not experimentally validated; the only validation performed was for the calculation of the burned gases' equilibrium temperature. Other types of validation, such as those related to flame speed and species concentration, remain as a perspective of this work.

Figure 5.15 shows the results obtained from both approaches. Results show that the temperatures obtained for EL using RMG and Ghosh et al. mechanism were the same. We can note that the RMG results for BL show the same trend as those for EL. Also, we can confirm that results from the 1^{st} law of thermodynamics are the highest ones. However, the difference for small values of ϕ is not very significant. Equations 5.22 and 5.23 illustrate the chemical reactions considered to apply the first approach for EL and BL when ϕ=1.0, respectively.

$$C_7H_{12}O_3 + 8.5(O_2 + 3.76N_2) \rightarrow 7CO_2 + 6H_2O + 31.98N_2 \tag{5.22}$$

$$C_9H_{16}O_3 + 11.5(O_2 + 3.76N_2) \rightarrow 9CO_2 + 8H_2O + 43.26N_2 \tag{5.23}$$

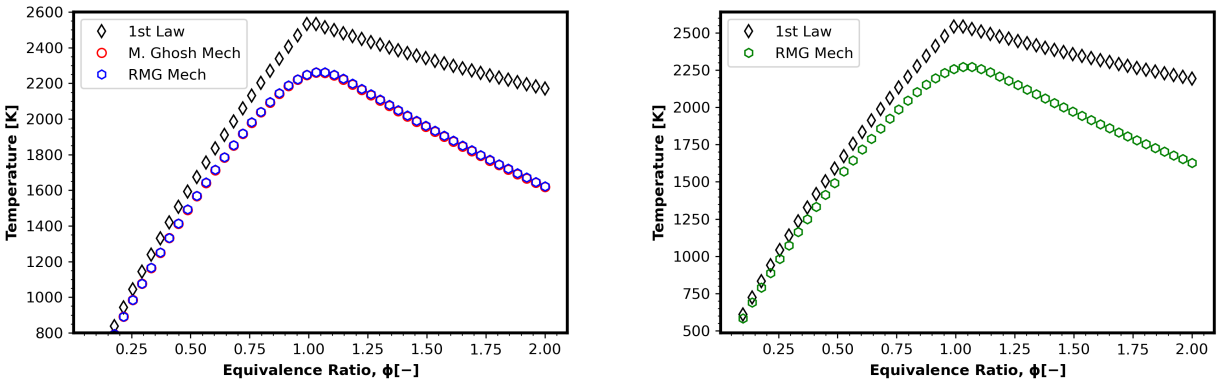

(a) EL $T_f^{adi,eq}$ vs ϕ.

(b) BL $T_f^{adi,eq}$ vs ϕ.

Figure 5.15 Elthyl Levulinate and Butyl Levulinate equilibrium temperatures versus equivalence ratio.

Blends Kerosene/Butyl Levulinate

Finally, we aim to obtain a reaction mechanism to calculate the equilibrium temperature $T_f^{adi,eq}$ of burned gases from the combustion of Kerosene/BL blends. For safety reasons, in the HAR-Tur facility, combustion is carried out at equivalence ratios $\phi \leq 0.7$ to ensure that the burned gases temperatures are below the thermal resistance limit of the facility. The global two-step BFER mechanism is the simplest one that allows an accurate calculation of the equilibrium temperature of kerosene.

In order to calculate the equilibrium temperature of any blend Kero/BL, we have added the two chemical reactions of the BFER mechanism to the BL reaction mechanism obtained from the RMG program. Thus, the resulting mechanism with 111 species and 1225 reactions, called RMG+BFER, can be used to calculate the equilibrium temperature of any blend Kero/BL.

Our interest in these reaction mechanisms is limited to calculating equilibrium temperature $T_f^{adi,eq}$ of the burned gases issued from the combustion. That is why, in order to validate the RMG+BFER mechanism, we have calculated the equilibrium temperature for a mixture of burned gasses coming from the combustion of pure kerosene with air, and we compared this result with the results obtained with all the reaction mechanisms discussed in this subsection.

Figure 5.16 shows the equilibrium temperature obtained from BFER, Luche, Dagaut, and RMG+BFER mechanisms. Here, we can see that the results obtained from the RMG+BFER mechanism and the ones obtained from the detailed and semi-detailed mechanisms (Dagaut and Luche, respectively) are basically the same, throughout the range of ϕ values. It should be noted that even the differences presented by the BFER mechanism for ϕ values greater than 0.75 were adjusted when it was merged with the RMG mechanism of BL. In conclusion, the RMG+BFER mechanism is a suitable tool for calculating the equilibrium temperature for any blend of Kero/BL.

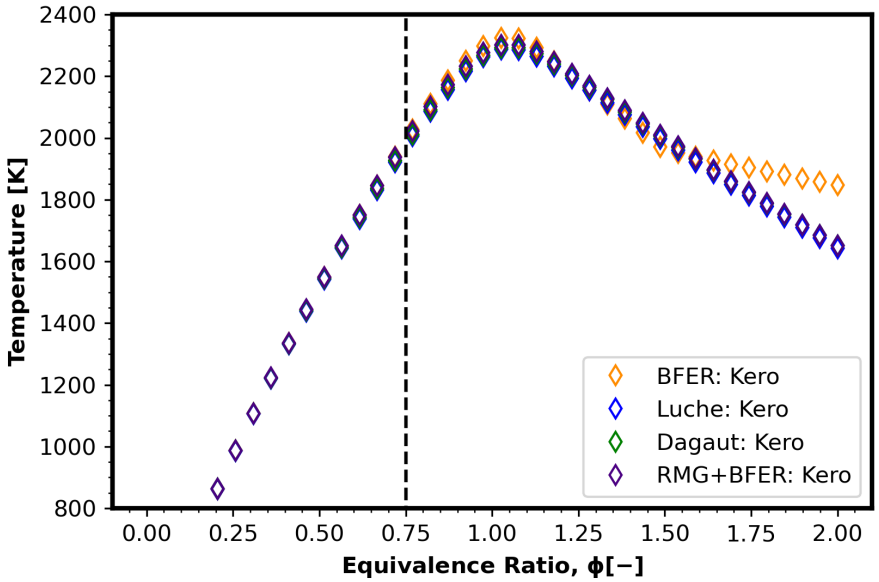

Figure 5.16 Validation of the reaction mechanism to calculate the burned gases equilibrium temperature.

5.3.3 Operating Limits

One of our main objectives is to determine how the operating limits of kerosene are affected when BL is added. Determining the operating limits consists of determining for which values of the equivalence ratio (ϕ) the combustion is complete ($\eta \cong 1$) and the value of ϕ at which there is lean flame extinction. We calculated the operating limits for the four blends Kero/BL at the two operating conditions OP_1 (293 K and 103 kPa) and OP_3 (258 K and 54 kPa).

For each operating point (OP_1 and OP_3), the primary air and dilution air mass flow rates ($\dot{m}_{air,1}$ and $\dot{m}_{air,2}$, respectively) are kept constant and equal to their nominal value shown in Table 5.1. The initial fuel mass flow rate ($\dot{m}_{fuel}$) is fixed according to the nominal value of the equivalence ratio (ϕ) for each operating condition. The nominal ϕ value is 0.6 and 0.7 for OP_1 and OP_3, respectively. Then, starting from the initial fuel mass flow rate, we proceed to its progressive decrease until lean flame extinction is reached.

Figure 5.19 shows the combustion efficiency curve and the extinction limit of pure kerosene obtained at OP_1. The curve obtained from this process can be divided into three different regions, which are:

1. The nominal region, represented by the blue square in Figure 5.19, where combustion efficiency η_{comb} is close to 1. By definition, in this region, the combustion is complete, and the heat losses in the chamber are minimal, as explained previously. Thus, T_f is very close or similar to $T_f^{adi,eq}$. The equivalence ratio for which the combustion efficiency starts to decrease is the critical equivalence ratio ϕ_{crit} and defines the critical point of the combustion efficiency curve. To determine the value of ϕ_{crit}, we do a curve fit with the experimental data, and we set that ϕ_{crit} is the value below which the combustion efficiency is less than 0.95. The curve-fit has been done considering an exponential behavior, so we used the Equation 5.24 for this purpose.

$$\eta_{comb} = 1 - a \cdot \exp(-b \cdot \phi) \tag{5.24}$$

Equation 5.24 can be solve to calculate the value of ϕ_{crit}, for which η_{comb}=0.95, and we obtain as result Equation 5.25.

$$\phi_{crit} = -\frac{1}{b} \ln\left(\frac{1 - \eta_{comb}}{a}\right) \tag{5.25}$$

2. The degraded region is where the combustion efficiency η_{comb} is less than 0.95 before reaching the flame extinction. In this region, the combustion efficiency strongly depends on the equivalence ratio. Here, the combustion is incomplete, and the burned gases crossing the nozzle are composed of unburned products. Consequently, T_f is smaller than $T_f^{adi,eq}$.

3. The extinction limit, given the operating condition of T_0, P, and air flow rate, the extinction limit is the value of the equivalence ratio for which the flame is not stabilized in the combustion chamber, and consequently, the extinction occurs. This one is noted as ϕ_{ext}.

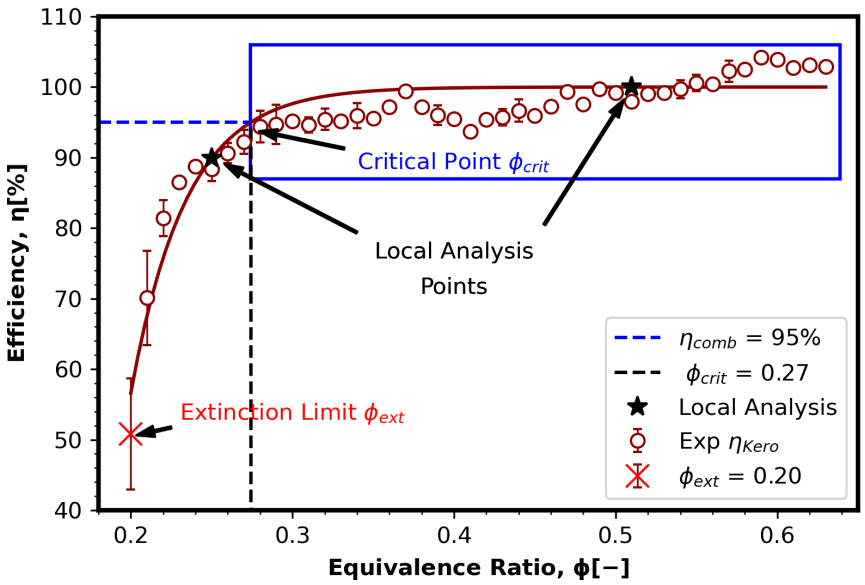

Figure 5.17 Combustion efficiency and extinction limit for kerosene at OP_1 operating conditions.

The black stars in Figure 5.19 are the points used for the local spray/flame analysis regarding the equivalence ratio and combustion efficiency. The local analysis corresponds to atomization spray and flame structure analysis and will be presented in Section 5.4. We decided to perform the local analysis both in the nominal region and in the degraded region in order to compare these results when $\eta_{comb} \cong 1$, and when $\eta_{comb} < 0.95$.

The efficiency curves obtained for the different blends Kero/BL at operating conditions OP_1 and OP_3 are shown in Figure 5.18. From these efficiency curves, it was possible to determine the operating limits of these blends for each operating condition. The values of the critical equivalence ratio and the lean extinction equivalence ratio are summarized in Table 5.3.

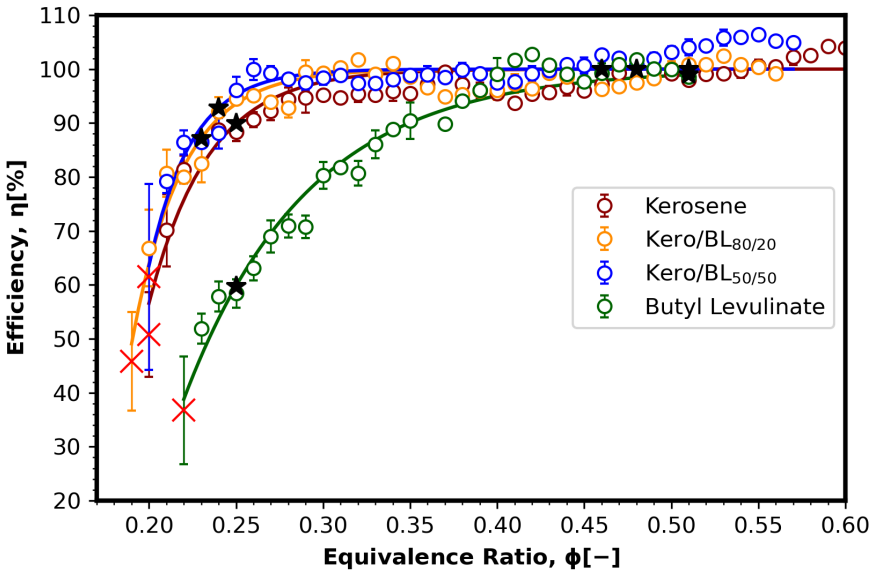

(a) Combustion efficiency versus ϕ at OP_1.

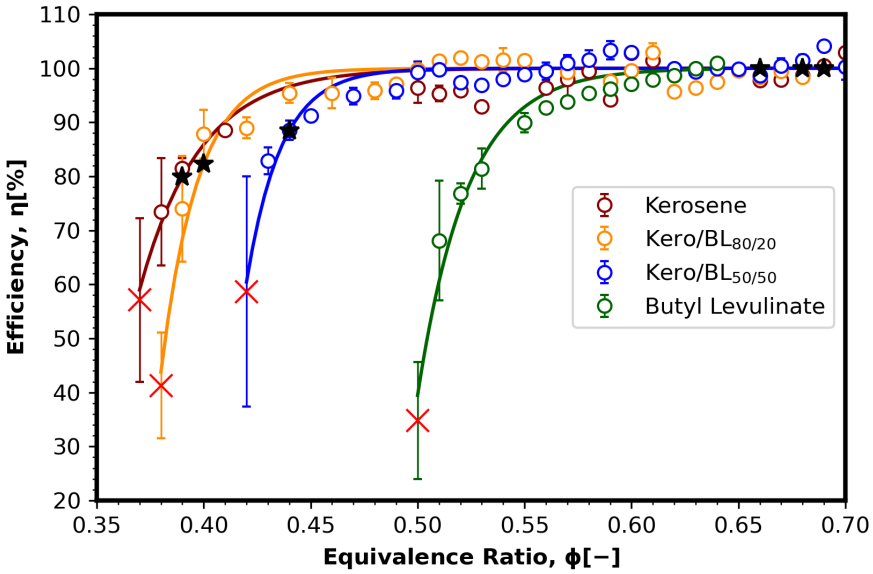

(b) Combustion efficiency versus ϕ at OP_3.

Figure 5.18 Combustion efficiency and extinction limit results for Kero/BL mixtures at OP_1 and OP_3 operating conditions.

From the results obtained at OP_1, Figure 5.18a, we can see that the operating limits for pure kerosene Kero/$BL_{80/20}$ and Kero/$BL_{50/50}$ are very similar. However, the operating limits of pure BL are notably different from others under the same operating conditions. On the other hand, the results obtained at the operating conditions OP_3, Figure 5.18b show that there is an important difference between the operating limits among the different blends Kero/BL.

Pure BL is the fuel with the lowest operability range, and pure kerosene has the highest. These results indicate that combustion efficiency, and therefore operating limits, are affected by the viscosity of fuels. An increase in viscosity decreases the performance of the combustion chamber injection system, and these adverse effects on the injection system are enhanced by decreasing the temperature since a decrease in temperature significantly increases viscosity, as we have already seen in Section 5.2.

Table 5.3 Critical and extinction equivalence ratio for Kero/BL blends at OP_1 and OP_3.

Mixture	OP_1		OP_3	
	ϕ_{ext}	ϕ_{crit}	ϕ_{ext}	ϕ_{crit}
Pure Kerosene	0.20	0.27	0.37	0.43
$Kero/BL_{80/20}$	0.19	0.26	0.38	0.42
$Kero/BL_{50/50}$	0.20	0.25	0.42	0.45
Pure Butyl Levulinate	0.22	0.40	0.50	0.56

The results obtained at the different operating points, i.e., OP_1 and OP_3, can be exploited in different ways. One of them is to construct the operating limit maps as a function of the temperature of the inlet temperature of reactants in the combustion chamber T_0 (it could also be a function of the pressure). We chose temperature because it is the variable that most affects viscosity; Figure 5.19 shows an example of a kerosene operating limit map.

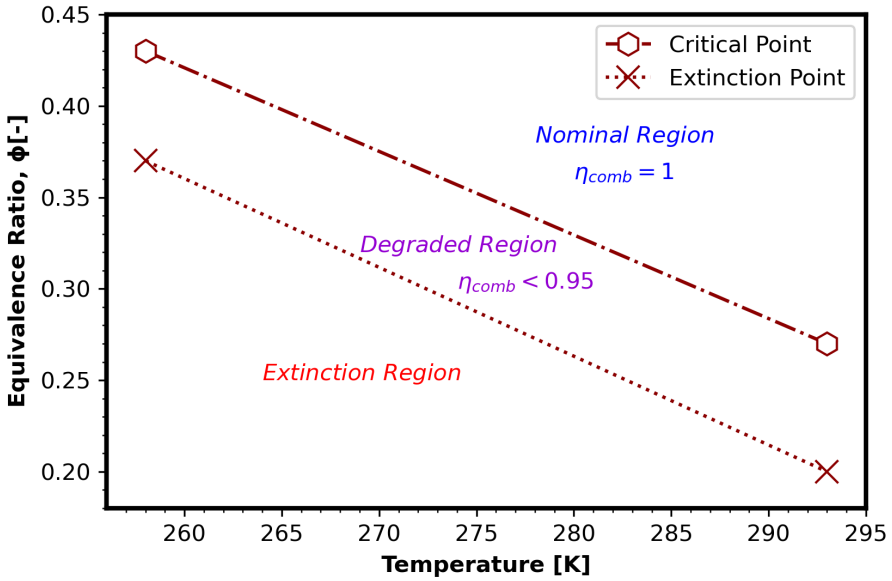

Figure 5.19 Kerosene operating limit map.

From the values in Table 5.3, we constructed the operation maps for the different blend Kero/BL, Figure 5.20. In these maps, we can identify for which combination of global equivalence ratios ϕ and fresh gases temperatures T_0 we would obtain *(i)* $\eta_{comb} \cong 1$, nominal region, *(ii)* $\eta_{comb} < 0.95$, degraded region, and *(iii)* where flame extinction would occur. Figure 5.20 shows that the critical and extinction equivalence ratios increase for all the mixtures when the temperature of the fresh gases decreases. In addition, we can notice that the lower the temperature of the fresh gases T_0, the shorter the degraded region, i.e., the difference between ϕ_{crit} and ϕ_{ext}. This means the lower the temperature, the faster lean extinction will be reached from the critical point.

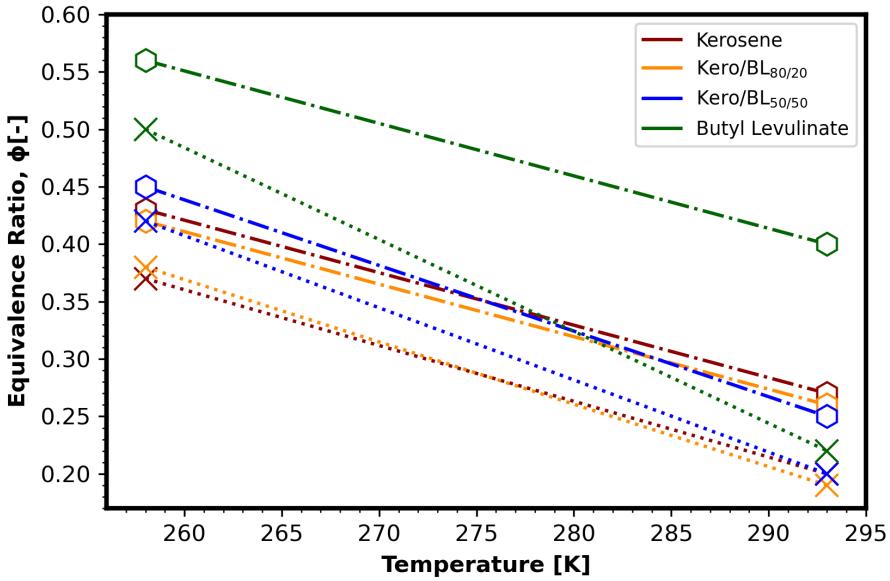

Figure 5.20 Operating limit maps of Kero/BL blends at OP_1 and OP_3 operating conditions.

To construct these operating limit maps, we only had two different temperature points, 258 K and 293 K, which, when joined together, resulted in a line segment. It is important to know that the lines used to join these points do not represent the actual values but rather is a visual aid that allows us to distinguish the three different operating regions for the blends Kero/BL.

As we already know, viscosity is one of the fuel properties that impact combustion efficiency and, therefore, the operating limits. Therefore, it is normal to ask about the relationship that may exist between both the critical and extinction equivalence ratios (ϕ_{crit} and ϕ_{ext}) with the fuel viscosity in a given injection system.

To analyze the possible relationship between the critical equivalence ratio ϕ_{crit} and viscosity ν, we have plotted ϕ_{crit} as a viscosity function ($\phi_{crit} = f(\nu)$), taking into consideration the results obtained with Kero/BL blends at OP_1 and OP_3. These results are shown in Figure 5.21. These results suggest an undefined trend between viscosity and ϕ_{crit}. At OP_1 conditions, we can see that, for pure kerosene, Kero/$BL_{80/20}$ and Kero/$BL_{50/50}$ we have practically the same value of ϕ_{crit}. However, at OP_3 conditions, the data suggest that ϕ_{crit} and ν are directly proportional.

One of the most interesting results of this chapter corresponds to the analysis of the relationship between the lean extinction equivalence ratio (ϕ_{ext}) and the viscosity (ν) for the different blends Kero/BL at OP_1 and OP_3 operating conditions. The results obtained are shown in Figure 5.22; in this figure, we plotted ϕ_{ext} as a function of the viscosity ($\phi_{ext} = f(\nu)$) for each blend. These results show a linear relationship between viscosity and ϕ_{ext} for each operating condition. In addition to our results, we have included the results obtained by M. Clavel [7], the ones connected by the black dashed line in the figure. During M. Clavel's doctoral thesis, she determined the extinction limits of pure kerosene in the same injection system that we used at the four operating conditions shown in Table 5.1 and in Figure 5.6. From our comparison, we can conclude that the lean extinction limits follow a linear trend with viscosity, whether the viscosity is increased by temperature reduction effects or by the addition of viscous compounds in the fuel.

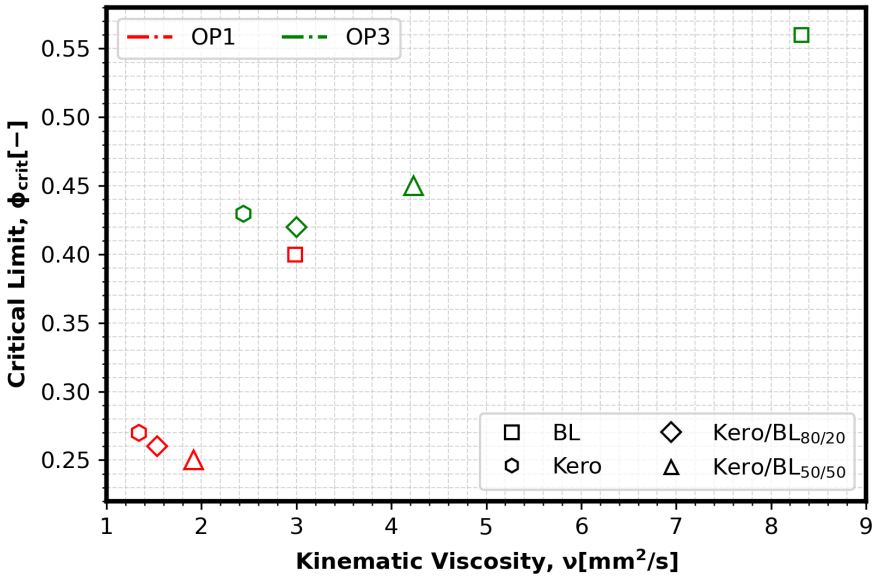

Figure 5.21 Critical equivalence ratio ϕ_{crit} versus fuel viscosity.

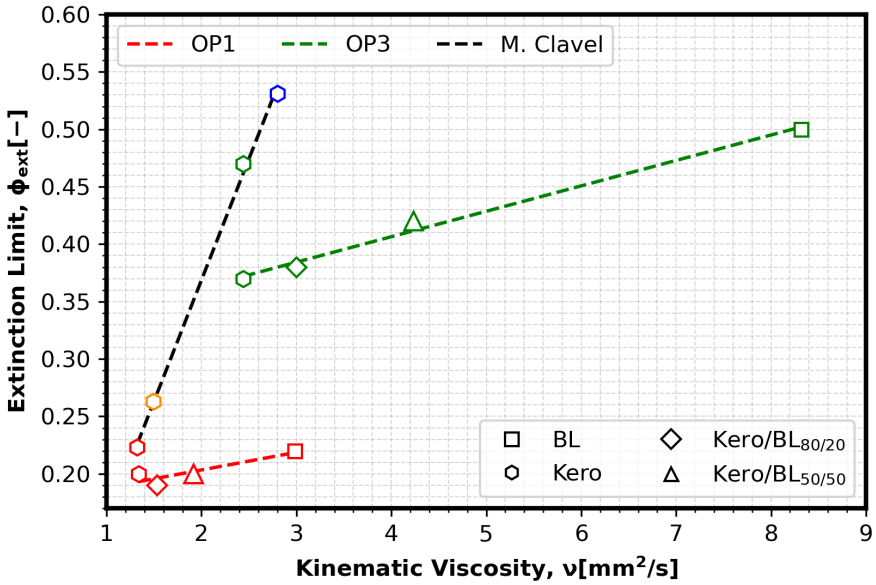

Figure 5.22 Extinction equivalence ratio ϕ_{ext} versus fuel viscosity.

In Figure 5.22, we can see that the slopes of the straight lines of the blends Kero/BL are similar for OP_1 and OP_3 conditions. However, the slope of the extinction limits when we increase the viscosity by decreasing the temperature is markedly different (black dashed line, which corresponds to the results from M. Clavel's thesis). Our hypothesis to justify this result is that the flame speed is different when viscosity increases due to temperature decrease than when viscosity increases due to the addition of viscous compounds. The flame speed decreases when the temperature decreases. A comparison between the flame speeds of the different blends Kero/BL is proposed as a perspective to verify or reject this hypothesis.

5.3.4 Pollutant Emissions

During the assessment of BL as a potential kerosene additive, we analyzed the burned gases issues from the combustion of the different blends Kero/BL. This analysis focused on the pollutants: carbon dioxide CO_2, carbon monoxide CO, and nitrogen oxides NO_x ($NO_x \equiv NO + NO_2$). We focused on these three pollutants due to their significant environmental impact [131, 132]. The pollutant analysis used the *HORIBA PG-250* gas analyzer. Pollutants can be analyzed only at OP_1 operating conditions; this is because the gas analyzer works with a suction pump and under low-pressure conditions, such as OP_3, this equipment is not able to capture the gases coming from the combustion chamber in the facility. The gas analyzer sampling rod is placed in the sampling point of the combustion chamber located after the nozzle, allowing the capture of gases coming from the combustion process.

As done for the combustion efficiency curve, the pollutant analysis is reported based on the equivalence ratio of the blends Kero/BL. For each point of analysis, the measurement lasts three minutes to calculate the mean and the standard deviation. Results are shown in Figure 5.23. These results are reported in dry milligrams per kWh.

Regarding CO_2 results, Figure 5.23a shows that the lower the equivalence ratio (ϕ), the higher are CO_2 emissions. These results show that CO_2 emissions of kerosene are reduced when BL is added. CO emissions present a similar trend to the CO_2 one, Figure 5.23b. CO trend can be linked to the combustion efficiency (η_{comb}); in fact, when $\eta_{comb} \cong 1$, the combustion is complete and the chemical equilibrium is reached, meaning that the concentration of unburned compounds such as CO is minimal. Near the lean extinction limit, CO emissions from pure BL combustion are notably higher than the others, suggesting incomplete combustion that fully agrees with the combustion efficiency results in Figure 5.18. In the degraded region and near extinction, we visually noted local extinction and high flame instability in the combustion chamber.

On the other hand, we have NO_x emissions, which increase as the equivalence ratio (ϕ) increases, Figure 5.23c. It is well known that NO_x formation during the combustion process depends quite a lot on the final temperature of the burned gases. The maximum production of NO_x is always found near to stoichiometric conditions ($\phi \approx 1$ because at these conditions, we have the highest temperature of burned gases. Based on this, NO_x emissions can also be linked to the combustion efficiency results. In the degraded region ($\eta_{comb} < 0.95$), the temperature of the burned gases is lower than the equilibrium temperature, and therefore the NO_x production is lower; however, in the nominal region ($\eta_{comb} \cong 1$) the temperature of the burned gases is close to or equal to the equilibrium temperature and therefore the NO_x production is higher. From the results obtained, we can note that the highest production of NO_x corresponds to pure kerosene, followed by the Kero/$BL_{80/20}$ blend.

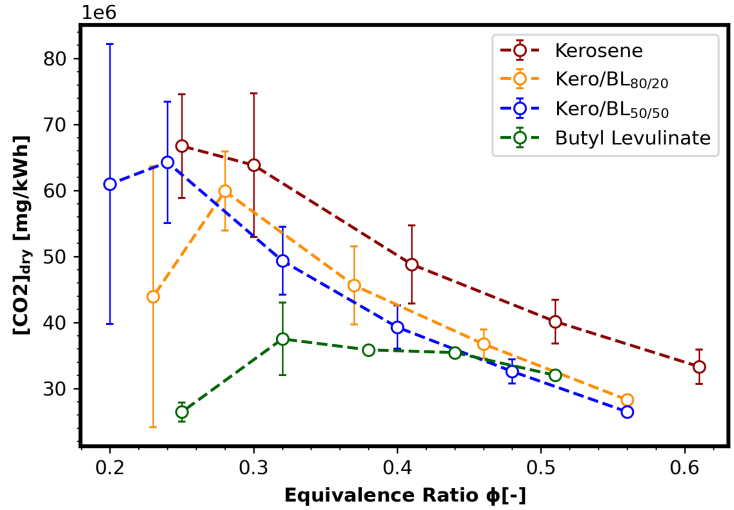

(a) CO_2 emissions versus ϕ.

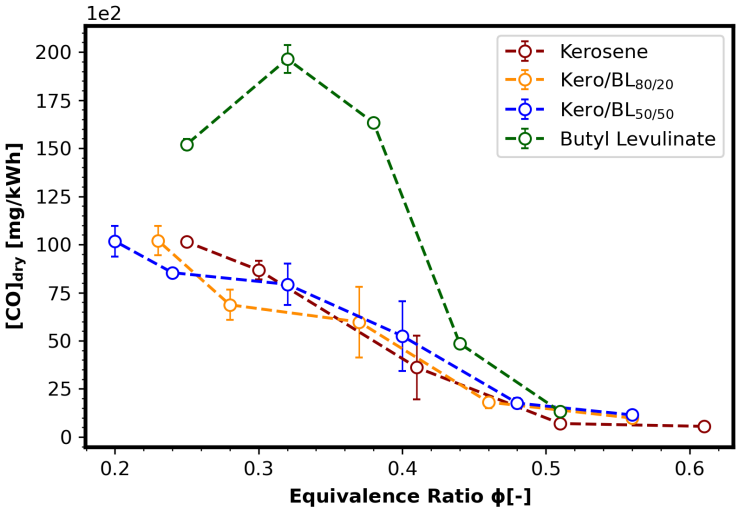

(b) CO emissions versus ϕ.

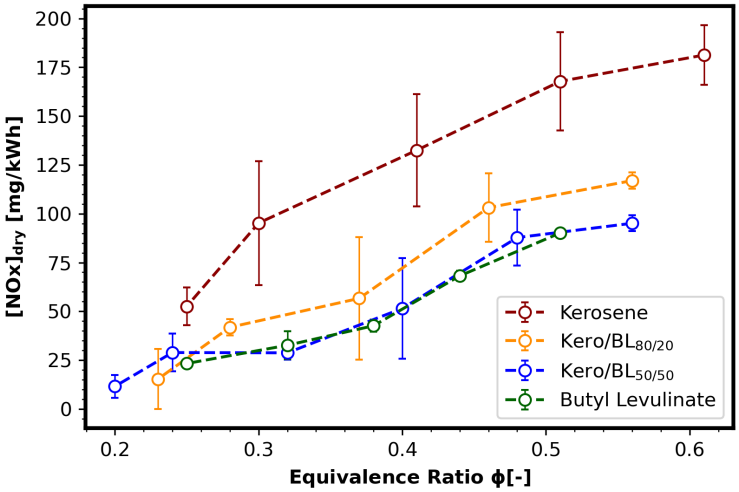

(c) NO_x emissions versus ϕ.

Figure 5.23 CO_2, CO and NO_x analysis for Kero/BL blends at OP_1 operating conditions.

5.4 Local Analysis of Spray and Flame Structure

As we have seen in the previous section, viscosity, driven by temperature, plays an important role in injection system performance and combustion efficiency. This macroscopic approach, which assesses operating limits, can be complemented with a local assessment that studies the atomization spray and flame structure; this complementary study will help us to understand the phenomena that lead to a decrease in combustion efficiency and flame extinction. Thanks to the four optical accesses of the combustion chamber, it is possible to implement optical diagnostics that allow us to study both atomization and flame structure during the combustion chamber.

To complement our assessment of BL as a kerosene additive, we implemented the laser tomography technique to study the atomization spray in the combustion chamber and the chemiluminescence technique to analyze the flame structure. These two techniques were applied to the different blends Kero/BL already defined at OP_1 and OP_3 operating conditions, except for pure BL, which was not analyzed at OP_3 conditions.

5.4.1 Spray Structure Analysis

The spray structure was studied by implementing the laser tomography technique. This technique allows the fuel droplets in the combustion chamber to be visualized. A dual-cavity Nd:YLF laser, *Darwin Dual Quantronix*, was used to illuminate the fuel flow at 5.0 kHz frequency and approximately 10 mJ energy pulse at 527 nm of wavelength. The laser beam is transformed, via a combination of cylindrical and spherical lenses, into a plane that passes through the longitudinal vertical median plane of the combustion chamber with a typical thickness of 300 μm. Therefore, only the fuel droplets in this plane are illuminated.

Images of light scattered by the fuel droplets are recorded by a high-speed camera, *Photron Fastcam SA1.2*, at 5 kHz into a 1024×1024 matrix of pixels. The units of pixels are then transformed into units of length using a calibration grid. *DaVis 10.2.0* software was used to determine the relationship between pixels and millimeters from calibration images. The quality of each instantaneous image taken during experiments is improved thanks to pre-processing, which mainly involves removing background noise; in this way, we obtain only instantaneous images corresponding to the spray.

The pre-processing is carried out over an instantaneous image taken at the instant t represented by $I^{raw}_{Tomo}(t,x,y)$, where x and y represent the positions of the pixels in the image. Remember that each image is a 1024 ×1024 matrix where each element represents the signal captured by the camera. The background noise is generated from a set of images containing 10 instantaneous images taken before instant t and 10 images taken after instant t. Thus, the background noise is generated taking the minimum value of the set of images for each position (x,y) and is represented by $\min_{t-10\leq t\leq t+10}\{I^{raw}_{Tomo}(t,x,y)\}$. Finally, to get the instantaneous image of the spray $I_{Tomo}(t,x,y)$, we subtract the background noise from the instantaneous image. This pre-processing works under the hypothesis that a drop of liquid lasts no more than 0.004 seconds in the same position (x,y). Equation 5.26 is the mathematical representation of the pre-processing process. A typical instantaneous image of spray is reported in Figure 5.24; in this figure, the scale of the axes is adjusted so that the origin of the coordinated axes coincides with the combustion chamber injector.

$$I_{Tomo}(t,x,y) = I^{raw}_{Tomo}(t,x,y) - \min_{t-10\leq t\leq t+10}\{I^{raw}_{Tomo}(t,x,y)\} \tag{5.26}$$

The assessment of spray instantaneous images allows us to determine the quality of the atomization; this also allows the analysis of the temporal evolution of the spray angle and thickness. These temporal analyses allow us to determine the stability of the atomization process under different operating conditions. Our main goal with local analysis is to understand which factors lead to a decrease in combustion efficiency (η_{comb}) and a subsequent flame extinction. For this reason, our local analysis of both spray and flame structure was carried out in both the nominal region (where $\eta_{comb} \cong 1$) and in the degraded region (where $\eta_{comb} < 0.95$), in order to compare and establish the main differences in both regions. The conditions at which the local analysis was carried out are those marked with black stars in Figure 5.18. Spray analysis is based on a set of 1000 instantaneous images taken under the different operating conditions for the different blends Kero/BL.

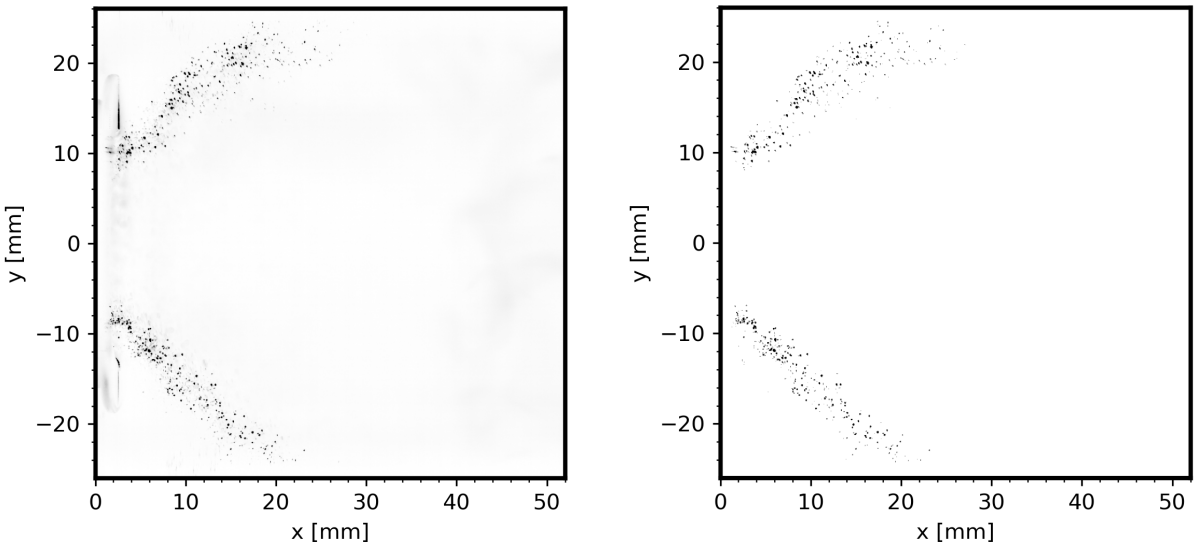

(a) Instantaneous image.

(b) Pre-processing image.

Figure 5.24 Spray instantaneous image of pure kerosene at OP_1 and ϕ=0.51.

First, we performed a qualitative analysis of the spray spray. It consisted of calculating the mean image of the spray $\langle I_{Tomo}(t,x,y)\rangle$ and its standard deviation $I'_{Tomo}(t,x,y)$. These images were obtained from a set of 1000 instantaneous images taken under different operating conditions for different blends of Kero/BL. These results are shown in Tables 5.4 -5.7. It is important to highlight that the images for pure BL at OP_1 conditions and the images for OP_3 were affected by the accumulation of residues in the upper window of the combustion chamber. These residues came mainly from the incomplete combustion of the different blends under unfavored conditions. These residues, mainly accumulated in the first millimeters of the window, reduced the power delivered by the laser to the fuel droplets at the exit of the injector. Thus, droplet signals near the injector were captured with a lower light intensity.

Table 5.4 Mean spray $\langle I_{Tomo}(t,x,y)\rangle$ results for Kero/BL blends at OP_1.

Blend	**OP_1**	
	$\eta_{comb} \cong 1$	$\eta_{comb} < 0.95$
Kerosene	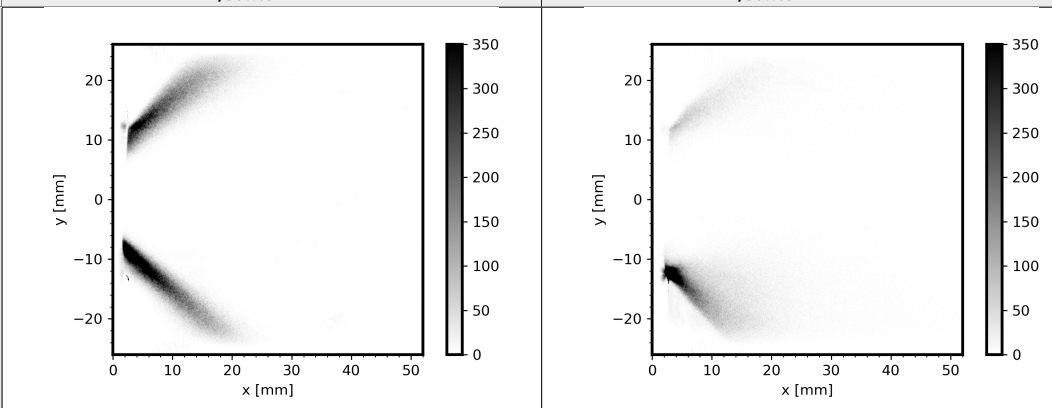	
Kero/BL (80/20)	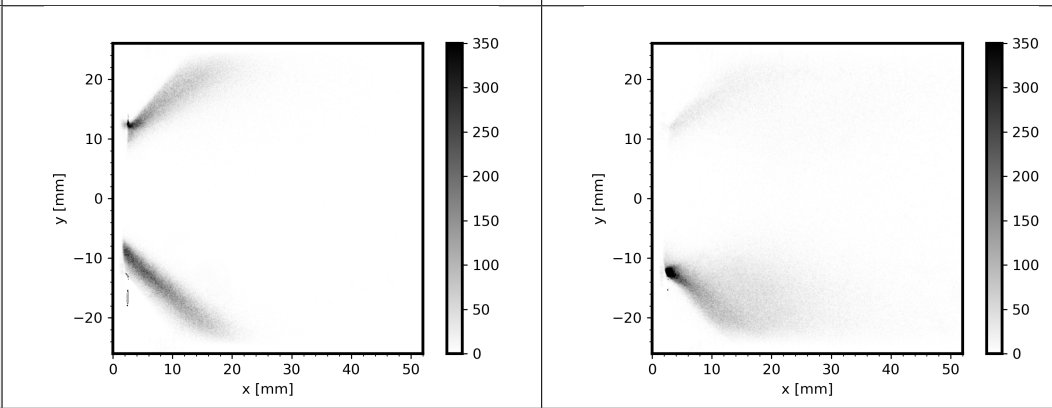	
Kero/BL (50/50)	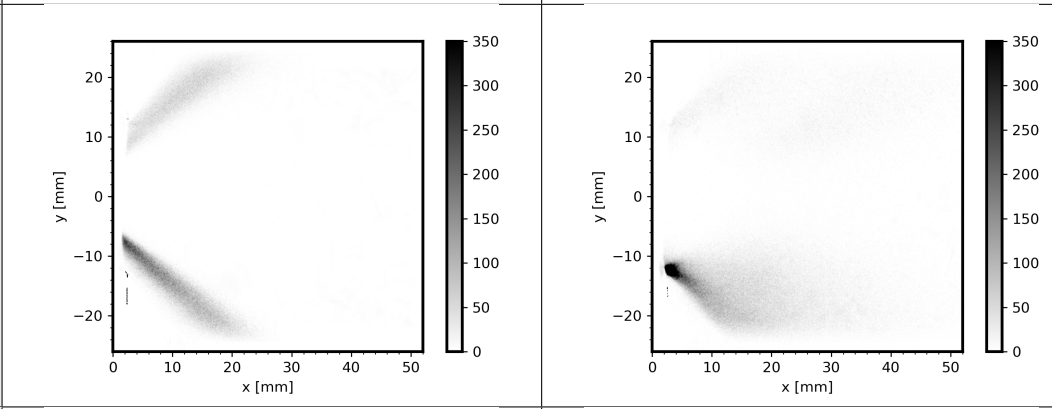	
Butyl Levulinate	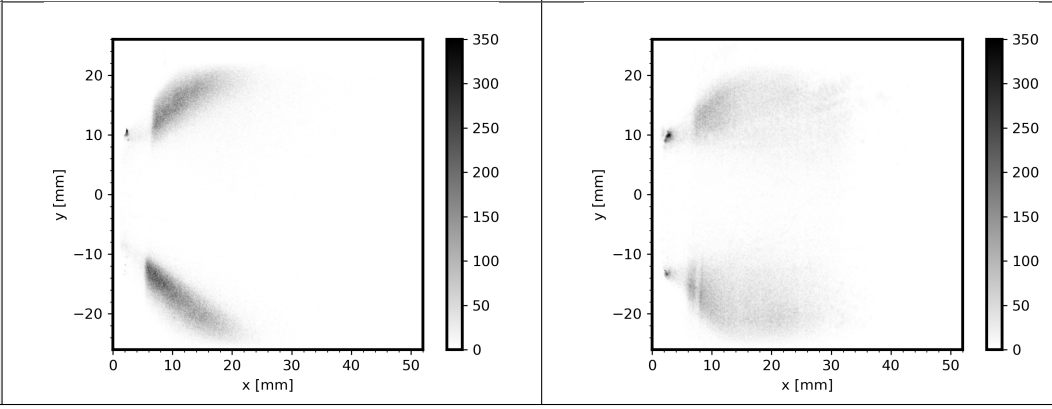	

Table 5.5 Standard deviation $I'_{Tomo}(t, x, y)$ results for Kero/BL blends at OP_1.

Blend	**OP_1**	
	$\eta_{comb} \cong 1$	$\eta_{comb} < 0.95$
Kerosene	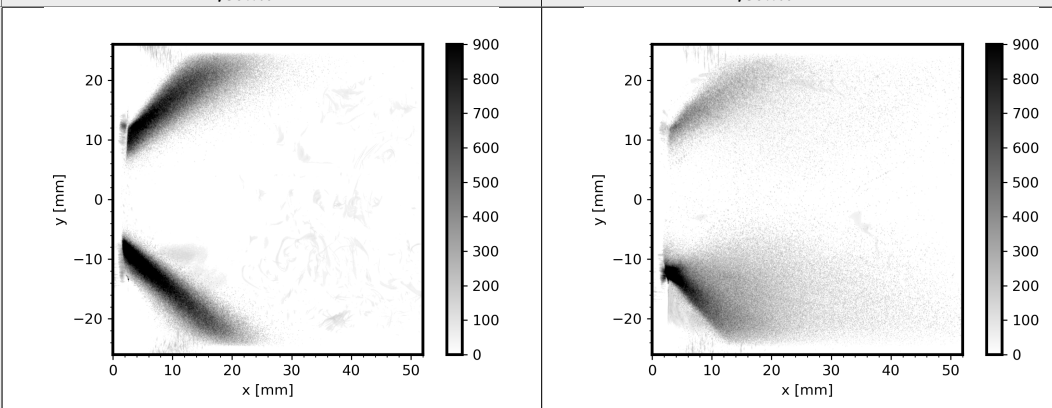	
Kero/BL (80/20)	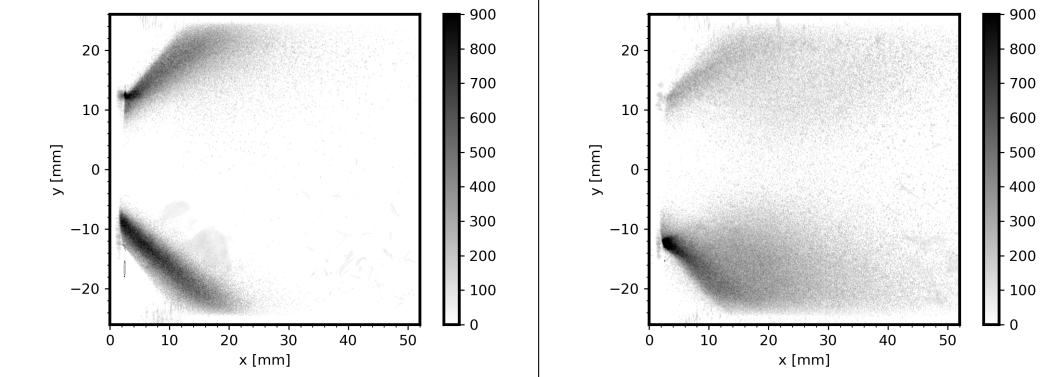	
Kero/BL (50/50)	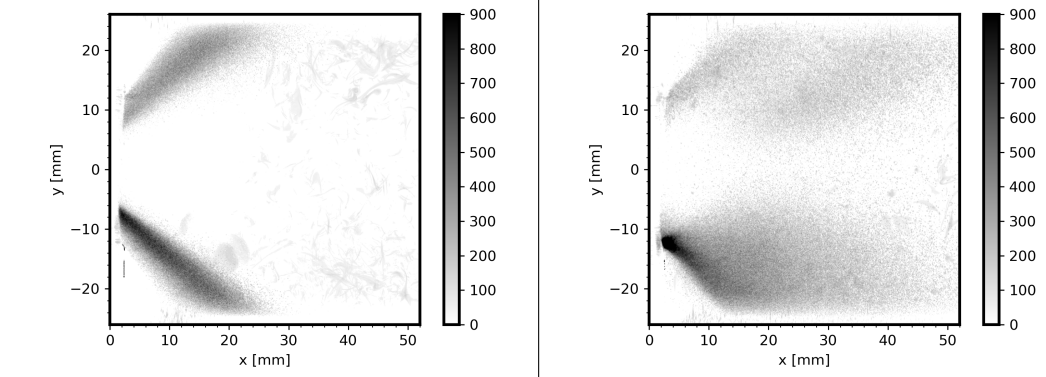	
Butyl Levulinate	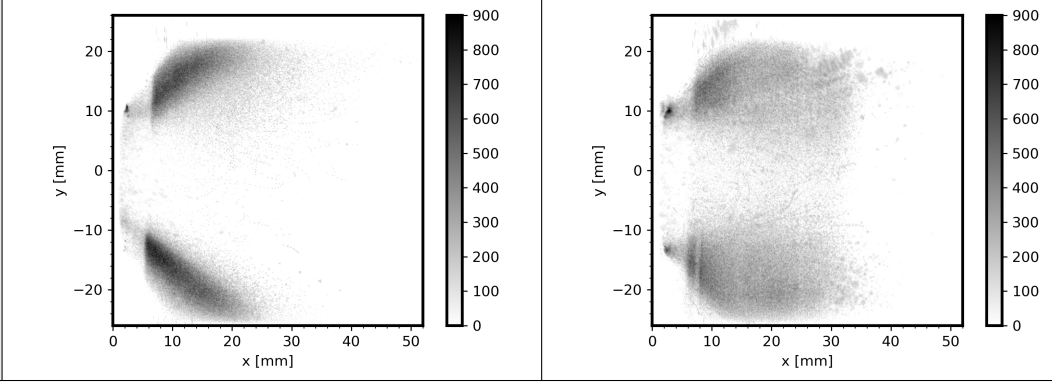	

Table 5.6 Mean spray $\langle I_{Tomo}(t,x,y)\rangle$ results for Kero/BL blends at OP_3.

Blend	**OP_3**	
	$\eta_{comb} \cong 1$	$\eta_{comb} < 0.95$
Kerosene	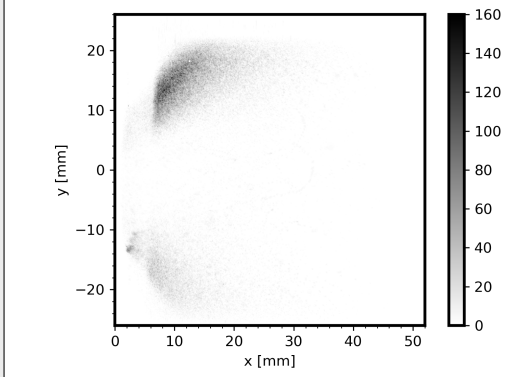	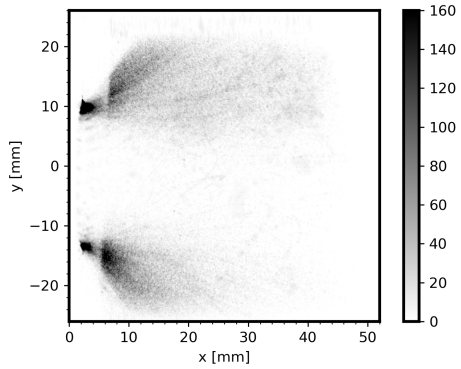
Kero/BL (80/20)	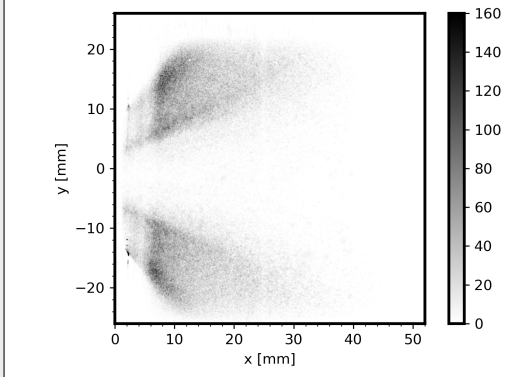	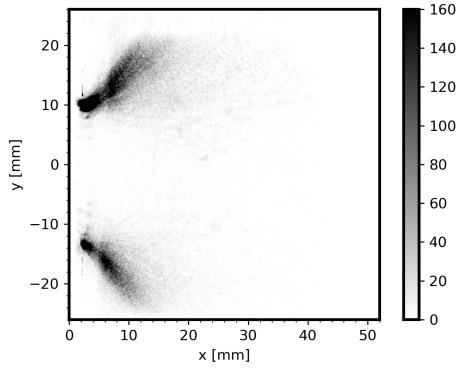
Kero/BL (50/50)	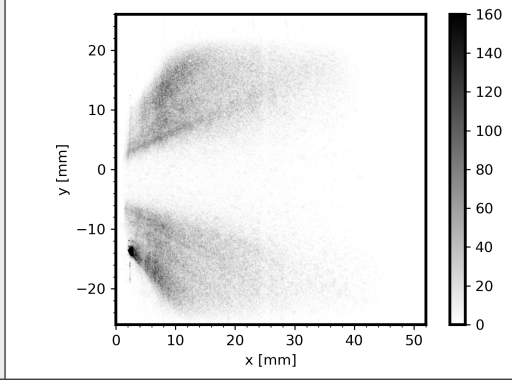	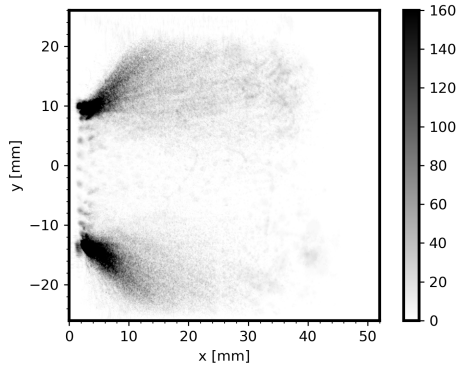

Table 5.7 Standard deviation $I'_{Tomo}(t,x,y)$ results for Kero/BL blends at OP_3.

Blend	**OP_3**	
	$\eta_{comb} \cong 1$	$\eta_{comb} < 0.95$
Kerosene	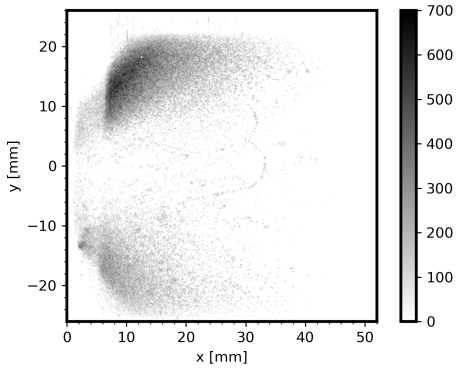	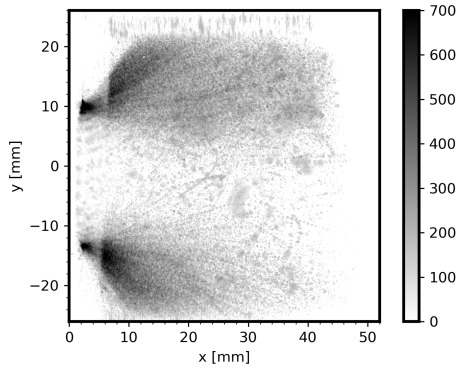
Kero/BL (80/20)	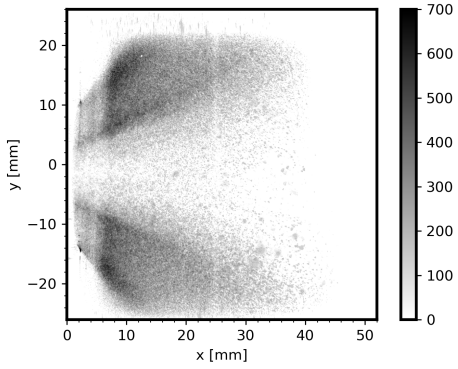	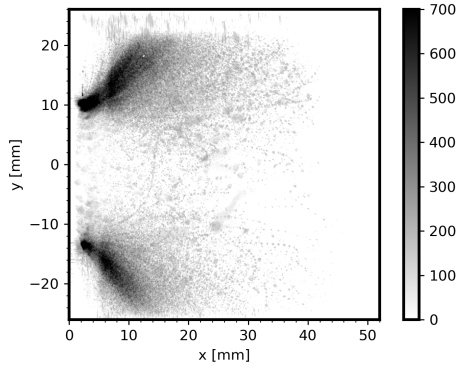
Kero/BL (50/50)	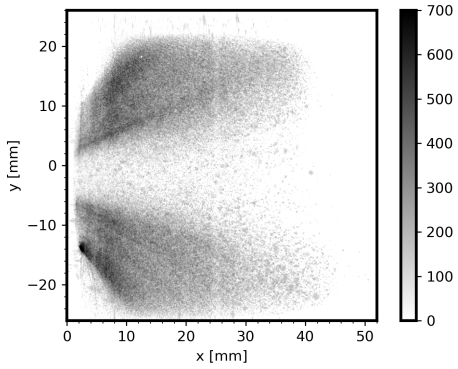	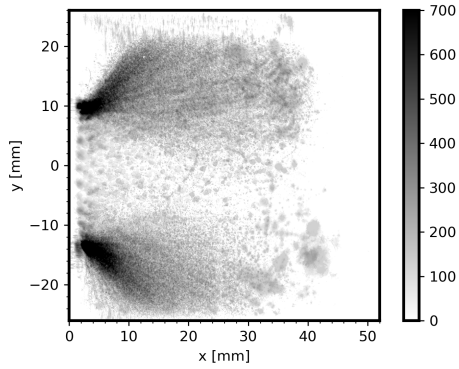

From mean spray results, we can realize that for the OP_1 operating conditions, the blends pure kerosene, Kero/$BL_{80/20}$ and Kero/$BL_{50/50}$ have a similar mean spray, which explains why their critical and extinction points are so similar. On the other hand, at OP_1 conditions, we can see that the results obtained for pure BL show a bigger fluctuation than the other blends, which explains why its critical and extinction points are different from other blends. Regarding the results at OP_3 conditions, we can first say that the mean sprays are very different from those obtained at OP_1 conditions. At OP_3 conditions, we can note that the spray fluctuates more for all the blends tested, whereas pure kerosene fluctuates the least. The standard deviation results for OP_3 conditions show that the quality of the atomization is lower than at OP_1 conditions because, at OP_3, we can see the presence of large droplets and ligaments of liquid.

The qualitative analysis suggests that at OP_3 operating conditions, spray fluctuations are more important. One way to verify these results is by analyzing the temporal evolution spray angle (θ) and thickness (δ). To calculate the angle (θ) and thickness(δ), we proceed as follows: For a given instantaneous image $I_{Tomo}(t, x, y)$, we treated each droplet of liquid as a point in space (x, y), and by curve-fitting, we defined the line equations that represent the upper-spray and the lower-spray of the image. These equations of the line are in the form $y = ax + b$. And then, we calculate the angle between the two lines, corresponding to the angle of spray θ. The thickness of the spray, δ, is defined as the perpendicular distance to the spray at which at least 80% of the spray droplets are contained. Figure 5.25 shows an example of spray angle and thickness identification. The temporal evolution of the spray angle and the thickness at OP_1 and OP_3 operating conditions for the different blends Kero/BL mixtures are shown in Tables 5.8 – 5.11.

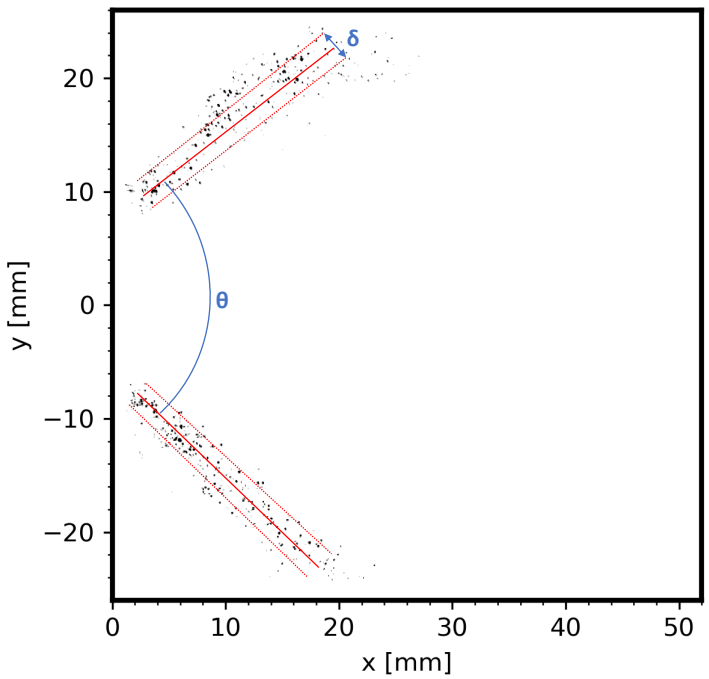

Figure 5.25 Angle and thickness detection pure kerosene spray instantaneous image at OP_1 and ϕ=0.51.

Table 5.8 Spray angle θ results for Kero/BL blends at OP_1.

Blend	OP_1	
	$\eta_{comb} \cong 1$	$\eta_{comb} < 0.95$
Kerosene	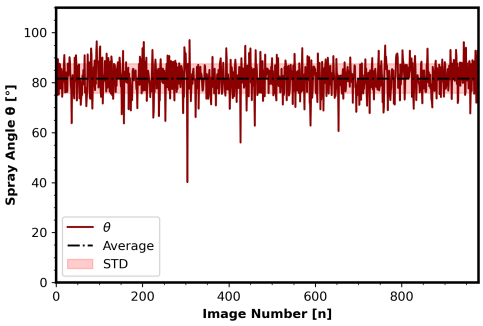	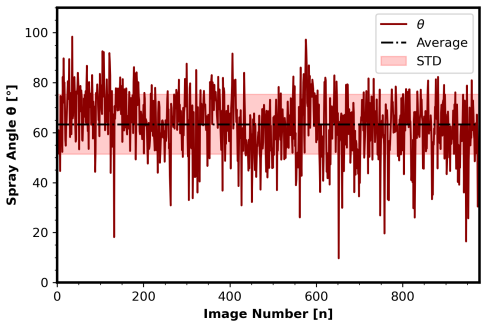
Kero/BL (80/20)	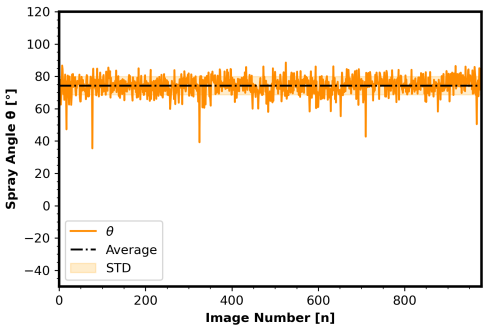	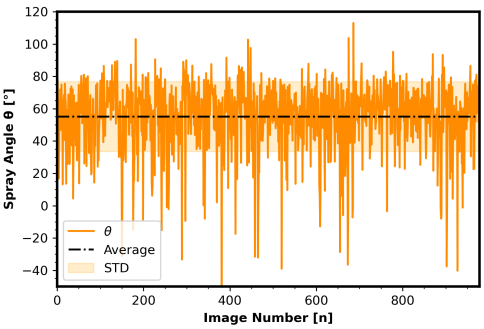
Kero/BL (50/50)	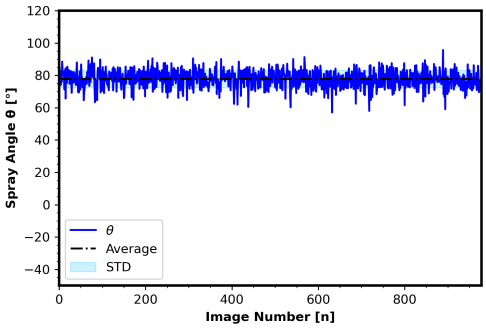	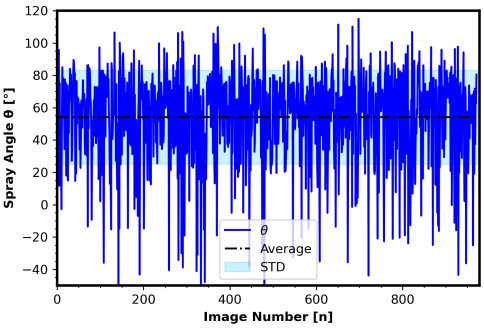
Butyl Levulinate	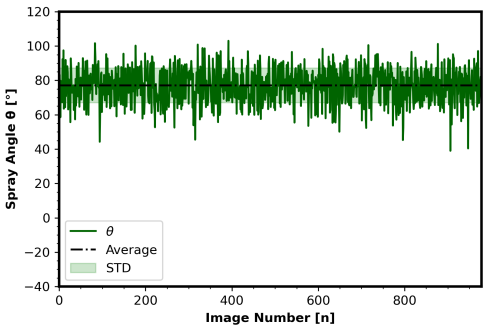	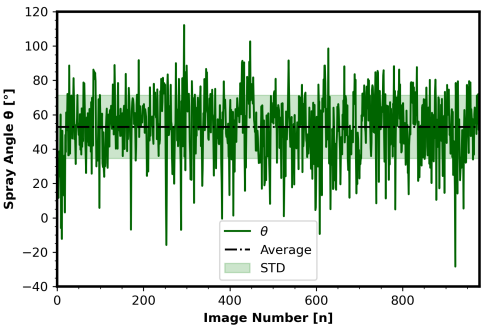

Table 5.9 Spray angle θ results for Kero/BL blends at OP_3.

Blend	OP_3	
	$\eta_{comb} \cong 1$	$\eta_{comb} < 0.95$
Kerosene	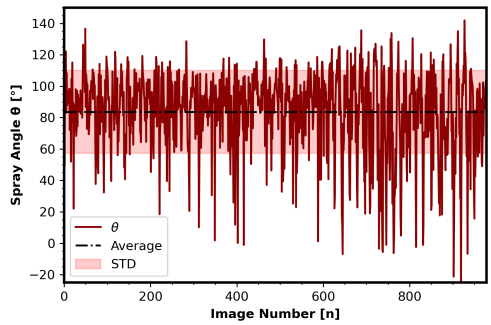	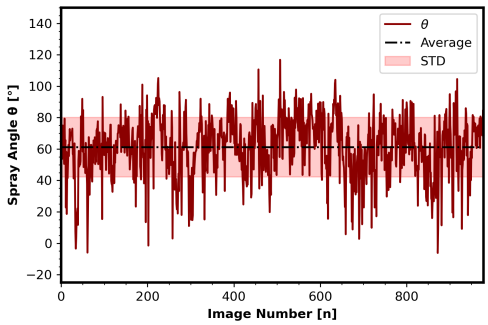
Kero/BL (80/20)	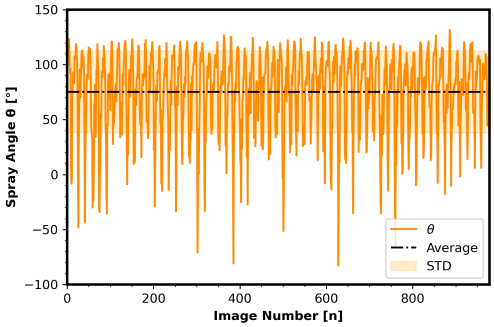	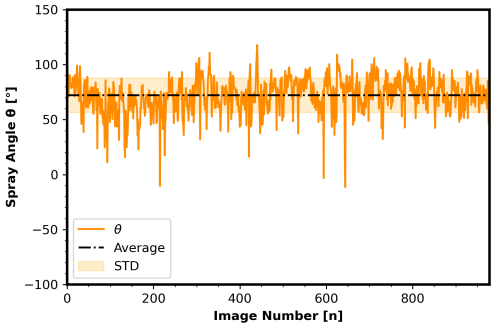
Kero/BL (50/50)	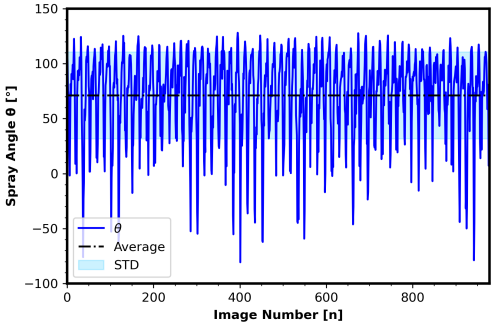	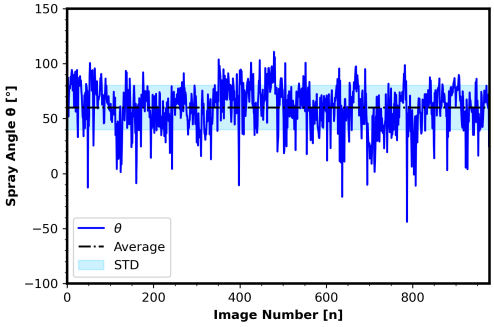

Table 5.10 Spray thickness δ results for Kero/BL blends at OP_1.

Blend	OP_1	
	$\eta_{comb} \cong 1$	$\eta_{comb} < 0.95$
Kerosene	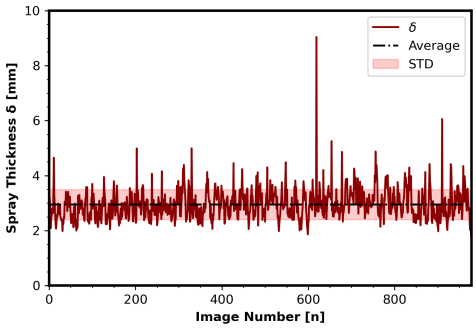	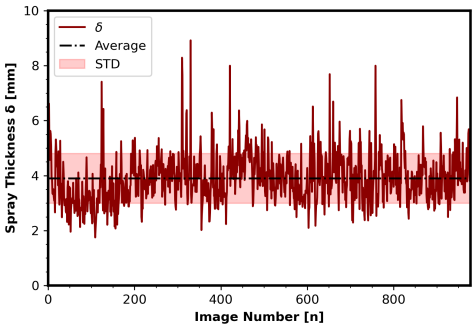
Kero/BL (80/20)	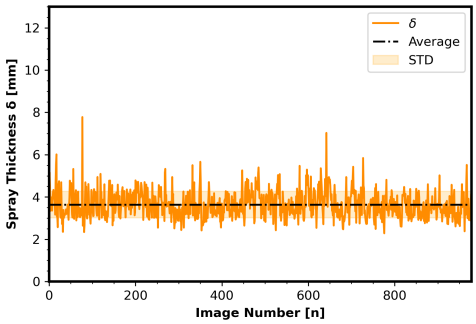	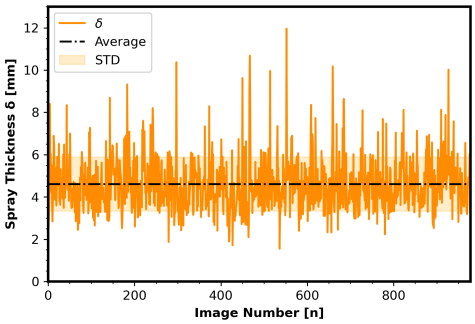
Kero/BL (50/50)	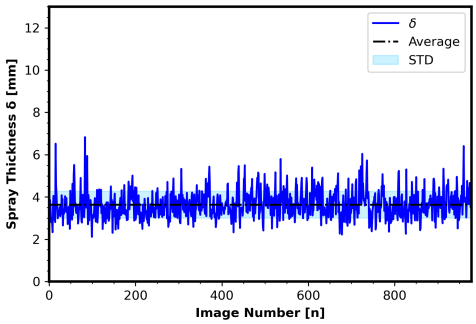	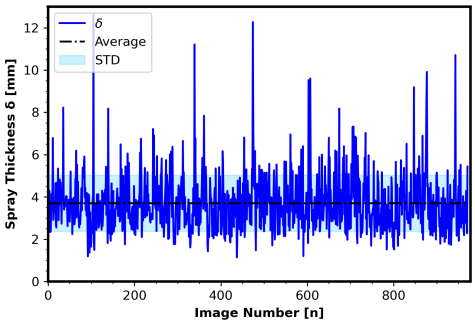
Butyl Levulinate	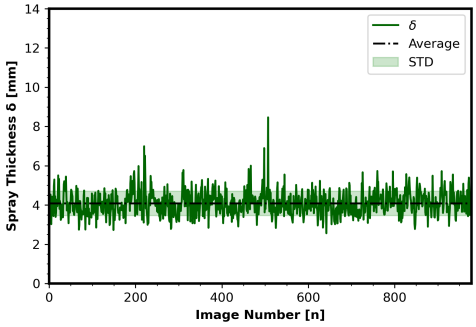	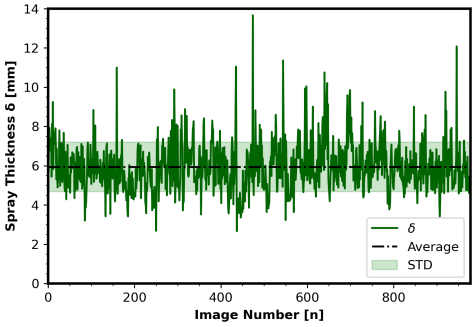

Table 5.11 Spray thickness δ results for Kero/BL blend at OP_3.

Blend	OP_3	
	$\eta_{comb} \cong 1$	$\eta_{comb} < 0.95$
Kerosene	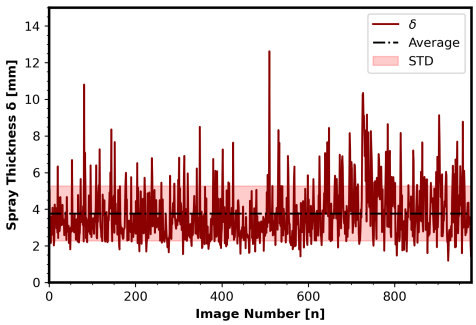	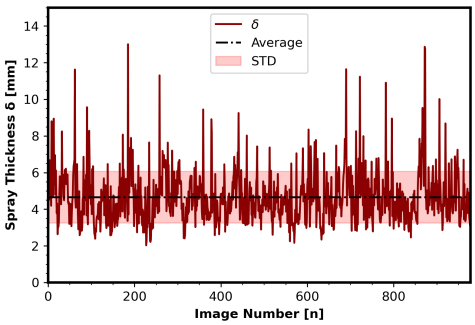
Kero/BL (80/20)	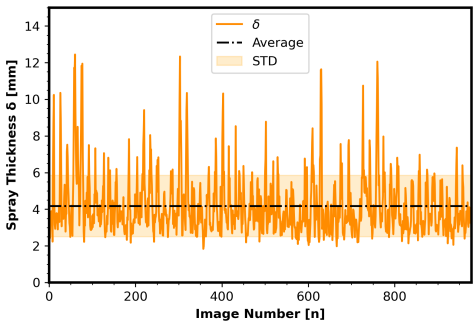	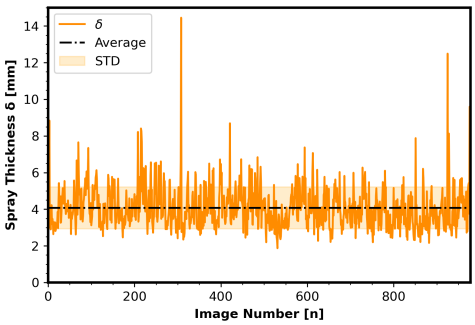
Kero/BL (50/50)	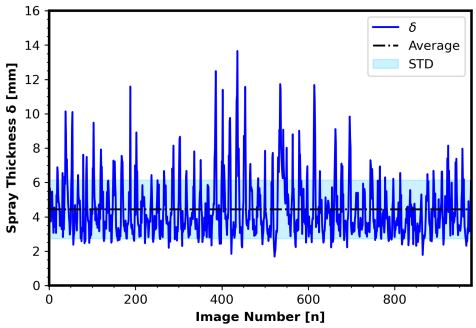	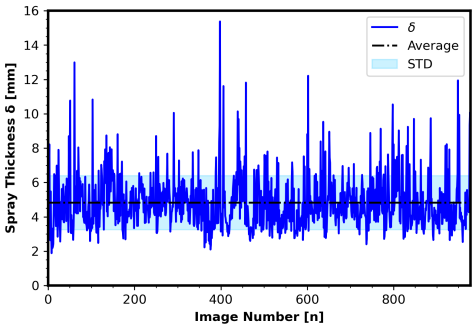

The temporal evolution spray angle and thickness results are summarized in Tables 5.12 – 5.15. In these tables, we present the mean values of these two parameters ($\overline{\theta}$ and $\overline{\delta}$) and their respective standard deviations. These results were plotted as a function of viscosity in Figure 5.26 to identify any possible trends.

Table 5.12 Spray angle θ results at OP_1.

OP_1	$\eta_{comb} \cong 1$			$\eta_{comb} < 0.95$		
Blend	$\overline{\theta}$ [^{o}]	STD	STD %	$\overline{\theta}$ [^{o}]	STD	STD %
Kerosene	81.60	5.90	7.23%	63.29	11.96	18.90%
Kero/$BL_{80/20}$	74.17	5.59	7.54%	55.07	21.58	39.19%
Kero/$BL_{50/50}$	77.72	5.34	6.87%	54.10	28.98	53.57%
Butyl Levulinate	77.05	10.06	13.06%	52.94	18.34	34.64%

Table 5.13 Spray angle θ results at OP_3.

OP_3	$\eta_{comb} \cong 1$			$\eta_{comb} < 0.95$		
Blend	$\overline{\theta}$ [^{o}]	STD	STD %	$\overline{\theta}$ [^{o}]	STD	STD %
Kerosene	83.59	26.36	31.53%	61.19	18.93	30.94%
Kero/$BL_{80/20}$	75.27	37.29	49.54%	72.21	15.80	21.88%
Kero/$BL_{50/50}$	71.05	39.36	55.40%	60.08	20.22	33.66%

Table 5.14 Spray thickness δ results at OP_1.

OP_1	$\eta_{comb} \cong 1$			$\eta_{comb} < 0.95$		
Blend	$\overline{\delta}$ [mm]	STD	STD %	$\overline{\delta}$ [mm]	STD	STD %
Kerosene	2.94	0.55	18.71%	3.90	0.90	23.08 %
Kero/$BL_{80/20}$	3.64	0.63	17.31%	4.60	1.27	27.61 %
Kero/$BL_{50/50}$	3.63	0.63	17.35%	3.69	1.33	36.04 %
Butyl Levulinate	4.08	0.62	15.20%	5.94	1.26	21.21%

Table 5.15 Spray thickness δ results at OP_3.

OP_3	$\eta_{comb} \cong 1$			$\eta_{comb} < 0.95$		
Blend	$\overline{\delta}$ [mm]	STD	STD %	$\overline{\delta}$ [mm]	STD	STD %
Kerosene	3.76	1.50	39.89%	4.65	1.43	30.75%
Kero/$BL_{80/20}$	4.17	1.67	40.05%	4.08	1.15	28.19%
Kero/$BL_{50/50}$	4.42	1.70	38.46%	4.83	1.57	32.50%

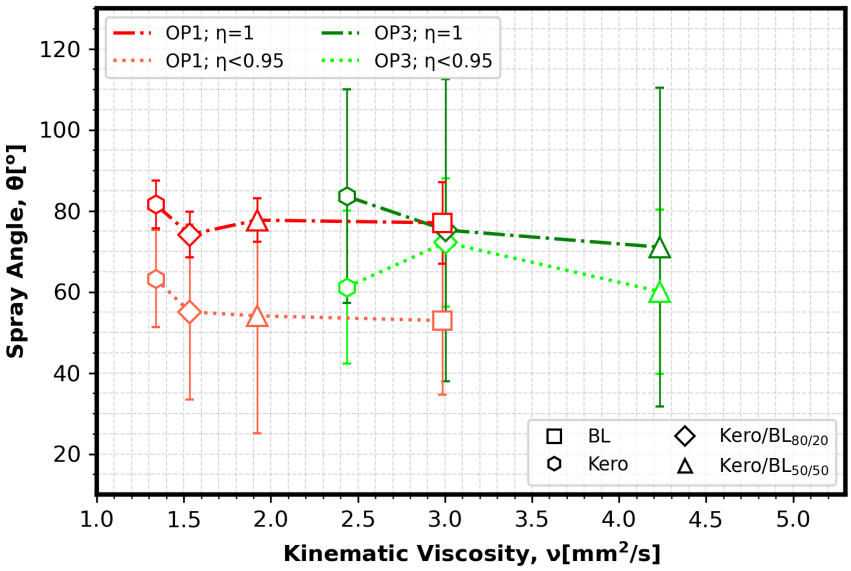

(a) Angles versus viscosity.

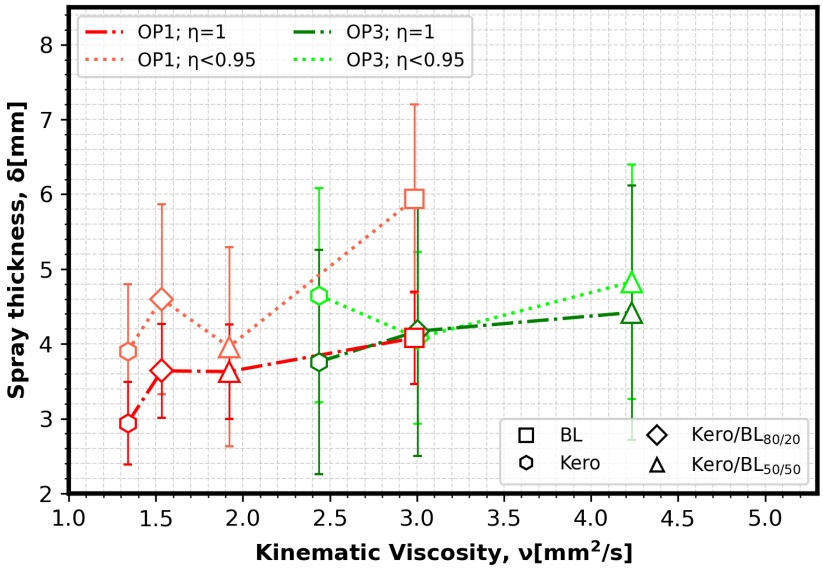

(b) Thickness versus viscosity.

Figure 5.26 Spray angle and thickness results summary.

In general, the results mean spray angle ($\overline{\theta}$) and mean spray thickness ($\overline{\delta}$) do not present any clear tendency concerning the viscosity in the range that we investigated. For OP_1 operating conditions, we can see that when we move from the nominal region ($\eta_{comb} \cong 1$) to the degraded region ($\eta_{comb} < 0.95$), the mean spray angle values decrease. However, the fluctuations become more important for all blends. This means that the atomization spray becomes unstable close to the flame extinction. On the other hand, at the same OP_1 operating conditions, the spray thicknesses increase slightly, as do the fluctuations when we move from the nominal to the degraded region. At OP_3 operating conditions, the average values of the angles are similar to those of the OP_1 conditions. However, the fluctuations at OP_3 conditions are considerably more significant, up to 55% in the nominal region. At OP_3 conditions, the value of the mean angle decreases, as do the oscillations when we move from the nominal region to the degraded region.

This proves that an increase in viscosity (driven by a decrease in temperature) does not greatly impact the mean value of the spray angle. However, it generates important fluctuations in the atomization spray, which can be observed in the standard deviation values. If we compare the results obtained for pure kerosene and the blend Kero/$BL_{80/20}$, we obtain basically the same values for spray mean angle and mean thickness and their corresponding fluctuations.

5.4.2 Flame Structure Analysis

In this section, we seek to evaluate and compare the structure of the flame generated during the combustion of the different blends of Kero/BL. This evaluation was carried out by implementing a chemiluminescence analysis. Chemiluminescence in flames refers to the spontaneous light emissions from excited species by an electronic exchange process. The generation of chemiluminescence mainly includes two reaction steps: *1)* the formation of an excited radical from parent species and *2)* the spontaneous transition of excited-state radicals to its ground state by the emission of one photon, this process is represented by Equations 5.27 and 5.28. It is important to highlight that not all excited-state radicals can generate chemiluminescence [133]. Chemiluminescence can be used to measure flame structure, heat release rate, equivalence ratio, concentration, and other variables during a combustion process [134].

$$A + B \longrightarrow R^* + others \tag{5.27}$$

$$R^* \longrightarrow R + h\nu \text{ (phothon)} \tag{5.28}$$

The blue color in flames is mainly due to the chemiluminescence emitted by the excited radicals OH^* (309 nm), CH^* (431 nm), C_2^* (516 nm) and CO_2^* (350-600 nm), while the yellow and orange colors in flames are mainly due to the black body radiation of the soot that is generated and heating-up during combustion [135]. For hydrocarbon flames, the most important excited-stated radicals are OH^* and CH^*. De Leo et al.[136] studied the OH^* and CH^* luminescence in opposed flow methane oxy-flames. They conclude that these two excited radicals are formed in the reaction zone, and their concentration peaks indicate the flame position. To study the flame structure of the different blends Kero/BL via chemiluminescence, we used *intensified CCD camera PI-MAX 4* combined with the light filter *SCHOTT BG12*. This combination allows an increase in the light signal emitted during combustion thanks to the camera intensifier and mainly eliminates light emissions in the yellow and orange color spectrum, as shown in Figure 5.27, thus reducing the radiation signal emitted by soot formation. This filter allows to capture mainly the light signal emitted by CH^* (431 nm) radicals and part of the signal emitted by CO_2^* (350-600 nm). The measurement of CH^* radicals is used to identify the areas where the combustion reaction occurs, which correspond to the areas where the energy release is greatest, representing the flame structure in the combustion chamber.

In this section, we focus on a qualitative analysis of flame structure. This consists of determining the mean structure of the reaction zone, i.e., the flame structure, in the combustion chamber via CH^* detection during the combustion of the different blends Kero/BL at OP_1 and OP_3 operating conditions. As we did in the Spray analysis, the mean image and the standard deviation of the reaction zone were determined for the nominal region, where $\eta_{comb} \cong 1$, and for the degraded region, where $\eta_{comb} < 0.95$. Flame structure was based on a set of 500 images taken at a frequency of 1000 Hz. It should be noted that the pure BL was not analyzed under OP_3 operating conditions. The results are shown in Tables 5.16 - 5.19.

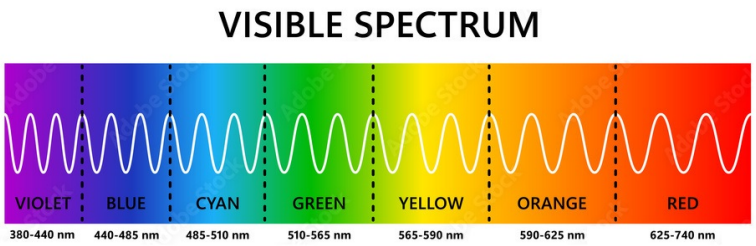

(a) Visible spectrum wavelength.

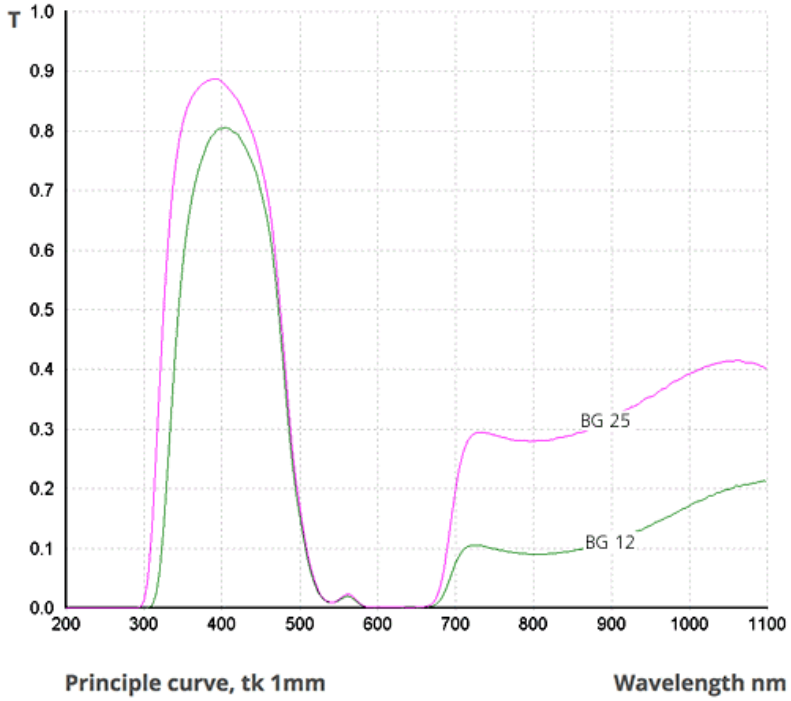

(b) Optical transmission of filter SCHOTT BG12 and BG25, taken from [137].

Figure 5.27 Visible spectrum wavelength and optical transmission of filter SCHOTT BG12 and BG25.

The results obtained at OP_1 conditions show that the flame structure and fluctuations are similar for the pure kerosene, Kero/$BL_{80/20}$, and Kero/$BL_{50/50}$ blend. However, pure BL exhibits a different flame structure and fluctuations than other blends in nominal and degraded regions. On the other hand, at OP_3 conditions, the flame structure and fluctuations are different for all the blends Kero/BL analyzed. However, the blend Kero/$BL_{80/20}$ has a similar flame structure and fluctuations to pure kerosene.

Table 5.16 Chemiluminescence mean images at OP_1.

Blends	**OP_1**	
	$\eta_{comb} \cong 1$	$\eta_{comb} < 0.95$
Kerosene	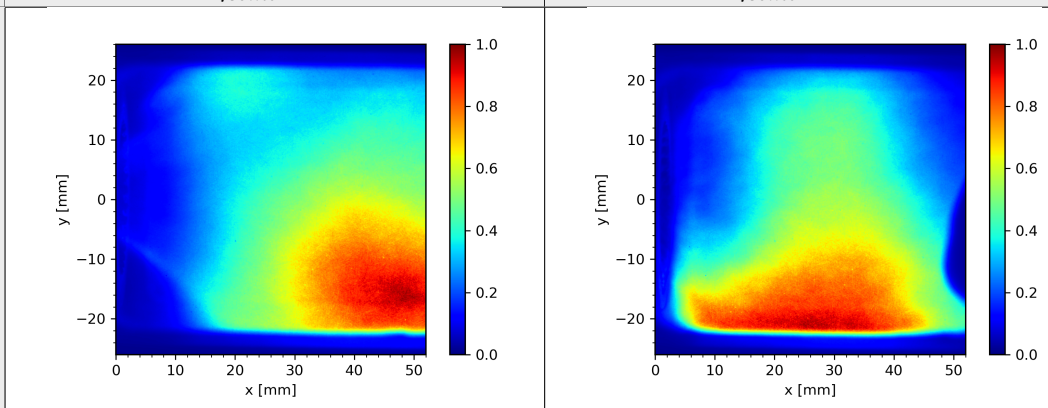	
Kero/BL (80/20)	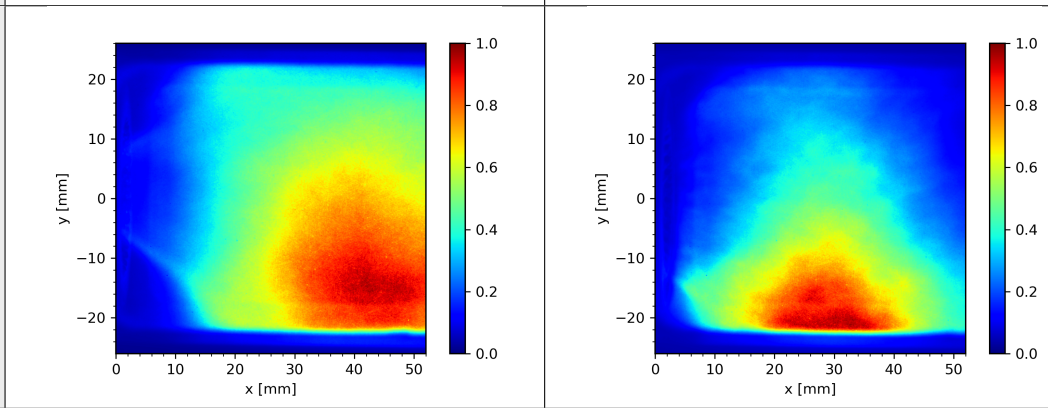	
Kero/BL (50/50)	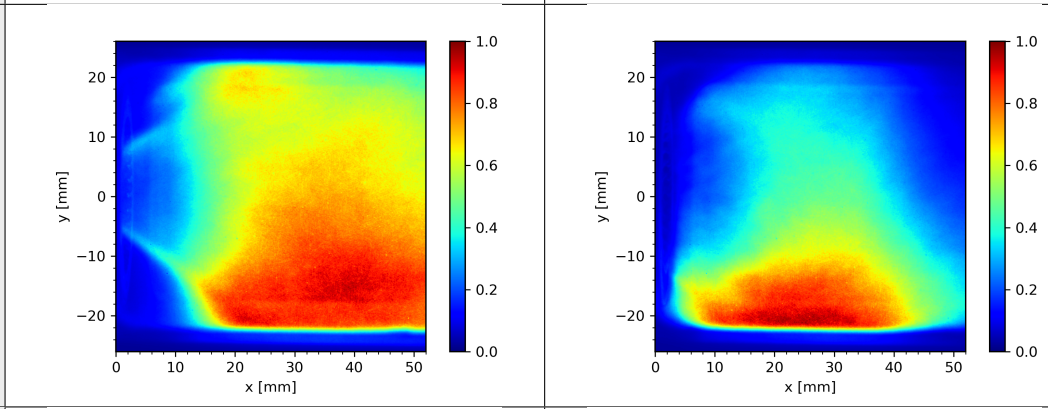	
Butyl Levulinate	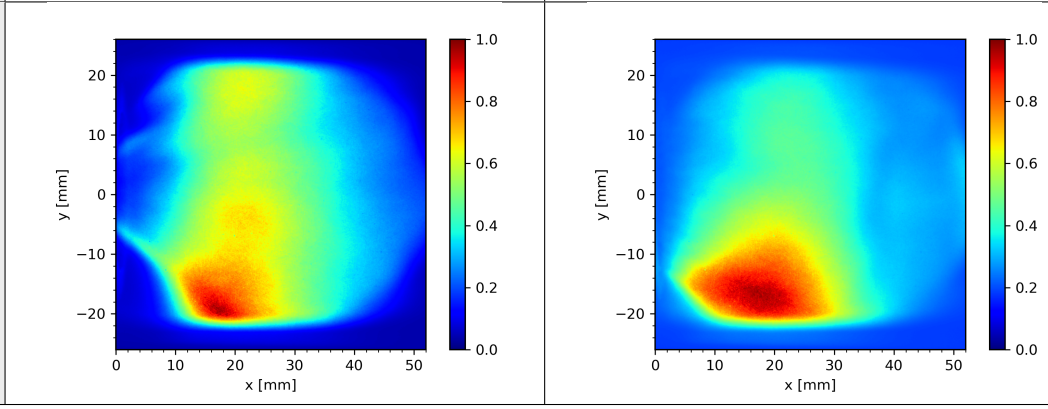	

Table 5.17 Chemiluminescence standard deviation images at OP_1.

Blends	**OP_1**	
	$\eta_{comb} \cong 1$	$\eta_{comb} < 0.95$
Kerosene	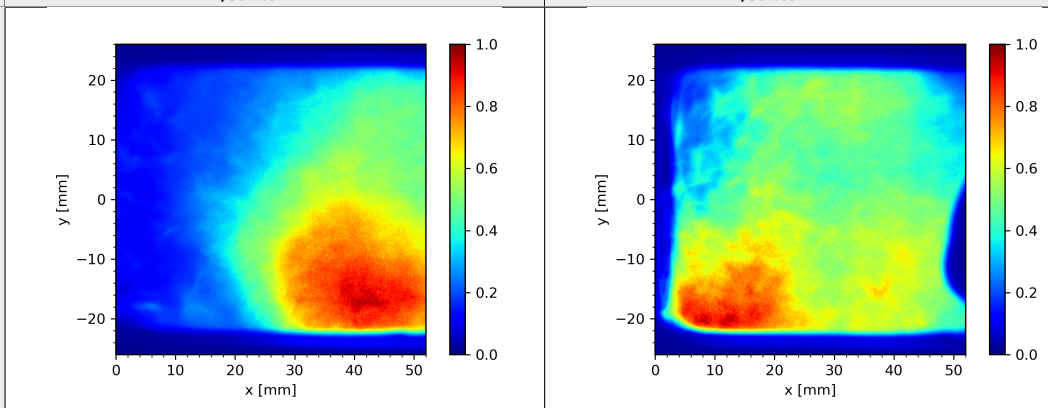	
Kero/BL (80/20)	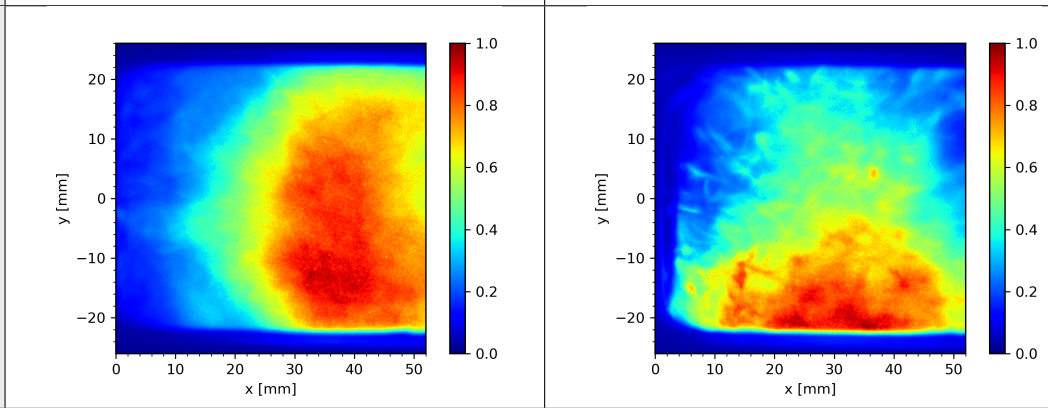	
Kero/BL (50/50)	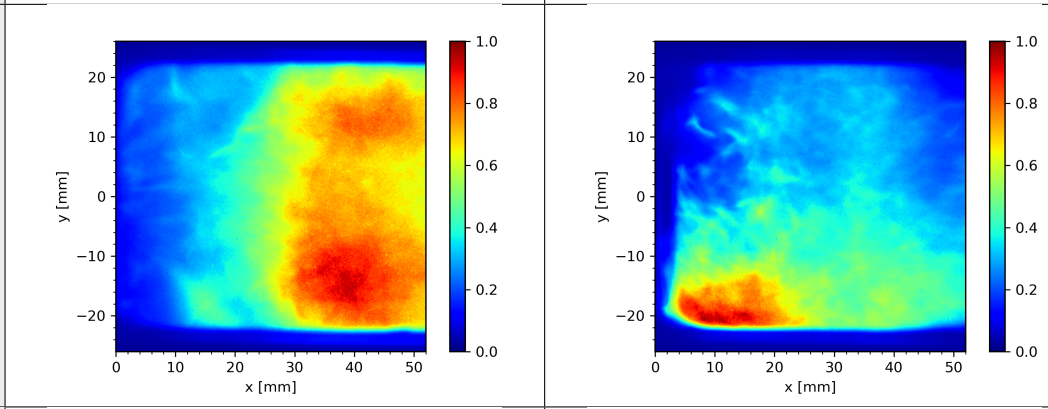	
Butyl Levulinate	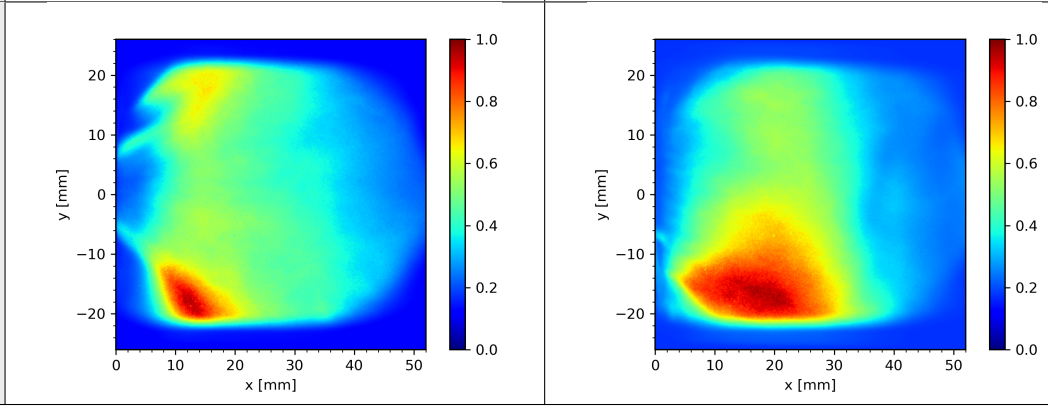	

Table 5.18 Chemiluminescence mean images at OP_3.

Blends	**OP_3**	
	$\eta_{comb} \cong 1$	$\eta_{comb} < 0.95$
Kerosene	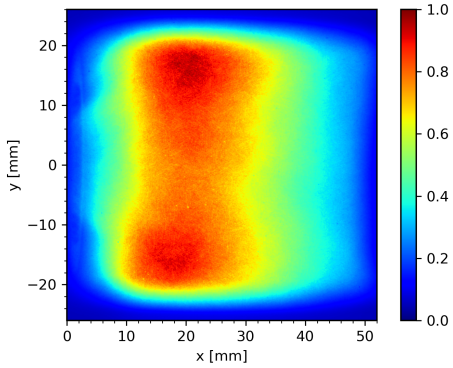	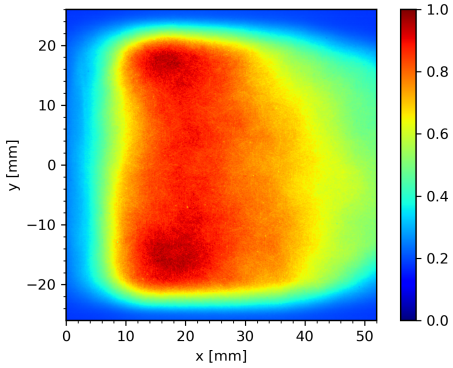
Kero/BL (80/20)	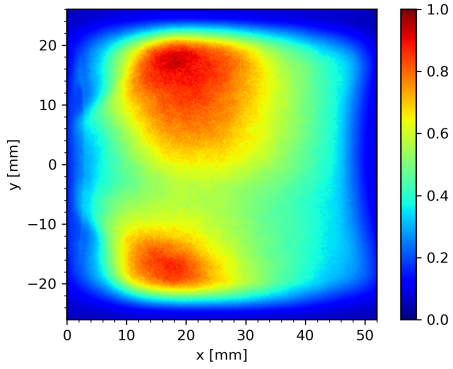	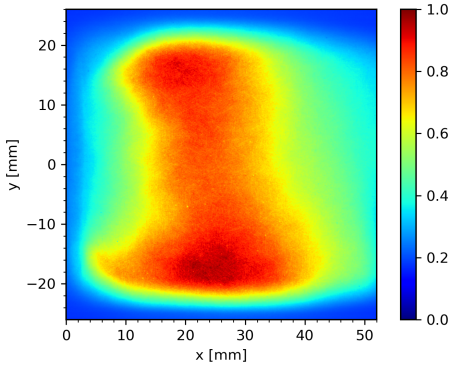
Kero/BL (50/50)	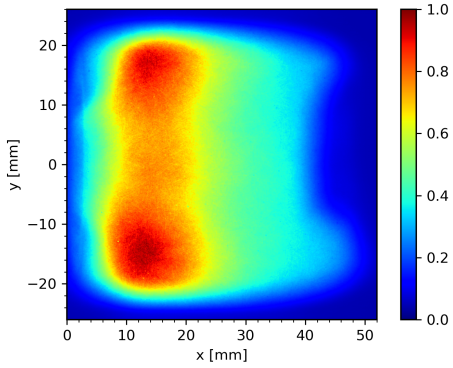	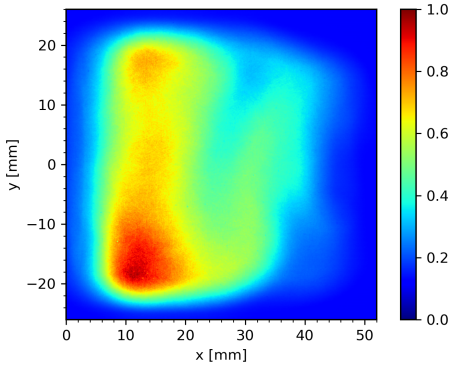

Table 5.19 Chemiluminescence standards deviation images at OP_3.

Blends	**OP_3**	
	$\eta_{comb} \cong 1$	$\eta_{comb} < 0.95$
Kerosene	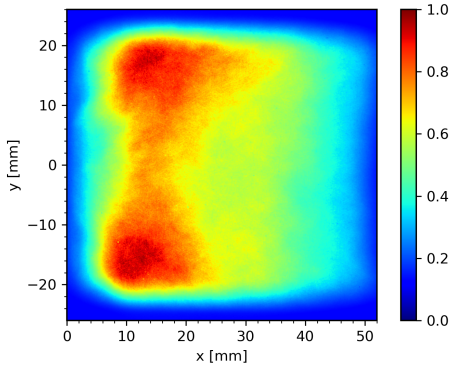	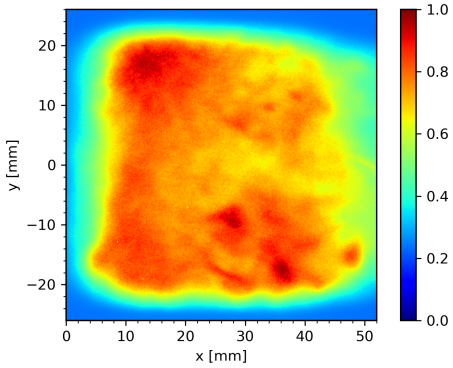
Kero/BL (80/20)	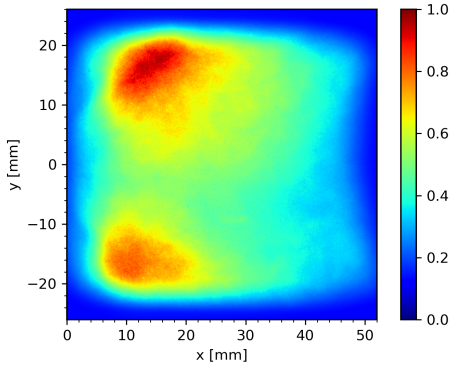	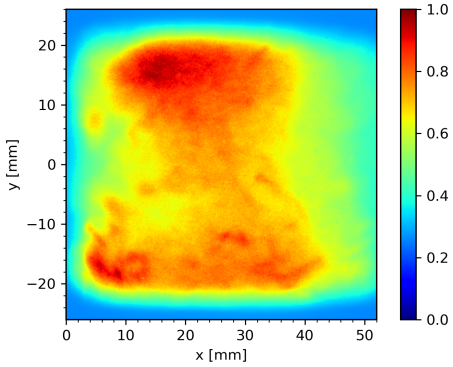
Kero/BL (50/50)	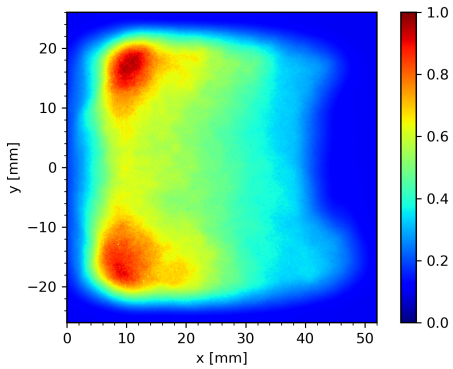	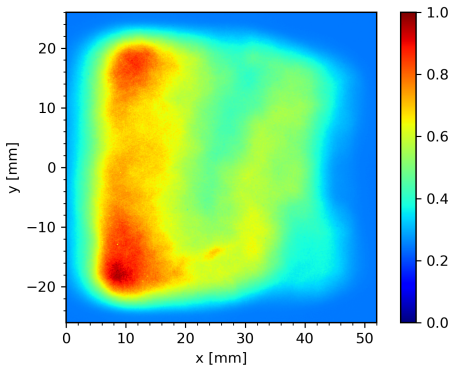

5.5 Conclusions

The design and development of new SAF is a process that must consider various aspects of the operability of aircraft engines. As we have already seen, an aircraft's reignition process at altitude differs from when it is done on the ground. Specifically, during the pull-away phase, we have seen that the operating conditions in the combustion chamber (HP compressor) evolve until idle conditions are reached. In order to evaluate the suitability of BL as a kerosene additive, we have studied the combustion process of different blends of kerosene and butyl levulinate inside a combustion chamber that works with an injection system identical to those used in aircraft gas turbines. Our study considered the real conditions to which kerosene is exposed during the pull-away phase at altitude, i.e., low pressures and temperatures. Our main objective was to determine how adding BL affects kerosene's operating limits and its combustion efficiency.

Our evaluation began with the determination of the lower heating value (LHV), density, viscosity, and surface tension of pure kerosene, a blend of 80% kerosene and 20% BL (Kero/$BL_{80/20}$), another of 50% kerosene and 50% BL (Kero/$BL_{50/50}$), and pure BL. Our results showed that the LHV of kerosene is reduced by 9%, 21%, and 35% due to the addition of BL, respectively. Regarding viscosity, there is a difference between pure kerosene and pure BL, and this difference becomes more important at low temperatures. As expected, the blend of 80% kerosene and 20% BL (Kero/$BL_{80/20}$) is the most similar to kerosene in all physical properties.

We established a methodology that allows us to compare combustion efficiency at different operating conditions, i.e., the inlet pressure and temperature, for different fuels based on the pressure drop across a nozzle. In our work, we measure the combustion efficiency of the different blends Kero/BL at OP_1 (293 K and 103 kPa) and OP_3 (258 K and 54 kPa) operating conditions. Our results showed that under OP_1 conditions, the operating limits, i.e., the value of the critical equivalence ratio and the extinction limit, for pure kerosene, Kero/$BL_{80/20}$, and Kero/$BL_{50/50}$ blend, are very similar. Where the different results correspond to pure BL, on the other hand, there is a marked difference at OP_3 operating conditions for all the blends Kero/BL, being the results obtained from blend Kero/$BL_{80/20}$ similar to pure kerosene.

The data we obtained show that there is a linear relationship between the viscosity of the fuel at a given operating condition and the lean extinction limit of fuel, i.e., the more the viscosity of the fuel increases, the more its operability range is reduced. Thanks to the comparison we made with the data obtained by M. Clavel related to the extinction limits of kerosene, we can conclude that for a given injection system, the extinction limits, ϕ_{ext}, have a linear relationship with fuel viscosity. ϕ_{ext} increases if viscosity increases either by a decrease in temperature or due to the replacement of the fuel by another with higher viscosity. Regarding pollutant emissions, we see that adding BL to kerosene significantly reduces the NO_x emissions and keeps more or less constant CO emissions. Nevertheless, CO emissions coming from pure BL combustion are considerably higher in the degraded region.

The local analysis of spray and flame structure shows that at the OP_1 operating conditions, pure kerosene and mixtures Kero/$BL_{80/20}$ and Kero/$BL_{50/50}$ have similar behavior in both the nominal and degraded regions. Whereas at OP_3 conditions, we can see that the fluctuations of the atomization spray (angle) increase considerably, and the flame structure is different for each blend Kero/BL. Given the method of analysis used to analyze the flame structure, we know that there is a possibility that our measurements were affected by CO_2^* and soot noise signals. For this reason, this study related to the flame structure can be considered preliminary for subsequent implementation of planar laser-induced fluorescence over OH^* radicals (PLIH-OH) for a correct characterization of the flame structure.

Finally, based on all our measurements and analyses, we can conclude that adding butyl levulinate up to 20%, in mass proportions, does not significantly affect the operating limits of kerosene at the operating conditions studied. We present in Table 5.20 a comparison between all the blends Kero/BL considered during the combustion assessment.

Table 5.20 Kero/BL blends comparison summary.

Properties	**ASTM**[1]	**Kerosene**	**Kero/$BL_{80/20}$**	**Kero/$BL_{50/50}$**	**BL**
LHV [MJ/kg]	43.2-42.9	45.3	42.1	37.2	29.2
Density [kg/m^3] at 288 K	840-775	789.3	824.5	880.9	977.9
Energy density [MJ/m^3]	36288-33248	35755	34711	32770	28555
Viscosity [mm^2/s] at 253 K	Max 8.0	(2.2-1.3)[2]	(2.8-1.5)2	(4.0-1.9)[2]	(7.3-3.0)[2]
ϕ_{crit} [-] at OP_1	-	0.27	0.26	0.25	0.40
ϕ_{crit} [-] at OP_3	-	0.43	0.42	0.45	0.56
ϕ_{ext} [-] at OP_1	-	0.20	0.19	0.20	0.22
ϕ_{ext} [-] at OP_3	-	0.37	0.38	0.42	0.50
θ $[^o]$[3] at OP_1	-	81.6±5.9	74.2±5.6	77.7±5.3	77.0±10.0
θ $[^o]$[3] at OP_3	-	83.6±26.4	75.3±37.3	71.0±39.4	-
δ [mm][3] at OP_1	-	2.94±0.55	3.64±0.63	3.63±0.63	4.08±0.62
δ [mm][3] at OP_3	-	3.76±1.50	4.17±1.67	4.42±1.70	-
θ $[^o]$[4] at OP_1	-	63.3±12.0	55.1±21.6	54.1±29.0	52.9±18.3
θ $[^o]$[4] at OP_3	-	61.2±18.9	72.2±15.8	60.1±20.2	-
δ [mm][4] at OP_1	-	3.90±0.90	4.60±1.27	3.69±1.33	5.94±1.26
δ [mm][4] at OP_3	-	4.65±1.43	4.08±1.15	4.83±1.57	-

[1]Standard for jet A-1 fuel.
[2]These values correspond to the temperature range 258-293 K.
[3]Nominal region values, where $\eta_{comb} \cong 1$.
[4]Degraded region values, where $\eta_{comb} < 1$.

Chapter 6
General Conclusions and Perspectives

Lignocellulosic biomass (LCB) is a renewable feedstock that can be transformed into various high-value products, such as materials, fuels, and other high-value chemicals. In this work, we have proposed a promising route for the complete valorization of this type of biomass, Figure 1.10, which shows how the main components of LCB (cellulose, hemicellulose, and lignin) can be transformed into sustainable aviation fuels (SAF). Cellulose and hemicellulose can be used to produce alkyl levulinates, which in turn are used to produce gamma-valerolactone (GVL), which can then be used for the production of paraffin, olefins, and aromatic compounds. The remaining component of LCB, lignin, is a source for the production of aromatic compounds.

Thus, thanks to this valorization route, we can produce the main components of kerosene: olefins, paraffins, and aromatic compounds. Therefore, it would be possible to produce sustainable aviation fuel from LCB capable of replacing conventional kerosene from fossil oil and reduce greenhouse gas (GHG) emissions thanks to LCB's life cycle. In addition, an advantage of this valorization route lies in the production of gamma-valerolactone (GVL). GVL is considered a high-value platform molecule due to its diverse applications; it can be used as a solvent or additive and as a raw material. Therefore, this route not only covers the need for a sustainable aviation fuel but also has the potential to meet other demands of modern society, such as the production of other types of fuels (gasoline and diesel), solvents, polymers, etc.

The industrial-scale implementation of this valorization route is limited in the short term, first due to the large number of transformation stages needed and the lack of information on some of the transformation stages. Our work was focused on covering part of these limitations, mainly two aspects, of which their conclusions and perspectives are presented below.

6.1 GVL Production from BL

The production of GVL from BL is a fundamental stage in the valorization route to transform LCB into SAF. This transformation stage connects the LCB derivatives with the SAF production process from GVL. Given the importance of the production of GVL from BL and the different applications of GVL as a platform molecule, its production at an industrial scale is of great importance from a social and environmental point of view.

The chemical reaction, described in Chapter 3, shows that GVL production via hydrogenation of BL over Ru/C takes place in two steps. The first one is the hydrogenation step, and the second is the cyclization step. Through the use of different calorimeter reactors, we measured the energy that is released or absorbed in each of these steps. The energy released during the hydrogenation step is $\mathbf{\Delta H_{hyd}} = -35.28\,kJ/mol \pm 1.00\,kJ/mol$, and the energy absorbed during the cyclization step is equal to $\mathbf{\Delta H_{cyc}} = 6.34\,kJ/mol \pm 0.93\,kJ/mol$. This shows that the hydrogenation step is an exothermic reaction while the cyclization step is an endothermic reaction, where exothermic behavior dominates.

In this part, our main objective was to develop an advanced kinetic model considering isothermal and non-isothermal operating conditions, i.e., isothermal, isoperibolic, and adiabatic conditions. These types of models are capable of predicting the yield of the reaction as well as the thermal risk linked to the reaction. According to our results, the Non-Competitive Langmuir-Hinshelwood kinetic models are suitable to predict the evolution of GVL concentration and reaction temperature in heterogeneous systems. It should be noted that there were no indications or evidence of decomposition reactions in the operating range tested during the experiments carried out under adiabatic conditions, where the thermal risk is highest. The development of this type of kinetic model, in both isothermal and non-isothermal conditions, makes it possible to optimize reactant conversion and energy recovery and reduce the risk of accidents due to thermal runaway.

We have assessed the thermal stability of the production of GVL in a continuous stirred tank reactor (CSTR). This assessment applied the Van-Heerden criterion, the steady state bifurcations, the dynamic thermal stability criterion, and the parametric sensitivity analysis to determine the safest conditions to perform this reaction in a CSTR. The results obtained showed that for values of $\mathbf{Ua} > 1500\,\mathrm{W/m^3/K}$ the risk of runaway due to thermal instabilities is minimized. Finally, we can conclude that the production of GVL is possible from the hydrogenation of BL over Ru/C, and the thermal risk linked to this reaction is moderate because the energy released is relatively low and is also compensated by the endothermic effects of the cyclization step-reaction. Therefore, the risk of runaway is quite low in a continuous reactor, even for relatively small values of **Ua**.

6.1.1 Perspectives

In the valorization route of lignocellulosic biomass (LCB) into sustainable aviation fuels (SAF), the next stage is to study the butenes production from gamma-valerolactone (GVL) and their subsequent oligomerization to produce paraffin, olefins, and aromatic compounds. Some aspects that may help to complement the work we have done are presented below.

While estimating the kinetic parameters, we found that our estimation method, quadratic regression based on Bayesian statistics and the quasi-newton algorithm, had problems estimating the adsorption equilibrium constants of the different compounds. That is why we propose a research focused on determining these equilibrium constants; this research can be based on quantum mechanics or the application of machine learning.

Another interesting aspect is the influence of thermal modes, i.e., isothermal, isoperibolic, and adiabatic experiments, in the estimated parameters. This means to address questions like: What is the appropriate number of experiments to be carried out in isothermal and non-isothermal conditions to have the optimal kinetic parameters? Is a kinetic model developed only with adiabatic experiments as robust and accurate as one developed only with isoperibolic experiments? etc.

Regarding the analysis of the thermal stability of a continuous stirrer-tank reactor (CSTR), our work was limited to simulation results. An experimental validation of the results obtained would help to strengthen the viability of the industrial implementation of this chemical reaction. Thermal stability during the non-stationary period can also be studied, as well as the study of thermal risk in tubular reactors.

6.2 BL as Kerosene Additive

The short-term implementation of SAF production from LCB at an industrial scale is challenging due to the many transformation stages required. To achieve greenhouse gas (GHG) reduction targets in the aviation sector, it is worth exploring the potential use as a kerosene additive of different LCB derivatives. In our case, this exploration was focused on butyl levulinate (BL), which is a derivative of LCB.

Our study consisted of the evaluation of BL as a kerosene additive. Our goal was to determine how adding BL affected the operating limits of kerosene during combustion. For these purposes, we studied four blends: pure kerosene, 80% kerosene and 20% BL (Kero/$BL_{80/20}$), 50% kerosene and 50% BL (Kero/$BL_{50/50}$), and pure BL. The combustion assessment of these four blends was carried out in a combustion chamber capable of operating under low pressure and low-temperature conditions. Similar to the combustion conditions of aircraft engines at high altitudes during the pull-away phase.

Butyl levulinate has a lower heating value (LHV) that is 35% lower than kerosene. Adding BL to kerosene reduces its lower heating value by 9% and 21% when 20% and 50% of butyl levulinate are added, respectively. Another point to highlight is that BL has a higher density than kerosene; this compensates a little for its lower heating value. For example, in 1 m^3 at 293 K, the energy content of kerosene, Kero/$BL_{80/20}$, Kero/$BL_{50/50}$ and pure BL are: 35559 MJ, 33969 MJ, 31292 MJ, and 28414 MJ, respectively. This represents a reduction 4%, 12% and 20% for Kero/$BL_{80/20}$, Kero/$BL_{50/50}$ and pure BL compare kerosene. In terms of viscosity, we could see that there is a considerable difference between pure kerosene and pure BL, which becomes considerably greater as the temperature decreases, but the blend Kero/$BL_{80/20}$ has similar values even at temperatures around 263 K.

Based on our methodology to calculate the combustion efficiency, at standard conditions of pressure and temperature (OP_1), the operating limits of pure kerosene, Kero/$BL_{80/20}$ and Kero/$BL_{50/50}$ are very similar. However, under low pressure and low temperature (OP_3) conditions, we noted that the operating limits for the 4 blends Kero/BL are different, being the closest one to kerosene the ones for the blend Kero/$BL_{80/20}$. According to our results, for the same operating point (pressure and temperature), there is a linear trend between the extinction limit and the fuel viscosity. This shows that viscosity, driven by temperature, plays an important role in the operating limits of a gas turbine engine. Another important point to note is that the addition of BL to kerosene decreases carbon dioxide (CO_2) emissions and especially nitrogen oxides (NO_x) emissions.

From the local analysis, i.e., laser tomography and chemiluminescence, we obtained that atomization spray and flame structure for kerosene and the blend Kero/$BL_{80/20}$ are similar. Nevertheless, the fluctuations in the angle of the atomization spray are more important for the blend Kero/$BL_{80/20}$ at low temperatures, reinforcing the conclusion that viscosity is the parameter that most influence the combustion efficiency in a gas turbine.

Finally, we conclude that the blend Kero/$BL_{80/20}$ has physical and energy properties similar to kerosene. The operating limits of this blend, even at OP_3 operating conditions, are close to those of pure kerosene. Based on our results, BL can be added up to 20% to kerosene without drastically affecting its operating limits.

6.2.1 Perspectives

According to our literature review, BL is the most promising intermediate compound as an additive for kerosene in our valorization route. However, it does not guarantee that BL is the only one with potential applications as a kerosene additive. Therefore, exploring other potential additives obtained from lignocellulosic biomass (LCB) is an open question. The advantage is that the HARTur facility can test other SAF.

The perspectives are to study the operating limits of the blends Kero/BL at the missing operating conditions in HARTur facility, i.e., at OP_2 and OP_4, to determine the operating limits at these conditions, and to verify if the linear trend between fuel viscosity and extinction limits is maintained. And also to analyze the behavior of the flame rate when the viscosity increases due to a decrease in temperature versus an increase in viscosity due to the addition of viscous compounds.

When temperature decreases, spray instabilities increase. Such types of instabilities may influence the behavior of the flow inside the combustion chamber. An analysis of the combustion chamber's flow may help us better understand why operating limits are reduced at low temperatures. Thus, we suggest a PIV (Particle Image Velocimetry) analysis to characterize the flow inside the combustion chamber for the different blends of Kero/BL at low-temperature conditions.

Another perspective is implementing PLIF-OH (planar laser-induced fluorescence on OH^* radicals) to characterize the flame structure. Since the technique we implemented is limited and there is a possibility that our results have been interfered with CO_2 emissions.

Our study assessed the operating limits during the pull-away phase at low pressures and temperatures. However, after the pull-away phase, the thrust generation by burning fuel will change the operating conditions in the combustion chamber. The operating conditions become high pressures and temperatures; therefore, an experimental study of the combustion process of blends Kero/BL would be the ideal complement to determine the potential use of blends Kero/BL in current aircraft engines. This type of study can be performed in the Heron (High-pressure facility for aero-engines combustion) facility at the CORIA research unit [138].

References

[1] Destination zero: The technology journey to 2050 - ati 2022 technology strategy.

[2] Integration of sustainable aviation fuels into the air transport system.

[3] Furkan H. Isikgor and C. Remzi Becer. Lignocellulosic biomass: a sustainable platform for the production of bio-based chemicals and polymers. *Polym. Chem.*, 6:4497–4559, 2015.

[4] Khwaja Alamgir Ahmad, Mohammad Haider Siddiqui, Kamal K. Pant, K.D.P. Nigam, Nagaraj P. Shetti, Tejraj M. Aminabhavi, and Ejaz Ahmad. A critical review on suitability and catalytic production of butyl levulinate as a blending molecule for green diesel. *Chemical Engineering Journal*, 447:137550, 2022.

[5] David Martin Alonso, Stephanie G. Wettstein, and James A. Dumesic. Gamma-valerolactone, a sustainable platform molecule derived from lignocellulosic biomass. *Green Chem.*, 15:584–595, 2013.

[6] Zhihao Yu, Xuebin Lu, Chen Liu, Yiwen Han, and Na Ji. Synthesis of γ-valerolactone from different biomass-derived feedstocks: Recent advances on reaction mechanisms and catalytic systems. *Renewable and Sustainable Energy Reviews*, 112:140–157, 2019.

[7] Marie-Eve Clavel. *Étude expérimentale des interactions spray, flamme et turbulence dans des conditions de rallumage en altitude: Application à des injecteurs RQL.* PhD thesis, École Doctorale Physique, Science de l'ingénieur,Matériaux, Énergie, 2023.

[8] Turbomeca and Snecma Group. Gas turbine engines. 2004.

[9] Reza Alidoost Dafsari, Hyung Ju Lee, Jeongsik Han, Dong-Chang Park, and Jeekeun Lee. Viscosity effect on the pressure swirl atomization of an alternative aviation fuel. *Fuel*, 240:179–191, 2019.

[10] Frederico Afonso, Martin Sohst, Carlos M.A. Diogo, Simão S. Rodrigues, Ana Ferreira, Inês Ribeiro, Ricardo Marques, Francisco F.C. Rego, Abdolrasoul Sohouli, Joana Portugal-Pereira, Hugo Policarpo, Bruno Soares, Bruna Ferreira, Edgar C. Fernandes, Fernando Lau, and Afzal Suleman. Strategies towards a more sustainable aviation: A systematic review. *Progress in Aerospace Sciences*, 137:100878, 2023.

[11] Ivo Abrantes, Ana F. Ferreira, André Silva, and Mário Costa. Sustainable aviation fuels and imminent technologies - co2 emissions evolution towards 2050. *Journal of Cleaner Production*, 313:127937, 2021.

[12] Junmeng Cai, Yifeng He, Xi Yu, Scott W. Banks, Yang Yang, Xingguang Zhang, Yang Yu, Ronghou Liu, and Anthony V. Bridgwater. Review of physicochemical properties and analytical characterization of lignocellulosic biomass. *Renewable and Sustainable Energy Reviews*, 76:309–322, 2017.

[13] Peng Wu, Changlin Miao, Xinshu Zhuang, Wuhuan Li, Xuesong Tan, and Tianhua Yang. Physicochemical characterization of levulinate esters with different alkyl chain lengths blended with fuel. *Energy Science & Engineering*, 11(1):164–177, 2023.

[14] Earl Christensen, Aaron Williams, Stephen Paul, Steve Burton, and Robert L. McCormick. Properties and performance of levulinate esters as diesel blend components. *Energy & Fuels*, 25(11):5422–5428, 2011.

[15] Shanta Dutta, Iris K.M. Yu, Daniel C.W. Tsang, Yun Hau Ng, Yong Sik Ok, James Sherwood, and James H. Clark. Green synthesis of gamma-valerolactone (gvl) through hydrogenation of biomass-derived levulinic acid using non-noble metal catalysts: A critical review. *Chemical Engineering Journal*, 372:992–1006, 2019.

[16] Xing Tang, Xianhai Zeng, Zheng Li, Lei Hu, Yong Sun, Shijie Liu, Tingzhou Lei, and Lu Lin. Production of γ-valerolactone from lignocellulosic biomass for sustainable fuels and chemicals supply. *Renewable and Sustainable Energy Reviews*, 40:608–620, 2014.

[17] Daniele Di Menno Di Bucchianico, Jean-Christophe Buvat, Mélanie Mignot, Valeria Casson Moreno, and Sébastien Leveneur. Role of solvent in enhancing the production of butyl levulinate from fructose. *Fuel*, 318:123703, 2022.

[18] Juliet Davenport and Nick Wayth. Statistical review of world energy. Technical report, Energy Institute, 2023.

[19] Robert Polack, Shelly Wood, and Kimyatta N. Smith. An analysis of fossil-fuel dependence in the united states with implications for community social work. *Critical Social Work*, 11, 2010.

[20] Michael McGovern, Sophie Heald, and Jamie Pirie. A study for transport and environment oil dependency in the eu. Technical report, Cambridge Econometrics, 2020.

[21] Adam Mayer. Fossil fuel dependence and energy insecurity. *Energy, Sustainability and Society*, 12:27, 2022.

[22] Binod Sharma and Ashish Shrestha. Petroleum dependence in developing countries with an emphasis on nepal and potential keys. *Energy Strategy Reviews*, 45:101053, 2023.

[23] Sivasubramanian Manikandan, Sundaram Vickram, Ranjna Sirohi, Ramasamy Subbaiya, Radhakrishnan Yedhu Krishnan, Natchimuthu Karmegam, C. Sumathijones, Rajinikanth Rajagopal, Soon Woong Chang, Balasubramani Ravindran, and Mukesh Kumar Awasthi. Critical review of biochemical pathways to transformation of waste and biomass into bioenergy. *Bioresource Technology*, 372:128679, 2023.

[24] Bosco Amerit, Joseph M. Ntayi, Muhammed Ngoma, Hassan Bashir, Simon Echegu, and Maria Nantongo. Commercialization of biofuel products: A systematic literature review. *Renewable Energy Focus*, 44:223–236, 2023.

[25] Yiyuan Jiang, Zao Li, Yuncong Li, Long Chen, Heng Zhang, Hu Li, and Song Yang. Recent advances in sustainable catalytic production of 5-methyl-2-pyrrolidones from bio-derived levulinate. *Fuel*, 334:126629, 2023.

[26] Veeramuthu Ashokkumar, Radhakrishnan Venkatkarthick, Shanmugam Jayashree, Santi Chuetor, Selvakumar Dharmaraj, Gopalakrishnan Kumar, Wei-Hsin Chen, and Chawalit Ngamcharussrivichai. Recent advances in lignocellulosic biomass for biofuels and value-added bioproducts - a critical review. *Bioresource Technology*, 344:126195, 2022.

[27] Wu-Jun Liu and Han-Qing Yu. Thermochemical conversion of lignocellulosic biomass into mass-producible fuels: Emerging technology progress andenvironmental sustainability evaluation. *ACS Environmental Au*, 2(2):98–114, 2022.

[28] Julia Tomei and Richard Helliwell. Food versus fuel? going beyond biofuels. *Land Use Policy*, 56:320–326, 2016.

[29] Farrukh Jamil, Muhammad Saleem, Obaid Ali Qamar, M Shahzad Khurram, Ala'a H Al-Muhtaseb, Abrar Inayat, Parveen Akhter, Murid Hussain, Sikander Rafiq, Hyunji Yim, and Young-Kwon Park. State-of-the-art catalysts for clean fuel (methyl esters) production—a comprehensive review. *Journal of Physics: Energy*, 5(1):014005, dec 2022.

[30] Anuj K. Chandel, Vijay Kumar Garlapati, S. P. Jeevan Kumar, Meenu Hans, Akhilesh K. Singh, and Sachin Kumar. The role of renewable chemicals and biofuels in building a bioeconomy. *Biofuels, Bioproducts and Biorefining*, 14(4):830–844, 2020.

[31] Bikash Kumar and Pradeep Verma. Biomass-based biorefineries: An important architype towards a circular economy. *Fuel*, 288:119622, 2021.

[32] Debalina Sengupta and Ralph W. Pike. *Chemicals from Biomass: Integrating Bioprocesses into Chemical Production Complexes for Sustainable Development*. CRC Press, 1st edition, 2012.

[33] Mustafa Balat, Havva Balat, and Cahide Öz. Progress in bioethanol processing. *Progress in Energy and Combustion Science*, 34(5):551–573, 2008.

[34] Ayhan Demirbas. Competitive liquid biofuels from biomass. *Applied Energy*, 88(1):17–28, 2011.

[35] Hazariah M. Noh, Arturo Benito, and Gustavo Alonso. Study of the current incentive rules and mechanisms to promote biofuel use in the eu and their possible application to the civil aviation sector. *Transportation Research Part D: Transport and Environment*, 46:298–316, 2016.

[36] Kok Siew Ng, Danial Farooq, and Aidong Yang. Global biorenewable development strategies for sustainable aviation fuel production. *Renewable and Sustainable Energy Reviews*, 150:111502, 2021.

[37] Inc. Coordinating Research Council. Handbook of aviation fuel properties. Technical report, Society of Automotive Engineers Publications Department, 2004 Third Edition.

[38] *Gas Turbine Combustion, Alternative Fuels and Emissions*. Taylor & Francis Group, 2010.

[39] Adenise Lorenci Woiciechowski, Carlos José Dalmas Neto, Luciana Porto de Souza Vandenberghe, Dão Pedro de Carvalho Neto, Alessandra Cristine Novak Sydney, Luiz Alberto Junior Letti, Susan Grace Karp, Luis Alberto Zevallos Torres, and Carlos Ricardo Soccol. Lignocellulosic biomass: Acid and alkaline pretreatments and their effects on biomass recalcitrance – conventional processing and recent advances. *Bioresource Technology*, 304:122848, 2020.

[40] Muhammad Mujtaba, Leonardo Fernandes Fraceto, Mahyar Fazeli, Sritama Mukherjee, Susilaine Maira Savassa, Gerson Araujo de Medeiros, Anderson do Espírito Santo Pereira, Sandro Donnini Mancini, Juha Lipponen, and Francisco Vilaplana. Lignocellulosic biomass from agricultural waste to the circular economy: a review with focus on biofuels, biocomposites and bioplastics. *Journal of Cleaner Production*, 402:136815, 2023.

[41] Jipeng Yan, Oluwafemi Oyedeji, Juan H. Leal, Bryon S. Donohoe, Troy A. Semelsberger, Chenlin Li, Amber N. Hoover, Erin Webb, Elizabeth A. Bose, Yining Zeng, C. Luke Williams, Kastli D. Schaller, Ning Sun, Allison E. Ray, and Deepti Tanjore. Characterizing variability in lignocellulosic biomass: A review. *ACS Sustainable Chemistry & Engineering*, 8(22):8059–8085, 2020.

[42] Lei Ye, Yiwen Han, Jing Feng, and Xuebin Lu. A review about gvl production from lignocellulose: Focusing on the full components utilization. *Industrial Crops and Products*, 144:112031, 2020.

[43] Sivasamy Sethupathy, Gabriel Murillo Morales, Lu Gao, Hongliang Wang, Bin Yang, Jianxiong Jiang, Jianzhong Sun, and Daochen Zhu. Lignin valorization: Status, challenges and opportunities. *Bioresource Technology*, 347:126696, 2022.

[44] Filippo Brienza, David Cannella, Diego Montesdeoca, Iwona Cybulska, and Damien P. Debecker. A guide to lignin valorization in biorefineries: traditional, recent, and forthcoming approaches to convert raw lignocellulose into valuable materials and chemicals. *RSC Sustain.*, 2:37–90, 2024.

[45] Long Yan, Qian Yao, and Yao Fu. Conversion of levulinic acid and alkyl levulinates into biofuels and high-value chemicals. *Green Chem.*, 19:5527–5547, 2017.

[46] Shireen Quereshi, Ejaz Ahmad, K.K. Pant, and Suman Dutta. Insights into the metal salt catalyzed ethyl levulinate synthesis from biorenewable feedstocks. *Catalysis Today*, 291:187–194, 2017. Catalysis for Clean Energy and Environmentally Friendly Chemical Production.

[47] Daniele Di Menno Di Bucchianico, Yanjun Wang, Jean-Christophe Buvat, Yong Pan, Valeria Casson Moreno, and Sébastien Leveneur. Production of levulinic acid and alkyl levulinates: a process insight. *Green Chem.*, 24:614–646, 2022.

[48] Manik Kumer Ghosh, Mícheál Séamus Howard, Yingjia Zhang, Khalil Djebbi, Gianluca Capriolo, Aamir Farooq, Henry J. Curran, and Stephen Dooley. The combustion kinetics of the lignocellulosic biofuel, ethyl levulinate. *Combustion and Flame*, 193:157–169, 2018.

[49] Jinfan Yang, Guangyi Li, Lulu Zhang, and Sufeng Zhang. Efficient production of n-butyl levulinate fuel additive from levulinic acid using amorphous carbon enriched with oxygenated groups. *Catalysts*, 8(1), 2018.

[50] Jimmy Nelson Appaturi, Mohd Rafie Johan, R. Jothi Ramalingam, Hamad A. Al-Lohedan, and J. Judith Vijaya. Efficient synthesis of butyl levulinate from furfuryl alcohol over ordered mesoporous ti-kit-6 catalysts for green chemistry applications. *RSC Adv.*, 7:55206–55214, 2017.

[51] Dhara H. Morawala, Dharmesh R. Lathiya, Ajay K. Dalai, and Kalpana C. Maheria. Ttab mediated synthesis of meso-h-bea and its application in the production of n-butyl levulinate. *Catalysis Today*, 348:177–186, 2020. SI: Catalysts and Catalysis.

[52] Daniele Di Menno Di Bucchianico, Mélanie Mignot, Jean-Christophe Buvat, Valeria Casson Moreno, and Sébastien Leveneur. Production of butyl levulinate from the solvolysis of high-gravity fructose over heterogeneous catalyst: In-depth kinetic modeling. *Chemical Engineering Journal*, 465:142914, 2023.

[53] Sravanthi Veluturla, Archna Narula, Saddam Sharieff, and Ashwini N. Continuous flow synthesis of butyl levulinate using a microreactor –rtd and kinetic studies. *Current Research in Green and Sustainable Chemistry*, 5:100281, 2022.

[54] Earl Christensen, Janet Yanowitz, Matthew Ratcliff, and Robert L. McCormick. Renewable oxygenate blending effects on gasoline properties. *Energy & Fuels*, 25(10):4723–4733, 2011.

[55] Gourav Shrivastav, Tuhin S. Khan, Manish Agarwal, and M. Ali Haider. Reformulation of gasoline to replace aromatics by biomass-derived alkyl levulinates. *ACS Sustainable Chemistry & Engineering*, 5(8):7118–7127, 2017.

[56] Christopher J. Chuck and Joseph Donnelly. The compatibility of potential bioderived fuels with jet a-1 aviation kerosene. *Applied Energy*, 118:83–91, 2014.

[57] Tirath Raj, K. Chandrasekhar, Rajesh Banu, Jeong-Jun Yoon, Gopalakrishnan Kumar, and Sang-Hyoun Kim. Synthesis of γ-valerolactone (gvl) and their applications for lignocellulosic deconstruction for sustainable green biorefineries. *Fuel*, 303:121333, 2021.

[58] Jesse Q. Bond, David Martin Alonso, Dong Wang, Ryan M. West, and James A. Dumesic. Integrated catalytic conversion of γ-valerolactone to liquid alkenes for transportation fuels. *Science*, 327(5969):1110–1114, 2010.

[59] Stephanie G. Wettstein, David Martin Alonso, Yuxuan Chong, and James A. Dumesic. Production of levulinic acid and gamma-valerolactone (gvl) from cellulose using gvl as a solvent in biphasic systems. *Energy Environ. Sci.*, 5:8199–8203, 2012.

[60] Yanjun Wang, Igor Plazl, Lamiae Vernières-Hassimi, and Sébastien Leveneur. From calorimetry to thermal risk assessment: γ-valerolactone production from the hydrogenation of alkyl levulinates. *Process Safety and Environmental Protection*, 144:32–41, 2020.

[61] István T. Horváth, Hasan Mehdi, Viktória Fábos, László Boda, and László T. Mika. γ-valerolactone—a sustainable liquid for energy and carbon-based chemicals. *Green Chem.*, 10:238–242, 2008.

[62] Ákos Bereczky, Kristóf Lukács, Mária Farkas, and Sándor Dóbé. Effect of γ-valerolactone blending on engine performance, combustion characteristics and exhaust emissions in a diesel engine. *Natural Resources*, 5(5):177–191, 2014.

[63] Daolai Sun, Takeshi Saito, Shota Otsuka, Tomohiro Ozawa, Yasuhiro Yamada, and Satoshi Sato. Selective hydrogenation of γ-valerolactone to 2-methyltetrahydrofuran over cu/al2o3 catalyst. *Applied Catalysis A: General*, 590:117309, 2020.

[64] David Martin Alonso, Jesse Q. Bond, Juan Carlos Serrano-Ruiz, and James A. Dumesic. Production of liquid hydrocarbon transportation fuels by oligomerization of biomass-derived c9 alkenes. *Green Chem.*, 12:992–999, 2010.

[65] Elif I. Gürbüz, David Martin Alonso, Jesse Q. Bond, and James A. Dumesic. Reactive extraction of levulinate esters and conversion to γ-valerolactone for production of liquid fuels. *ChemSusChem*, 4(3):357–361, 2011.

[66] Leo E Manzer. Catalytic synthesis of α-methylene-γ-valerolactone: a biomass-derived acrylic monomer. *Applied Catalysis A: General*, 272(1):249–256, 2004.

[67] Jean-Paul Lange, Jan Z. Vestering, and René J. Haan. Towards 'bio-based' nylon: conversion of γ-valerolactone to methyl pentenoate under catalytic distillation conditions. *Chem. Commun.*, pages 3488–3490, 2007.

[68] Zhi-pei Yan, Lu Lin, and Shijie Liu. Synthesis of γ-valerolactone by hydrogenation of biomass-derived levulinic acid over ru/c catalyst. *Energy & Fuels*, 23(8):3853–3858, 2009.

[69] Omar Ali Abdelrahman, Andreas Heyden, and Jesse Q. Bond. Analysis of kinetics and reaction pathways in the aqueous-phase hydrogenation of levulinic acid to form γ-valerolactone over ru/c. *ACS Catalysis*, 4(4):1171–1181, 2014.

[70] Pravin P. Upare, Jong-Min Lee, Dong Won Hwang, Shiva B. Halligudi, Young Kyu Hwang, and Jong-San Chang. Selective hydrogenation of levulinic acid to γ-valerolactone over carbon-supported noble metal catalysts. *Journal of Industrial and Engineering Chemistry*, 17(2):287–292, 2011.

[71] Ruimei Cao, Jiayu Xin, Zhan Zhang, Zhuo Liu, Xingmei Lu, Baozeng Ren, and Suojiang Zhang. Efficient conversion of α-angelica lactone into γ-valerolactone with ionic liquids at room temperature. *ACS Sustainable Chemistry & Engineering*, 2(4):902–909, 2014.

[72] M. Chalid, A.A. Broekhuis, and H.J. Heeres. Experimental and kinetic modeling studies on the biphasic hydrogenation of levulinic acid to γ-valerolactone using a homogeneous water-soluble ru–(tppts) catalyst. *Journal of Molecular Catalysis A: Chemical*, 341(1):14–21, 2011.

[73] Yuxuan Yi, Huiying Liu, Ling-Ping Xiao, Bo Wang, and Guoyong Song. Highly efficient hydrogenation of levulinic acid into γ-valerolactone using an iron pincer complex. *ChemSusChem*, 11(9):1474–1478, 2018.

[74] Eleni Anagnostopoulou, Panagiotis Lilas, Perikleia Diamantopoulou, Christos Fakas, Ioannis Krithinakis, Eleni Patatsi, Elpida Gabrielatou, Antoine P. van Muyden, Paul J. Dyson, and Georgios Papadogianakis. Hydrogenation of the pivotal biorefinery platform molecule levulinic acid into renewable fuel γ-valerolactone catalyzed by unprecedented highly active and stable ruthenium nanoparticles in aqueous media. *Renewable Energy*, 192:35–45, 2022.

[75] Carmen Moreno-Marrodan and Pierluigi Barbaro. Energy efficient continuous production of γ-valerolactone by bifunctional metal/acid catalysis in one pot. *Green Chem.*, 16:3434–3438, 2014.

[76] María S. Leguizamón-Aparicio, Juan J. Musci, Maia Montaña, Leticia J. Méndez, María L. Barbelli, Elena Rodríguez-Aguado, Juan A. Cecilia, Enrique Rodríguez-Castellón, Ileana D. Lick, and Mónica L. Casella. High-performance supported ru catalysts for the aqueous-phase hydrogenation of levulinic acid to γ-valerolactone. *ChemCatChem*, n/a(n/a):e202301719, 2023.

[77] Deyang Zhao, Yantao Wang, Frederic Delbecq, and Christophe Len. Continuous flow conversion of alkyl levulinates into γ-valerolactone in the presence of ru/c as catalyst. *Molecular Catalysis*, 475:110456, 2019.

[78] Sarah Capecci, Yanjun Wang, Jose Delgado, Valeria Casson Moreno, Mélanie Mignot, Henrik Grénman, Dmitry Yu. Murzin, and Sébastien Leveneur. Bayesian statistics to elucidate the kinetics of γ-valerolactone from n-butyl levulinate hydrogenation over ru/c. *Industrial & Engineering Chemistry Research*, 60(31):11725–11736, 2021.

[79] Haijun Guo, Shuai Ding, Hairong Zhang, Can Wang, Fen Peng, Lian Xiong, Xinde Chen, and Xinping Ouyang. Improvement on the catalytic performances of butyl levulinate hydrogenation to γ-valerolactone over self-regenerated cunicob/palygorskite catalyst. *Molecular Catalysis*, 504:111483, 2021.

[80] Fukun Li, Liam John France, Zhenping Cai, Yingwen Li, Sijie Liu, Hongming Lou, Jinxing Long, and Xuehui Li. Catalytic transfer hydrogenation of butyl levulinate to γ-valerolactone over zirconium phosphates with adjustable lewis and brønsted acid sites. *Applied Catalysis B: Environmental*, 214:67–77, 2017.

[81] Hongtao Wang, Yushan Wu, Tao Jin, Chenglong Dong, Jiebang Peng, Haochen Du, Yubin Zeng, and Mingyue Ding. Oriented conversion of γ-valerolactone to gasoline range fuels via integrated catalytic system. *Molecular Catalysis*, 498:111267, 2020.

[82] Jaewon Byun and Jeehoon Han. Impact of uncertainty in technological cycle on circular economy: Bio-based jet fuel range alkenes and pentanediols production. *Journal of Industrial and Engineering Chemistry*, 104:356–361, 2021.

[83] Yan Zhao, Yao Fu, and Qing-Xiang Guo. Production of aromatic hydrocarbons through catalytic pyrolysis of γ-valerolactone from biomass. *Bioresource Technology*, 114:740–744, 2012.

[84] M. Guisnet and N.S. Gnep. Mechanism of short-chain alkane transformation over protonic zeolites. alkylation, disproportionation and aromatization. *Applied Catalysis A: General*, 146(1):33–64, 1996. C2C5 Alkane Activation.

[85] Brendan Paxton. Systems design and experimental evaluation of a high-altitude relight test facility. Master's thesis, University of Cincinnati, 2015.

[86] Houda Ariba, Yanjun Wang, Christine Devouge-Boyer, Roumiana P. Stateva, and Sébastien Leveneur. Physicochemical properties for the reaction systems: Levulinic acid, its esters, and γ-valerolactone. *Journal of Chemical & Engineering Data*, 65(6):3008–3020, 2020.

[87] Xiaojia Lu, Yanjun Wang, Lionel Estel, Narendra Kumar, Henrik Grénman, and Sébastien Leveneur. Evolution of specific heat capacity with temperature for typical supports used for heterogeneous catalysts. *Processes*, 8(8), 2020.

[88] Michael Johnson, Peter J. Heggs, and Tariq Mahmud. Assessment of overall heat transfer coefficient models to predict the performance of laboratory-scale jacketed batch reactors. *Organic Process Research & Development*, 20(2):204–214, 2016.

[89] José Fernández-Seara, Francisco J. Uhía, Jaime Sieres, and Antonio Campo. A general review of the wilson plot method and its modifications to determine convection coefficients in heat exchange devices. *Applied Thermal Engineering*, 27(17):2745–2757, 2007.

[90] Helisoa Rakotondramaro, Johan Wärnå, Lionel Estel, Tapio Salmi, and Sébastien Leveneur. Cooling and stirring failure for semi-batch reactor: Application to exothermic reactions in multiphase reactor. *Journal of Loss Prevention in the Process Industries*, 43:147–157, 2016.

[91] Frédéric Lavanchy. *Development of Reaction Calorimetry applied to Supercritical CO2 and Methanol-CO2 critical mixture: Heat Transfer, Heat Flow and Hydrodynamics*. PhD thesis, École Polytechnique Fédérale de Lausanne, 2005.

[92] Yanjun Wang, Mariasole Cipolletta, Lamiae Vernières-Hassimi, Valeria Casson-Moreno, and Sébastien Leveneur. Application of the concept of linear free energy relationships to the hydrogenation of levulinic acid and its corresponding esters. *Chemical Engineering Journal*, 374:822–831, 2019.

[93] Khashayar Nasrifar. Comparative study of eleven equations of state in predicting the thermodynamic properties of hydrogen. *International Journal of Hydrogen Energy*, 35(8):3802–3811, 2010.

[94] Sarah Capecci, Yanjun Wang, Valeria Casson Moreno, Christoph Held, and Sébastien Leveneur. Solvent effect on the kinetics of the hydrogenation of n-butyl levulinate to γ-valerolactone. *Chemical Engineering Science*, 231:116315, 2021.

[95] Xuan-Tien Pham, Vy Anh Tran, Lan-Trinh Thi Tran, Tram Ngoc P. Nguyen, Thong Hoang Le, Huy Hoang, Thi-Hiep Nguyen, Khanh B. Vu, and Thanh Khoa Phung. Hierarchical porous activated carbon-supported ruthenium catalysts for catalytic cleavage of lignin model compounds. *Energies*, 15(22), 2022.

[96] *Introduction to Chemical Engineering Kinetics and Reactor Design*. John Wiley & Sons, Inc., Hoboken, New Jersey., 2014.

[97] Sebastian Matera, William F. Schneider, Andreas Heyden, and Aditya Savara. Progress in accurate chemical kinetic modeling, simulations, and parameter estimation for heterogeneous catalysis. *ACS Catalysis*, 9(8):6624–6647, 2019.

[98] Warren E. Stewart, Mike Caracotsios, and Jan P. Sørensen. Parameter estimation from multiresponse data. *AIChE Journal*, 38(5):641–650, 1992.

[99] Jan Kopyscinski, Jinsoon Choi, and Josephine M. Hill. Comprehensive kinetic study for pyridine hydrodenitrogenation on (ni)wp/sio2 catalysts. *Applied Catalysis A: General*, 445-446:50–60, 2012.

[100] M.A.J.S. VAN BOEKEL. Statistical aspects of kinetic modeling for food science problems. *Journal of Food Science*, 61(3):477–486, 1996.

[101] Makis Caracotsios and Warren E. Stewart. Sensitivity analysis of initial value problems with mixed odes and algebraic equations. *Computers & Chemical Engineering*, 9(4):359–365, 1985.

[102] Warren E. Stewart and Michael Caracotsios. Computer-aided modeling of reactive systems. 2008.

[103] Kenneth Toch, Joris W. Thybaut, and Guy B. Marin. A systematic methodology for kinetic modeling of chemical reactions applied to n-hexane hydroisomerization. *AIChE Journal*, 61(3):880–892, 2015.

[104] Alex Kummer and Tamás Varga. What do we know already about reactor runaway? – a review. *Process Safety and Environmental Protection*, 147:460–476, 2021.

[105] Jose Delgado, Wenel Naudy Vasquez Salcedo, Giulia Bronzetti, Valeria Casson Moreno, Mélanie Mignot, Julien Legros, Christoph Held, Henrik Grénman, and Sébastien Leveneur. Kinetic model assessment for the synthesis of γ-valerolactone from n-butyl levulinate and levulinic acid hydrogenation over the synergy effect of dual catalysts ru/c and amberlite ir-120. *Chemical Engineering Journal*, 430:133053, 2022.

[106] Sang Thanh Nguyen, Ngoc Ha Hoang, and Mohamed Azlan Hussain. Analysis of the steady-state multiplicity behavior for polystyrene production in the cstr. *Chemical Product and Process Modeling*, 12(4):20170027, 2017.

[107] Rowena Ball. Thermal oscillations in the decomposition of organic peroxides: Identification of a hazard, utilization, and suppression. *Industrial & Engineering Chemistry Research*, 52(2):922–933, 2013.

[108] Miguel Ángel Gómez García, Izabela Dobrosz-Gómez, and Juan Carlos Ojeda Toro. Thermal stability and dynamic analysis of the acetic anhydride hydrolysis reaction. *Chemical Engineering Science*, 142:269–276, 2016.

[109] Jean-Marc Schweitzer, Clementina López-García, and Daniel Ferré. Thermal runaway analysis of a three-phase reactor for lco hydrotreatment. *Chemical Engineering Science*, 65(1):313–321, 2010. 20th International Symposium in Chemical Reaction Engineering—Green Chemical Reaction Engineering for a Sustainable Future.

[110] W. Govaerts. Numerical bifurcation analysis for odes. *Journal of Computational and Applied Mathematics*, 125(1):57–68, 2000. Numerical Analysis 2000. Vol. VI: Ordinary Differential Equations and Integral Equations.

[111] Mark Blyth, Ludovic Renson, and Lucia Marucci. Tutorial of numerical continuation and bifurcation theory for systems and synthetic biology, 2020.

[112] N.S. Jayakumar, A. Agrawal, M.A. Hashim, and J.N. Sahu. Experimental and theoretical investigation of parametric sensitivity and dynamics of a continuous stirred tank reactor for acid catalyzed hydrolysis of acetic anhydride. *Computers & Chemical Engineering*, 35(7):1295–1303, 2011.

[113] Na Zang, Xin-Ming Qian, Chi-Min Shu, and Dejian Wu. Parametric sensitivity analysis for thermal runaway in semi-batch reactors: Application to cyclohexanone peroxide reactions. *Journal of Loss Prevention in the Process Industries*, 70:104436, 2021.

[114] Epaminondas Mastorakos. Ignition of turbulent non-premixed flames. *Progress in Energy and Combustion Science*, 35(1):57–97, 2009.

[115] E. Mastorakos. Forced ignition of turbulent spray flames. *Proceedings of the Combustion Institute*, 36(2):2367–2383, 2017.

[116] Zhongtao Kang, Zhen-Guo Wang, Qinglian Li, and Peng Cheng. Effects of trumpet on the flow characteristics of pressure swirl injectors. *Propulsion and Power*, 34, 2018.

[117] Xiaoye Han, Ming Zheng, and Jianxin Wang. Fuel suitability for low temperature combustion in compression ignition engines. *Fuel*, 109:336–349, 2013.

[118] Joonsik Hwang, Youngsoo Park, Choongsik Bae, Jinwoo Lee, and Soonchan Pyo. Fuel temperature influence on spray and combustion characteristics in a constant volume combustion chamber (cvcc) under simulated engine operating conditions. *Fuel*, 160:424–433, 2015.

[119] Guillermo Centeno, Gabriela Sánchez-Reyna, Jorge Ancheyta, José A.D. Muñoz, and Nayeli Cardona. Testing various mixing rules for calculation of viscosity of petroleum blends. *Fuel*, 90(12):3561–3570, 2011. Environmental Modeling of Catalytic Reactions in the Oil Refining Industry.

[120] European standard. Measurement of fluid flow by means of pressure differential devices inserted in circular cross-section conduits running full. *EN ISO 5167*, 2003.

[121] Sumer Dirbude, Vinayak Eswaran, and Abhijit Kushari. Numerical modelling of droplet evaporation with convection for n-alkanes and kerosene fuel. *Atomization and Sprays*, 21(9), 2011.

[122] Ahmet Uyumaz. An experimental investigation into combustion and performance characteristics of an hcci gasoline engine fueled with n-heptane, isopropanol and n-butanol fuel blends at different inlet air temperatures. *Energy Conversion and Management*, 98:199–207, 2015.

[123] David G. Goodwin, Harry K. Moffat, Ingmar Schoegl, Raymond L. Speth, and Bryan W. Weber. Cantera: An object-oriented software toolkit for chemical kinetics, thermodynamics, and transport processes. `https://www.cantera.org`, 2023. Version 3.0.0.

[124] ELISEO RANZI, ALESSIO FRASSOLDATI, ALESSANDRO STAGNI, MATTEO PELUCCHI, ALBERTO CUOCI, and TIZIANO FARAVELLI. Reduced kinetic schemes of complex reaction systems: Fossil and biomass-derived transportation fuels. *International Journal of Chemical Kinetics*, 46(9):512–542, 2014.

[125] Philippe Dagaut and Michel Cathonnet. The ignition, oxidation, and combustion of kerosene: A review of experimental and kinetic modeling. *Progress in Energy and Combustion Science*, 32(1):48–92, 2006.

[126] Jocelyn Luche. *Obtention de modèles cinétiques réduits de combustion: Application à un mécanisme du kérosène*. PhD thesis, Universite d'Orleans, 2003.

[127] B. Franzelli, E. Riber, M. Sanjosé, and T. Poinsot. A two-step chemical scheme for kerosene–air premixed flames. *Combustion and Flame*, 157(7):1364–1373, 2010.

[128] Connie W. Gao, Joshua W. Allen, William H. Green, and Richard H. West. Reaction mechanism generator: Automatic construction of chemical kinetic mechanisms. *Computer Physics Communications*, 203:212–225, 2016.

[129] Mengjie Liu, Alon Grinberg Dana, Matthew S. Johnson, Mark J. Goldman, Agnes Jocher, A. Mark Payne, Colin A. Grambow, Kehang Han, Nathan W. Yee, Emily J. Mazeau, Katrin Blondal, Richard H. West, C. Franklin Goldsmith, and William H. Green. Reaction mechanism generator v3.0: Advances in automatic mechanism generation. *Journal of Chemical Information and Modeling*, 61(6):2686–2696, 2021. PMID: 34048230.

[130] Manik Kumer Ghosh, Mícheál Séamus Howard, Yingjia Zhang, Khalil Djebbi, Gianluca Capriolo, Aamir Farooq, Henry J. Curran, and Stephen Dooley. The combustion kinetics of the lignocellulosic biofuel, ethyl levulinate. *Combustion and Flame*, 193:157–169, 2018.

[131] Eric M. Leibensperger, Loretta J. Mickley, Daniel J. Jacob, and Steven R.H. Barrett. Intercontinental influence of nox and co emissions on particulate matter air quality. *Atmospheric Environment*, 45(19):3318–3324, 2011.

[132] Mansoureh Naderipour and Mahdi Alinaghian. Measurement, evaluation and minimization of co2, nox, and co emissions in the open time dependent vehicle routing problem. *Measurement*, 90:443–452, 2016.

[133] Yao Liu, Jianguo Tan, Minggang Wan, Lang Zhang, and Xiao Yao. Quantitative measurement of oh* and ch* chemiluminescence in jet diffusion flames. *ACS Omega*, 5(26):15922–15930, 2020. PMID: 32656412.

[134] Javier Ballester and Tatiana García-Armingol. Diagnostic techniques for the monitoring and control of practical flames. *Progress in Energy and Combustion Science*, 36(4):375–411, 2010.

[135] Zhicong Li, Chun Lou, and Benjamin M. Kumfer. Revealing the competitive relationship between soot formation and chemiluminescence. *Combustion and Flame*, 245:112335, 2022.

[136] Maurizio De Leo, Alexei Saveliev, Lawrence A. Kennedy, and Serguei A. Zelepouga. Oh and ch luminescence in opposed flow methane oxy-flames. *Combustion and Flame*, 149(4):435–447, 2007.

[137] PGO. Optical transmission of schott bg12 and bg25, 2024.

[138] Aurélien Perrier. *Étude expérimentale de la formation et l'oxydation des particules de suie dans des chambres de combustion RQL (Rich-burn, Quick-mix, Lean-burn) fonctionnant à haute pression.* PhD thesis, PSIME, 2022.

Appendix A
Appendix: Complementary Results

A.1 Kinetic Modeling Results

Kinetic constants for hydrogenation rate are on dry catalyst basis.

A.1.1 Eley-Rideal Model with no hydrogen adsorption (ER1)

Table A.1 Estimated values at T_{ref}=398.15 K with statistical data for ER1.

Parameter	Units	Value	HPD	HPD %
$\ln(k_{hyd}(T_{ref}))$	$m^3/kg/s$	1.86	0.0248	1.33
$\ln(k_{cyc}(T_{ref}))$	$1/s$	-10.20	0.0300	0.29
$Ea_{hyd}/R/T_{ref}$	J/mol	7.91	0.8350	10.55
$Ea_{cyc}/R/T_{ref}$	J/mol	7.70	0.6094	7.91
$\ln(K_{BL})$	m^3/mol	0.011	-	-
$\ln(K_{BHP})$	m^3/mol	8.24	-	-

Table A.2 Normalized parameter covariance matrix for ER1.

	$\ln(k_{hyd}(T_{ref}))$	$\ln(k_{cyc}(T_{ref}))$	$Ea_{hyd}/R/T_{ref}$	$Ea_{cyc}/R/T_{ref}$
$\ln(k_{hyd}(T_{ref}))$	1			
$\ln(k_{cyc}(T_{ref}))$	-0.005	1		
$Ea_{hyd}/R/T_{ref}$	-0.204	-0.034	1	
$Ea_{cyc}/R/T_{ref}$	-0.031	-0.671	-0.081	1

A.1.2 Langmuir-Hinshelwood Model with hydrogen adsorption (LH1)

Table A.3 Estimated values at T_{ref}=398.15 K with statistical data for LH1.

Parameter	Units	Value	HPD	HPD %
$\ln(k_{hyd}(T_{ref}))$	$mol/kg/s$	8.79	0.0312	0.36
$\ln(k_{cyc}(T_{ref}))$	$1/s$	-10.20	0.0290	0.28
$Ea_{hyd}/R/T_{ref}$	J/mol	8.69	1.0100	11.59
$Ea_{cyc}/R/T_{ref}$	J/mol	8.70	0.5910	6.79
$\ln(K_{BL})$	m^3/mol	-0.784	-	-
$\ln(K_{H_2})$	m^3/mol	3.59	-	-
$\ln(K_{BHP})$	m^3/mol	5.20	-	-

Table A.4 Normalized parameter covariance matrix for LH1.

	$\ln(k_{hyd}(T_{ref}))$	$\ln(k_{cyc}(T_{ref}))$	$Ea_{hyd}/R/T_{ref}$	$Ea_{cyc}/R/T_{ref}$
$\ln(k_{hyd}(T_{ref}))$	1			
$\ln(k_{cyc}(T_{ref}))$	-0.068	1		
$Ea_{hyd}/R/T_{ref}$	-0.222	-0.016	1	
$Ea_{cyc}/R/T_{ref}$	0.008	-0.663	-0.131	1

A.1.3 Langmuir-Hinshelwood Model with hydrogen adsorption and dissociation (LH2)

Table A.5 Estimated values at T_{ref}=398.15 K with statistical data for LH2.

Parameter	Units	Value	HPD	HPD %
$\ln(k_{hyd}(T_{ref}))$	$mol/kg/s$	10.00	0.0312	0.31
$\ln(k_{cyc}(T_{ref}))$	$1/s$	-10.20	0.0290	0.28
$Ea_{hyd}/R/T_{ref}$	J/mol	8.68	1.0100	11.59
$Ea_{cyc}/R/T_{ref}$	J/mol	8.70	0.5912	6.80
$\ln(K_{BL})$	m^3/mol	-3.88	-	-
$\ln(K_{H_2})$	m^3/mol	3.48	-	-
$\ln(K_{BHP})$	m^3/mol	1.87	-	-
$\ln(K_i)$	–	-4.66	-	-

Table A.6 Normalized parameter covariance matrix for LH2.

	$\ln(k_{hyd}(T_{ref}))$	$\ln(k_{cyc}(T_{ref}))$	$Ea_{hyd}/R/T_{ref}$	$Ea_{cyc}/R/T_{ref}$
$\ln(k_{hyd}(T_{ref}))$	1			
$\ln(k_{cyc}(T_{ref}))$	-0.068	1		
$Ea_{hyd}/R/T_{ref}$	-0.222	-0.016	1	
$Ea_{cyc}/R/T_{ref}$	0.008	-0.663	-0.131	1

A.1.4 Non-Competitive Langmuir-Hinshelwood Model with hydrogen adsorption (NCLH1)

Table A.7 Estimated values at T_{ref}=398.15 K with statistical data for NCLH1.

Parameter	Units	Value	HPD	HPD %
$\ln(k_{hyd}(T_{ref}))$	$mol/kg/s$	5.34	0.1160	2.17
$\ln(k_{cyc}(T_{ref}))$	$1/s$	-10.20	0.0289	0.28
$Ea_{hyd}/R/T_{ref}$	J/mol	9.25	0.7330	7.92
$Ea_{cyc}/R/T_{ref}$	J/mol	8.09	0.5885	7.27
$\ln(K_{BL})$	m^3/mol	0.011	-	-
$\ln(K_{H_2})$	m^3/mol	-2.91	0.2600	8.93
$\ln(K_{BHP})$	m^3/mol	7.96	-	-

Table A.8 Normalized parameter covariance matrix for NCLH1.

	$\ln(k_{hyd}(T_{ref}))$	$\ln(k_{cyc}(T_{ref}))$	$Ea_{hyd}/R/T_{ref}$	$Ea_{cyc}/R/T_{ref}$	$\ln(K_{H_2})$
$\ln(k_{hyd}(T_{ref}))$	1				
$\ln(k_{cyc}(T_{ref}))$	0.070	1			
$Ea_{hyd}/R/T_{ref}$	-0.163	-0.047	1		
$Ea_{cyc}/R/T_{ref}$	-0.086	-0.671	-0.059	1	
$\ln(K_{H_2})$	-0.981	-0.071	0.123	0.081	1

A.1.5 Non-Competitive Langmuir-Hinshelwood Model with hydrogen adsorption and dissociation (NCLH2)

Table A.9 Estimated values at T_{ref}=398.15 K with statistical data for NCLH2.

Parameter	Units	Value	HPD	HPD %
$\ln(k_{hyd}(T_{ref}))$	$mol/kg/s$	4.56	0.0263	0.58
$\ln(k_{cyc}(T_{ref}))$	$1/s$	-10.40	0.0327	0.31
$Ea_{hyd}/R/T_{ref}$	J/mol	4.09	0.8290	20.27
$Ea_{cyc}/R/T_{ref}$	J/mol	12.6	0.6377	5.08
$\ln(K_{BL})$	m^3/mol	-1.09	-	-
$\ln(K_{H_2})$	m^3/mol	5.00	-	-
$\ln(K_{BHP})$	m^3/mol	8.64	-	-
$\ln(K_i)$	–	-2.02	-	-

Table A.10 Normalized parameter covariance matrix for NCLH2.

	$\ln(k_{hyd}(T_{ref}))$	$\ln(k_{cyc}(T_{ref}))$	$Ea_{hyd}/R/T_{ref}$	$Ea_{cyc}/R/T_{ref}$
$\ln(k_{hyd}(T_{ref}))$	1			
$\ln(k_{cyc}(T_{ref}))$	-0.079	1		
$Ea_{hyd}/R/T_{ref}$	-0.136	-0.041	1	
$Ea_{cyc}/R/T_{ref}$	-0.015	-0.577	-0.149	1

A.2 Physical Properties Results

A.2.1 Lower Heating Value (LHV)

Table A.11 Blends kerosene/BL: Lower heating values.

$\mathbf{x}_{Kero}^{vol}$	$\mathbf{x}_{BL}^{vol}$	$\mathbf{x}_{Kero}^{mass}$	$\mathbf{x}_{BL}^{mass}$	LHV_{exp} [MJ/kg]	STD	$LHV_{MixRule}$ [MJ/kg]
0.00	1.00	0.00	1.00	29.2	0.2	29.2
0.50	0.50	0.46	0.54	35.7	0.5	36.5
0.80	0.20	0.77	0.23	41.4	0.6	41.6
1.00	0.00	1.00	0.00	45.3	0.3	45.3

A.2.2 Density

Table A.12 Blends kerosene/BL: Density at low temperatures.

T [K]	**Density [kg/m3]**					
	Pure BL	**Kero/BL$_{50/50}$**		**Kero/BL$_{80/20}$**		**Kerosene**
	Exp Val	Exp Val	Mix Rule	Exp Val	Mix Rule	Exp Val
263	999.6	897.6	902.5	836.9	844.3	805.5
268	995.4	897.7	900.1	840.3	842.9	804.8
273	991.2	893.4	895.9	836.3	838.7	800.6
278	986.9	889.3	891.9	832.4	834.9	796.9
283	982.4	885.1	887.8	828.5	831.0	793.2
288	977.9	880.9	883.6	824.5	827.0	789.3
293	973.0	876.8	879.3	820.6	823.2	785.7

A.2.3 Dynamic Viscosity

Table A.13 Blends kerosene/BL: Dynamic viscosity at low temperatures.

T [K]	**Dynamic Viscosity [Pa·s]**					
	Pure BL	**Kero/BL$_{50/50}$**		**Kero/BL$_{80/20}$**		**Kerosene**
	Exp Val	Exp Val	Mix Rule	Exp Val	Mix Rule	Exp Val
263	7.284×10^{-3}	3.621×10^{-3}	3.615×10^{-3}	2.298×10^{-3}	2.374×10^{-3}	1.794×10^{-3}
268	5.993×10^{-3}	3.152×10^{-3}	3.158×10^{-3}	2.099×10^{-3}	2.151×10^{-3}	1.665×10^{-3}
273	5.096×10^{-3}	2.681×10^{-3}	2.763×10^{-3}	1.831×10^{-3}	1.913×10^{-3}	1.498×10^{-3}
278	4.351×10^{-3}	2.366×10^{-3}	2.432×10^{-3}	1.646×10^{-3}	1.716×10^{-3}	1.360×10^{-3}
283	3.762×10^{-3}	2.098×10^{-3}	2.160×10^{-3}	1.488×10^{-3}	1.548×10^{-3}	1.240×10^{-3}
288	3.291×10^{-3}	1.877×10^{-3}	1.938×10^{-3}	1.351×10^{-3}	1.410×10^{-3}	1.141×10^{-3}
293	2.907×10^{-3}	1.693×10^{-3}	1.748×10^{-3}	1.234×10^{-3}	1.288×10^{-3}	1.051×10^{-3}

A.2.4 Kinematic Viscosity

Table A.14 Blends kerosene/BL: Kinematic viscosity at low temperatures.

T [K]	Kinematic Viscosity [m^2/s]					
	Pure BL	**Kero/BL$_{50/50}$**		**Kero/BL$_{80/20}$**		**Kerosene**
	Exp Val	Exp Val	Mix Rule	Exp Val	Mix Rule	Exp Val
263	7.288×10^{-6}	4.042×10^{-6}	4.030×10^{-6}	2.756×10^{-6}	2.824×10^{-6}	2.228×10^{-6}
268	6.021×10^{-6}	3.511×10^{-6}	3.529×10^{-6}	2.498×10^{-6}	2.561×10^{-6}	2.068×10^{-6}
273	5.141×10^{-6}	3.001×10^{-6}	3.101×10^{-6}	2.189×10^{-6}	2.290×10^{-6}	1.871×10^{-6}
278	4.409×10^{-6}	2.661×10^{-6}	2.743×10^{-6}	1.978×10^{-6}	2.063×10^{-6}	1.706×10^{-6}
283	3.830×10^{-6}	2.370×10^{-6}	2.447×10^{-6}	1.796×10^{-6}	1.870×10^{-6}	1.564×10^{-6}
288	3.365×10^{-6}	2.003×10^{-6}	2.205×10^{-6}	1.638×10^{-6}	1.712×10^{-6}	1.445×10^{-6}
293	2.986×10^{-6}	1.931×10^{-6}	1.999×10^{-6}	1.504×10^{-6}	1.571×10^{-6}	1.338×10^{-6}

A.2.5 Surface Tension

Table A.15 Blends kerosene/BL: Surface tension at low temperatures.

T [K]	Surface Tension [N/m]			
	Pure BL	**Kero/BL$_{50/50}$**	**Kero/BL$_{80/20}$**	**Kerosene**
273	0.0316	0.0318	0.0292	0.0272
278	0.0317	0.0317	0.0302	0.0269
283	0.0317	0.0312	0.0288	0.0266
288	0.0315	0.0310	0.0296	0.0263
293	0.0312	0.0305	0.0293	0.0260

Appendix B
Appendix: List of Publications

B.1 Article: Kinetic model assessment for the synthesis of γ-valerolactone from n-butyl levulinate and levulinic acid hydrogenation over the synergy effect of dual catalysts Ru/C and Amberlite IR-120

Chemical Engineering Journal 430 (2022) 133053

Contents lists available at ScienceDirect

Chemical Engineering Journal

journal homepage: www.elsevier.com/locate/cej

Kinetic model assessment for the synthesis of γ-valerolactone from *n*-butyl levulinate and levulinic acid hydrogenation over the synergy effect of dual catalysts Ru/C and Amberlite IR-120

Jose Delgado [a,d,1], Wenel Naudy Vasquez Salcedo [a,1], Giulia Bronzetti [a,b], Valeria Casson Moreno [b], Mélanie Mignot [c], Julien Legros [c], Christoph Held [e], Henrik Grénman [d], Sébastien Leveneur [a,*]

[a] Normandie Univ, INSA Rouen, UNIROUEN, LSPC, EA4704, 76000 Rouen, France
[b] Dipartimento di Ingegneria Chimica, Civile, Ambientale e dei Materiali, Alma Mater Studiorum—Università di Bologna, via Terracini 28, 40131 Bologna, Italy
[c] Normandie Université, INSA Rouen, UNIROUEN, CNRS, COBRA Laboratory, F-76000 Rouen, France
[d] Laboratory of Industrial Chemistry & Reaction Engineering, Johan Gadolin Process Chemistry Centre, Åbo Akademi University, FI-20500 Åbo-Turku, Finland
[e] Laboratory of Thermodynamics, TU Dortmund, Germany

ARTICLE INFO

Keywords:
γ-valerolactone
Kinetic modeling
Bayesian statistics
Cross-validation
Levulinic acid

ABSTRACT

The production of platform molecules from the valorization of lignocellulosic biomass is increasing. Among these plateform molecules, γ-valerolactone (GVL) is a promising one and could be used for different industrial applications. This molecule is synthesized from levulinic acid (LA) or alkyl levulinates (AL) through a tandem hydrogenation/cyclization (lactonization) cascade. A lot of investigations have been carried out to develop the best catalyst for the hydrogenation step by using solely LA or AL. However, one should keep in mind that in the AL production via fructose alcoholysis, there is also LA production, and both are present in the product mixture during the further conversion. To the best of our knowledge, no article exists describing the hydrogenation of LA and AL simultaneously in one-pot. Also, the literature reporting the use of solid catalyst for the second cyclization step is rare. To fill this gap, the hydrogenation of levulinic acid and butyl levulinate (BL) was studied over Ru/C and Amberlite IR-120. Several kinetic models were evaluated via Bayesian inference and K-fold approach. The kinetic assessment showed that a non-competitive Langmuir-Hinshelwood with no dissociation of hydrogen where LA, BL and H_2 are adsorbed on different sites (NCLH1.2) and non-competitive Langmuir-Hinshelwood with dissociation of hydrogen where LA, BL and H_2 are adsorbed on different sites (NCLH2.2) are the best model to describe this system. The presence of LA and Amberlite IR-120 allows to increase the kinetics of cyclization steps, and *in fine* to accelerate the production of GVL.

1. Introduction

The valorization of biomass to chemicals, fuels, or materials is essential to decrease the use of fossil raw materials, reduce CO_2 emission, and favor circular economies [1,2]. To make biorefineries efficient in production and energy consumption, knowledge ok kinetics, catalysis, and thermodynamics is vital [3]. Currently, academia and the private sectors are focusing their efforts on the valorization of lignocellulosic biomass (LCB) to avoid the dilemma of "food versus fuels" [4].

There are several platform molecules that can be derived from the valorization of LCB [5–7] such as 1,4-diacid, 5-HMF and 2,5-FDCA, 3-HPA, aspartic acid, glutamic acid, glucaric acid, itaconic acid, sorbitol, ABE or levulinic acid.

Research interest at the academy and industrial levels for the utilization of levulinic acid platform chemicals is increasing. Levulinic acid (LA) or alkyl levulinate (AL) are produced from the solvolysis or alcoholysis of cellulose-hemicellulose [8,9]. The market for these molecules (LA or AL) is growing [10,11] due to the versatile use and valorization of these molecules in different industrial sectors.

The hydrogenation of LA or AL leads to the production of γ-valerolactone (GVL), also considered as a platform molecule [12–14]. GVL is

* Corresponding author.
E-mail address: sebastien.leveneur@insa-rouen.fr (S. Leveneur).
[1] These authors contributed equally to the work.

https://doi.org/10.1016/j.cej.2021.133053
Received 23 September 2021; Accepted 14 October 2021
Available online 21 October 2021

Notation

Ea_i	activation energy of reaction *i* [J.mol^{-1}]
$f(\partial)$	estimated concentration
He	Henry's coefficient [mol.m^{-3}.bar^{-1}]
k_i	rate constant of reaction *i*
Ki	adsorption rate of specie i
k_L.a	volumetric mass transfer coefficient [s^{-1}]
P	pressure [bar]
R_i	reaction rate *i* [mol.m^{-3}.s^{-1}]
R	gas constant [J.K^{-1}.mol^{-1}]
$S(\partial)$	objective funtion
T	temperature [K]
$\lvert v(\partial) \rvert$	determinant of the covariance matrix of responses
Y_i	experimental concentration of specie i

Greek letters

Θ	catalyst active sites
θ_i	active sites occupied by specie i
$\omega_{Cat.}$	catalyst loading [kg.m^{-3}]

Subscripts and superscripts

Ref	reference
*	interfacial value

Abbreviations

AIC	Akaike information criterion
AL	Alkyl levulinate
Amb	Amberlite IR-120
BL	Butyl levulinate
BHP	Butyl 4-hydroxypentanoate
ER	Eley-Rideal kinetic model without hydrogen adsorption
GC	Gas chromatography
GVL	γ-valerolactone
HPA	4-hydroxypentanoic acid
HDP	Highest Posterior Density
LA	Levulinic acid
LCB	Lignocellulosic biomass
LH1	Langmuir-Hinshelwood kinetic model without hydrogen dissociation
LH2	Langmuir-Hinshelwood kinetic model with hydrogen dissociation
NCLH1.1	Non-competitive Langmuir-Hinshelwood kinetic model without hydrogen dissociation, where BL and LA are in competitive adsorption on the same site but not hydrogen
NCLH1.2	Non-competitive Langmuir-Hinshelwood kinetic model without hydrogen dissociation, where BL, LA and hydrogen are adsorbed on different sites
NCLH2.1	Non-competitive Langmuir-Hinshelwood kinetic model with hydrogen dissociation, where BL and LA are in competitive adsorption on the same site but not hydrogen
NCLH2.2	Non-competitive Langmuir-Hinshelwood kinetic model with hydrogen dissociation, where BL, LA and hydrogen are adsorbed on different sites
ODEs	Ordinary differential equation system
ROH	Co-product of the ciclyzation step(water or butanol)
Ru/C	Ruthenium on activated carbon
SSR	Sum of squared residuals

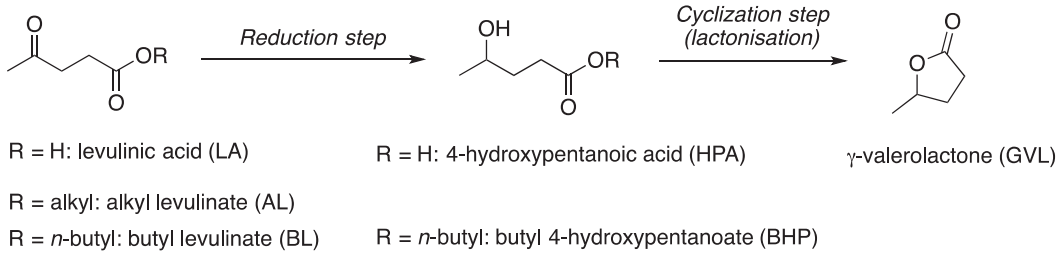

Fig. 1. Hydrogenation of LA or AL to GVL over Ru/C.

regarded as an excellent green aprotic polar solvent [15–18] due to its low vapor pressure and high flash point [14,19,20]. GVL is stable, renewable and non-toxic [21]. This platform molecule can be used as an intermediate in the production of many value-added chemicals [1]. From an energetic viewpoint, GVL is a good intermediate for bio-jet fuel production via its decomposition into butene [22,23].

There are several routes for the production of GVL [24,25]; among those involving the hydrogenation of AL or LA, one can distinguish:

-use of molecular hydrogen [26–38];

-*in situ* decomposition of formic acid into hydrogen [39–47];

-the Meerwein – Ponndorf – Verley reaction, i.e., the use of alcohols for catalytic transfer hydrogenation [48–50].

Hence, one can notice that the literature concerning the production of GVL from the hydrogenation of AL or LA is quite vast. Researchers have put a lot of effort into developong catalysts, evaluating reaction pathway, and using different feedstock.

The most common method for the production of GVL is the hydrogenation of AL or LA with molecular hydrogen over Ru/C, since it provides the best atom economy. This reaction comprises of two steps [38] (Fig. 1) : the hydrogenation of the substrate to obtain an intermediate, and the cyclization of the intermediate to GVL. During the first step, the carbonyl group of AL or LA is hydrogenated. During the second step, the hydroxyl group of the intermediate reacts with the ester group leading to a cyclization.

One should remember that the alcoholysis of fructose leads to LA and the corresponding AL [51]. Thus, in the case of GVL production from fructose via alcoholysis and consecutive hydrogenation, LA is also present in this chemical system. Piskun et al. [38] observed that protons from LA dissociation can catalyze the cyclization step. Thus, it could be beneficial for the production of GVL to start from the products of fructose alcoholysis, namely the presence of LA and AL.

Highly concentrated LA solutions present a corrosion risk, which is why, the use of AL has gained interest, but its reactivity is lower compared to LA. A good compromise could be to use a mixture of both reactants. Methyl, ethyl and n-butyl levulinates are the three most studied AL. A thermal risk assessment of AL hydrogenation [36] showed that the risk of thermal runaway for the hydrogenation of methyl levulinate is higher than for butyl levulinate (BL), and the use of butanol for

Table 1
Experimental matrix for the kinetic study of the reaction scheme shown in Fig. 1.

Run	Pressure bar	Temp K	mcat_Ru kg (50% weight moisture)	mcat_Ambkg (dried)	m0GVL kg	m0BL kg	m0LA kg	BL_0mol/m^3	GVL_0mol/m^3	LA_0mol/m^3
1	20.6	404.15	0.0005	0	0.083	0.027	0.015	1272	7703	1105
2	20	403.15	0.0005	0	0.083	0.042	0	1912	6311	0
3	20.6	404.15	0.0005	0	0.083	0.027	0.015	1249	6606	1029
4	22	383.15	0.0005	0	0.083	0.027	0.015	1249	6606	1029
5	10.9	403.15	0.0005	0	0.083	0.027	0.015	1351	7169	1029
6	21.5	402.15	0.0005	0	0.083	0.022	0.02	1055	6831	1372
7	21.4	374.15	0.0005	0	0.083	0.027	0.015	1450	6606	1300
8	21.6	373.15	0.001	0	0.083	0.027	0.015	1313	6841	1077
9	21.7	383.15	0.0015	0	0.083	0.022	0.02	879	5950	719
10	21.3	385.15	0.0015	0.010479	0.083	0.022	0.02	1093	6819	1390
11	9.7	375.15	0.0012	0.010	0.083	0.022	0.025	1117	6769	1597
12	9.5	414.15	0.0010	0.000	0.083	0.027	0.010	1415	7431	582
13	10.5	391.15	0.0012	0.010	0.083	0.022	0.025	1058	6586	1707
14	15.4	394.15	0.0012	0.006	0.083	0.03	0.015	1337	6515	1154

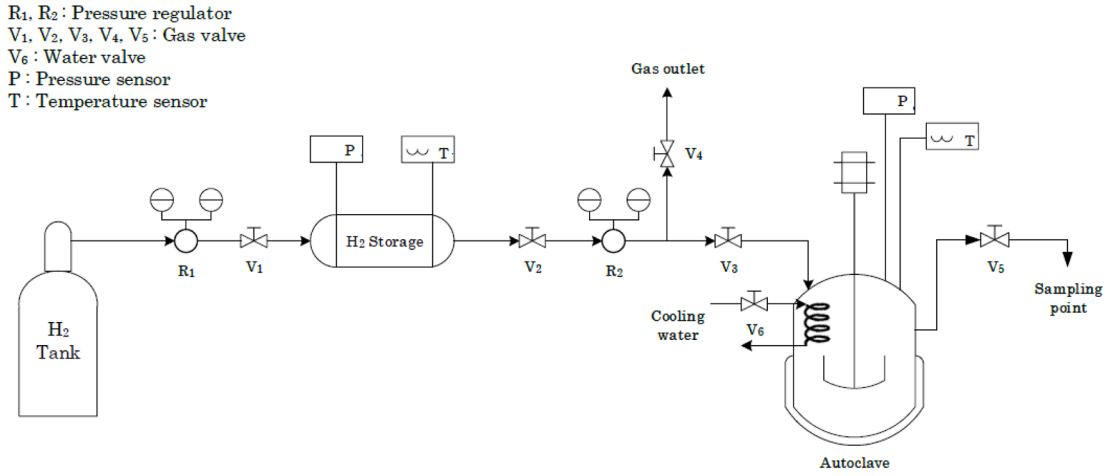

Fig. 2. Experimental setup of the autoclave.

the alcoholysis of carbohydrates into BL is a promising route [52].

The choice of solvent is also important. A previous study showed that the solubility of hydrogen is higher in GVL solvent [28]. Besides, the hydrogenation of BL in GVL solvent allows to work at higher temperature due to the high vapor pressure of the different chemicals [52].

For that reason, the current study focuses on:

1) the hydrogenation of LA and BL reactants into GVL.

2) the use of cation exchange resins under H form to catalyze the cyclization reaction. The cyclization step has been shown to be slower for alkyl levulinates than for LA [38]. The use of such acid resin catalyst can significantly increase the reaction kinetics. To the best of our knowledge, there are few studies in this field [53,54]. In the first study, Moreno-Marrodan and Barbaro [53] demonstrated that the use of heterogeneous catalyst based on sulfonated cation exchange resin and embedded Ru nanoparticles leads to the complete conversion of LA to GVL with remarkable selectivity at low temperatures and H_2 pressure, as well as excellent catalyst durability and no need for additives.The second study [54] analysed the hydrogenation of LA to GVL catalysed by a commercial Ru supported catalyst in combination with Amberlyst A70, showing a high selectivity to GVL also at mild processing conditions.

This article aims to assess different plausible kinetic models for the hydrogenation of BL and LA synergically catalyzed by Ru/C and Amberlite IR-120 via Bayesian inference. The Bayesian approach to developing a kinetic model for catalytic systems has become increasingly popular [55–59].

Traditionally, kinetic models are evaluated mainly by the fit to experimental data and the coefficient of determination. Some researchers incorporate in the assessment: the residual analysis, the credible intervals of the estimated parameters, the number of parameters via the Akaike information criterion (AIC) [60] and the correlation matrix. All these analyses are done solely on the training dataset, and few studies use a validation dataset to evaluate prediction quality of the kinetic model. The validation stage is rarely done because some experimental data are not used in the regression stage, so the model accuracy is lower. To overcome this issue, cross-validation, and more particularly the K-fold approach, is used in this investigation [61]. Cross-validation is also a way to determine the best model.

2. Materials and methods

2.1. Chemicals

Chemicals used in this work, without further purification, are described in this section. Hydrogen gas (H_2 purity > 99.999 vol%) from Linde. *n*-Butyl levulinate (BL purity = 98 wt%), CAS: 2052–15-5, was purchased from Alfa-Aesar. Levulinic acid (LA purity > 98 wt%), CAS: 123–76-2, was purchased from Acros Organics. γ-Valerolactone (GVL purity ≥ 99 wt%), CAS: 108–29- 2, was purchased from Sigma Aldrich. Acetone (analytical grade), CAS: 67–64-1, was bought from VWR. Ruthenium, 5% on activated carbon powder, reduced, nominally 50% water, CAS: 7440–18-8, was purchased from Alfa-Aesar. Amberlite IR120, H-Form, ion-exchange resin, CAS: 78922–04-0, was purchased from Acros Organics.

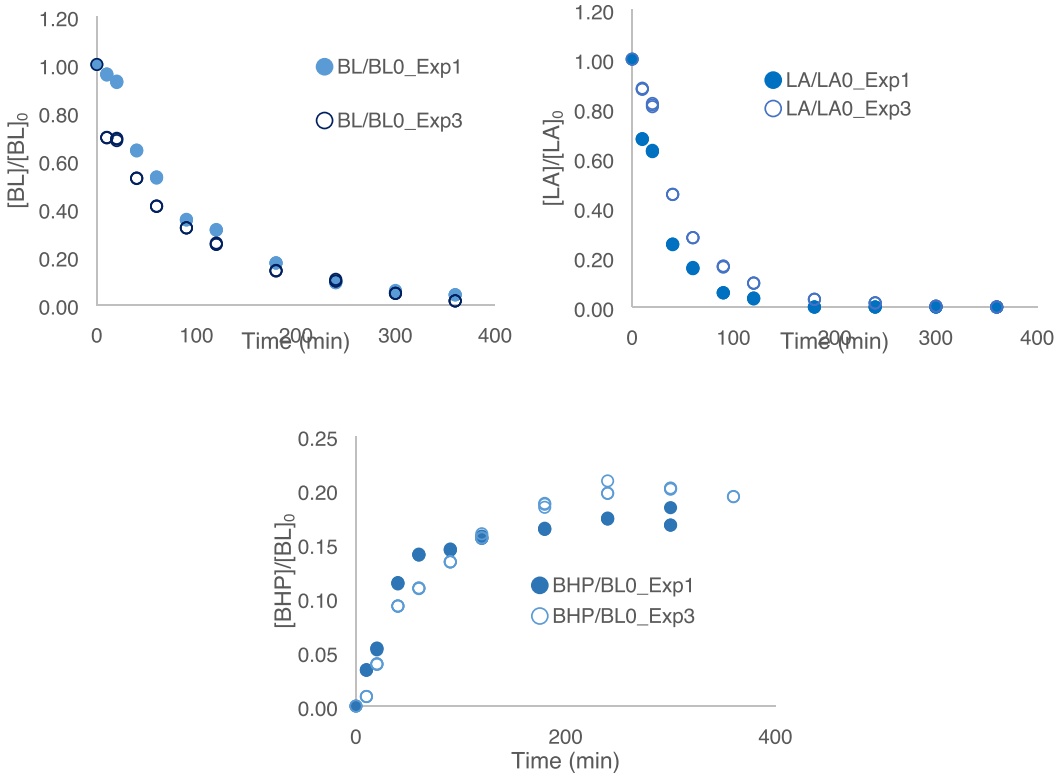

Fig. 3. Evolution of $[BL]/[BL]_0$, $[LA]/[LA]_0$ and $[BHP]/[BL]_0$ for experiments 1&3.

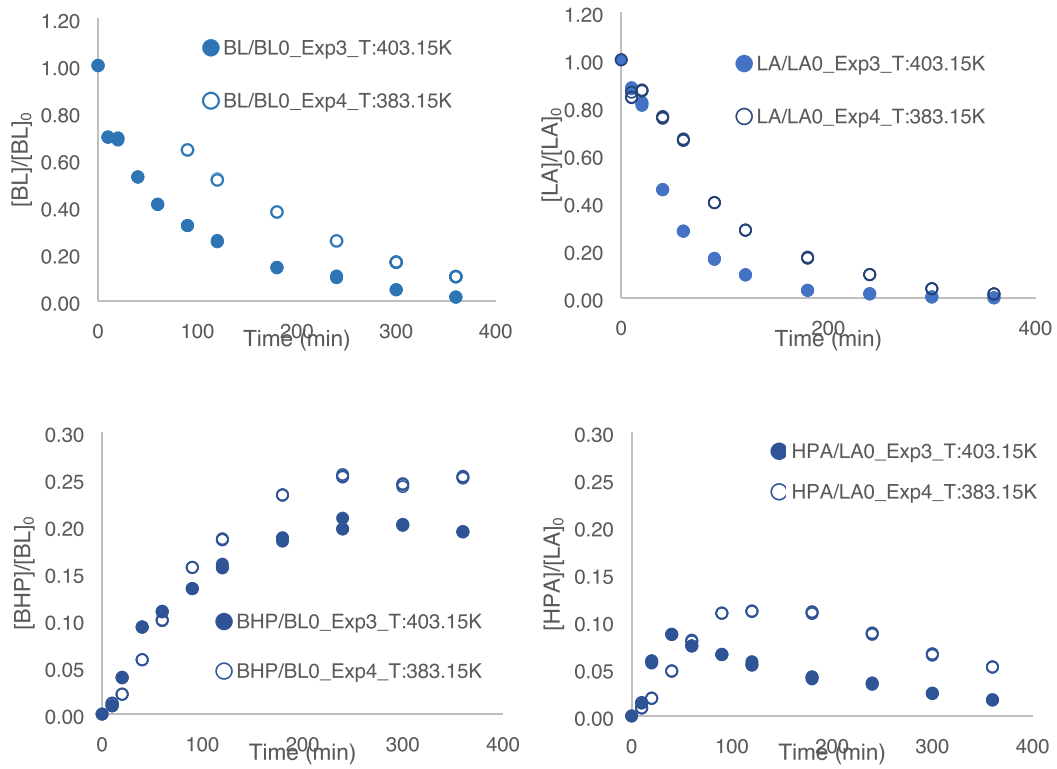

Fig. 4. Effect of temperature on hydrogenation and cyclization reactions for experiments 3&4.

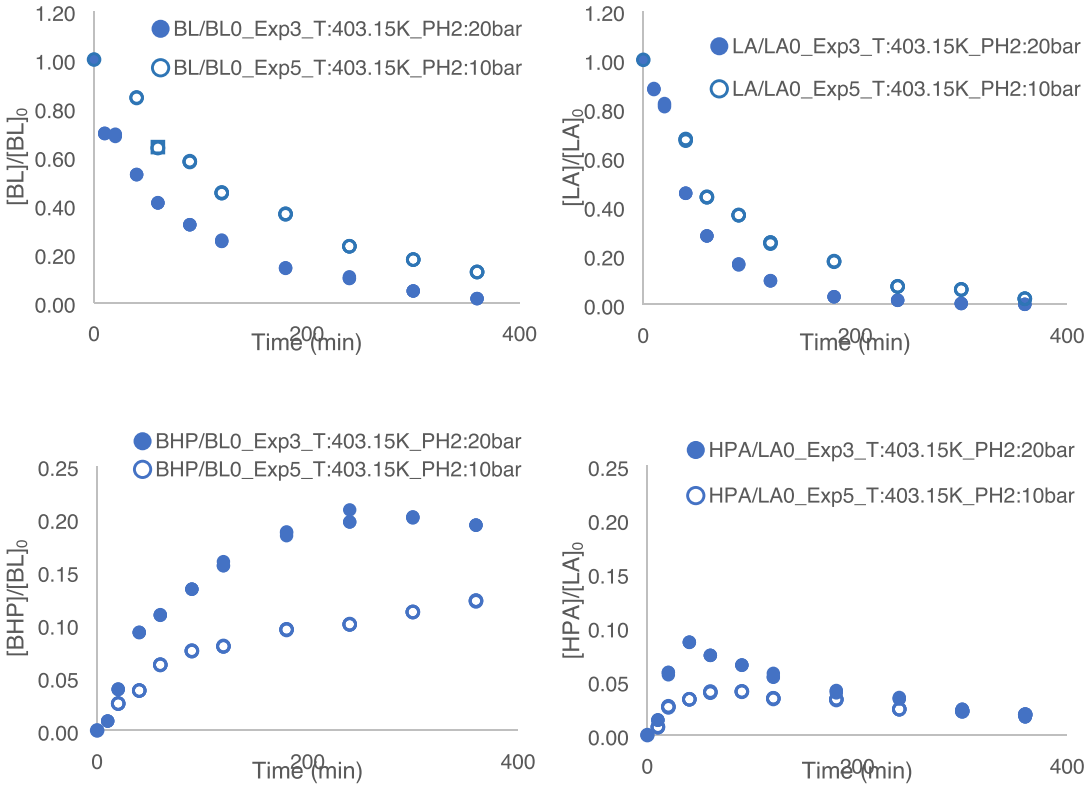

Fig. 5. Effect of pressure on the kinetics of hydrogenation and cyclization steps for experiments 3&5.

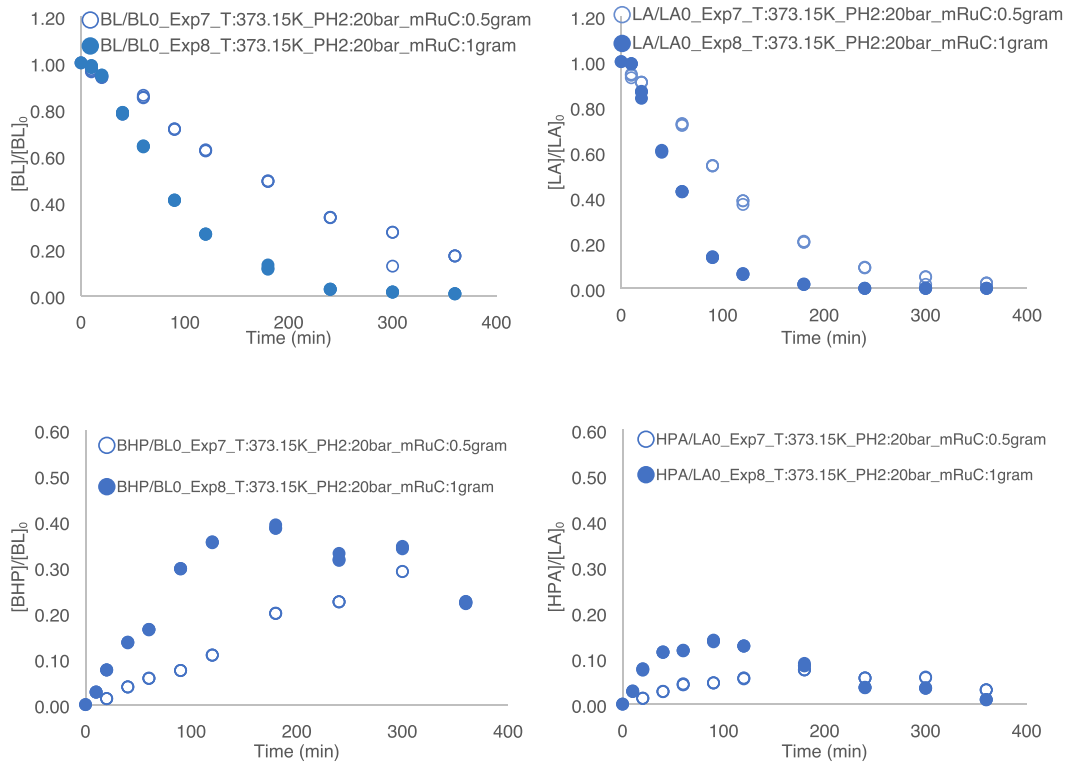

Fig. 6. Effect of Ru/C loadings on the kinetics for Experiments 7&8.

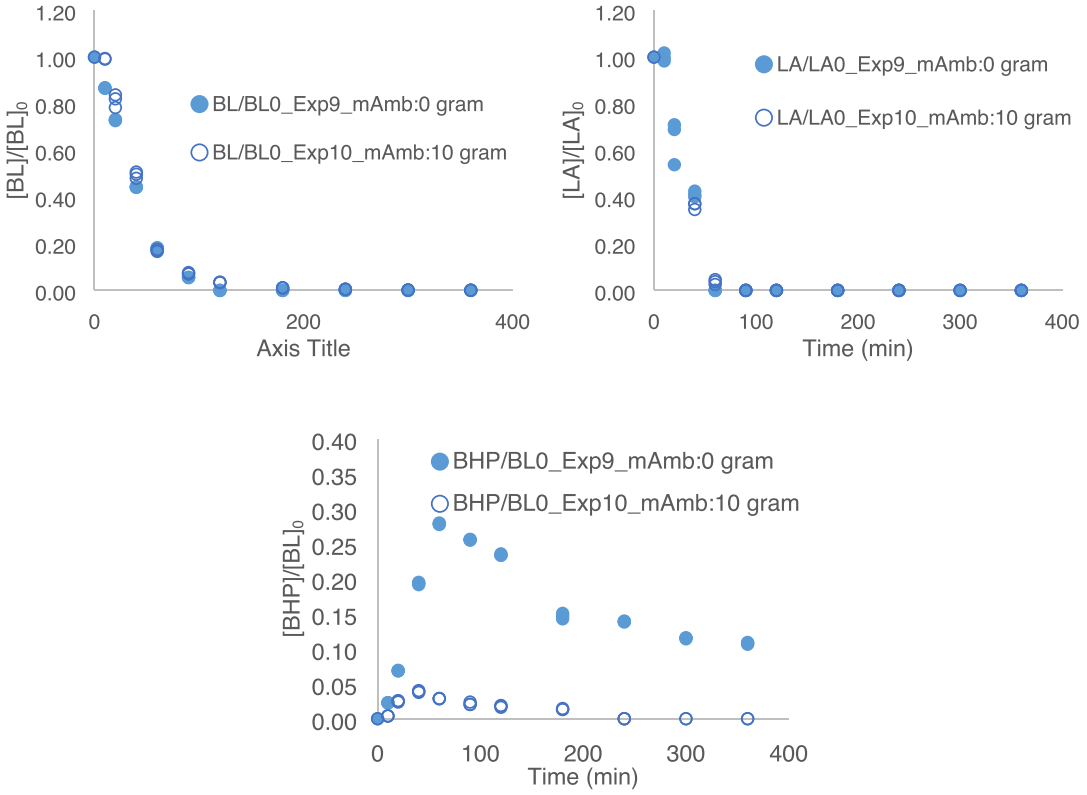

Fig. 7. Effect of Amberlite IR120 loadings on the kinetics of hydrogenation and cyclization for Experiments 9&10.

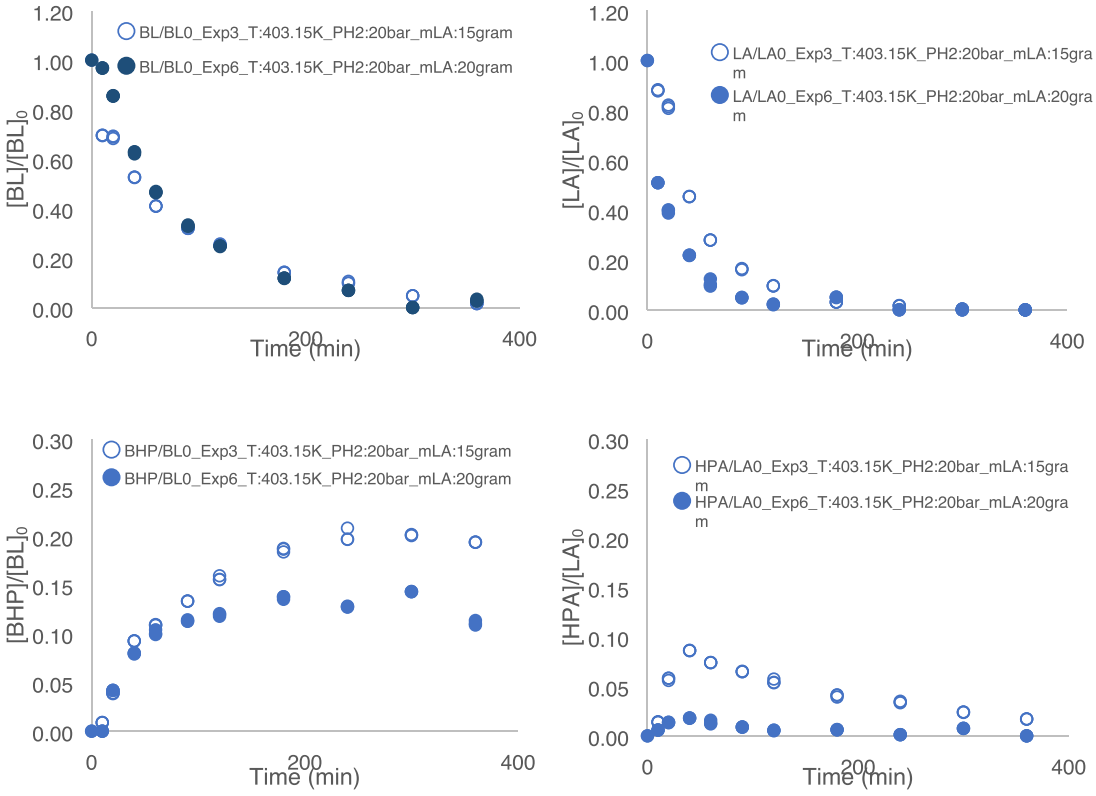

Fig. 8. Effect of LA concentration on the kinetics of hydrogenation and cyclization steps for Experiments 3&6.

Table 2
Rate expression for the hydrogenation steps.

MODELS	Rate expression for BL, $R_{BL,Hyd}$	Rate expression for LA, $R_{LA,Hyd}$
(LH1)	$\frac{k_1{}^*[H_2]^*[BL]^*\omega_{Cat.}}{\left(\begin{matrix}K_{H2}{}^*[H_2]+K_{BL}{}^*[BL]+K_{BHP}{}^*[BHP]\\ +K_{LA}{}^*[LA]+K_{HPA}{}^*[HPA]+1\end{matrix}\right)^2}$	$\frac{k_1{}^*[H_2]^*[LA]^*\omega_{Cat.}}{\left(\begin{matrix}K_{H2}{}^*[H_2]+K_{BL}{}^*[BL]+K_{BHP}{}^*[BHP]\\ +K_{LA}{}^*[LA]+K_{HPA}{}^*[HPA]+1\end{matrix}\right)^2}$
(LH2)	$\frac{k_1{}^*[H_2]^*[BL]^*\omega_{Cat.}}{\left(\begin{matrix}\boldsymbol{K_H}{}^*\sqrt{[H_2]}+K_{BL}{}^*[BL]+K_{BHP}{}^*[BHP]+K_i{}^*[BL]^*\sqrt{[H_2]}\\ +K_{LA}{}^*[LA]+K_{HPA}{}^*[HPA]+K_{i2}{}^*[LA]^*\sqrt{[H_2]}+1\end{matrix}\right)^2}$	$\frac{k_1{}^*[H_2]^*[LA]^*\omega_{Cat.}}{\left(\begin{matrix}\sqrt{K_H{}^*[H_2]}+K_{BL}{}^*[BL]+K_{BHP}{}^*[BHP]+K_i{}^*[BL]^*\sqrt{[H_2]}\\ +K_{LA}{}^*[LA]+K_{HPA}{}^*[HPA]+K_{i2}{}^*[LA]^*\sqrt{[H_2]}+1\end{matrix}\right)^2}$
(ER1)	$\frac{k_1{}^*[H_2]^*[BL]^*\omega_{Cat.}}{\left(\begin{matrix}K_{BL}{}^*[BL]+K_{BHP}{}^*[BHP]+K_{LA}{}^*[LA]\\ +HPA^*[HPA]+1\end{matrix}\right)}$	$\frac{k_1{}^*[H_2]^*[LA]^*\omega_{Cat.}}{\left(\begin{matrix}K_{BL}{}^*[BL]+K_{BHP}{}^*[BHP]\\ +K_{LA}{}^*[LA]+HPA^*[HPA]+1\end{matrix}\right)}$
(NCLH1.1)	$\frac{k_1{}^*[H_2]}{(1+K_{H2}{}^*[H_2])}{}^*\frac{[BL]^*\omega_{Cat.}}{\left(\begin{matrix}1+K_{BHP}{}^*[BHP]+K_{BL}{}^*[BL]\\ +K_{HPA}{}^*[HPA]+K_{LA}{}^*[LA]\end{matrix}\right)}$	$\frac{k_1{}^*[H_2]}{(1+K_{H2}{}^*[H_2])}{}^*\frac{[LA]^*\omega_{Cat.}}{\left(\begin{matrix}1+K_{BHP}{}^*[BHP]+K_{BL}{}^*[BL]\\ +K_{HPA}{}^*[HPA]+K_{LA}{}^*[LA]\end{matrix}\right)}$
(NCLH1.2)	$\frac{k_1{}^*[H_2]}{(1+K_{H2}{}^*[H_2])}{}^*\frac{[BL]^*\omega_{Cat.}}{(1+K_{BHP}{}^*[BHP]+K_{BL}{}^*[BL])}$	$\frac{k_1{}^*[H_2]}{(1+K_{H2}{}^*[H_2])}{}^*\frac{[LA]^*\omega_{Cat.}}{(1+K_{HPA}{}^*[HPA]+K_{LA}{}^*[LA])}$
(NCLH2.1)	$\frac{k_1{}^*[H_2]}{K_H{}^*\sqrt{[H_2]}+1}{}^*\frac{[BL]^*\omega_{Cat.}}{\left(\begin{matrix}K_{BL}.[BL]+\boldsymbol{K_C}.\sqrt{[H_2]}.[BL].+K_{BHP}.[BHP]+K_{LA}.[LA]\\ +\boldsymbol{K_{C2}}.\sqrt{[H_2]}.[LA]+K_{HPA\wedge}.[HPA]+1\end{matrix}\right)}$	$\frac{k_1{}^*[H_2]}{\sqrt{K_H{}^*[H_2]}+1}{}^*\frac{[LA]^*\omega_{Cat.}}{\left(\begin{matrix}K_{BL}.[BL]+K_C.\sqrt{[H_2]}.[BL].+K_{BHP}.[BHP]+K_{LA}.[LA]\\ +K_{C2}.\sqrt{[H_2]}.[LA]+K_{HPA\wedge}.[HPA]+1\end{matrix}\right)}$
(NCLH2.2)	$\frac{k_1{}^*[H_2]}{K_H{}^*\sqrt{[H_2]}+1}{}^*\frac{[BL]^*\omega_{Cat.}}{(K_{BL}.[BL]+\boldsymbol{K_C}.\sqrt{[H_2]}.[BL].+K_{BHP}.[BHP]+1)}$	$\frac{k_1{}^*[H_2]}{\sqrt{K_H{}^*[H_2]}+1}{}^*\frac{[LA]^*\omega_{Cat.}}{(K_{LA}.[LA]+K_{C2}.\sqrt{[H_2]}.[LA]+K_{HPA\wedge}.[HPA]+1)}$

2.2. Analytical methods

For the quantitative analysis of the samples, gas chromatography coupled with flame ionization detection technique was used. The equipment (GC) used is from supplier Scion Instruments, equipped with a GC capillary column ZB-5, a versatile, low polarity column. This column is composed of 95% of dimethylpolysiloxane and 5% of phenyl groups. The column has 30 m of length, 0.32 mm of diameter and 0.25 μm of film internal coating.

Helium (99.99%) was used as the carrier gas at a constant flow rate of 1.2 mL.min-1 to transfer the sample from the injector, through the column, and into the FID-detector. The temperature of the injector and the detector were set at 250 °C. The oven temperature ramp was set to 50 °C (1 min) − 20 °C min^{-1} – 200 °C (1 min). Samples were diluted in acetone and injected into the GC. The injection volume was 1 μL, and the split ratio was 20:1.

2.3. Kinetic experiments

To develop kinetic models for GVL synthesis from the hydrogenation of *n*- BL with LA, a total of 14 experiments were carried out varying the initial operating conditions such as pressure, temperature, initial concentrations of the reactants, and catalyst loadings (Table 1). GVL was used as a solvent. Experiments carried out with Amberlite IR 120 were done at a reaction temperature lower than 120 °C to avoid the leaching of sulfonic groups.

The autoclave (stirred tank reactor) used for these experiments is a stainless- steel laboratory-scale vessel with a capacity of 300 mL, which is equipped with a stirrer set at 1000 RPM, an electrically heating jacket, a cooling coil, a pressure sensor, and a temperature sensor (Fig. 2). Each

Table 3
Regression parameters for each model.

	SSR	Objective function	Number of estimated parameters	AIC
LH1	11,693,900	24,125	19	13224.9
LH2	11,665,200	24,127	19	13221.3
NCLH1.1	11,697,000	24,154	19	13225.3
NCLH1.2	10,757,800	23,987	19	13102.4
ER1	11,685,300	24,153	19	13223.8
NCLH2.1	11,773,600	24,142	17	13230.9
NCLH2.2	10,443,600	23,940	18	13056.9

Table 4
Estimated Values at T_{ref} = 392.72 K and statistical Data for NCLH1.2.

Parameters		Units	Estimates	HPD%
Par1	$k_{BL\_hyd}(T_{Ref})$	$m^3.mol^{-1}.s^{-1}$. kg_dry basis RuC^{-1}	3.11E-06	14.57
Par2	Ea_{BL_hyd}	$J.mol^{-1}$	3.62E + 04	7.43
Par3	$K_{H2.}$	$m^3.mol^{-1}$	7.36E-04	>100%
Par4	$K_{BL\wedge}$	$m^3.mol^{-1}$	9.14E-04	29.02
Par5	$K_{BHP\wedge}$	$m^3.mol^{-1}$	Fixed to zero	–
Par6	$k'_{BHP\_cat\_Amb}(T_{Ref})$	s^{-1}. kg_dry basis Amb^{-1}	4.17E-05	49.21
Par7	$Ea'_{BHP\_cat\_Amb}$	$J.mol^{-1}$	Fixed to zero	–
Par8	$k_{BHP\_noncat}(T_{Ref})$	s^{-1}	5.78E-05	30.35
Par9	Ea_{BHP_noncat}	$J.mol^{-1}$	8.67E + 04	32.38
Par10	$k_{LA\_hyd}(T_{Ref})$	$m^3.mol^{-1}.s^{-1}$. kg_dry basis RuC^{-1}	8.08E-06	12.03
Par11	Ea_{LA_hyd}	$J.mol^{-1}$	4.65E + 04	6.47
Par12	$K_{LA\wedge}$	$m^3.mol^{-1}$	1.75E-03	15.80
Par13	$K_{HPA\wedge}$	$m^3.mol^{-1}$	Fixed to zero	–
Par14	$k'_{HPA\_cat\_Amb}(T_{Ref})$	s^{-1}. kg_dry basis Amb^{-1}	4.84E-04	49.37
Par15	$Ea'_{HPA\_cat\_Amb}$	$J.mol^{-1}$	Fixed to zero	–
Par16	$k_{HPA\_noncat}(T_{Ref})$	s^{-1}	1.12E-06	>100%
Par17	Ea_{HPA_noncat}	$J.mol^{-1}$	4.22E + 05	23.87
Par18	$K_{BHP-SO3H}$	$m^3.mol^{-1}$	Fixed to zero	–
Par19	$K_{HPA-SO3H}$	$m^3.mol^{-1}$	Fixed to zero	–
Par20	$k_{BHP\_RuC}(T_{Ref})$	s^{-1}. kg_dry basis RuC^{-1}	2.43E-05	16.96
Par21	Ea_{BHP_RuC}	$J.mol^{-1}$	Fixed to zero	–
Par22	$k_{HPA\_RuC}(T_{Ref})$	s^{-1}. kg_dry basis RuC^{-1}	5.80E-05	7.69
Par23	Ea_{HPA_RuC}	$J.mol^{-1}$	Fixed to zero	–
Par24	K_{BHP}	$m^3.mol^{-1}$	Fixed to zero	–
Par25	K_{HPA}	$m^3.mol^{-1}$	Fixed to zero	–
Par26	$k_{BHP\_diss}(T_{Ref})$	$m^3.mol^{-1}.s^{-1}$	1.70E-06	16.83
Par27	Ea_{BHP_diss}	$J.mol^{-1}$	1.06E + 05	13.31
Par28	$k_{HPA\_diss}(T_{Ref})$	$m^3.mol^{-1}.s^{-1}$	4.73E-06	6.99
Par29	Ea_{HPA_diss}	$J.mol^{-1}$	6.78E + 04	7.96

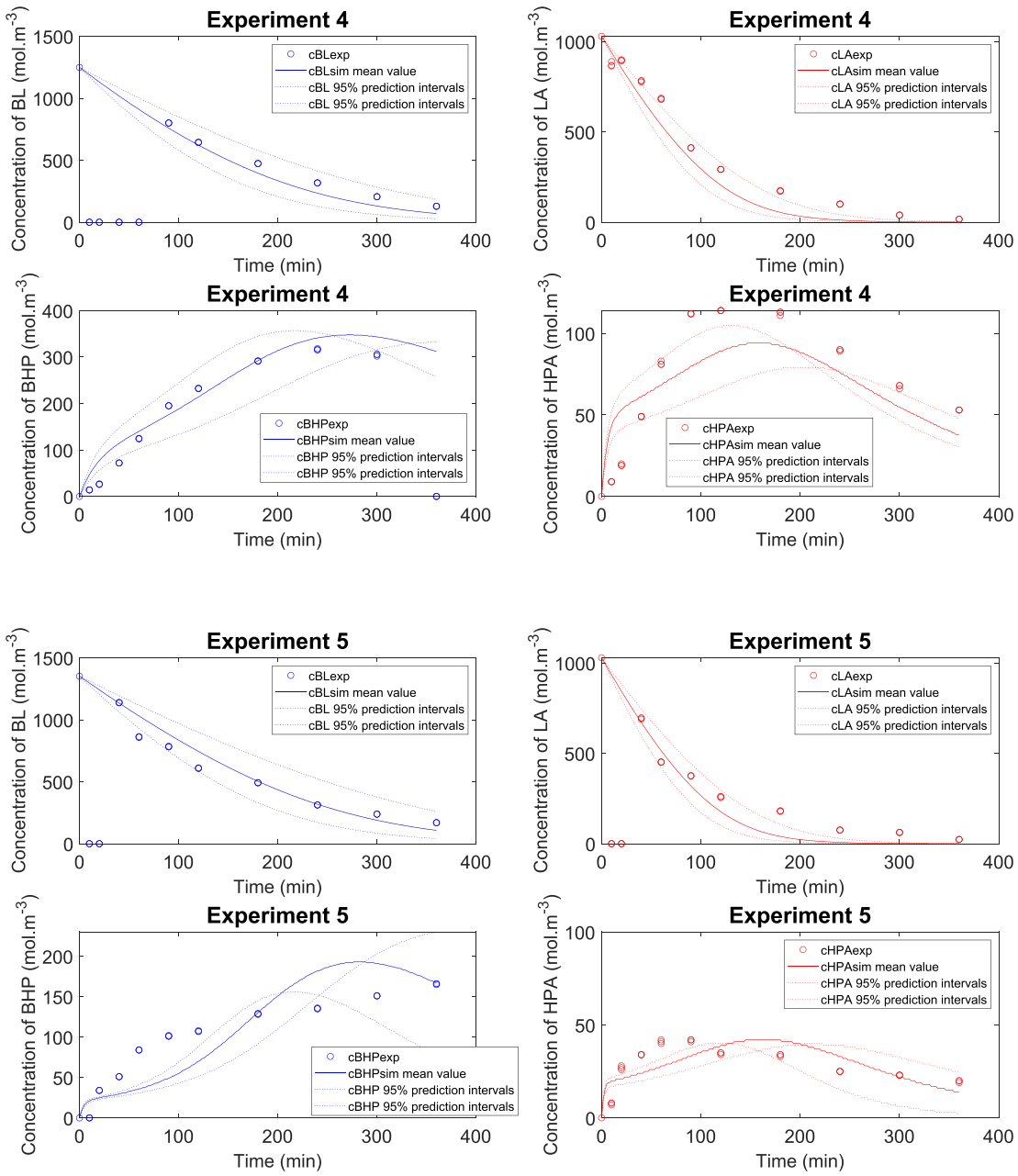

Fig. 9. Fit of Model NCLH1.2 to the experimental concentrations with prediction intervals.

experiment was carried out in isothermal and isobaric conditions. During these experiments, samples were taken at different times and then analyzed via GC-FID.

The concentration measurement uncertainty was evaluated via the standard deviation of replicate measurements. Each sample was analyzed thrice.

3. Results

This section describes the effects of experimental parameters such as temperature, pressure, and concentrations. on the hydrogenation and cyclization reactions from a phenomenological viewpoint. The hydrogenation of butyl levulinate or levulinic acid over Ru/C to GVL is a two-step reaction illustrated by Fig. 1[28,29,36,38]. In the first step, the carbonyl group of BL or LA is hydrogenated. In the second step, the hydroxyl group of the intermediate attacks the ester group leading to a cyclization.

The hydrogenation step was evaluated by the ratios $[BL]/[BL]_0$ and $[LA]/[LA]_0$. The cyclization step was assessed by the ratios $[BHP]/[BL]_0$ and $[HPA]/[LA]_0$. The standard deviations for BL, LA, BHP and HPA concentrations were found to be in average 1.76%, 3.64%, 2.41% and 3.64%, respectively. All the samples were analyzed three times. In Figs. 3-8, the replicated points are also displayed.

3.1. Repeatability

In addition, to replicate three times the sample analysis, two similar experiments were reproduced to evaluate the repeatability of the results. Experiments 1 and 3 (Table 1) were carried in similar operating conditions in the experimental matrix. Fig. 3 shows that the protocol used in this study is repeatable. Experiments 1 and 3 resulted in practice in identical results.

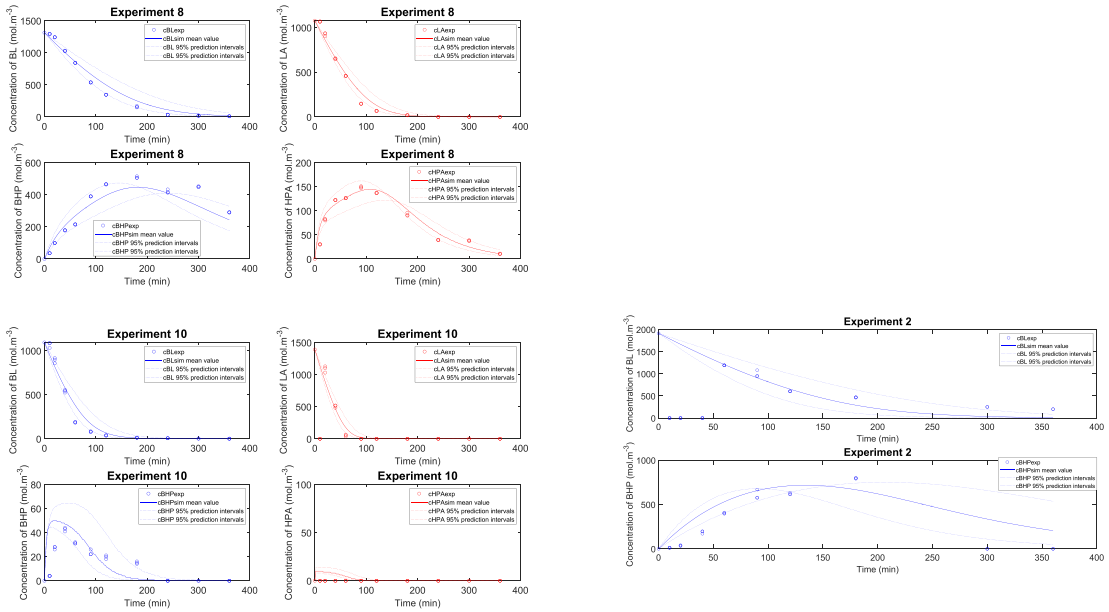

Fig. 9. (*continued*).

Table 5
Estimated Values at T_{ref} = 392.72 K and Statistical Data for NCLH2.2.

Parameters		Estimates	HPD%
Par1	$k_{BL\_hyd}(T_{Ref})$	3.02E-06	11.42
Par2	Ea_{BL_hyd}	3.69E + 04	7.17
Par3	$K_{H2.}$	Fixed to zero	–
Par4	$K_{BL^{\wedge}}$	Fixed to zero	–
Par5	$K_{BHP^{\wedge}}$	Fixed to zero	–
Par6	$k'_{BHP\_cat\_Amb}(T_{Ref})$	4.36E-05	48.29
Par7	$Ea'_{BHP\_cat\_Amb}$	Fixed to zero	–
Par8	$k_{BHP\_noncat}(T_{Ref})$	5.93E-05	30.40
Par9	Ea_{BHP_noncat}	7.78E + 04	35.92
Par10	$k_{LA\_hyd}(T_{Ref})$	7.75E-06	9.17
Par11	Ea_{LA_hyd}	4.61E + 04	6.51
Par12	$K_{LA^{\wedge}}$	1.69E-03	15.86
Par13	$K_{HPA^{\wedge}}$	Fixed to zero	–
Par14	$k'_{HPA\_cat\_Amb}(T_{Ref})$	4.79E-04	49.34
Par15	$Ea'_{HPA\_cat\_Amb}$	Fixed to zero	–
Par16	$k_{HPA\_noncat}(T_{Ref})$	1.25E-06	>100%
Par17	Ea_{HPA_noncat}	4.15E + 05	24.08
Par18	$K_{BHP-SO3H}$	Fixed to zero	–
Par19	$K_{HPA-SO3H}$	Fixed to zero	–
Par20	$k_{BHP\_RuC}(T_{Ref})$	2.41E-05	17.61
Par21	Ea_{BHP_RuC}	Fixed to zero	–
Par22	$k_{HPA\_RuC}(T_{Ref})$	5.74E-05	7.61
Par23	Ea_{HPA_RuC}	Fixed to zero	–
Par24	K_{BHP}	Fixed to zero	–
Par25	K_{HPA}	Fixed to zero	–
Par26	Kc	1.59E-04	25.39
Par27	Kc2	Fixed to zero	–
Par28	$k_{BHP\_diss}(T_{Ref})$	1.69E-06	16.19
Par29	Ea_{BHP_diss}	1.09E + 05	12.83
Par30	$k_{HPA\_diss}(T_{Ref})$	4.73E-06	6.71
Par31	Ea_{HPA_diss}	6.70E + 04	8.01

3.2. *Effect of temperature*

The effect of temperature on the kinetics was evaluated through Experiments 3 and 4 (Table 1) because only temperature change in these two experiments. Fig. 4 shows that hydrogenation steps are faster with increasing temperature. The temperature increase leads to a rise in the cyclization kinetics, and hence the decrease of the intermediate concentrations (BHP and HPA) is faster.

3.3. *Effect of hydrogen hydrostatic pressure*

Fig. 5 shows the H_2 pressure effect by comparing Experiments 3 and 5 (Table 1). One can observe that the increase of hydrostatic pressure leads to accelerate the hydrogenation steps. The consequence of this acceleration is an increase of intermediate concentrations (BHP and HPA). The pressure has an indirect effect on the cyclization step.

3.4. *Effect of catalyst Ru/C*

The effect of Ru/C loading on the kinetics were evaluated by comparing Experiments 7 and 8. The increase of Ru/C augments hydrogenation kinetics, leading to the rise of intermediate concentrations (Fig. 6).

3.5. *Effect of catalyst Amberlite IR-120*

Experiments 9 and 10 (Table 1) give information on the catalytic effect of Amberlite IR-120. Fig. 7 shows that this catalyst does not have an impact on the first reaction step as expected. The HPA concentrations were too low to be detected, but one can notice that Amberlite IR-120 strongly affects the consumption kinetics of the intermediate (BHP).

3.6. *Effect of LA amount*

Levulinic acid dissociates in the reaction mixture producing protons, which can catalyze the second reaction step. To verify this assumption,

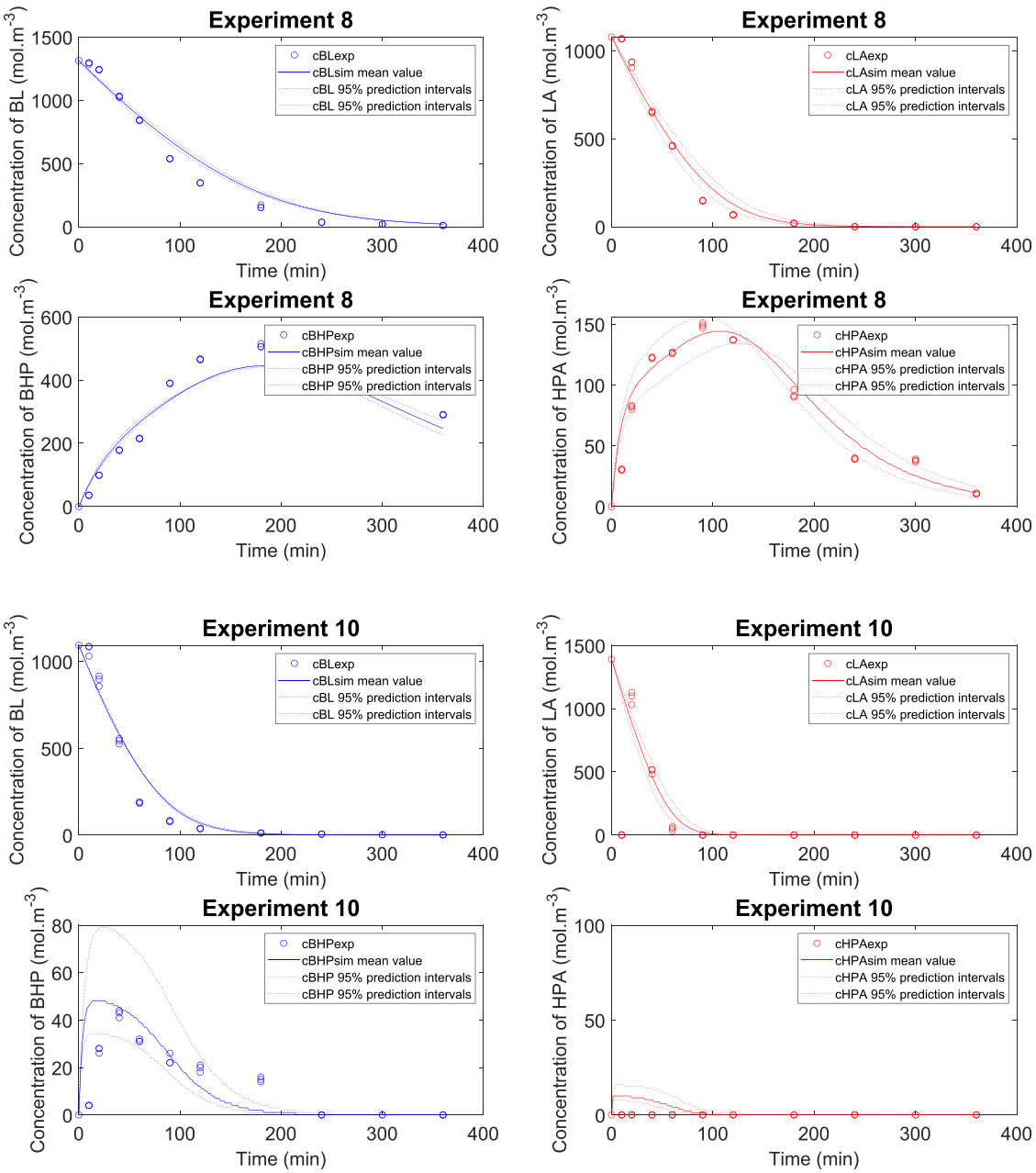

Fig. 10. Fit of Model NCLH2.2 with prediction intervals to the experimental concentrations.

the results from Experiments 3 and 6 were compared. The kinetics of BL hydrogenation are similar (Fig. 8). The kinetics of LA hydrogenation is to be slightly faster when the concentration of LA is higher. One can notice that the increase of LA concentration accelerates the cyclization of HPA and BHP steps (Fig. 8).

4. Discussion

4.1. Kinetics

From the Results section, several reaction mechanisms are possible for the hydrogenation and cyclization steps. The work of Capecci et al. [29] described that the surface reaction for the hydrogenation step of BL followss a non-competitive Langmuir-Hinshelwood model with no dissociation of molecular hydrogen. It means that there are two kinds of Ru sites and that the carbonyl group and hydrogen adsorb on each of them without competing. It was also found that the cyclization step can be catalyzed by Ru/C catalyst.

In this reaction system, BL and LA underwent similar reaction pathways. We neglected the esterification reaction of levulinic acid by butanol, because from the experimental data levulinic acid consumption is faster than the BHP cyclization.

Therefore, in the present work, seven kinetic models were evaluated for the hydrogenation step:

- competitive Langmuir-Hinshelwood with no dissociation of hydrogen (LH1),
- competitive Langmuir-Hinshelwood with dissociation of hydrogen (LH2),
- non-competitive Langmuir-Hinshelwood with no dissociation of hydrogen where LA and BL are in competitive adsorption on the same site but not hydrogen (NCLH1.1),

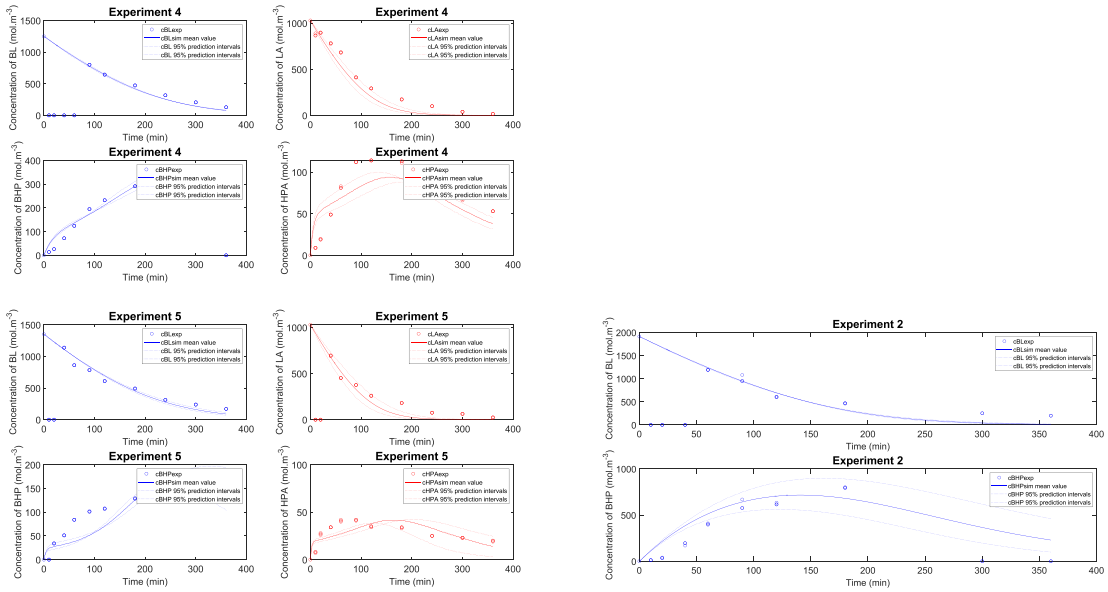

Fig. 10. (*continued*).

Table 6
Distribution of the 14 experiments in the 7 folds.

Fold	Experiments
Fold 1	10
	11
Fold 2	14
	9
Fold 3	8
	1
Fold 4	13
	7
Fold 5	12
	2
Fold 6	6
	4
Fold 7	5
	3

Table 7
Different Sets for regression and validation.

Set	Regression/Train	Validation/Test
Set 1	Folds 1–2-3–4-5–6	Fold 7
Set 2	Folds 7–1-2–3-4–5	Fold 6
Set 3	Folds 6–7-1–2-3–4	Fold 5
Set 4	Folds 5–6-7–1-2–3	Fold 4
Set 5	Folds 4–5-6–7-1–2	Fold 3
Set 6	Folds 3–4-5–6-7–1	Fold 2
Set 7	Folds 2–3-4–5-6–7	Fold 1

Table 8
$CV_{(K)}$ and standard deviation for each model.

	$CV_{(K)}$	$SD(CV_{(K)})$/%
LH1	3 586 050	99.88
LH2	3 656 893	93.19
NCLH1.1	3 635 269	94.19
NCLH1.2	2 168 016	28.66
ER1	3 595 498	95.09
NCLH2.1	3 690 655	92.00
NCLH22	1 978 294	27.47

- non-competitive Langmuir-Hinshelwood with no dissociation of hydrogen where LA, BL and H_2 are adsorbed on different sites (NCLH1.2),
- Eley-Rideal with no adsorption of hydrogen on the active sites (ER),
- non-competitive Langmuir-Hinshelwood with dissociation of hydrogen where LA and BL are in competitive adsorption on the same site but not hydrogen (NCLH2.1),
- non-competitive Langmuir-Hinshelwood with dissociation of hydrogen where LA, BL and H2 are adsorbed on different sites (NCLH2.2).

For the sake of clarity, the derivation of the seven kinetic models are described in Supplementary Material (S1). Table 2 displays the hydrogenation rate expression for each model.

For the second cyclization reaction, four different types of reaction were considered: non-catalytic cyclization of BHP and HPA, the catalytic routes due to the presence of acid sites on Ru/C, the acidic groups on Amberlite IR-120 and the protons from the dissociation of levulinic acid. Due to space limitation, the derivation for these rate equations are explained in Supplementary Material (S3).

Rate equations for the cyclization steps are:

$$R_{BHP\_noncat} = k_{BHP\_noncat} \cdot [\mathrm{BHP}] \quad (1)$$

$$R_{HPA\_noncat} = k_{HPA\_noncat} \cdot [\mathrm{HPA}] \quad (2)$$

$$R_{BHP\_RuC} = k_{BHP\_RuC} \cdot [\mathrm{BHP}] \cdot \frac{1}{K_{\mathrm{HPA}} \cdot [\mathrm{HPA}] + K_{\mathrm{BHP}} \cdot [\mathrm{BHP}] + 1.\omega_{\mathrm{Cat.RuC}}} \quad (3)$$

$$R_{HPA\_RuC} = k_{HPA\_RuC} \cdot [\mathrm{HPA}] \cdot \frac{1}{K_{\mathrm{HPA}} \cdot [\mathrm{HPA}] + K_{\mathrm{BHP}} \cdot [\mathrm{BHP}] + 1 \cdot \omega_{\mathrm{Cat.RuC}}} \quad (4)$$

$$R_{BHP\_SO3H} = k_{BHP\_SO3H} \cdot [\mathrm{BHP}] \cdot \frac{1}{K_{\mathrm{SO3H-HPA}} \cdot [\mathrm{HPA}] + K_{\mathrm{SO3H-BHP}} \cdot [\mathrm{BHP}] + 1.\omega_{\mathrm{Cat.Amb}}} \quad (5)$$

$$R_{HPA\_SO3H} = k_{HPA\_SO3H} \cdot [\mathrm{HPA}] \cdot \frac{1}{K_{\mathrm{SO3H-HPA}} \cdot [\mathrm{HPA}] + K_{\mathrm{SO3H-BHP}} \cdot [\mathrm{BHP}] + 1 \cdot \omega_{\mathrm{Cat.RuC}}} \quad (6)$$

$$R_{BHP\_diss} = k_{BHP\_diss} \cdot [\mathrm{BHP}] \cdot [\mathrm{LA}] \quad (7)$$

$$R_{HPA\_diss} = k_{HPA\_diss} \cdot [\mathrm{HPA}] \cdot [\mathrm{LA}] \quad (8)$$

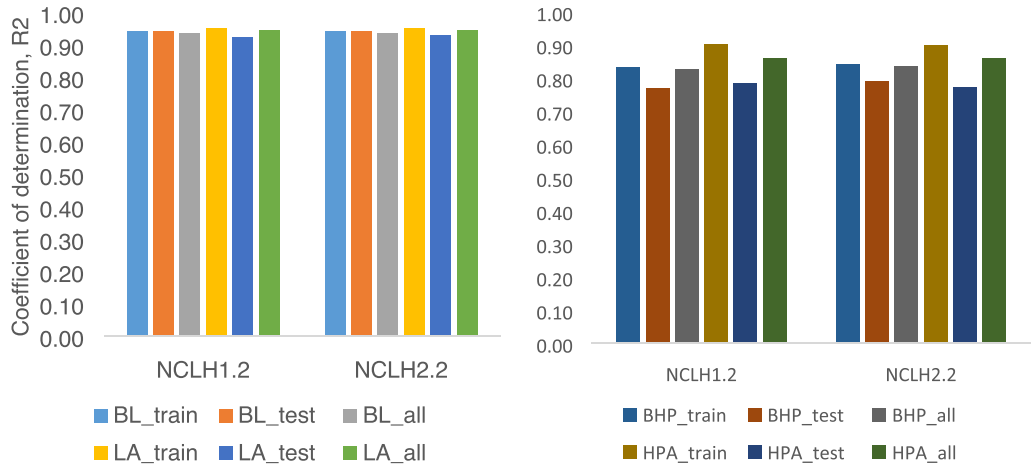

Fig. 11. Coefficient of determinations for training, test and all for the different models.

4.2. Material balances

Kinetic experiments were carried out under isobaric and isothermal conditions. Our previous study [46] found that external and internal mass transfer can be assumed to be negligible by using the operating conditions described in Section 2.

Material balances for different compounds in the liquid phase can be expressed as:

$$\frac{dC_{BL}}{dt} = -R_{BL\_hyd} \tag{9}$$

$$\frac{d[H_2]_{liq}}{dt} = k_L.a^*\left([H_2]^*_{liq} - [H_2]_{liq}\right) - R_{BL\_hyd} - R_{LA\_hyd} \tag{10}$$

$$\frac{dC_{BHP}}{dt} = R_{BL\_hyd} - R_{BHP\_noncat} - R_{BHP\_RuC} - R_{BHP\_SO3H} - R_{BHP\_diss} \tag{11}$$

$$\frac{dC_{BuOH}}{dt} = R_{BHP\_noncat} + R_{BHP\_RuC} + R_{BHP\_SO3H} + R_{BHP\_diss} \tag{12}$$

$$\frac{dC_{LA}}{dt} = -R_{LA\_hyd} \tag{13}$$

$$\frac{dC_{HPA}}{dt} = R_{LA\_hyd} - R_{HPA\_noncat} - R_{HPA\_RuC} - R_{HPA\_SO3H} - R_{HPA\_diss} \tag{14}$$

$$\frac{dC_{Water}}{dt} = R_{HPA_{noncat}} + R_{HPA_{RuC}} + R_{HPA_{SO3H}} + R_{HPA\_diss} \tag{15}$$

$$\frac{dC_{GVL}}{dt} = R_{BHP_{noncat}} + R_{BHP_{RuC}} + R_{BHP_{SO3H}} + R_{BHP\_diss} + R_{HPA_{noncat}} + R_{HPA_{RuC}} + R_{HPA_{SO3H}} + R_{HPA\_diss} \tag{16}$$

The term $[H_2]^*_{liq}$ is the concentration of hydrogen at the gas–liquid interface. The values of this term were determined through Henry's constant in GVL solvent $He(T) = \frac{[H_2]^*_{liq}}{P_{H_2,Reactor}}$ [38]. In this study the values of $k_L.a$, i.e., volumetric gas to liquid mass transfer coefficient for hydrogen was expressed as a function of density, viscosity and temperature [19].

4.3. Modeling

The commercial software Athena Visual Studio, using Bayesian statistics, was used for the simulation and estimation stages [62,63]. A Bayesian framework is considered to be more suitable for multi-response parameter estimation than the classical method of nonlinear least squares [55,64]. For the parameter estimation in Bayesian, one needs to determine the determinant criterion [65].

The concentrations of BL, BHP, LA and HPA were used as observables during the parameter estimation stage. The ODEs (9–16) were integrated by the DDAPLUS solver, included in Athena Visual Studio software. This solver is a modified Newton algorithm with a fixed leading coefficient backward difference formula to approximate the first-order derivative [66].

The subroutine package named GREGPLUS, was used to minimize the objective function $S(\partial)$, to calculate the credible intervals for each estimated parameter and to produce the normalized parameter covariance matrix.

To minimize the objective function $S(\partial)$, GREGPLUS uses successive quadratic programming starting from the user's initial guesses [62,64].

$$S(\partial) = (a+b+1)\bullet\ln|v(\partial)| \tag{17}$$

where, a is the number of events in response, b is the number of responses and $|v(\partial)|$ is the determinant of the covariance matrix of the responses. Each element of this matrix is defined as

$$v_{ij}(\partial) = \sum_{u=1}^{n}[Y_{iu} - f_{iu}(\partial)]\bullet[Y_{ju} - f_{ju}(\partial)] \tag{18}$$

With Y_{iu} the experimental concentration and $f_{iu}(\partial)$ the estimated value for response i and event u; Y_{ju} the experimental concentration and $f_{ju}(\partial)$ the estimated value for response j and event u.

The interval estimates for each estimated parameter are calculated from the final quadratic expansion of the objective function. The precision of the estimated parameters was evaluated by the marginal highest posterior density (HPD). The 95% marginal HPD was calculated by GREGPLUS package.

The modified Arrhenius equation is used to decrease the correlation

between the pre-exponential factor and the activation energy.

$$k(T_R) = k(T_{ref}) \bullet \exp\left(-\frac{E_a}{Rx`}\left(\frac{1}{T_R} - \frac{1}{T_{ref}}\right)\right) \quad (19)$$

where T_{ref} is the reference temperature chosen in the considered experimental temperature range.

During the modeling stage of the seven models, the following constants tended to approach zero during the preliminary iteration:

-the adsorption constants for BHP and HPA on Ru/C for the hydrogenation steps,

-the activation energy for the cyclization of BHP and HPA over Amberlite IR-120,

-the adsorption constants for BHP and HPA over Amberlite IR-120 for the cyclization steps,

-the activation energy for the cyclization of BHP and HPA due to the acid sites from Ru/C,

-the adsorption constant for BHP and HPA over the acid sites from Ru/C,

-The equilibrium constant K_{C2} was also found to be low in model NCLH2.2.

For that reason, it was deemed reasonable to fix the values of these estimated parameters to zero. Table 3 shows the regression parameters for each model:

-Sum of Squared Residuals (SSR) $\left(Y_{ju} - f_{ju}(\partial)\right)^2$

-Objective function defined by Equation (17) $S(\partial)$

-Number of estimated parameters

- Akaike information criterion (AIC) calculated by

$$AIC : numberofindependantevent \bullet \ln\left(\frac{\left[Y_{ju} - f_{ju}(\partial)\right]^2}{numberofindependantevent}\right) + 2.Numberofestimatedparameters \quad (20)$$

The AIC value [60] allows including the number of estimated parameters in the model discrimination. Models with low AIC are the most reliable.

Table 3 shows that NCLH1.2 and NCLH2.2 yield to low values of SSR, objective function and AIC. Due to space limitation, the estimated parameters, normalized covariance matrix and fit of these two models hereby reported, whereas the results obtained for the rest of the models analysed are included in the Supplementary Materials (S3). The results obtained in the present work is in agreement with with our previous work [29], where we found that NCLH1 was the most probable model for the hydrogenation of BL.

NCLH12

Table 4 shows the estimated values and the associated credible intervals (HPD%). The credible intervals for K_{H2} and for $k_{HPA\_noncat}(T_{Ref})$ are large due to the difficulty of estimating these values. The difficulty in estimating K_{H2} is linked to the fact that the hydrogen pressure does not significantly affect the kinetics. The high uncertainty for $k_{HPA\_noncat}(T_{Ref})$ is linked to the difficulty to tract HPA due to its high reactivity. The HPD intervals can be considered as low or medium for the other estimated parameters showing that the variation of the operating conditions was significant. Table 4 shows that the rate constant of LA hydrogenation is higher than the one of BL hydrogenation. The rate constants of HPA cylization are higher than the ones of BHP cyclization (Table 4).

Table S3.11 shows the correlation between the estimated parameters. In general, the correlations are low. The significant correlation between $k_{BL\_hyd}(T_{Ref})$ and $K_{BL^\wedge}$ are due to the difficulty to estimate the adsorption constant, and the strong correlation $k_{BHP\_noncat}(T_{Ref})$ and Ea_{BHP_noncat} is because the non-catalytic cyclization of BHP is relatively slow.

Fig. S4.1 displays the parity plots for BL, BHP, LA and HPA. NCLH2.1 model can predict BL and LA concentrations very well. The prediction of BHP and HPA concentrations is slightly lower due to the difficulty of tracking these intermediates.

Fig. 9 shows the fit of the model to the experimental concentrations with the 95% Prediction Intervals and the mean estimated values. From these graphs, one can notice that the model fits the experiments, and most of the experimental concentrations lie between the intervals. The intermediate concentrations for Experiment 10 are low due to the presence of Amberlite IR-120.

NCLH22

Table 5 displays the estimated values and their credible intervals. During the modeling for this model, it was not possible to estimate K_{H2}. and $K_{BL^\wedge}$ for that reason, their values were fixed to zero. The 95% HPD for $k_{HPA\_noncat}(T_{Ref})$ is higher due to the high reactivity of HPA. The HPD intervals for the other parameters can be assumed to be medium or low. From Table 5, one can notice that the rate constant of LA hydrogenation is higher than the one of BL. The rate constants of HPA cylization (from LA dissociation, Ru/C and Amerlite IR-120) are higher than the ones of BHP cyclization (Table 5).

Table S3.12 shows the correlation between the estimated parameters. One can notice a significant correlation between the following parameters: $k_{BL\_hyd}(T_{Ref})$ and Kc; $k_{BHP\_noncat}(T_{Ref})$ and Ea_{BHP_noncat}; $k_{LA\_hyd}(T_{Ref})$ and $K_{LA^\wedge}$ and $k_{HPA\_noncat}(T_{Ref})$ and Ea_{HPA_noncat}.

Fig. S4.2 shows the parity plot for BL, LA, BHP and HPA. Similar to Model NCLH1.2, the prediction for BL and LA is better than for the intermediates.

Fig. 10 shows the fit of the model to the experimental concentrations with the 95% prediction. The fitting is similar to the previous model.

4.4. Cross-validation: K-fold

The final stage of the assessment was the cross-validation one. Cross-validation was used to evaluate the predictability of the models and to determine the most probable one. The K-fold method was used [61]. The14 experiments were divided randomly into 7 folds (Table 6). The regressions (a.k.a traning) were made on 6 folds and validation (a.k.a testing) on the remaining fold as illustrated by Table 7.

The kinetic constants are estimated from each regression, and these estimated constants are used for the validation. To evaluate the prediction capacity of a model the $CV_{(K)}$ number is calculated.

$$CV_{(K)} = \frac{1}{7} \bullet \sum_{K=1}^{7} \left(Y_{i,experimental} - Y_{i,simulated}\right)_K^2 \quad (21)$$

The lower the $CV_{(K)}$, the better the model is predictable. Table 8 shows that $CV_{(K)}$ number is lower for NCLH1.2 and NCLH2.2. The standard deviation of $CV_{(K)}$ was calculated for each model, and it was found that the standard deviation was lower for NCLH1.2 and NCLH2.2. This means that the validation step was similar for each set.

In Supplementary Materials (S5), the estimated values for each regression set were displayed for NCLH1.2 and NCLH2.2. One can notice that the estimation was similar for each set compared to the estimation with the whole experimental data, i.e., the ones displayed in Tables 4 and 6.

To validate the models by cross-validation, Fig. 11 displays the coefficient of determination for the training step, test set and all data (i.e., Figs S4.1 and S4.2). One can notice that these values are similar, meaning that both models are validated.

5. Conclusions

One of the most common routes for the production of GVL is the hydrogenation of levulinic acid or alkyl levulinates. When alkyl levulinates produced from the alcoholysis of fructose, there is the presence of levulinic acid is also produced in the system. This paper proposed to investigate the kinetics of the hydrogenation of butyl levulinate and levulinic acid in GVL solvent over Ru/C. To increase the kinetics of the cyclization step, Amberlite IR-120 catalyst was added in the reaction mixture.

In the first analysis, it was found that the presence of LA can increase the kinetics of cyclization and Amberlite IR-120 has a significant catalytic effect on this reaction.

In the second step, several kinetic models, via Bayesian inference, were evaluated for the hydrogenation steps throughout K-fold approach. Seven kinetic models were evaluated: competitive Langmuir-Hinshelwood with no dissociation of hydrogen (LH1), competitive Langmuir-Hinshelwood with dissociation of hydrogen (LH2), non-competitive Langmuir-Hinshelwood with no dissociation of hydrogen where LA and BL are in competitive adsorption on the same site but not hydrogen (NCLH1.1), non-competitive Langmuir-Hinshelwood with no dissociation of hydrogen where LA, BL and H_2 are adsorbed on different sites (NCLH1.2), Eley-Rideal with no adsorption of hydrogen on the active sites (ER), non-competitive Langmuir-Hinshelwood with dissociation of hydrogen where LA and BL are in competitive adsorption on the same site but not hydrogen (NCLH2.1), and non-competitive Langmuir-Hinshelwood with dissociation of hydrogen where LA, BL and H2 are adsorbed on different sites (NCLH2.2). It was found that NCLH1.2 and NCLH2.2 were the most probable models, and the prediction capacity of these models was higher compared to the other.

This paper showed the benefit to using such reaction mixture system for the production of GVL. From an industrial viewpoint, the hydrogenation of levulinic acid and alkyl levulinate can be consecutive to the alcoholysis process. Quantum mechanics calculation could give more information concerning the adosption mechanism.

Declaration of Competing Interest

The authors declare that they have no known competing financial interests or personal relationships that could have appeared to influence the work reported in this paper.

Acknowledgments

The authors thank the *Maîtrise des Risques et Environementaux department*, and the Erasmus programme to make the research project of Giulia Bronzetti possible. The authors thank the Ministry of High Education, Science and Technology of Dominican Republic (MESCYT). For the analytical part, the authors thank University of Rouen Normandy, INSA Rouen Normandy, the Centre National de la Recherche Scientifique (CNRS), European Regional Development Fund (ERDF) N° HN0001343, Labex SynOrg (ANR-11-LABX-0029), Carnot Institute I2C, the graduate school for reasearch XL-Chem (ANR-18-EURE-0020 XL CHEM) and Region Normandie for their support. GC/FID was financed by FEDER RIN Green Chem 2019NU01FOBC08 N° 17P04374.

This research was funded, in whole or in part, by [ANR-DFG, ANR-20-CE92-0002 Deutsche Forschungsgemeinschaft (DFG) - Project number 446436621].

Appendix A. Supplementary data

Supplementary data to this article can be found online at https://doi.org/10.1016/j.cej.2021.133053.

References

[1] A.K. Chandel, V.K. Garlapati, S.P. Jeevan Kumar, M. Hans, A.K. Singh, S. Kumar, The role of renewable chemicals and biofuels in building a bioeconomy, Biofuels, Bioprod. Biorefining. 14 (4) (2020) 830–844, https://doi.org/10.1002/bbb.v14.410.1002/bbb.2104.

[2] B. Kumar, P. Verma, Biomass-based biorefineries: An important architype towards a circular economy, Fuel. 288 (2021) 119622, https://doi.org/10.1016/j.fuel.2020.119622.

[3] D. Sengupta, R.W. Pike, Chemicals from biomass: Integrating bioprocesses into chemical production complexes for sustainable development, CRC Press, Boca Raton, FL, USA, 2012. https://doi.org/10.1201/b12341.

[4] P.B. Thompson, The agricultural ethics of biofuels: The food vs. fuel debate, Agric. 2 (2012) 339–358. https://doi.org/10.3390/agriculture2040339.

[5] F.H. Isikgor, C.R. Becer, Lignocellulosic biomass: a sustainable platform for the production of bio-based chemicals and polymers, Polym. Chem. 6 (25) (2015) 4497–4559, https://doi.org/10.1039/C5PY00263J.

[6] S. Takkellapati, T. Li, M.A. Gonzalez, An overview of biorefinery-derived platform chemicals from a cellulose and hemicellulose biorefinery, Clean Technol. Environ, Policy 20 (7) (2018) 1615–1630, https://doi.org/10.1007/s10098-018-1568-5.

[7] K. Kohli, R. Prajapati, B.K. Sharma, Bio-Based Chemicals from Renewable Biomass for Integrated Biorefineries, Energies 2019, Vol. 12, Page 233. 12 (2019) 233. https://doi.org/10.3390/EN12020233.

[8] R. Liu, J. Chen, X. Huang, L. Chen, L. Ma, X. Li, Conversion of fructose into 5-hydroxymethylfurfural and alkyl levulinates catalyzed by sulfonic acid-functionalized carbon materials, Green Chem. 15 (2013) 2895–2903, https://doi.org/10.1039/C3GC41139G.

[9] S.-H. Pyo, S.J. Glaser, N. Rehnberg, R. Hatti-Kaul, Clean Production of Levulinic Acid from Fructose and Glucose in Salt Water by Heterogeneous Catalytic Dehydration, ACS Omega. 5 (24) (2020) 14275–14282, https://doi.org/10.1021/acsomega.9b04406.

[10] Levulinic Acid Market Size, Share & Trends | 2021 - 2026, (n.d.). https://www.marketdataforecast.com/market-reports/levulinic-acid-market (accessed August 28, 2021).

[11] Levulinic Acid Market Size | Industry Trends, Growth and Forecast to 2020-2030, (n.d.). https://www.psmarketresearch.com/market-analysis/levulinic-acid-market (accessed August 28, 2021).

[12] D.M. Alonso, S.G. Wettstein, J.A. Dumesic, Gamma-valerolactone, a sustainable platform molecule derived from lignocellulosic biomass, Green Chem. 15 (2013) 584–595, https://doi.org/10.1039/C3GC37065H.

[13] K. Yan, Y. Yang, J. Chai, Y. Lu, Catalytic reactions of gamma-valerolactone: A platform to fuels and value-added chemicals, Appl. Catal. B Environ. 179 (2015) 292–304, https://doi.org/10.1016/j.apcatb.2015.04.030.

[14] I.T. Horváth, H. Mehdi, V. Fábos, L. Boda, L.T. Mika, γ-Valerolactone—a sustainable liquid for energy and carbon-based chemicals, Green Chem. 10 (2) (2008) 238–242, https://doi.org/10.1039/B712863K.

[15] A.K. Chew, T.W. Walker, Z. Shen, B. Demir, L. Witteman, J. Euclide, G.W. Huber, J. A. Dumesic, R.C. Van Lehn, Effect of Mixed-Solvent Environments on the Selectivity of Acid-Catalyzed Dehydration Reactions, ACS Catal. 10 (3) (2020) 1679–1691, https://doi.org/10.1021/acscatal.9b0346010.1021/acscatal.9b03460.s00110.1021/acscatal.9b03460.s002.

[16] C. Laurence, S. Mansour, D. Vuluga, J. Legros, Measurement of the hydrogen bond acceptance of ionic liquids and green solvents by the 19F solvatomagnetic comparison method, Green Chem. 23 (4) (2021) 1816–1822, https://doi.org/10.1039/D0GC04104A.

[17] H. Lin, J. Chen, Y. Zhao, S. Wang, Conversion of C5 Carbohydrates into Furfural Catalyzed by SO3H-Functionalized Ionic Liquid in Renewable γ-Valerolactone, Energy & Fuels. 31 (4) (2017) 3929–3934, https://doi.org/10.1021/acs.energyfuels.6b0197510.1021/acs.energyfuels.6b01975.s001.

[18] C. Liu, M. Wei, J. Wang, J. Xu, J. Jiang, K. Wang, Facile Directional Conversion of Cellulose and Bamboo Meal Wastes over Low-Cost Sulfate and Polar Aprotic Solvent, ACS Sustain. Chem. Eng. 8 (14) (2020) 5776–5786, https://doi.org/10.1021/acssuschemeng.0c01280.

[19] H. Ariba, Y. Wang, C. Devouge-Boyer, R.P. Stateva, S. Leveneur, Physicochemical Properties for the Reaction Systems: Levulinic Acid, Its Esters, and γ-Valerolactone, J. Chem. Eng. Data. 65 (6) (2020) 3008–3020, https://doi.org/10.1021/acs.jced.9b0096510.1021/acs.jced.9b00965.s001.

[20] V. Pokorný, V. Štejfa, M. Fulem, C. Červinka, K. Růžička, Vapor Pressures and Thermophysical Properties of Ethylene Carbonate, Propylene Carbonate, γ-Valerolactone, and γ-Butyrolactone, J. Chem. Eng. Data. 62 (12) (2017) 4174–4186, https://doi.org/10.1021/acs.jced.7b0057810.1021/acs.jced.7b00578.s001.

[21] W.R.H. Wright, R. Palkovits, Development of heterogeneous catalysts for the conversion of levulinic acid to γ-valerolactone, ChemSusChem. 5 (9) (2012) 1657–1667, https://doi.org/10.1002/cssc.v5.910.1002/cssc.201200111.

[22] J.Q. Bond, D.M. Alonso, D. Wang, R.M. West, J.A. Dumesic, Integrated Catalytic Conversion of γ-Valerolactone to Liquid Alkenes for Transportation Fuels, Science (80-.). 327 (2010) 1110–1114. https://doi.org/10.1126/SCIENCE.1184362.

[23] J. Han, Integrated process for simultaneous production of jet fuel range alkenes and N-methylformanilide using biomass-derived gamma-valerolactone, J. Ind. Eng. Chem. 48 (2017) 173–179, https://doi.org/10.1016/J.JIEC.2016.12.036.

[24] Z. Zhang, Synthesis of γ-Valerolactone from Carbohydrates and its Applications, ChemSusChem. 9 (2) (2016) 156–171, https://doi.org/10.1002/cssc.v9.210.1002/cssc.201501089.

[25] Z. Yu, X. Lu, C. Liu, Y. Han, N. Ji, Synthesis of γ-valerolactone from different biomass-derived feedstocks: Recent advances on reaction mechanisms and catalytic systems, Renew. Sustain. Energy Rev. 112 (2019) 140–157, https://doi.org/10.1016/J.RSER.2019.05.039.

[26] M.G. Al-Shaal, W.R.H. Wright, R. Palkovits, Exploring the ruthenium catalysed synthesis of γ-valerolactone in alcohols and utilisation of mild solvent-free reaction conditions, Green Chem. 14 (2012) 1260–1263, https://doi.org/10.1039/C2GC16631C.

[27] H. Xu, D.i. Hu, M. Zhang, Y. Wang, Z. Zhao, Z. Jiang, H.F. Garces, K. Yan, Bimetallic NiCu Alloy Catalysts for Hydrogenation of Levulinic Acid, ACS Appl. Nano Mater. 4 (4) (2021) 3989–3997, https://doi.org/10.1021/acsanm.1c0033910.1021/acsanm.1c00339.s001.

[28] S. Capecci, Y. Wang, V. Casson Moreno, C. Held, S. Leveneur, Solvent effect on the kinetics of the hydrogenation of n-butyl levulinate to γ-valerolactone, Chem. Eng. Sci. 231 (2021) 116315, https://doi.org/10.1016/j.ces.2020.116315.

[29] S. Capecci, Y. Wang, J. Delgado, V. Casson Moreno, M. Mignot, H. Grénman, D. Y. Murzin, S. Leveneur, Bayesian Statistics to Elucidate the Kinetics of γ-Valerolactone from n-Butyl Levulinate Hydrogenation over Ru/C, Ind. Eng. Chem. Res. 60 (31) (2021) 11725–11736, https://doi.org/10.1021/acs.iecr.1c0210710.1021/acs.iecr.1c02107.s001.

[30] A.S. Piskun, H.H. van de Bovenkamp, C.B. Rasrendra, J.G.M. Winkelman, H. J. Heeres, Kinetic modeling of levulinic acid hydrogenation to γ-valerolactone in water using a carbon supported Ru catalyst, Appl. Catal. A Gen. 525 (2016) 158–167, https://doi.org/10.1016/j.apcata.2016.06.033.

[31] A.M. Hengne, C.V. Rode, Cu–ZrO2 nanocomposite catalyst for selective hydrogenation of levulinic acid and its ester to γ-valerolactone, Green Chem. 14 (2012) 1064–1072, https://doi.org/10.1039/C2GC16558A.

[32] W. Luo, U. Deka, A.M. Beale, E.R.H. van Eck, P.C.A. Bruijnincx, B.M. Weckhuysen, Ruthenium-catalyzed hydrogenation of levulinic acid: Influence of the support and solvent on catalyst selectivity and stability, J. Catal. 301 (2013) 175–186, https://doi.org/10.1016/j.jcat.2013.02.003.

[33] H. Mehdi, V. Fábos, R. Tuba, A. Bodor, L.T. Mika, I.T. Horváth, Integration of Homogeneous and Heterogeneous Catalytic Processes for a Multi-step Conversion of Biomass: From Sucrose to Levulinic Acid, γ-Valerolactone, 1,4-Pentanediol, 2-Methyl-tetrahydrofuran, and Alkanes, Top. Catal. 48 (1-4) (2008) 49–54, https://doi.org/10.1007/s11244-008-9047-6.

[34] K.-I. Shimizu, S. Kanno, K. Kon, Hydrogenation of levulinic acid to γ-valerolactone by Ni and MoOx co-loaded carbon catalysts, Green Chem. 16 (8) (2014) 3899–3903, https://doi.org/10.1039/C4GC00735B.

[35] O.A. Abdelrahman, A. Heyden, J.Q. Bond, Analysis of kinetics and reaction pathways in the aqueous-phase hydrogenation of levulinic acid to form γ-Valerolactone over Ru/C, ACS Catal. 4 (4) (2014) 1171–1181, https://doi.org/10.1021/cs401177p.

[36] Y. Wang, I. Plazl, L. Vernières-Hassimi, S. Leveneur, From calorimetry to thermal risk assessment: γ-Valerolactone production from the hydrogenation of alkyl levulinates, Process Saf. Environ. Prot. 144 (2020) 32–41, https://doi.org/10.1016/j.psep.2020.07.017.

[37] Y. Wang, L. Vernières-Hassimi, V. Casson-Moreno, J.-P. Hébert, S. Leveneur, Thermal Risk Assessment of Levulinic Acid Hydrogenation to γ-Valerolactone, Org. Process Res. Dev. 22 (9) (2018) 1092–1100, https://doi.org/10.1021/acs.oprd.8b0012210.1021/acs.oprd.8b00122.s001.

[38] Y. Wang, M. Cipolletta, L. Vernières-Hassimi, V. Casson-Moreno, S. Leveneur, Application of the concept of Linear Free Energy Relationships to the hydrogenation of levulinic acid and its corresponding esters, Chem. Eng. J. 374 (2019) 822–831, https://doi.org/10.1016/j.cej.2019.05.218.

[39] P.A. Son, S. Nishimura, K. Ebitani, Production of γ-valerolactone from biomass-derived compounds using formic acid as a hydrogen source over supported metal catalysts in water solvent, RSC Adv. 4 (2014) 10525–10530, https://doi.org/10.1039/C3RA47580H.

[40] J. Yuan, S.-S. Li, L. Yu, Y.-M. Liu, Y. Cao, H.-Y. He, K.-N. Fan, Copper-based catalysts for the efficient conversion of carbohydrate biomass into γ-valerolactone in the absence of externally added hydrogen, Energy Environ. Sci. 6 (2013) 3308–3313, https://doi.org/10.1039/C3EE40857D.

[41] L.i. Deng, J. Li, D.-M. Lai, Y. Fu, Q.-X. Guo, Catalytic Conversion of Biomass-Derived Carbohydrates into γ-Valerolactone without Using an External H2 Supply, Angew. Chemie Int. Ed. 48 (35) (2009) 6529–6532, https://doi.org/10.1002/anie.v48:3510.1002/anie.200902281.

[42] L.i. Deng, Y. Zhao, J. Li, Y. Fu, B. Liao, Q.-X. Guo, Conversion of Levulinic Acid and Formic Acid into γ-Valerolactone over Heterogeneous Catalysts, ChemSusChem. 3 (10) (2010) 1172–1175, https://doi.org/10.1002/cssc.v3:1010.1002/cssc.201000163.

[43] V. Fábos, L.T. Mika, I.T. Horváth, Selective Conversion of Levulinic and Formic Acids to γ-Valerolactone with the Shvo Catalyst, Organometallics. 33 (1) (2014) 181–187, https://doi.org/10.1021/om400938h.

[44] C. Fellay, Paulâ P.J Dyson, G. Laurenczy, A Viable Hydrogen-Storage System Based On Selective Formic Acid Decomposition with a Ruthenium Catalyst, Angew. Chemie Int. Ed. 47 (21) (2008) 3966–3968, https://doi.org/10.1002/anie.v47:2110.1002/anie.200800320.

[45] H. Heeres, R. Handana, D. Chunai, C.B. Rasrendra, B. Girisuta, H.J. Heeres, Combined dehydration/(transfer)-hydrogenation of C6-sugars (D-glucose and D-fructose) to γ-valerolactone using ruthenium catalysts, Green Chem. 11 (2009) 1247–1255, https://doi.org/10.1039/B904693C.

[46] A.M. Hengne, A.V. Malawadkar, N.S. Biradar, C.V. Rode, Surface synergism of an Ag–Ni/ZrO2 nanocomposite for the catalytic transfer hydrogenation of bio-derived platform molecules, RSC Adv. 4 (2014) 9730–9736, https://doi.org/10.1039/C3RA46495D.

[47] A.M. Ruppert, M. Jędrzejczyk, O. Sneka-Płatek, N. Keller, A.S. Dumon, C. Michel, P. Sautet, J. Grams, Ru catalysts for levulinic acid hydrogenation with formic acid as a hydrogen source, Green Chem. 18 (7) (2016) 2014–2028, https://doi.org/10.1039/C5GC02200B.

[48] H.u. Li, Z. Fang, S. Yang, Direct Conversion of Sugars and Ethyl Levulinate into γ-Valerolactone with Superparamagnetic Acid-Base Bifunctional ZrFeOx Nanocatalysts, ACS Sustain. Chem. Eng. 4 (1) (2016) 236–246, https://doi.org/10.1021/acssuschemeng.5b0148010.1021/acssuschemeng.5b01480.s001.

[49] M. Chia, J.A. Dumesic, Liquid-phase catalytic transfer hydrogenation and cyclization of levulinic acid and its esters to γ-valerolactone over metal oxide catalysts, Chem. Commun. 47 (2011) 12233–12235, https://doi.org/10.1039/C1CC14748J.

[50] H.u. Li, Z. Fang, S. Yang, Direct Catalytic Transformation of Biomass Derivatives into Biofuel Component γ-Valerolactone with Magnetic Nickel-Zirconium Nanoparticles, Chempluschem. 81 (1) (2016) 135–142, https://doi.org/10.1002/cplu.v81.110.1002/cplu.201500492.

[51] E. Ramírez, R. Bringué, C. Fité, M. Iborra, J. Tejero, F. Cunill, Assessment of ion exchange resins as catalysts for the direct transformation of fructose into butyl levulinate, Appl. Catal. A Gen. 612 (2021) 117988, https://doi.org/10.1016/j.apcata.2021.117988.

[52] J.N. Appaturi, M.R. Johan, R.J. Ramalingam, H.A. Al-Lohedan, J.J. Vijaya, Efficient synthesis of butyl levulinate from furfuryl alcohol over ordered mesoporous Ti-KIT-6 catalysts for green chemistry applications, RSC Adv. 7 (87) (2017) 55206–55214, https://doi.org/10.1039/C7RA10289E.

[53] C. Moreno-Marrodan, P. Barbaro, Energy efficient continuous production of γ-valerolactone by bifunctional metal/acid catalysis in one pot, Green Chem. 16 (2014) 3434–3438, https://doi.org/10.1039/C4GC00298A.

[54] A.M.R. Galletti, C. Antonetti, V. De Luise, M. Martinelli, A sustainable process for the production of γ-valerolactone by hydrogenation of biomass-derived levulinic acid, Green Chem. 14 (2012) 688–694, https://doi.org/10.1039/C2GC15872H.

[55] J. Kopyscinski, J. Choi, J.M. Hill, Comprehensive kinetic study for pyridine hydrodenitrogenation on (Ni)WP/SiO2 catalysts, Appl. Catal. A Gen. 445–446 (2012) 50–60, https://doi.org/10.1016/j.apcata.2012.08.027.

[56] S.-H. Hsu, S.D. Stamatis, J.M. Caruthers, W.N. Delgass, V. Venkatasubramanian, G. E. Blau, M. Lasinski, S. Orcun, Bayesian framework for building kinetic models of catalytic systems, Ind. Eng. Chem. Res. 48 (10) (2009) 4768–4790, https://doi.org/10.1021/ie801651y.

[57] J. Kopyscinski, T.J. Schildhauer, F. Vogel, S.M.A. Biollaz, A. Wokaun, Applying spatially resolved concentration and temperature measurements in a catalytic plate reactor for the kinetic study of CO methanation, J. Catal. 271 (2) (2010) 262–279, https://doi.org/10.1016/j.jcat.2010.02.008.

[58] N. Thakar, R.J. Berger, F. Kapteijn, J.A. Moulijn, Modelling kinetics and deactivation for the selective hydrogenation of an aromatic ketone over Pd/SiO2, Chem. Eng. Sci. 62 (18-20) (2007) 5322–5329, https://doi.org/10.1016/j.ces.2007.01.059.

[59] J.P. Bernacki, R.M. Murphy, Model discrimination and mechanistic interpretation of kinetic data in protein aggregation studies, Biophys. J. 96 (7) (2009) 2871–2887, https://doi.org/10.1016/j.bpj.2008.12.3903.

[60] M.A. McDonald, L. Bromig, M.A. Grover, R.W. Rousseau, A.S. Bommarius, Kinetic model discrimination of penicillin G acylase thermal deactivation by non-isothermal continuous activity assay, Chem. Eng. Sci. 187 (2018) 79–86, https://doi.org/10.1016/j.ces.2018.04.046.

[61] Y. Slotboom, M.J. Bos, J. Pieper, V. Vrieswijk, B. Likozar, S.R.A. Kersten, D.W. F. Brilman, Critical assessment of steady-state kinetic models for the synthesis of methanol over an industrial Cu/ZnO/Al2O3 catalyst, Chem. Eng. J. 389 (2020) 124181, https://doi.org/10.1016/j.cej.2020.124181.

[62] W.E. Stewart, M. Caracotsios, Computer-Aided Modeling of Reactive Systems, Wiley & So, Wiley & Sons, New Jersey, 2008.

[63] W.E. Stewart, M. Caracotsios, Athena Visual Studio, (n.d.). www.athenavisual.com.

[64] W.E. Stewart, M. Caracotsios, J.P. Sørensen, Parameter estimation from multiresponse data, AIChE J. 38 (5) (1992) 641–650, https://doi.org/10.1002/(ISSN)1547-590510.1002/aic.v38:510.1002/aic.690380502.

[65] M.A.J.S. BOEKEL, Statistical Aspects of Kinetic Modeling for Food Science Problems, J. Food Sci. 61 (3) (1996) 477–486, https://doi.org/10.1111/jfds.1996.61.issue-310.1111/j.1365-2621.1996.tb13138.x.

[66] M. Caracotsios, W.E. Stewart, Sensitivity analysis of initial value problems with mixed odes and algebraic equations, Comput. Chem. Eng. 9 (4) (1985) 359–365, https://doi.org/10.1016/0098-1354(85)85014-6.

B.2 Article: Reaction enthalpies for the hydrogenation of alkyl levulinates and levulinic acid on Ru/C – influence of experimental conditions and alkyl chain length

Process Safety and Environmental Protection 171 (2023) 289–298

Contents lists available at ScienceDirect

Process Safety and Environmental Protection

journal homepage: www.journals.elsevier.com/process-safety-and-environmental-protection

Reaction enthalpies for the hydrogenation of alkyl levulinates and levulinic acid on Ru/C– influence of experimental conditions and alkyl chain length

Jose Delgado [a,c], Wenel Naudy Vásquez Salcedo [a,e], Christine Devouge-Boyer [b], Jean-Pierre Hebert [a], Julien Legros [b], Bruno Renou [e], Christoph Held [d], Henrik Grenman [c], Sébastien Leveneur [a,*]

[a] INSA Rouen Normandie, University Rouen Normandie, Normandie Université, LSPC, UR 4704, F-76000 Rouen, France
[b] Normandie Univ, INSA de Rouen, Université de Rouen, CNRS, COBRA (UMR 6014), Avenue de l'Université, Saint-Etienne-du-Rouvray 76800, France
[c] Laboratory of Industrial Chemistry and Reaction Engineering, Johan Gadolin Process Chemistry Centre, Åbo Akademi University, Henriksgatan 2, FI-20500 Åbo/Turku, Finland
[d] Laboratory of Thermodynamics, TU Dortmund University, Emil-Figge-Str. 70, 44227 Dortmund, Germany
[e] INSA Rouen-Normandie, UNIROUEN, CNRS, CORIA, Normandie University, F-76000 Rouen, France

ARTICLE INFO

Keywords:
Tian-Calvet calorimeter
RC1
Hydrogenation
Levulinate
Levulinic acid

ABSTRACT

The development of process flow diagrams requires knowledge of reaction enthalpy for pinch analysis and thermal risk assessment. Such information is missing for some biomass processes, such as the production of γ-valerolactone (GVL) from the hydrogenation of levulinic acid or alkyl levulinate. To fill this gap, this manuscript describes a detailed calorimetric study on the hydrogenation of levulinic acid (LA), methyl levulinate (ML), ethyl levulinate (EL), propyl levulinate (PrL), butyl levulinate (BL) and pentyl levulinate (PeL) over Ru/C. This reaction system occurs through a two-step pathway with a domino hydrogenation/cyclization sequence. The cyclization step (lactonization) was found to be endothermic and was evaluated by a Tian-Calvet C80 microcalorimeter, whereas the hydrogenation step was found to be exothermic and was tracked by a RC1 Mettler Toledo High-Pressure calorimeter. It was verified that reaction enthalpy is independent of reaction temperature (in the operating conditions used in this work), levulinate concentration and solvent (levulinate, corresponding alcohol or GVL). It was also found that reaction enthalpy for both steps did not depend linearly on alkyl chain length.

1. Introduction

The knowledge of reaction enthalpy for chemical processes is fundamental from a safety and energy optimization standpoint (Dakkoune et al., 2019; Stoessel, 2008). In process safety, reaction enthalpy determines the severity of a chemical reaction in the case of thermal runaway. This thermodynamic property is essential for developing an efficient process flow diagram to find the optimum operating conditions to decrease energy consumption.

Biomass valorization represents a challenge in the field of thermodynamics because many biomass compounds physicochemical properties are unavailable. Thus, new models need to be developed. It is crucial to develop accurate thermodynamic models for such processes without gambling on existing petrochemical thermodynamic models. In order to make an accurate pinch analysis, the knowledge of reaction enthalpies is vital and aids in finding the optimum design from an energy consumption standpoint.

Lignocellulosic biomass raw materials can sustain the chemical industry because it is not in competition with the alimentary sector. For two decades, industry and academia have aimed to produce renewable platform molecules from cellulose or hemicellulose. Among these platform molecules, γ-valerolactone (GVL) is a promising one.

GVL is a versatile molecule used in different sectors, such as fuels or

Abbreviations: AL, alkyl levulinate; BL, butyl levulinate; BHP, n-butyl 4-hydroxypentanoate; EL, ethyl levulinate; EHP, ethyl 4-hydroxypentanoate; GVL, γ-valerolactone; HPA, 4-hydroxypentanoic acid; LA, levulinic acid; ML, methyl levulinate; MHP, methyl 4-hydroxypentanoate; PeL, pentyl levulinate; PeHL, pentyl 4-hydroxypentanoate; PrL, propyl levulinate; PrHP, propyl 4-hydroxypentanoate; ROH, co-product of the second reaction (methanol, ethanol, ect); STD, Standard deviation.

* Corresponding author.
E-mail address: sebastien.leveneur@insa-rouen.fr (S. Leveneur).

https://doi.org/10.1016/j.psep.2023.01.025
Received 4 July 2022; Received in revised form 22 December 2022; Accepted 10 January 2023
Available online 11 January 2023

Nomenclature

C_P	Specific heat-capacity [J/(kg.K)].
$\Delta H^m_{R,i}$	Reaction enthalpy [J/mol].
V_{liq}	Volume of liquid [L].
m_{insert}	Insert mass [kg].
P	Pressure [bar].
Q_{C80}	Total energy released or absorbed and measured by C80 [J].
Q_{RC1}	Total energy released or absorbed and measured by RC1 [J].
R_i	Reaction rate *i* [mol/(L.s)].

valerolactone (GVL) (Sigma Aldrich, >99%, CAS: 108–29–2); levulinic acid (Acros Organics, 99%, CAS: 123–76–2); methyl levulinate (Sigma-Aldrich, 99%, CAS: 624–45–3); ethyl levulinate (Sigma Aldrich, 99%, CAS: 539–88–8); n-propyl levulinate (Sigma Aldrich, 95%, CAS: 645–67–0); n-butyl levulinate (Alfa-Aesar, 98%, 2052–15–5); methanol (Fischer Scientific, 99%, CAS: 67–56–1); ethanol (Carlo Erba, anhydrous, 99%, CAS: 64–17–5); n-propanol (Carlo Erba, 99%, 71–23–8); 1-butanol (Lab Line, 99%, CAS: 71–36–3); 1-pentanol (Carlo Erba, 99%, CAS: 71–41–0); Ru/activated charcoal (Alfa-Aesar, 5% Ru, powder, reduced, 50% nominally wet, CAS: 7440–18–8); amberlite IR-120, H form (Acros Organics) and acetone (Fischer Scientific, 99%, CAS: 67–64–1).

Reaction mixtures with high concentrations on intermediates (all 4-hydroxyalkyllevulinates) were obtained from the calorimetric experiments described in this article. Propyl levulinate (PrL) and pentyl levulinate (PeL) were obtained from methyl levulinate and ethyl levulinate transesterification experiments, respectively (Melchiorre et al., 2020).

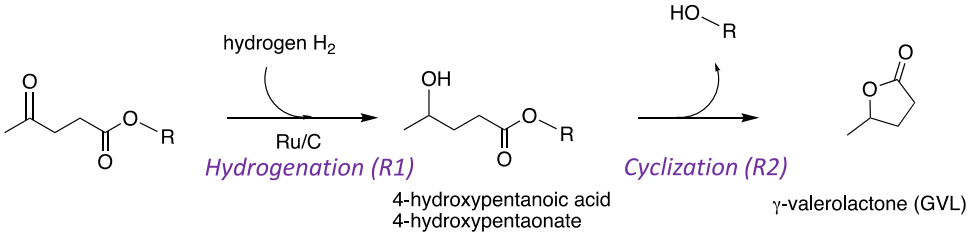

Fig. 1. Hydrogenation of levulinic acid (LA) or alkyl levulinate (AL) to γ-valerolactone (GVL) over Ru/C.

materials. It is also known to be a suitable solvent because of its low vapor pressure, high solubility capacity and high flash point values (Chew et al., 2020; Horváth et al., 2008; Lin et al., 2017; Liu et al., 2020; Pokorný et al., 2017). GVL has been successfully used as a solvent for the alcoholysis of fructose (Di Menno Di Bucchianico et al., 2022).

There are different routes for the production of GVL from the hydrogenation of levulinic acid or alkyl levulinate: molecular hydrogenation, decomposition of alcohol or formic acid to produce hydrogen (Kuwahara et al., 2017a; Liu et al., 2019). The most convenient method is the hydrogenation of levulinic acid (LA) or alkyl levulinates (ALs) over Ru/C using molecular hydrogen (Fig. 1).

Several investigations have been performed on the choice of catalysts (Dutta et al., 2019; Kuwahara et al., 2017b; Liguori et al., 2015; Tang et al., 2014; Yan et al., 2013, 2009; Yang et al., 2014), kinetic modeling (Capecci et al., 2021a, 2021b; Delgado et al., 2022; Mamun et al., 2017; Piskun et al., 2016a, 2016b; Wang et al., 2019) and some on physicochemical properties (Ariba et al., 2020) or thermal risk assessment (Casson Moreno et al., 2019; Wang et al., 2020, 2018). To the best of our knowledge, there are no studies on the evolution of the reaction enthalpies for different substituents in different solvents and temperatures. Such information is crucial to find the optimum process design.

To investigate this, the hydrogenation of levulinic acid (LA), methyl levulinate (ML), ethyl levulinate (EL), n-propyl levulinate (PrL), n-butyl levulinate (BL) and n-pentyl levulinate (PeL) were studied over Ru/C.

In the first stage of this work, the influence of substrate concentration, reaction temperature and solvents were done on the hydrogenation of butyl levulinate were studied. In the second stage, the reaction enthalpies of the different compounds were determined. We developed an original approach to study the hydrogenation of PrL and PeL because it was challenging to obtain this compound in high concentration from a manufacturer.

2. Experimental section

Most of the reagents, used for analytical identification and experiments, were obtained from different providers and used without further purification: hydrogen gas, H_2 (Linde, 99.99%, CAS: 1333–74–0); γ

2.1. Analytical equipment and methods

Quantitative analysis was performed using gas chromatography (GC) coupled with a flame ionization detector (GC-FID). GC-FID specs: (SCION Instruments); low polarity column (Phenomenex, ZB-5, length: 30 m, internal diameter: 0.32 mm, coating width: 0.25 μm composed of 95% dimethyl siloxane and 5% phenyl groups); carrier gas: He (99.99%), gas flow: 1.2 ML/min; injector temperature, 250 °C; detector temperature: 250 °C; temperature ramp: 50 °C (2 min) – 20 °C/min – 260 °C; injection volume, 1 μL; split ratio 1:20. All samples were diluted in acetone prior to GC-FID analysis, and each measurement was repeated three times.

High-concentrated ML, EL, PrL and BL solutions were used to carry out calibration curves in the GC-FID. To quantify the intermediates (MHP, EHP, PrHP, BHP and PeHP), we used the calibration curve of the corresponding alkyl levulinate, since alkyl levulinate and the corresponding intermediate have similar structure, similar retention time, similar interaction through the retention column and present the same shape for the integration peak in the chromatogram.

The calibration curve for pentyl levulinate (PeL) was done by extrapolation from the calibration curves of ML, EL, PrL and BL.

Analytical identification of compounds was performed by GC-FID, for store-bought compounds, and for chemicals synthesized in experiments, a gas chromatography coupled with a mass spectrometer (GC-MS) method was employed. GC-MS Specs GC: System: (Perkin Elmer Clarus 580); Mass Spectrometer: (SQ8S); Column (Phenomenex ZB-5MS plus (Length: 30 m, internal diameter: 0,25 mm, internal coating width: 0,25 μm composed of 95% Dimethylpolysiloxane and 5% Phenyl-Arylene); Carrier gas: He (99.99%), gas flow: 1 ML/min; Injector temperature: 250 °C; Split Ratio: 1/20; Ramp: 50 °C (1 min) – 10 °C/min – 245 °C (1 min); Source Temperature: 150 °C, Transfer line temperature: 170 °C; Ionization mode: EI 70 eV; Identification method: Mode SCAN, with database NIST 03 from 40 to 600 *m/z*.

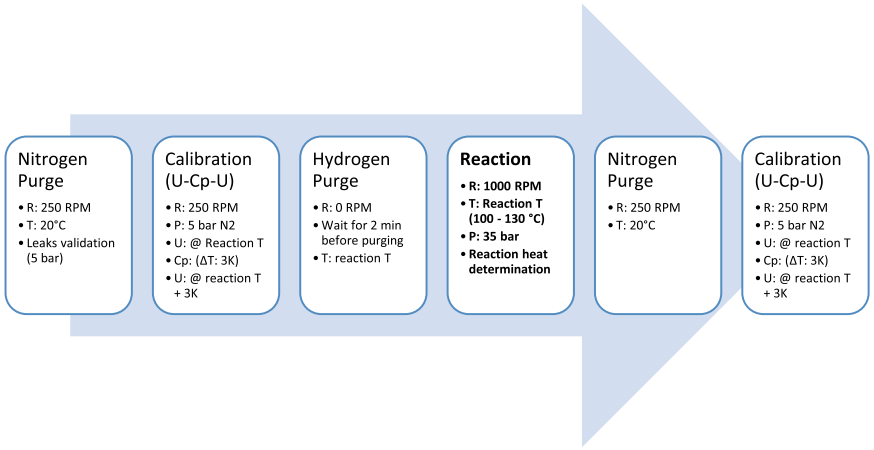

Fig. 2. Steps performed in RC1 experiments.

2.2. Calorimeters

In order to estimate the reaction enthalpy of both reaction steps, two different calorimeters were used. The Tian-Calvet C80 micro-calorimeter was used for the second reaction step, i.e., cyclization; and the Mettler Toledo RC1mx calorimeter was used for the first reaction step, i.e., hydrogenation.

In the Tian-Calvet C80 calorimeter, two 12.5 ML cells are used, one for reference and the other for measurement. The energy flow is measured by the tension difference between these cells with a resolution of 0.10 μW and a sensitivity of 30 μV/mW. Hastelloy reversal mixing cells were used for all experiments due to their resistance to corrosion. Each cell has two different compartments to contain different liquids; in the inner compartment of both cells the same sample is introduced, while in the annular compartment, a reactive solution (10 mol/m^3 of H_2SO_4 in GVL solvent) is placed on the measurement cell, and high-concentrated GVL solution is placed in the reference cell. Once temperature and heat flow between the cells are stable, the calorimeter is allowed to turn 180° back and forth, allowing the mixing of each separate cells to start the reaction. Experiments in C80 calorimeter were performed at isothermal conditions.

The Mettler Toledo RC1mx reactor has a split heating and cooling loop, allowing it to regulate the temperature of the reaction media quickly. An external cooling system is attached to the calorimeter. The calorimeter was coupled with an HP100-SS reactor, a Hastelloy C22 metal vessel with 1500 ML capacity and 100 bar tolerance, an overhead gassing stirrer (internal diameter: 46 mm), a temperature sensor and calibration heater are in direct contact with the reaction media.

Fig. 2 shows the different steps for experiments carried out in RC1. The reaction mixture and catalyst were incorporated into the vessel, which is then closed, and stirring was set to 250 RPM. Afterward, N_2 was used to purge the air from the head of the reactor and filled with 5 bars of N_2. The reaction mixture was then heated to the reaction temperature, and an initial calibration step was performed to estimate the Cp of the reaction mixture and the heat transfer coefficient between the reaction mixture and the heat carrier. Later, the stirrer was stopped for at least 2 min to let the catalyst settle down at the bottom of the reactor. N_2 was purged with H_2 in several washes, and the reactor pressure was set up to the desired value. Stirring was increased to 1000 RPM to commence the reaction. We selected 1000 RPM because the effect of mass transfer on kinetics was negligible at this rotating speed. When the reaction heat flow reached zero, the reactor was cooled down to 20 °C. The pressure was removed from the reactor, and a N_2 purge was performed. The pressure was set to 5 bars and the reaction mixture was heated up to the reaction temperature. After these conditions were reached, a second calibration step was performed to estimate the Cp and heat transfer coefficient.

Calorimetric measurements were repeated to be able to evaluate the standard deviation (STD) of the reaction enthalpy.

2.3. Synthesis and calorimetric study with propyl levulinate and pentyl levulinate

It is challenging to find a commercial solution for propyl and pentyl levulinates. Thus, transesterification of methyl levulinate and ethyl levulinate was performed. According to Melchiorre et al. (Melchiorre et al., 2020), high yields of PrL can be obtained from the trans-esterification of methyl levulinate by acid catalysis. Experiments were performed in a 300 ML glass batch reactor coupled with a temperature-regulated water bath, a stirrer, and a cool water condenser.

The solid acidic catalyst used in the experiments was a sulfonated resin, Amberlite IR 120 Hydrogen form, making the separation stage easier than a homogeneous catalyst. For the reaction (Fig. 3), high-concentrated methyl levulinate solution and catalyst were added to the reactor, then heated up to 80 °C. Separately, a 3:1 ratio of corresponding alcohol was heated to 80 °C and added to the reactor. The experiment lasted 5 h. Afterward, the reaction mixture and catalyst were removed and separated. To remove the remaining alcohol from the levulinates mixture, a rotavapor was used. Setting up at 70 °C and 100 mbar pressure, the alcohols were evaporated and separated. This operation was repeated until a 1:4 ratio mixture of methyl levulinate: propyl levulinate was obtained.

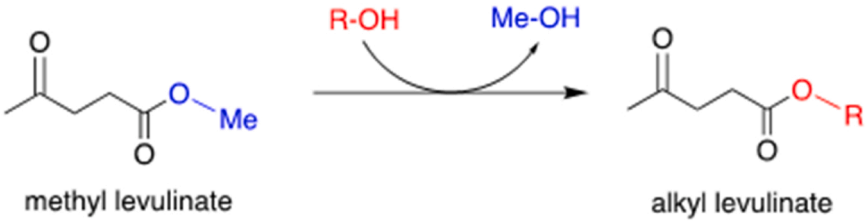

Fig. 3. Methyl levulinate (ML) transesterification into other levulinates.

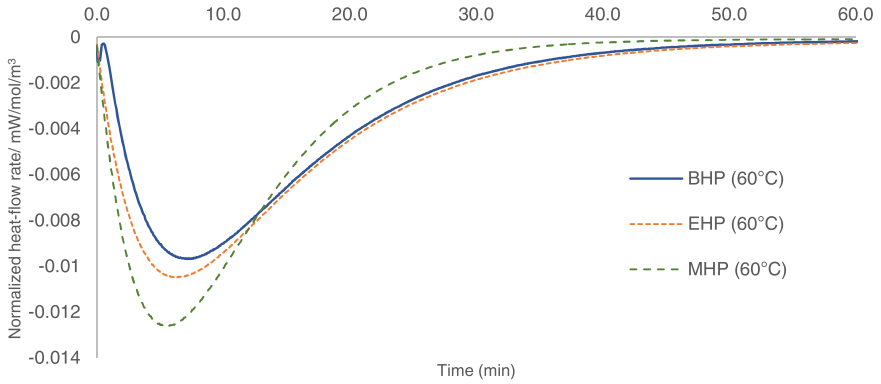

Fig. 4. Normalized heat-flow rates by the initial intermediate concentration for the cyclization of MHP, BHP and EHP and with 10 mol/m^3 of H_2SO_4 in GVL solvent at 60 °C versus time for C80 experiments.

For the obtention of pentyl levulinate (n-PeL), the same procedure was used successfully, EL was used instead of ML. Harsher conditions were used in the rotavapor to remove the alcohols remaining from the transesterification, notably 110 °C and 50 mbar. A 1:4 ratio mixture of ethyl levulinate: pentyl levulinate was also obtained.

3. Results and discussion

This section is divided into five different sections:

- -Enthalpy of cyclization for the intermediates from ML, EL and BL hydrogenation, the motivation to first discuss the cyclization enthalpy is because its calculation is more straightforward (one step), and the knowledge of its value is mandatory to calculate the hydrogenation enthalpy.
- -Influence of reaction temperatures, initial BL concentrations, solvent effect and catalyst loading on the BL hydrogenation enthalpy. The aim is to know the influence of these parameters on the reaction enthalpy.
- -Influence of levulinate substituents by studying the hydrogenation of LA, ML, EL and BL.
- -Determination of hydrogenation and cyclization enthalpies for the chemical systems: ML/PrL and EL/PeL

3.1. Calorimetric study of the cyclization reaction

After the hydrogenation of highly-concentrated solutions of ML, EL and BL, the remaining solutions were kept. These solutions were highly concentrated in intermediates methyl 4-hydroxypentanoate (MHP), ethyl 4-hydroxypentanoate (EHP) and butyl 4-hydroxypentanoate (BHP), respectively. Experiments in C80 micro-calorimeter were performed with these solutions to evaluate the second reaction enthalpy, i.e., the cyclization. This approach was not made with 4-hydroxypentanoic acid (HPA), intermediate of LA hydrogenation, because HPA is not stable for a long period. It is essential to stress that this study was done without Ru/C, which catalyzed the hydrogenation step. In this study, a small amount of sulfuric acid was added to accelerate the rate of cyclization to obtain a neat signal (Fig. 4).

By using the Tian-Calvet calorimeter Setaram C80 (Jogunola et al., 2017; Zheng et al., 2016), the reaction enthalpy of cyclization was calculated as

$$\Delta H^{m}_{R,2} = \frac{Q_{measuredbyC80}}{n_{Intermediate,0} - n_{Intermediate,final}} \quad (1)$$

where, $Q_{measured\ by\ C80}$ is the energy released or absorbed by the chemical system and measured by the micro-calorimeter C80, and the intermediate concentrations (MHP, EHP, BHP) were measured by GC.

Table 1
Operating conditions for the cyclization experiments in C80 in isothermal conditions.

Substrate	Initial substrate concentration (mol/m^3)	Final substrate concentration (mol/m^3)	Q_{C80} (J)	T (°C)	$\Delta H^{m}_{R,2}$ (kJ/mol)	STD (kJ/mol)
MHP	1945	291	-31.07	60	9.39	0.00
EHP	1142	140	-13.53	60	6.51	0.52
BHP	1407	248	-14.77	60	6.40	0.69

Table 1 shows the reaction enthalpy of cyclization for MHP, EHP and BHP and their experimental standard deviation values. Cyclization is an endothermic reaction, and the values are similar for EHP and BHP. The cyclization enthalpy for MHP is higher than EHP. The standard deviation values are low, showing the high repeatability of the experimental system. Fig. 4 shows that the cyclization of MHP is faster and absorbs more heat than the other levulinates. The normalized heat-flow rate is expressed as $\frac{\text{heat−flow rate due to chemical reaction[mW]}}{\text{Initial concentration of hydroxyalkyl levulinates[mol/m}^3\text{]}}$.

3.2. Calorimetric study of the hydrogenation of BL

The effect of reaction temperature, substrate concentration or solvents on the enthalpy of hydrogenation ($\Delta H^{m}_{R,1}$) was evaluated for the hydrogenation of BL in RC1 calorimeter. All experiments were conducted in isothermal conditions without withdrawing samples during the reaction. In this study, the catalyst Ru/C was used, except in Section 3.2.1.

The enthalpy of hydrogenation was expressed as (Wang et al., 2020):

$$\Delta H^{m}_{R,1} = \frac{Q_{RC1} + \left(n_{GVL_{final}} - n_{GVL_0}\right) * \Delta H^{m}_{R,2}}{n_{Substrate_{final}} - n_{Substrate_0}} \quad (2)$$

where, Q_{RC1} is the total energy released or absorbed during the reaction and evaluated by RC1, n_{GVL} is the number of moles of GVL in the reaction mixture and $n_{substrate}$ is the number of moles of levulinate in the reaction mixture and $\Delta H^{m}_{R,2}$ is the enthalpy of cyclization. Eq. (2) was used to estimate the enthalpy of hydrogenation. The values of $\Delta H^{m}_{R,2}$ obtained in Section 3.1 were found to be less sensitive to solvent or temperature and were used in Eq. (2). Also, the value of the second reaction enthalpy (cyclization) was found to be ca. four times lower than the first one (hydrogenation). Thus, the $\Delta H^{m}_{R,2}$ values from Section 3.1 were used in Eq. (2).

3.2.1. Hydrogenation in the absence of Ru/C in RC1

The hydrogenation in the absence of the Ru/C catalyst, named blank experiment, was studied in RC1. Fig. 5 shows the evolution of the heat-

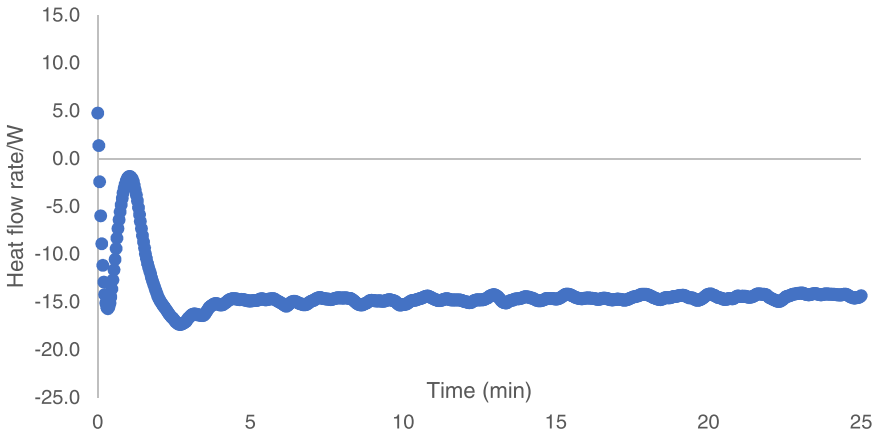

Fig. 5. Evolution of heat-flow rate for BL hydrogenation at 130 °C, 35 bars of hydrogen and with an initial BL concentration of 2032 mol/m^3 in GVL solvent.

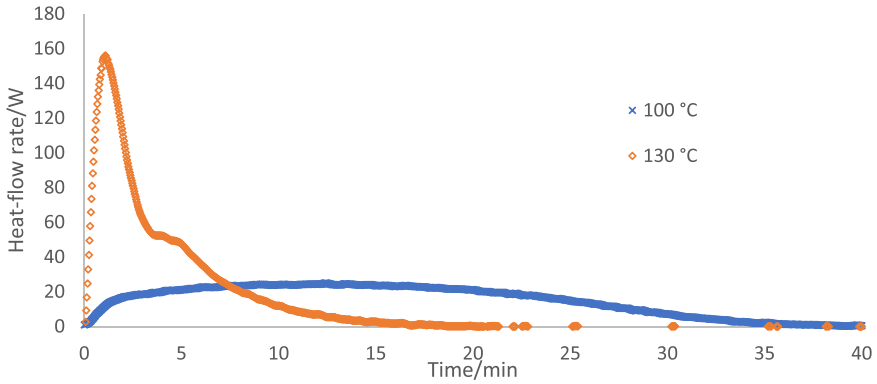

Fig. 6. Heat-flow rate evolution for the hydrogenation of BL in GVL solvent at different temperatures over Ru/C.

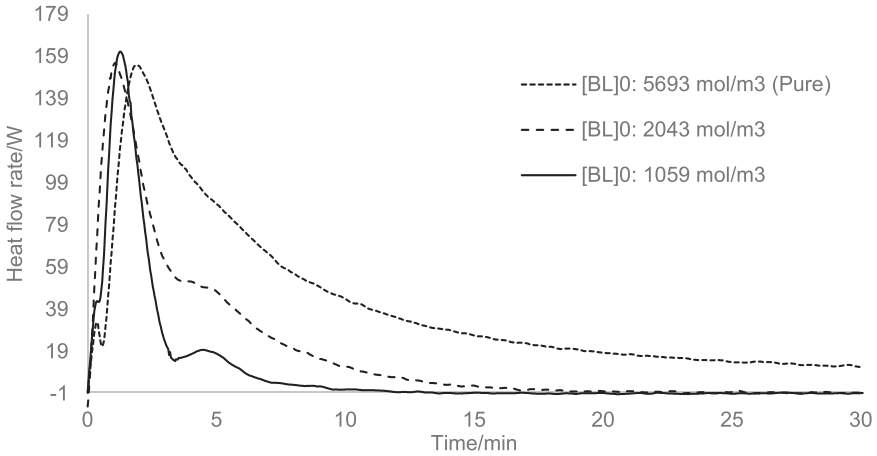

Fig. 7. BL concentration effect on heat-flow rate at isothermal and isobaric conditions: at130°C and hydrogen pressure of 35 bars over Ru/C.

flow rate in the absence of the Ru/C catalyst. One can notice that the heat-flow rate is negligible compared to the ones performed in the presence of the catalyst (Figs. 6–8). In the first stage, the heat-flow rate decreases due to the temperature difference between the vapor and liquid phases, then there is a slight exothermic phenomenon due to the heat of mixing (Fig. 5). The analysis of the liquid phase at the end of the experiment shows that there was no BL conversion. Fig. 5 shows that the heat of mixing and solubilization could be neglected.

3.2.2. *Effect of temperature*

The effect of temperature on the enthalpy of hydrogenation was evaluated for the hydrogenation of BL in GVL solvent. Table 2 summarizes the values obtained from GC analysis and RC1 calorimeter. Contrary to cyclization, hydrogenation is exothermic. Reaction enthalpy was evaluated from Eq. (2). One can notice that reaction enthalpy evaluated at 100 °C and 130 °C are similar within the range − 36.56 (−35.27 to 1.29) < $\Delta H^m_{R,1}$ < −33.98 (−35.27 +1.29) kJ/mol. Thus, the temperature does not affect the enthalpy of hydrogenation for this system in the studied temperature range. Fig. 6 shows the evolution of the heat-flow rate due to chemical reaction released during the hydrogenation of BL. Fig. 6 confirms that the kinetics are faster at the higher reaction temperature.

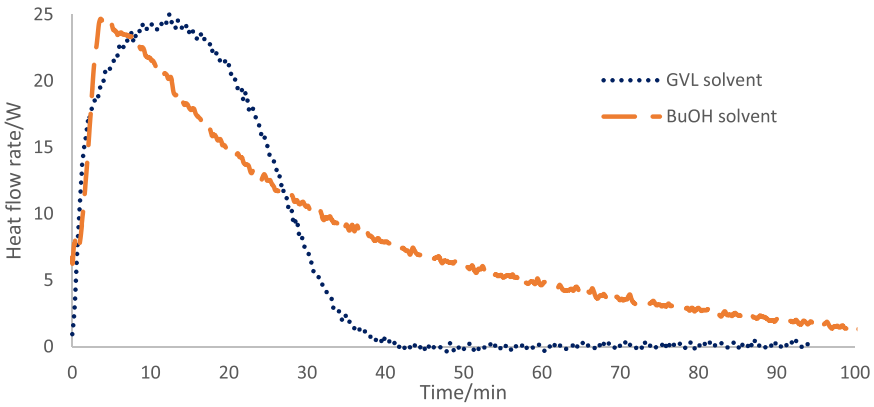

Fig. 8. Solvent effect on the heat-flow rate of BL hydrogenation at isothermal and isobaric conditions: 100 °C and 35 bar of hydrogen over Ru/C.

Table 2
GC and RC1 results for experiments in isothermal conditions at different temperatures for the hydrogenation of BL in GVL solvent at 35 bars of hydrogen.

Temperature (°C)	Total mass (kg)	Cat. mass Ru/C including 50% of water (kg)	$[BL]_0$ (mol/m^3)	$[BL]_{final}$ (mol/m^3)	$[GVL]_0$ (mol/m^3)	$[GVL]_{final}$ (mol/m^3)	$\Delta H^m_{R,1}$ (kJ/mol)	Standard deviation for $\Delta H^m_{R,1}$ (kJ/mol)
130	0.551	0.006	2050	10	6661	8607	-35.58	0.86
100	0.551	0.006	2043	13	7049	8142	-35.27	1.29

Table 3
GC and RC1 results for experiments in isothermal conditions at different initial BL concentrations for the hydrogenation of BL in GVL solvent at 35 bar of hydrogen.

Temperature (°C)	Total mass (kg)	Cat. mass Ru/C including 50% of water (kg)	$[BL]_0$ (mol/m^3)	$[BL]_{Final}$ (mol/m^3)	$[GVL]_0$ (mol/m^3)	$[GVL]_{Final}$ (mol/m^3)	$\Delta H^m_{R,1}$ (kJ/mol)	Standard deviation for $\Delta H^m_{R,1}$ (kJ/mol)
130	0.552	0.006	1059	11	8806	9297	-36.12	-
130	0.551	0.006	2050	10	6661	8607	-35.58	0.86
130	0.551	0.006	5693	10	0	2140	-34.18	-

Table 4
GC and RC1 results for experiments in isothermal and isobaric conditions for the hydrogenation of BL in GVL solvent and in butanol solvent at 100 °C and 35 bar of hydrogen.

Solvent	Temperature (°C)	Total mass (kg)	Cat. Ru/C mass including 50% of water (kg)	$[BL]_0$ (mol/m^3)	$[BL]_{final}$ (mol/m^3)	$[GVL]_0$ (mol/m^3)	$[GVL]_{final}$ (mol/m^3)	$\Delta H^m_{R,1}$ (kJ/mol)	Standard deviation for $\Delta H^m_{R,1}$ (kJ/mol)
GVL	100	0.551	0.006	2043	13	7049	8142	-35.27	1.29
BuOH	100	0.532	0.006	2180	4	13	1656	-37.96	0.40

3.2.3. *Effect of initial BL concentration*

The initial concentration of BL could affect the enthalpy of hydrogenation. Table 3 shows that the reaction enthalpy slightly decreases when BL concentration increases. Nevertheless, this slight change can be neglected and is within measurement uncertainty. Surprisingly, the initial concentration of BL does not affect the maximum heat-flow rate value (Fig. 7). However, increasing the initial BL concentration slows down the heat-flow rate decrease, which might be due to BL competitive adsorption on the catalyst surface.

Table 5
GC and RC1 results for experiments in isothermal conditions for the hydrogenation of substrates at 130 °C and 35 bar of hydrogen.

Subst.	Solvent	Total mass (kg)	Cat. mass Ru/C including 50% of water (kg)	Temperature (°C)	$[Subst.]_0$ (mol/m^3)	$[Subst.]_{final}$ (mol/m^3)	$[GVL]_0$ (mol/m^3)	$[GVL]_{final}$ (mol/m^3)	$\Delta H^m_{R,1}$ (kJ/mol)	Standard deviation for $\Delta H^m_{R,1}$ (kJ/mol)
LA	GVL	0.550	0.006	130	806	0	9296	10,504	-49.73 *	1.81
ML	GVL	0.610	0.006	130	2238	24	7964	8948	-36.84	0.83
EL	GVL	0.550	0.006	130	2164	9	7762	9128	-26.17	0.04
BL	GVL	0.551	0.006	130	2050	10	6661	8607	-35.58	0.86
ML	ML	0.550	0.006	130	7894	11	0	2387	-35.64	1.46
EL	EL	0.550	0.006	130	6589	3450	13	1337	-25.17	0.68
BL	BL	0.551	0.006	130	5693	10	0	2140	-34.18	-

*it is not the true reaction enthalpy because the second reaction was not estimated

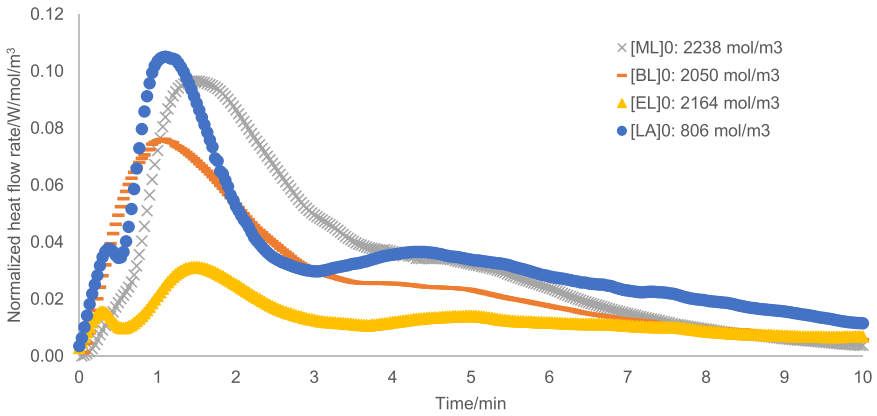

Fig. 9. Effect of substrates on the normalized heat-flow rate of hydrogenation at 130 °C and 35 bar of hydrogen over Ru/C.

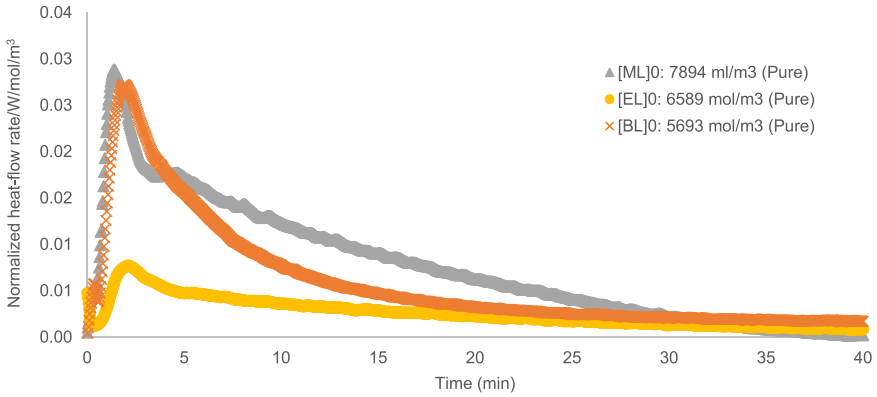

Fig. 10. Effect of substrates on the normalized heat-flow rate of hydrogenation at 130 °C and 35 bar of hydrogen over Ru/C.

3.2.4. *Effect of solvents*

The effect of the solvent was measured on the reaction enthalpy of the hydrogenation of BL. Table 4 shows that hydrogenation of BL is slightly more exothermic in butanol solvent, but this aspect can be neglected. The reaction enthalpy in butanol or GVL solvent is slightly higher compared to the hydrogenation enthalpy of BL in BL solvent (Table 4). However, Fig. 8 shows that the heat-flow rate due to chemical reaction is slower in butanol solvent. Due to the low value of the enthalpy of cyclization, the heat-flow rate is mainly governed by hydrogenation. Thus, the kinetics of hydrogenation is slower in butanol solvent, which was confirmed by a previous study (Capecci et al., 2021a).

3.3. *Effect of substrates on the hydrogenation enthalpy*

In Section 3.2, we have demonstrated that the dependence of the enthalpy of BL hydrogenation is negligible toward reaction temperature, substrate concentration, and solvent conditions. This dependency study was vital to compare the hydrogenation enthalpy of ML, BL, EL or LA. Even if the initial substrate concentrations are similar, the reaction environment can be different due to the different molar masses.

Table 5 shows that the hydrogenation enthalpies of ML, EL and BL in GVL and alkyl levulinate solvents are similar. One can notice that the hydrogenation enthalpy for ML and BL are similar, i.e., within the range − 37 to − 34 kJ/mol. The hydrogenation of EL is less exothermic, i.e., − 26.17 kJ/mol. By neglecting the enthalpy of HPA cyclization, thus the enthalpy of LA hydrogenation was found to be the highest, − 49.73 kJ/mol. Table 5 shows no linear correlation between the alkyl chain length and the reaction enthalpy values.

Figs. 9 and 10 show that the heat-flow release normalized by the initial concentration of substrate during the hydrogenation is more significant for ML substrate than EL or BL. Due to corrosion issues, the hydrogenation of LA was performed at a lower concentration. One can observe that the normalized heat-flow rate with LA is the highest. The normalized heat-flow rate for EL hydrogenation is lower than for BL. According to Wang et al. (Wang et al., 2019), the kinetics of EL hydrogenation is faster than that of BL. However, the hydrogenation of EL is less exothermic than for BL, explaining the lowest normalized heat-flow rate for EL.

The same trend was observed for the hydrogenation of a high-concentrated (pure) solution of alkyl levulinate (Fig. 10). The normalized heat-flow rate released evolves in the following order: ML>BL>EL.

Table 6
GC and RC1 results for experiments in isothermal conditions for the hydrogenation of EL-BL mixture in GVL solvent at 130 °C and 35 bar of hydrogen.

Total mass (kg)	Cat. mass of Ru/C* (kg)	[BL] Initial (mol/L)	[BL] Final (mol/l)	[EL] Initial (mol/L)	[EL] Final (mol/L)	[GVL] Initial (mol/L)	[GVL] Final (mol/L)	Heat released (kJ)	
								Measured	Estimated from Eq. (3)
0.551	0.006	1768	474	1999	491	3381	4669	-46.48	-44.39
0.550	0.006	1817	51	2172	54	3620	5109	-63.16	-62.30

* Including 50% of water

Table 7
Operating conditions for the cyclization experiment in C80 in isothermal conditions at 60 °C and 10 mol/m^3 of H_2SO_4 in GVL solvent.

Subst.	$[MHP]_0$ (mol/m^3)	$[MHP]_{final}$ (mol/m^3)	$[PrHP]_0$ (mol/m^3)	$[PrHP]_{final}$ (mol/m^3)	Q_C80 (J)	$\Delta H^m_{R,2from\ PrHP}$ (kJ/mol)	Standard deviation for $\Delta H^m_{R,2from\ PrHP}$ (kJ/mol)
MHP & PrHP	23	63	107	31	-6.645	15.96	2.91

Table 8
GC and RC1 results for experiments at isothermal conditions for the hydrogenation of substrates at 130 °C, 35 bar of hydrogen, reaction mass of 0.550 kg and catalyst mass of 0.006 kg (containing 50 wt% of water).

Temperature (°C)	$[ML]_0$ (mol/m^3)	$[ML]_{final}$ (mol/m^3)	$[PrL]_0$ (mol/m^3)	$[PrL]_{final}$ (mol/m^3)	$[GVL]_0$ (mol/ m^3)	$[GVL]_{final}$ (mol/m^3)	$[PrOH]_0$ (mol/m^3)	$[PrOH]_{final}$ (mol/m^3)	$\Delta H^m_{R,1from\ PrL}$ (kJ/mol)	Standard deviation for $\Delta H^m_{R,1from\ PrL}$ (kJ/mol)
130	604	160	1766	611	5875	6686	338	672	-36.60	6.80

3.4. Calorimetric study of mixed levulinate solution hydrogenation

3.4.1. Hydrogenation of BL/EL

In this section, we wanted to verify if the total energy released during the hydrogenation of two levulinates can be expressed by Eq. (3).

$$Q_{RC1} = \left(n_{BL_{final}} - n_{BL_0}\right) * \Delta H_{R,1(BL)} + \left(n_{BuOH_{final}} - n_{BuOH_0}\right) * \Delta H_{R,2(BL)} + \left(n_{EL_{final}} - n_{EL_0}\right) * \Delta H_{R,1(EL)} + \left(n_{EtOH_{final}} - n_{EtOH_0}\right) * \Delta H_{R,2(EL)} \quad (3)$$

Table 6 confirmed the linear addition of total reaction enthalpy, i.e., Eq. (3). The heat released measured is similar to the one estimated from Eq. (3). Thus, this approach can be applied to estimate the reaction enthalpies for PrL and PeL.

3.4.2. Hydrogenation of the mixture ML/PrL

Hydrogenation of a PrL and ML reaction mixture obtained from ML transesterification, was carried out in RC1 calorimeter. Thus the total energy due to the chemical reaction can be expressed as

$$Q_{RC1} = \left(n_{ML_{final}} - n_{ML_0}\right) * \Delta H^m_{R,1fromML} + \left(n_{PrL_{final}} - n_{PrL_0}\right) * \Delta H^m_{R,1fromPrL} - \left(n_{PrOH_{final}} - n_{PrOH_0}\right) * \Delta H^m_{R,2fromPrHP} - \left(n_{MeOH_{final}} - n_{MeOH_0}\right) * \Delta H^m_{R,2fromMHP} \quad (4)$$

Due to the low boiling point of methanol, it is challenging to track its concentration. Hence, the difference $\left(n_{MeOH_{final}} - n_{MeOH_0}\right)$ can be expressed as:

$$\left(n_{MeOH_{final}} - n_{MeOH_0}\right) = \left(n_{GVL_{final}} - n_{GVL_0}\right) - \left(n_{PrOH_{final}} - n_{PrOH_0}\right) \quad (5)$$

At the end of the RC1 experiment, the reaction mixture was concentrated in PrHP and MPH. This reaction mixture was used in C80 micro-calorimeter to access the reaction enthalpy of PrHP cyclization. The total energy due to cyclization in C80 can be expressed as

$$Q_{C80} = \left(n_{PrHP_{final}} - n_{PrHP_0}\right) * \Delta H^m_{R,2fromPrHP} + \left(n_{MHP_{final}} - n_{MHP_0}\right) * \Delta H^m_{R,2fromMHP} \quad (6)$$

In Eqs. (3) and (5), reaction enthalpies calculated previously ($\Delta H^m_{R,2from\ MHP}$ and $\Delta H^m_{R,1from\ ML}$) were used to determine the enthalpies for the hydrogenation of PrL. Tables 7 and 8 show the reaction enthalpy values calculated from the experimental data obtained with RC1 and C80 for the ML and PrL reaction mixture hydrogenation. The reaction enthalpy of PrL hydrogenation is of the same order of magnitude as for ML and BL. However, the cyclization enthalpy for PrHP is more endothermic than the others.

3.4.3. Hydrogenation of the mixture EL/PeL

A reaction mixture constituted of EL and PeL, obtained from the transesterification of EL by pentanol, was used to estimate the hydrogenation and cyclization enthalpies of pentyl levulinate (PeL).

The method for the estimation of the hydrogenation and cyclization enthalpies were the same as the method described previously. As seen in Tables 9 and 10, the hydrogenation enthalpy for PeL follows the trend as the other levulinates, but the cyclization enthalpy is similar to that of PrHP.

4. Conclusions

The knowledge of reaction enthalpy is vital in chemical processes to assess thermal risks and perform pinch analysis on process flow diagrams. In the case of biomass valorization, such information is still often missing from databases. To fill this gap, the current study utilized two types of calorimeters to evaluate reaction enthalpies for the production of GVL from the hydrogenation of alkyl levulinates or levulinic acid over Ru/C. Setaram C80 micro-calorimeter was used to evaluate the enthalpy of cyclization and RC1 Mettler Toledo to evaluate the enthalpy of hydrogenation.

It is commonly assumed that reaction temperature, reactant concentrations or solvent do not significantly affect the reaction enthalpy value. To verify this statement, hydrogenation of butyl levulinate was performed at different temperatures, initial BL concentrations and in different solvents: BL, butanol or GVL. From these experiments, it was confirmed that the enthalpy of hydrogenation was independent from these operating conditions.

A calorimetric study of propyl levulinate hydrogenation over Ru/C was also performed to evaluate the influence of chain length on the reaction enthalpy. In the first stage, propyl levulinate was prepared from the transesterification of methyl levulinate leading to a reaction mixture of methyl and propyl levulinates.

This study shows that the enthalpy of hydrogenation of LA, ML, EL, PrL, BL and PeL were exothermic and were equal to − 49.73 kJ/mol, − 36.84 kJ/mol, − 26.17 kJ/mol, − 36.60 kJ/mol, − 35.58 kJ/mol and − 38.61 kJ/mol, respectively. The enthalpy of cyclization was found to be endothermic, and were equal to 9.39 kJ/mol, 6.51 kJ/mol,

Table 9
Operating conditions for the cyclization experiment in C80 in isothermal conditions at 60 °C and 10 mol/m^3 of H_2SO_4 in GVL solvent.

Substituent.	$[EtOH]_0$ (mol/m^3)	$[EtOH]f_{inal}$ (mol/ m^3)	$[PeOH]_0$ (mol/ m^3)	$[PeOH]f_{inal}$ (mol/ m^3)	Q_C80 (J)	$\Delta H_{R,2}$Cyclization Enthalpy for PeHP (kJ/mol)	STD $\Delta H_{R,2}$Cyclization Enthalpy for PeHP (kJ/mol)
EHP & PeHP	254	376	661	887	-7.587	13.33	-

Table 10
GC and RC1 results for experiments at isothermal conditions for the hydrogenation of substrates at 130 °C, 35 bar of hydrogen, reaction mass of 0.550 kg and 0.0063 kg of Ru/C (containing 50 wt% of water).

$[EL]_{Initial}$ (mol/ m^3)	$[EL]_{final}$ (mol/ m^3)	$[PeL]_{Initial}$ (mol/ m^3)	$[PeL]_{final}$ (mol/ m^3)	$[GVL]_{Initial}$ (mol/ m^3)	$[GVL]_{final}$ (mol/ m^3)	$[PeOH]_{Initial}$ (mol/ m^3)	$[PeOH]_{final}$ (mol/ m^3)	$\Delta H_{R.1}$ Hydrogenation of PeL (kJ/mol)	STD $\Delta H_{R.1}$ Hydrogenation of PeL (kJ/mol)
909	259	224	665	4046	5122	31	911	-38.612	1.05

15.96 kJ/mol, 6.40 kJ/mol and 13.33 kJ/mol for MHP, EHP, PrHP, BHP and PeHP respectively. One can conclude that there is no linear correlation between reaction enthalpy and alkyl chain length for both reaction steps, hydrogenation and cyclization.

A further investigation of this study could be to evaluate the reaction enthalpies with different solid catalysts, noble and non-noble metals.

Declaration of Competing Interest

The authors declare that they have no known competing financial interests or personal relationships that could have appeared to influence the work reported in this paper.

Acknowledgements

The authors thank the Ministry of High Education, Science and Technology of Dominican Republic (MESCYT). For the analytical part, the authors thank University of Rouen Normandy, INSA Rouen Normandy, the Centre National de la Recherche Scientifique (CNRS), European Regional Development Fund (ERDF) N° HN0001343, Labex SynOrg (ANR-11-LABX-0029), Carnot Institute I2C, the Graduate School for Research XL-Chem (ANR-18-EURE-0020 XL CHEM) and Region Normandie for their support. GC/FID was financed by FEDER RIN Green Chem 2019NU01FOBC08 N° 17P04374. This research was funded, in whole or in part, by the ANR (French National Research Agency) and the DFG (German Research Foundation) through the project MUST (MicroflUidics for Structure-reactivity relationships aided by Thermodynamics & kinetics) [ANR-20-CE92-0002-01 - Project number 446436621].

References

Ariba, H., Wang, Y., Devouge-Boyer, C., Stateva, R.P., Leveneur, S., 2020. Physicochemical properties for the reaction systems: levulinic acid, its esters, and γ-valerolactone. J. Chem. Eng. Data 65, 3008–3020. https://doi.org/10.1021/acs.jced.9b00965.

Capecci, S., Wang, Y., Casson Moreno, V., Held, C., Leveneur, S., 2021a. Solvent effect on the kinetics of the hydrogenation of n-butyl levulinate to γ-valerolactone. Chem. Eng. Sci. 231, 116315 https://doi.org/10.1016/j.ces.2020.116315.

Capecci, S., Wang, Y., Delgado, J., Casson Moreno, V., Mignot, M., Grénman, H., Murzin, D.Y., Leveneur, S., 2021b. Bayesian statistics to elucidate the kinetics of γ-valerolactone from n-butyl levulinate hydrogenation over Ru/C. Ind. Eng. Chem. Res. 60, 11725–11736. https://doi.org/10.1021/acs.iecr.1c02107.

Casson Moreno, V., Garbetti, A.L., Leveneur, S., Antonioni, G., 2019. A consequences-based approach for the selection of relevant accident scenarios in emerging technologies. Saf. Sci. 112, 142–151. https://doi.org/10.1016/j.ssci.2018.10.024.

Chew, A.K., Walker, T.W., Shen, Z., Demir, B., Witteman, L., Euclide, J., Huber, G.W., Dumesic, J.A., Van Lehn, R.C., 2020. Effect of mixed-solvent environments on the selectivity of acid-catalyzed dehydration reactions. ACS Catal. 10, 1679–1691. https://doi.org/10.1021/acscatal.9b03460.

Dakkoune, A., Vernières-Hassimi, L., Leveneur, S., Lefebvre, D., Estel, L., 2019. Analysis of thermal runaway events in French chemical industry. J. Loss Prev. Process Ind. https://doi.org/10.1016/j.jlp.2019.103938.

Delgado, J., Vasquez Salcedo, W.N., Bronzetti, G., Casson Moreno, V., Mignot, M., Legros, J., Held, C., Grénman, H., Leveneur, S., 2022. Kinetic model assessment for the synthesis of γ-valerolactone from n-butyl levulinate and levulinic acid hydrogenation over the synergy effect of dual catalysts Ru/C and Amberlite IR-120. Chem. Eng. J. 430, 133053 https://doi.org/10.1016/J.CEJ.2021.133053.

Di Menno Di Bucchianico, D., Buvat, J.C., Mignot, M., Casson Moreno, V., Leveneur, S., 2022. Role of solvent the production of butyl levulinate from fructose. Fuel 318, 123703. https://doi.org/10.1016/j.fuel.2022.123703.

Dutta, S., Yu, I.K.M., Tsang, D.C.W., Ng, Y.H., Ok, Y.S., Sherwood, J., Clark, J.H., 2019. Green synthesis of gamma-valerolactone (GVL) through hydrogenation of biomass-derived levulinic acid using non-noble metal catalysts: a critical review. Chem. Eng. J. 372, 992–1006. https://doi.org/10.1016/j.cej.2019.04.199.

Horváth, I.T., Mehdi, H., Fábos, V., Boda, L., Mika, L.T., 2008. γ-Valerolactone—a sustainable liquid for energy and carbon-based chemicals. Green Chem. 10, 238–242. https://doi.org/10.1039/B712863K.

Jogunola, O., Salmi, T., Leveneur, S., Mikkola, J.P., 2017. Complexation equilibria studies of alkyl formate hydrolysis in the presence of 1-butylimidazole. Thermochim. Acta 652, 62–68. https://doi.org/10.1016/j.tca.2017.03.012.

Kuwahara, Y., Kaburagi, W., Osada, Y., Fujitani, T., Yamashita, H., 2017a. Catalytic transfer hydrogenation of biomass-derived levulinic acid and its esters to γ-valerolactone over ZrO2 catalyst supported on SBA-15 silica. Catal. Today 281, 418–428. https://doi.org/10.1016/J.CATTOD.2016.05.016.

Kuwahara, Y., Kango, H., Yamashita, H., 2017b. Catalytic transfer hydrogenation of biomass-derived levulinic acid and its esters to γ-valerolactone over sulfonic acid-functionalized UiO-66. ACS Sustain. Chem. Eng. 5, 1141–1152. https://doi.org/10.1021/acssuschemeng.6b02464.

Liguori, F., Moreno-Marrodan, C., Barbaro, P., 2015. Environmentally friendly synthesis of γ-valerolactone by direct catalytic conversion of renewable sources. ACS Catal. 5, 1882–1894. https://doi.org/10.1021/cs501922e.

Lin, H., Chen, J., Zhao, Y., Wang, S., 2017. Conversion of C5 carbohydrates into furfural catalyzed by SO3H-functionalized ionic liquid in renewable γ-valerolactone. Energy Fuels 31, 3929–3934. https://doi.org/10.1021/acs.energyfuels.6b01975.

Liu, C., Wei, M., Wang, J., Xu, J., Jiang, J., Wang, K., 2020. Facile directional conversion of cellulose and bamboo meal wastes over low-cost sulfate and polar aprotic solvent. ACS Sustain. Chem. Eng. 8, 5776–5786. https://doi.org/10.1021/acssuschemeng.0c01280.

Liu, M., Li, S., Fan, G., Yang, L., Li, F., 2019. Hierarchical flower-like bimetallic NiCu catalysts for catalytic transfer hydrogenation of ethyl levulinate into γ-valerolactone. Ind. Eng. Chem. Res. 58, 10317–10327. https://doi.org/10.1021/ACS.IECR.9B01774/SUPPL_FILE/IE9B01774_SI_001.PDF.

Mamun, O., Walker, E., Faheem, M., Bond, J.Q., Heyden, A., 2017. Theoretical investigation of the hydrodeoxygenation of levulinic acid to γ-valerolactone over Ru (0001. ACS Catal. 7, 215–228. https://doi.org/10.1021/acscatal.6b02548.

Melchiorre, M., Amendola, R., Benessere, V., Cucciolito, M.E., Ruffo, F., Esposito, R., 2020. Solvent-free transesterification of methyl levulinate and esterification of levulinic acid catalyzed by a homogeneous iron(III) dimer complex. Mol. Catal. 483, 110777 https://doi.org/10.1016/j.mcat.2020.110777.

Piskun, A., van de Bovenkamp, H.H., Rasrendra, C.B., Winkelman, J.G.M., Heeres, H.J., 2016. Kinetic modeling of levulinic acid hydrogenation to γ-valerolactone in water using a carbon supported Ru catalyst. Appl. Catal. A Gen. 525, 158–167. https://doi.org/10.1016/j.apcata.2016.06.033.

Piskun, A.S., van de Bovenkamp, H.H., Rasrendra, C.B., Winkelman, J.G.M., Heeres, H.J., 2016. Kinetic modeling of levulinic acid hydrogenation to γ-valerolactone in water using a carbon supported Ru catalyst. Appl. Catal. A Gen. 525, 158–167. https://doi.org/10.1016/j.apcata.2016.06.033.

Pokorný, V., Štejfa, V., Fulem, M., Červinka, C., Růžička, K., 2017. Vapor pressures and thermophysical properties of ethylene carbonate, propylene carbonate, γ-valerolactone, and γ-butyrolactone. J. Chem. Eng. Data 62, 4174–4186. https://doi.org/10.1021/acs.jced.7b00578.

Stoessel, F., 2008. Thermal Safety of Chemical Processes: Risk Assessment and Process Design, Thermal Safety of Chemical Processes: Risk Assessment and Process Design. Wiley-VCH. https://doi.org/10.1002/9783527621606.

Tang, X., Chen, H., Hu, L., Hao, W., Sun, Y., Zeng, X., Lin, L., Liu, S., 2014. Conversion of biomass to γ-valerolactone by catalytic transfer hydrogenation of ethyl levulinate over metal hydroxides. Appl. Catal. B Environ. 147, 827–834. https://doi.org/10.1016/j.apcatb.2013.10.021.

Wang, Y., Vernières-Hassimi, L., Casson-Moreno, V., Hébert, J.-P., Leveneur, S., 2018. Thermal risk assessment of levulinic acid hydrogenation to γ-valerolactone. Org. Process Res. Dev. 22, 1092–1100. https://doi.org/10.1021/acs.oprd.8b00122.

Wang, Y., Cipolletta, M., Vernières-Hassimi, L., Casson-Moreno, V., Leveneur, S., 2019. Application of the concept of Linear Free Energy Relationships to the hydrogenation of levulinic acid and its corresponding esters. Chem. Eng. J. 374, 822–831. https://doi.org/10.1016/J.CEJ.2019.05.218.

Wang, Y., Plazl, I., Vernières-Hassimi, L., Leveneur, S., 2020. From calorimetry to thermal risk assessment: γ-Valerolactone production from the hydrogenation of alkyl levulinates. Process Saf. Environ. Prot. https://doi.org/10.1016/j.psep.2020.07.017.

Yan, K., Lafleur, T., Wu, G., Liao, J., Ceng, C., Xie, X., 2013. Highly selective production of value-added γ-valerolactone from biomass-derived levulinic acid using the robust Pd nanoparticles. Appl. Catal. A Gen. 468, 52–58. https://doi.org/10.1016/j.apcata.2013.08.037.

Yan, Z.P., Lin, L., Liu, S., 2009. Synthesis of γ-valerolactone by hydrogenation of biomass- derivedLevulinic acid over Ru/C catalyst. Energy Fuels 23, 3853–3858. https://doi.org/10.1021/ef900259h.

Yang, Y., Gao, G., Zhang, X., Li, F., 2014. Facile fabrication of composition-tuned Ru-Ni bimetallics in ordered mesoporous carbon for levulinic acid hydrogenation. ACS Catal. 4, 1419–1425. https://doi.org/10.1021/cs401030u.

Zheng, J.L., Wärnå, J., Salmi, T., Burel, F., Taouk, B., Leveneur, S., 2016. Kinetic modeling strategy for an exothermic multiphase reactor system: application to vegetable oils epoxidation using Prileschajew method. AIChE J. 62, 726–741. https://doi.org/10.1002/aic.15037.

B.3 Article: Assessment of kinetic models for the production of γ-valerolactone developed in isothermal, adiabatic and isoperibolic conditions

Fuel 350 (2023) 128792

Contents lists available at ScienceDirect

Fuel

journal homepage: www.elsevier.com/locate/fuel

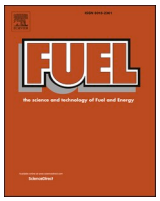

Full Length Article

Assessment of kinetic models for the production of γ-valerolactone developed in isothermal, adiabatic and isoperibolic conditions

Wenel Naudy Vásquez Salcedo [a,b], Mélanie Mignot [c], Bruno Renou [b], Sébastien Leveneur [a,*]

[a] INSA Rouen Normandie, UNIROUEN, Normandie Univ, LSPC, UR4704, F-76000 Rouen, France, France
[b] Normandie Univ., INSA Rouen, UNIROUEN, CNRS, CORIA, Rouen 76000, France
[c] Normandie Université, INSA Rouen, UNIROUEN, CNRS, COBRA Laboratory, F-76000 Rouen, France

ARTICLE INFO

Keywords:
Kinetic modeling
Gamma valerolactone
Levulinate
Calorimetry
Adiabatic

ABSTRACT

The use of lignocellulosic biomass as raw materials for the production of biofuels is increasing. There are several potential processes valorizing these raw materials, but the shift from lab-scale to industrial scale requires the development of reliable and robust kinetic models. Usually, these models are developed in isothermal mode, limiting their use for thermal risk assessment or pinch analysis. We developed and assessed several kinetic models for the hydrogenation of butyl levulinate to γ-valerolactone over Ru/C in different thermal modes, i.e., isothermal, isoperibolic and adiabatic modes. The reaction calorimeter Mettler-Toledo RC1 was used to perform kinetic experiments. Bayesian inference was used during the regression stage to calculate the credible intervals. The validation stage was done by a holdout method. From the regression and validation stage, we found that the non-competitive Langmuir Hinshelwood with hydrogen non-dissociation and dissociation were the most reliable models. These models can predict the kinetics of this reaction system in different thermal modes.

1. Introduction

Our dependency on fossil raw materials is very high in the modern society. Over 80% of the world's primary energy consumption in the energy sector was from fossil raw materials in 2020 [1].

The use of lignocellulosic biomass (LCB) for biofuel production is seen as a better alternative to fossil fuel because of its global availability, lower environmental impact, and cost [2–6]. Besides, such raw materials are not in competition with the alimentary sector, avoiding the dilemma of food versus fuel [7,8]. The sugar parts of LCB, i.e., cellulose and hemicellulose, are mainly used to produce chemicals, materials or fuels. The valorization of these polymers of sugar can lead to several platform molecules and their derivatives, such as succinic acid, furfural, 5-HMF, levulinic acid, glycerol, etc. [9–12].

The chemical γ-valerolactone (GVL), produced from the hydrogenation of levulinic acid or ester levulinate, is also considered as a platform molecule [13,14]. Hydrogenation of bio-based carboxylic acids, esters or related compounds is considered a step toward a sustainable and carbon–neutral process [15]. In fine chemistry, GVL is considered an excellent aprotic solvent [16–21] because of its low vapor pressure, high flash point, and potential to increase acid activity [22–26]. In polymer science, GVL is a promising starting material for producing greener monomers [27–30].

In the energy field, GVL cannot be used directly as a fuel [31], but it can be used as an additive fuel [32–35]. GVL is a promising feedstock for producing hydrocarbon fuels [31,36–42] or pentanoic biofuels [43].

From a safety, cost and environmental standpoint, determining the best operating conditions for the production of GVL is vital [44–46]. The literature proposes several routes for producing GVL by hydrogenating raw lignocellulosic biomass, cellulose, glucose or fructose [47]. These different routes require the hydrogenation of levulinic acid or alkyl levulinates, and there are three different hydrogenation options:

-use of molecular hydrogen [34,48–65].

-*in situ* FA decomposition producing hydrogen [66–74].

-Meerwein-Ponndorf-Verley reaction involving the use of alcohol for hydrogen transfer [75–82].

The use of molecular hydrogen and ruthenium-based catalyst is the most efficient system to produce GVL. Developing such a process at an industrial scale requires reliable and robust kinetic models. Such models are essential to optimize the operating cost to get the highest GVL yield. There are several models for the hydrogenation of levulinates or levulinic acid [52,53,57,64,83–87]. These models were developed using experiments performed in isothermal mode, and could limit their application to pinch analysis or process safety.

Generally speaking, the development of kinetic models in different

* Corresponding author.
E-mail address: sebastien.leveneur@insa-rouen.fr (S. Leveneur).

https://doi.org/10.1016/j.fuel.2023.128792
Received 8 March 2023; Received in revised form 9 May 2023; Accepted 23 May 2023

Nomenclature

Cp	Specific heat capacity [J.kg^{-1}.K^{-1}]
Ea	Activation energy [J.mol^{-1}]
$f_{iu}(\xi)$	Estimated concentration or temperature
He	Henry's coefficient [mol.m^{-3}.bar^{-1}]
k	Rate constant
K*i*	Adsorption rate of specie *i* [m^3.mol^{-1}]
$k_L.a$	Volumetric mass transfer coefficient [s^{-1}]
$(k_L.a)_{modified}$	Modified volumetric mass transfer coefficient [(Pa·s·K^{-1})$^{0.5}$(Pa·s·kg^{-1}·m^{-3})$^{0.25}$·s^{-1}]
m	Mass [kg]
P	Pressure [bar]
R_i	Reaction rate *i* [mol.m^{-3}.s^{-1}]
R	Gas constant [J.mol^{-1}.K^{-1}]
T	Temperature [K]
UA	Global heat transfer coefficient [W.K^{-1}]
$\lvert v(\xi) \rvert$	Determinant of the covariance matrix of responses
Y_i	Experimental concentration of specie i or temperature

Greek letters

$\omega_{Cat.}$	Catalyst loading [kg.m^{-3}]
μ_{liq}	Liquid viscosity [Pa·s]
ρ_{liq}	Mass density [kg·m^{-3}]

Subscripts and superscripts

Liq	Liquid phase
Ref	Reference
o	Initial
*	Interfacial value

Abbreviations

AIC	Akaike information criterion
BL	Butyl levulinate
BHP	Butyl 4-hydroxypentanoate
BuOH	Butanol
ER	Eley-Rideal kinetic model with no adsorption of hydrogen
GC	Gas chromatography
GVL	γ-valerolactone
HPD	Highest Posterior Density
LH1	Langmuir-Hinshelwood kinetic model with molecular adsorption of hydrogen
LH2	Langmuir-Hinshelwood kinetic model with hydrogen dissociation
NCLH1	Non-competitive Langmuir-Hinshelwood kinetic model with no dissociation of hydrogen
NCLH2	Non-competitive Langmuir-Hinshelwood kinetic model with hydrogen dissociation
ODEs	Ordinary differential equation system
OF (ξ)	Objective function
RKMC	Redlich-Kwong-Mathias-Copeman equation of state
Ru/C	Ruthenium on activated carbon

thermal modes, e.g., isothermal, adiabatic, isoperibolic, or dynamic modes, is quite seldom in the literature.

In adiabatic mode, one can only use the reaction temperature as an observable [88–90] allowing to obtain reliable models for thermal risk assessment [91]. It is impossible to withdraw samples during the reaction; otherwise, the reaction temperature signal is perturbed. Hence, kinetic models only developed in adiabatic mode are limited for thermal risk assessment.

In isoperibolic mode, for some chemical systems, it is possible to track the reaction temperature and withdraw some samples to track the concentration in the liquid phase [92–94], allowing the development of reliable kinetic models considering concentration and temperature as observables.

There is a need to have kinetic models developed in different thermal modes to improve their reliability and robustness and to be used universally for process safety, process intensification, and cost evaluation. To do that, one must carry out different experiments in isothermal conditions to track the species concentration and in non-isothermal conditions (isoperibolic and adiabatic modes) to track the reaction temperature.

To the best of the authors' knowledge, such an approach is highly seldom in the literature [94]. In this study, we developed kinetic models for the hydrogenation of butyl levulinate into GVL over Ru/C in three thermal modes: isothermal, isoperibolic and adiabatic. A high concentrated solution of BL was used to perform experiments. The state-of-the-art reaction calorimeter Mettler-Toledo RC1 was used to perform experiments in different thermal modes. The developed models were validated to assess their reliability and select the most reliable ones. Butyl levulinate was chosen because it is gaining a lot of interest as a platform molecule and can be used in different areas [16,95].

2. Experimental section

2.1. Chemicals

Chemicals used during this research for analytical and experimental purposes were purchased from different providers and used without further purification: n-Butyl levulinate (n-BL), acquired from Alfa Aesar with a purity ≥98%, CAS: 2052-15-5. Hydrogen gas (H_2), acquired from Linde group with a purity ≥99.99%, CAS: 1333-74-0. γ-Valerolactone (GVL), acquired from Sigma Aldrich with a purity ≥99%, CAS: 108-29-2. 1-Butanol (BuOH), acquired from LabLine with a purity ≥99%, CAS: 71-36-3. Ruthenium on activated carbon (Ru/C), acquired from Alfa Aesar, 5% of ruthenium powder, reduced, 50% nominally wet, CAS: 7440-18-8. Acetone, acquired from Fischer Scientific with a purity ≥99%, CAS: 67-64-1.

2.2. Analytical system

Gas chromatography coupled with a flame ionization detector (GC-FID) technique was applied to quantify the amount of chemicals in samples. GC-FID equipment is from Scion Instruments supplier. GC-FID was equipped with a low polarity column (Phenomenex, ZB-5) composed of 95% dimethyl siloxane and 5% of phenyl groups. Column dimensions: length: 30 m, internal diameter: 0.32 mm, coating width: 0.25 μm.

Helium (99.99%) was used as carrier gas at a constant flow rate of 1.2 mL/min. The temperature of the injector and the detector were set at 250 °C. The oven temperature ramp was set to 50 °C (1 min) – 20 °C/min – 200 °C (1 min). Samples were diluted in acetone to be analyzed, the injection volume was 1 μL and the split ratio was 20:1.

2.3. RC1 reactor

To develop a robust kinetic model for GVL production from n-BL, different experiments were performed in the Mettler-Toledo RC1mx

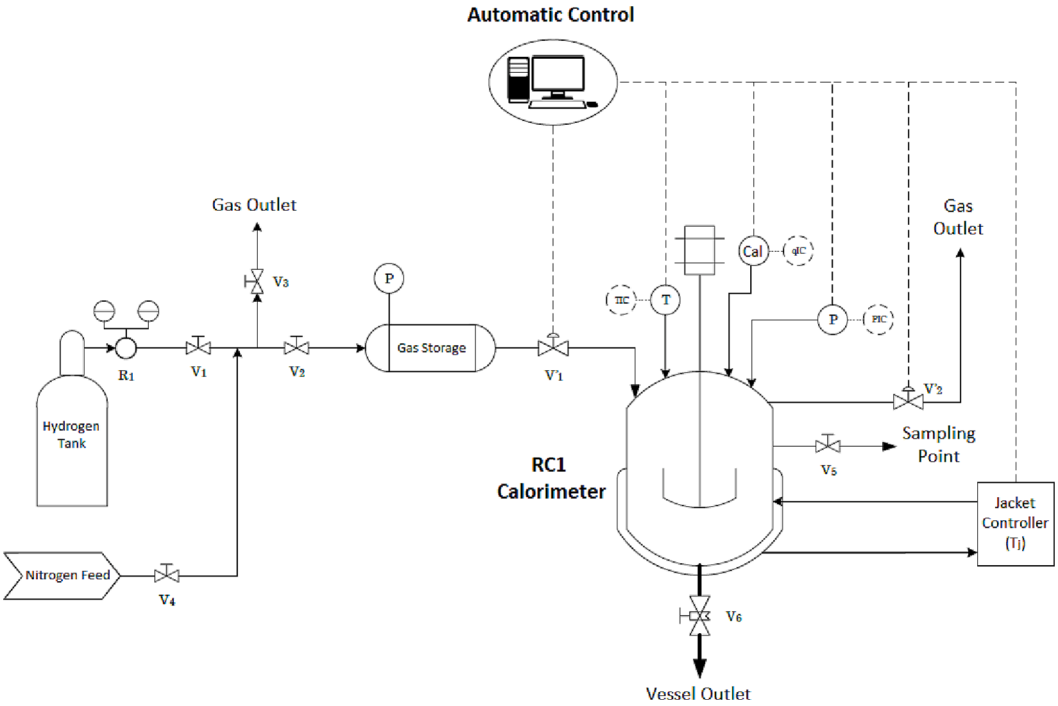

Fig. 1. RC1mx Calorimeter installation.

Table 1
Experimental matrix for gas–liquid mass transfer measurement.

Run	m_0BL (kg)	Tr_0 (K)	P (bar)
1_MT	0.520	373.15	25
2_MT	0.520	373.15	25
3_MT	0.520	413.15	25
4_MT	0.520	433.15	25

calorimeter, considering isothermal and non-isothermal conditions.

The RC1mx is a high-performance calorimeter with a heating and cooling loop system, allowing us to have a very accurate temperature control of the reaction media. The RC1mx vessel is made of Hastelloy C22 metal one, with a 1.8 L capacity and 100 bar of tolerance. A gas inlet and outlet system are connected to the vessel to control the pressure. A PID automatically controls this system. The RC1mx is also equipped with a calibration heater that evaluates the heat capacity (Cp) and the reaction media's global heat transfer coefficient (UA). Fig. 1 represents the RC1mx installation.

2.4. Determination of the global heat transfer

The global heat transfer UA plays a fundamental role in the energy balance to characterize the transfer between the heat carrier and reaction temperature. Thus, it is vital to measure it correctly. This value was determined by electrical calibration [92,96,97]. Calibration experiments were performed without catalysts, and a highly concentrated solution of BL, i.e., weight percentage higher than 98%, was used initially. We varied the temperature and rotating speed to be able to draw the Wilson plot.

2.5. Gas-liquid mass transfer measurement

Table 1 shows the experimental matrix for mass transfer study. These experiments were performed in the absence of catalyst to avoid chemical reactions. The Redlich–Kwong–Mathias–Copeman (RKMC) equation of state was used to quantify the number of moles of hydrogen into the gas phase. According to Nasrifar, the RKMC equation is more accurate and robust [98].

2.6. Kinetic modeling

Parameter estimation, simulation and curve fitting were performed using the commercial software Athena Visual Studio V.14.2 [99]. Athena Visual Studio uses a Bayesian framework more suitable for multi-response parameter estimation than the classical nonlinear least squares method [100,101]. Indeed, Bayesian inference requires calculating the determinant criterion [102].

The following observables were used for the parameter estimation stage: BL, BHP, GVL and reaction temperatures. Only two samples were withdrawn for experiments performed in isoperibolic or adiabatic conditions: at the beginning and the end of the reaction. Several samples were withdrawn for isothermal kinetic experiments, and the reaction temperature was constant.

The ODEs, obtained from material and energy balances, were integrated by the DDAPLUS solver, a modified Newton algorithm [103]. The GREGPLUS subroutine package was used to minimize the objective function OF(ζ) and to calculate the highest probability density HPD, i.e., credible intervals, of the estimated parameters and the normalized covariance matrix.

GREGPLUS uses successive quadratic programming starting from our initial guess values to minimize OF(ζ) [99].

$$OF(\xi) = (a+b+1)\cdot ln|v(\xi)| \tag{1}$$

where a is the number of events in response, b is the number of responses and $|v(\xi)|$ is the determinant of the covariance matrix of the responses.

Each element of the covariance matrix of the responses is

$$v_{ij}(\xi) = \sum_{u=1}^{n} \omega_u \cdot [Y_{iu} - f_{iu}(\xi)] \cdot [Y_{ju} - f_{ju}(\xi)] \tag{2}$$

where, ω_u is the weight factor, Y_{iu} the experimental concentration or temperature and $f_{iu}(\xi)$ the estimated value for response i and event u; Y_{ju} the experimental concentration and $f_{ju}(\xi)$ the estimated value for

Table 2
Experimental matrix for regression with initial conditions.

Run	P (bar)	m_0BL (kg)	m_0GVL (kg)	m_0Ru (kg)	Cp_0 ($J{\cdot}kg^{-1}{\cdot}K^{-1}$)	UA_0 ($W{\cdot}K^{-1}$)	$[BL]_0$ ($mol{\cdot}m^{-3}$)	$[BHP]_0$ ($mol{\cdot}m^{-3}$)	$[GVL]_0$ ($mol{\cdot}m^{-3}$)	$[BuOH]_0$ ($mol{\cdot}m^{-3}$)	Tr_0 (K)	Thermal mode
1	35	0.415	0.105	0.005	2736	17	4712	0	2082	29	393	isothermal
2	35	0.500	0.000	0.007	2736	19	5929	0	28	65	423	isothermal
3	35	0.500	0.000	0.007	2736	19	9	2222	3909	2883	432	isothermal
4	15	0.117	0.402	0.004	2736	17	1359	2	8198	8	403	isothermal
5	20	0.520	0.000	0.006	3131	17	6105	0	4	3	394	isothermal
1	22	0.500	0.000	0.005	2755	18	6114	0	0	0	412	isoperibolic
2	30	0.400	0.100	0.005	2773	17	4963	0	2079	0	392	isoperibolic
3	30	0.420	0.100	0.005	2646	17	4713	1	1853	31	403	isoperibolic
4	35	0.420	0.100	0.008	3131	17	5090	1	2040	3	393	isoperibolic
1	36	0.520	0.000	0.006	2751	17	5816	0	0	0	393	adiabatic
2	35	0.520	0.000	0.006	2789	15	6056	0	3	53	373	adiabatic
3	25	0.520	0.000	0.005	2704	15	5360	0	0	0	373	adiabatic
4	35	0.420	0.100	0.007	2624	15	4553	0	1786	31	373	adiabatic
5	25	0.520	0.000	0.006	2705	16	5635	0	20	37	383	adiabatic
6	30	0.350	0.170	0.008	2705	17	4223	4	3384	25	403	adiabatic
7	25	0.400	0.120	0.005	3131	18	4681	10	2337	30	413	adiabatic
8	20	0.520	0.000	0.004	3131	17	6339	0	8	62	403	adiabatic

Table 3
Experimental matrix with initial conditions for validation.

Run	P (bar)	m_0BL (kg)	m_0GVL (kg)	m_0Ru (kg)	Cp_0 ($J{\cdot}kg^{-1}{\cdot}K^{-1}$)	UA_0 ($W{\cdot}K^{-1}$)	$[BL]_0$ ($mol{\cdot}m^{-3}$)	$[BHP]_0$ ($mol{\cdot}m^{-3}$)	$[GVL]_0$ ($mol{\cdot}m^{-3}$)	$[BuOH]_0$ ($mol{\cdot}m^{-3}$)	Tr_0 (K)	Thermal mode
6	38	0.415	0.105	0.005	2736	17	1050	2202	3482	1356	403	isothermal
7	35	0.415	0.105	0.005	2736	15	5059	0	2092	0	373	isothermal
8	20	0.520	0.000	0.006	2736	16	5756	0	4	34	384	isothermal
5	35	0.520	0.000	0.007	2788	15	5857	0	0	0	373	isoperibolic
6	35	0.420	0.100	0.008	2728	16	4984	1	1993	33	383	isoperibolic

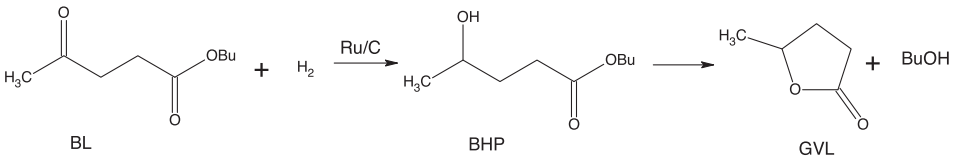

Fig. 2. Reaction pathway for the hydrogenation of BL over Ru/C.

response j and event u.

A modified Arrhenius equation was used to decrease the correlation between the pre-exponential factor and the activation energy by linearizing the original Arrhenius equation as

$$k(T) = exp\left[ln\left(k\left(T_{ref}\right)\right) + \frac{E_a}{R{\cdot}T_{ref}}{\cdot}\left(1 - \frac{T_{ref}}{T}\right)\right] \quad (3)$$

where, T_{ref} is the reference temperature chosen in the considered experimental temperature range.

Table 2 shows the experimental matrix for the regression and Table 3 shows the experimental matrix for the validation stage.

3. Results and discussion

3.1. Kinetics

The global kinetics for the hydrogenation of BL is a two-step reaction (Fig. 2).

The hydrogenation of the carbonyl group can take different routes, as illustrated in a previous article of our group [104]. In this work we considered five kinetic models to determine the most reliable, these kinetic models are described below:

- Eley-Rideal (ER1): This kinetic model considers that only BL is adsorbed into active sites of the catalyst, and then molecular hydrogen collides directly to the adsorbed BL.
- Langmuir Hinshelwood with molecular adsorption of H_2 (LH1): This kinetic model considers that all reactants, BL and molecular hydrogen, are adsorbed into the active sites of the catalyst without dissociation, then the chemical reaction takes place between adsorbed molecules.
- Langmuir Hinshelwood with hydrogen dissociation (LH2): As LH1 this kinetic model considers that all reactants, BL and molecular hydrogen, are adsorbed into the active sites of the catalyst. However, in this case, molecular hydrogen is dissociated into atomic hydrogen; then the chemical reaction takes place between adsorbed BL and adsorbed atomic hydrogen.
- Non-competitive Langmuir Hinshelwood with molecular adsorption of H_2 (NCLH1): This kinetic model considers that there is no competition between the reactants for the active sites of the catalyst, so that it is considered that BL and molecular hydrogen are adsorbed in different actives sites. Chemical reaction occurs between adsorbed BL and adsorbed molecular hydrogen without dissociation.
- Non-competitive Langmuir Hinshelwood with hydrogen dissociation (NCLH2): As NCLH1 this kinetic model consider that there is no competition between the reactants. BL and molecular hydrogen are adsorbed into different actives sites, then the adsorbed molecular hydrogen is dissociated into atomic hydrogen. The chemical reaction occurs between adsorbed BL and adsorbed atomic hydrogen.

Table 4
Kinetic expression for the different mechanisms for the hydrogenation step.

Kinetic model	Rate expression
Eley-Rideal with no adsorption of hydrogen (ER1)	$\frac{k_1 \cdot [H_2] \cdot K_{BL} \cdot [BL] \cdot \omega_{Cat.}}{(K_{BL} \cdot [BL] + K_{BHP} \cdot [BHP] + 1)}$
Langmuir Hinshelwood with molecular adsorption of H_2 (LH1)	$\frac{k_1 \cdot K_{H2} \cdot [H_2] \cdot K_{BL} \cdot [BL] \cdot \omega_{Cat.}}{(K_{H2} \cdot [H_2] + K_{BL} \cdot [BL] + K_{BHP} \cdot [BHP] + 1)^2}$
Langmuir Hinshelwood with hydrogen dissociation (LH2)	$\frac{k_1 \cdot K_H \cdot [H_2] \cdot K_i \cdot K_{BL} \cdot [BL] \cdot \omega_{Cat.}}{\left(\sqrt{K_H \cdot [H_2]} + K_{BL} \cdot [BL] + K_{BHP} \cdot [BHP] + K_i \cdot K_{BL} \cdot [BL] \cdot \sqrt{K_H \cdot [H_2]} + 1\right)^2}$
Non-competitive Langmuir Hinshelwood with no dissociation of hydrogen (NCLH1)	$\frac{k_1 \cdot K_{H2} \cdot [H_2]}{(1 + K_{H2} \cdot [H_2])} \cdot \frac{K_{BL^\wedge} \cdot [BL]}{(1 + K_{BHP^\wedge} \cdot [BHP] + K_{BL^\wedge} \cdot [BL])} \cdot \omega_{Cat.}$
Non-competitive Langmuir Hinshelwood with hydrogen dissociation (NCLH2)	$\frac{k_1 \cdot K_H \cdot K_C \cdot K_{BL^\wedge} \cdot [H_2]}{\sqrt{K_H \cdot [H_2]} + 1} \cdot \frac{[BL] \cdot \omega_{Cat.}}{K_{BL^\wedge} \cdot [BL] + K_C \cdot \sqrt{K_H \cdot [H_2]} \cdot K_{BL^\wedge} \cdot [BL] + K_{BHP^\wedge} \cdot [BHP] + 1}$

Table 5
Kinetic factors and estimated parameters.

Models	Kinetic factors	Estimated parameters
ER1	$exp\left(ln(K_{BL}) + ln(k_1(T_{ref})) + \frac{E_{a1}}{R \cdot T_{ref}} \cdot \left(1 - \frac{T_{ref}}{T}\right)\right)$	$ln(K_{BL}), ln(k_1(T_{ref})), \frac{E_{a1}}{R \cdot T_{ref}}$ and $ln(K_{BHP})$
LH1	$exp\left(ln(K_{H2}) + ln(K_{BL}) + ln(k_1(T_{ref})) + \frac{E_{a1}}{R \cdot T_{ref}} \cdot \left(1 - \frac{T_{ref}}{T}\right)\right)$	$ln(K_{H2}), ln(K_{BL}), ln(k_1(T_{ref})), \frac{E_{a1}}{R \cdot T_{ref}}$ and $ln(K_{BHP})$
LH2	$exp\left(ln(K_H) + ln(K_{BL}) + ln(K_i) + ln(k_1(T_{ref})) + \frac{E_{a1}}{R \cdot T_{ref}} \cdot \left(1 - \frac{T_{ref}}{T}\right)\right)$	$ln(K_H), ln(K_{BL}), ln(K_i), ln(k_1(T_{ref})), \frac{E_{a1}}{R \cdot T_{ref}}$ and $ln(K_{BHP})$
NCLH1	$\exp\left(ln(K_{H2}) + ln(K_{BL^\wedge}) + ln(k_1(T_{ref})) + \frac{E_{a1}}{R \cdot T_{ref}} \left(1 - \frac{T_{ref}}{T}\right)\right)$ f	$\ln(K_{H2}), \ln(K_{BL^\wedge}), \ln(K_{BHP^\wedge}), \ln(k_1(T_{ref}))$ and $\frac{E_{a1}}{R \cdot T_{ref}}$
NCLH2	$\exp\left(\ln(K_H) + \ln(K_{BL^\wedge}) + \ln(K_C) + \ln(k_1(T_{ref})) + \frac{E_{a1}}{R \cdot T_{ref}} \cdot \left(1 - \frac{T_{ref}}{T}\right)\right)$	$\ln(K_H), \ln(K_{BL^\wedge}), \ln(K_{BHP^\wedge}), \ln(K_c), \ln(k_1(T_{ref}))$ and $\frac{E_{a1}}{R \cdot T_{ref}}$

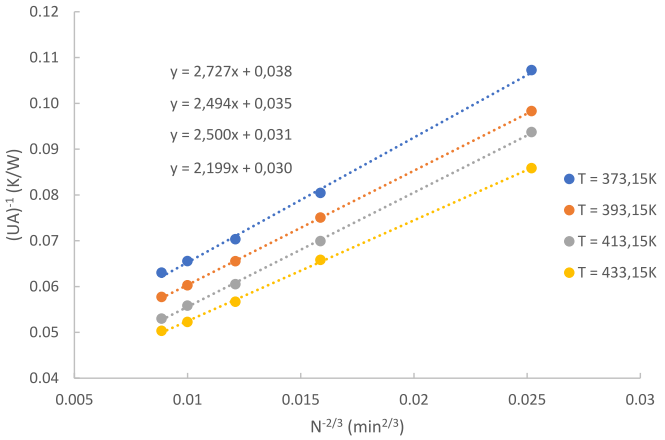

Fig. 3. Wilson plot.

Table 6
AIC values for each observable and model.

AIC					Number of parameters to estimate
	BL	BHP	GVL	Tr	
ER1	2529	2010	2151	36	6
LH1	2498	2008	2131	117	7
LH2	2500	2010	2133	118	8
NCLH1	2520	1993	2139	54	7
NCLH2	2508	2056	2161	38	8

Table 4 shows the rate expression for the different possible reaction mechanisms.

The kinetic expression for the second reaction step, i.e., the cyclization step, was expressed as

$$R_{Cyclization} = k_2 \cdot [BHP] \quad (4)$$

Table 7
Estimated values at $T_{ref} = 398.15$ K and statistical data for NCLH1.

	Units	Estimate	HPD	HPD%
$ln(k_1(T_{ref}))$	mol. kg_dry basis $RuC^{-1}.s^{-1}$	5.34	0.12	2.17
$ln(k_2(T_{ref}))$	s^{-1}	−10.19	0.03	0.28
$\frac{E_{a1}}{R \cdot T_{ref}}$	–	9.25	0.73	7.92
$\frac{E_{a2}}{R \cdot T_{ref}}$	–	8.09	0.59	7.27
$ln(K_H)$	$m^3 \cdot mol^{-1}$	−2.91	0.26	8.93
$\ln(K_{BL^\wedge})$	$m^3 \cdot mol^{-1}$	0.011	–	
$ln(K_{BHP^\wedge})$	$m^3 \cdot mol^{-1}$	7.961	–	

Table 8
Normalized parameter covariance matrix for NCLH1.

	$ln(k_1(T_{ref}))$	$ln(k_2(T_{ref}))$	$\frac{E_{a1}}{R \cdot T_{ref}}$	$\frac{E_{a2}}{R \cdot T_{ref}}$	$ln(K_H)$
$ln(k_1(T_{ref}))$	1				
$ln(k_2(T_{ref}))$	0.07	1			
$\frac{E_{a1}}{R \cdot T_{ref}}$	−0.163	−0.047	1		
$\frac{E_{a2}}{R \cdot T_{ref}}$	−0.086	−0.671	−0.059	1	
$ln(K_H)$	−0.981	−0.071	0.123	0.081	1

we applied linearization on the rate constant, and kinetic factors are displayed in Table 5.

3.2. Material and energy balances

Due to the vigorous stirring, ideal hydrodynamics was assumed in the RC1 reactor. Material balances for different compounds in the liquid phase leads to:

$$\frac{dC_{BL}}{dt} = -R_{Hydrogenation} \quad (5)$$

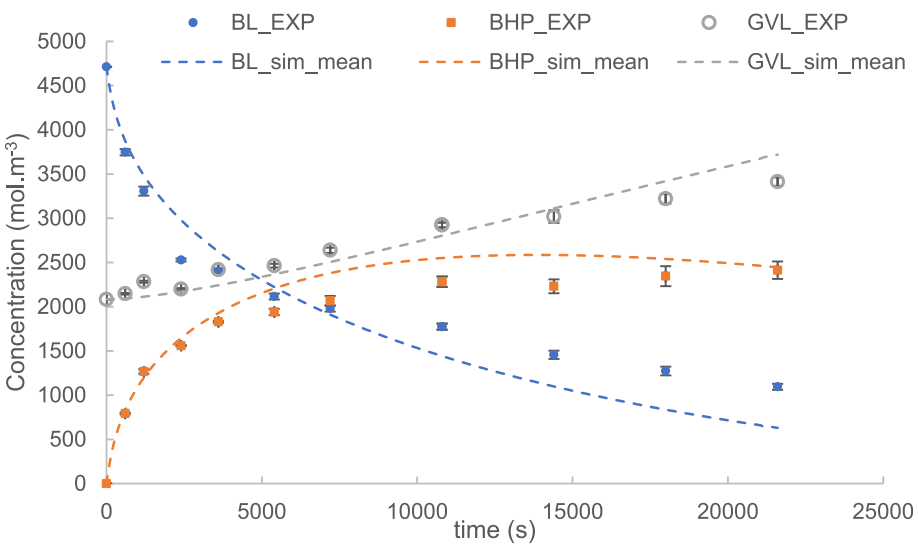

Fig. 4. Fit of the NCLH1 model to isothermal experimental data for Run 1.

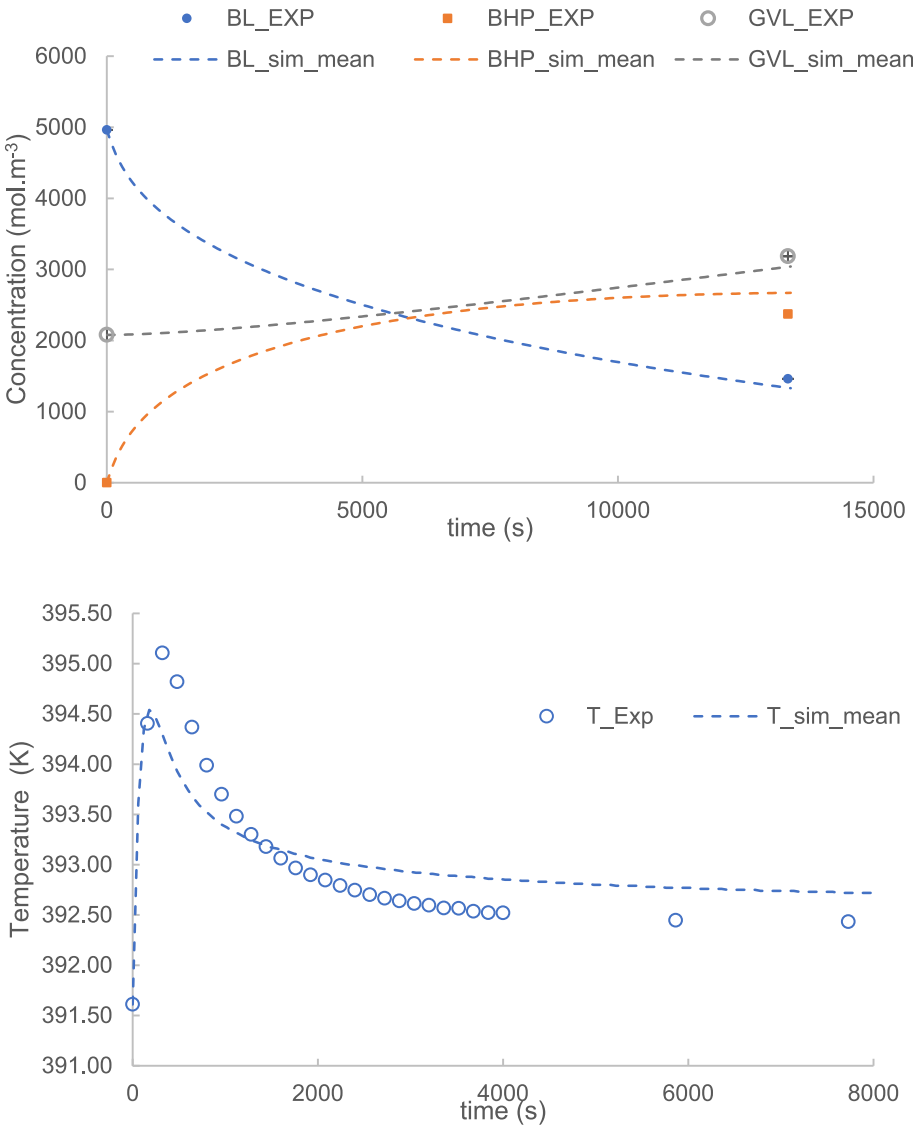

Fig. 5. Fit of the NCLH1 model to isoperibolic experimental data for Run 2.

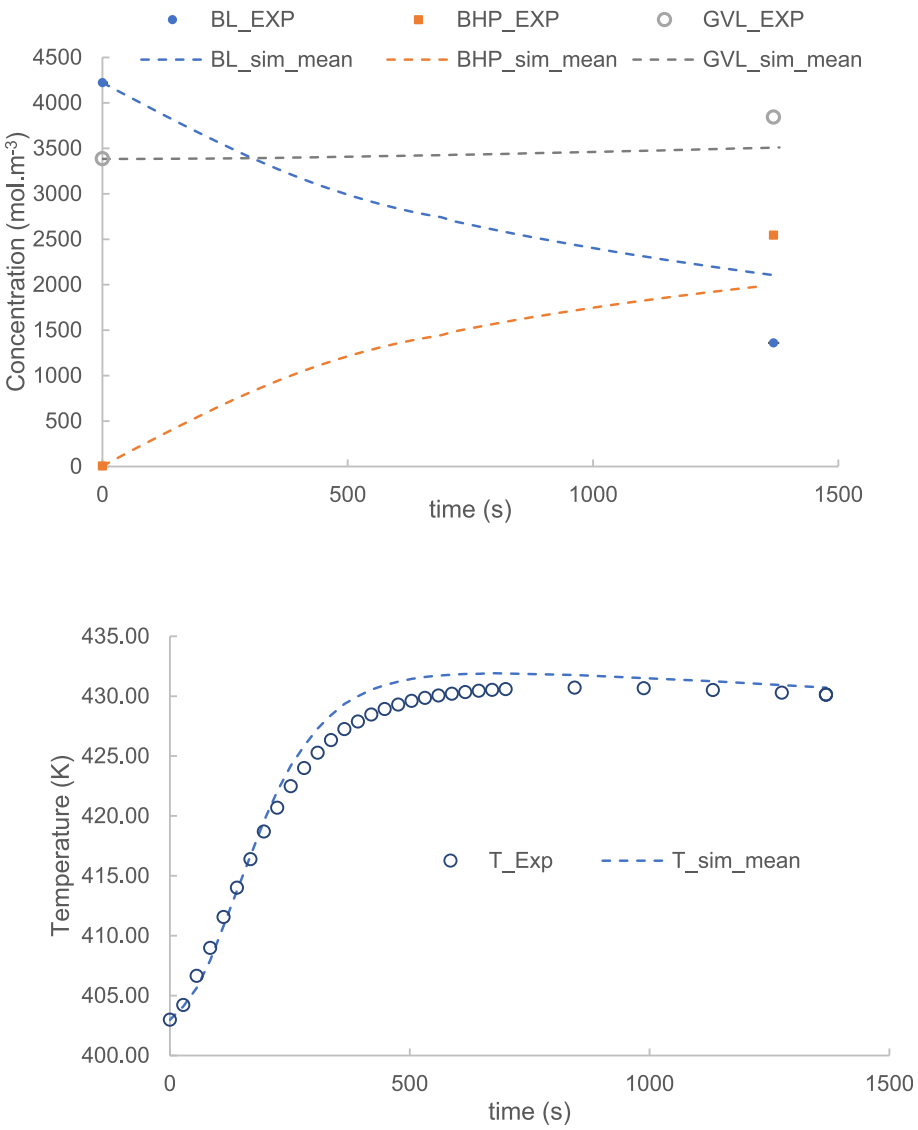

Fig. 6. Fit of the NCLH2 model to adiabatic experimental data for Run 6.

$$\frac{d[H_2]_{liq}}{dt} = k_L.a\cdot\left([H_2]^*_{liq} - [H_2]_{liq}\right) - R_{Hydrogenation} \quad (6)$$

$$\frac{dC_{BHP}}{dt} = R_{Hydrogenation} - R_{Cyclization} \quad (7)$$

$$\frac{dC_{BuOH}}{dt} = R_{Cyclization} \quad (8)$$

$$\frac{dC_{GVL}}{dt} = R_{Cyclization} \quad (9)$$

$$\frac{dT_R}{dt} = \frac{(-R_{Hydrogenation}\cdot\Delta H_{R,Hydrogenation}\cdot V - R_{Cyclization}\cdot\Delta H_{R,Cyclization}\cdot V) + UA\cdot(T_j - T_R) + \alpha\cdot(T_{amb} - T_R)}{m_R\cdot C_{PR} + m_{insert}\cdot Cp_{insert} + m_{catalyst}\cdot Cp_{catalyst}} \quad (10)$$

The term $[H_2]^*_{liq}$ is hydrogen concentration at the gas–liquid interface. This value depends on temperature and was determined through Henry's constant: $He(T) = \frac{[H_2]^*_{liq}}{P_{H_2,Reactor}}$ [54]. A separate mass transfer coefficient study was carried out to estimate the volumetric gas-to-liquid mass transfer coefficient for hydrogen. A similar methodology applied in a previous study of our group was used [57] to estimate this mass transfer coefficient by taking into account density and viscosity of the reaction mixture [24]. For the sake of clarity, this information was added in Supplementary Material (S1). The value of $He(T)$ can change with temperature and chemical composition, the results from Capecci et al. were used [54].

The heat balance equation for the liquid phase leads to

The term $\alpha\cdot(T_{amb} - T_R)$ represents the heat loss with the surroundings. The term $UA\cdot(T_j - T_R)$ is the heat flow rate exchanged with the heat carrier, and UA is the global heat transfer, T_j and T_R are the jacket and

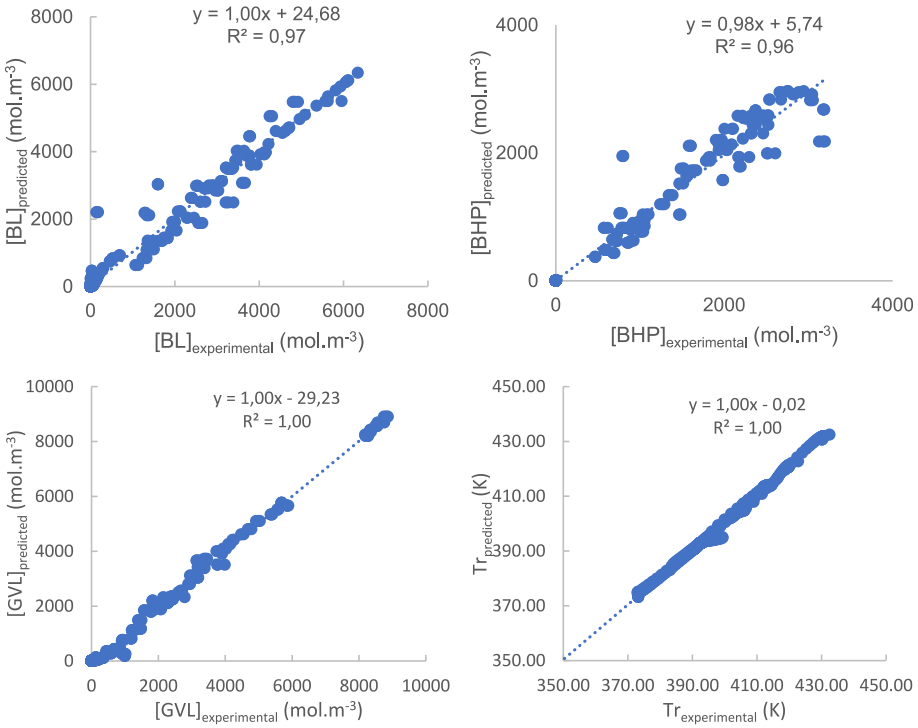

Fig. 7. Parity plots from regression stage (model NCLH1).

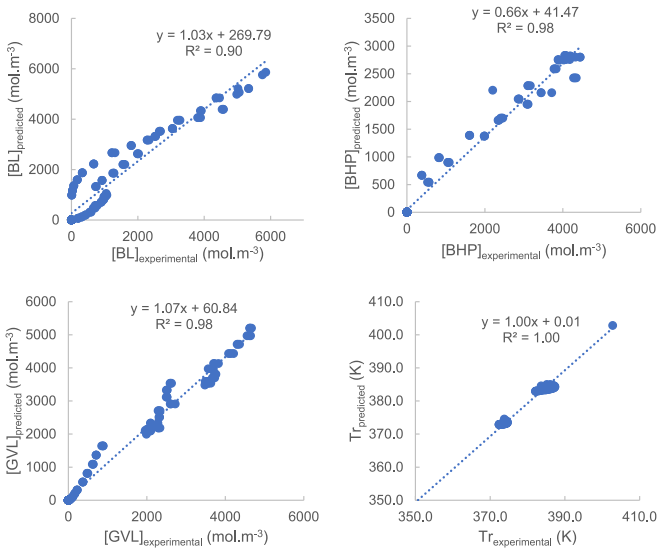

Fig. 8. Parity plots from validation stage (model NCLH1).

reaction temperatures. The term $m_R \cdot C_{PR} + m_{insert} \cdot Cp_{insert} + m_{catalyst} \cdot Cp_{catalyst}$ represents the thermal inertia, where $m_{insert} \cdot Cp_{insert}$ is equal to 52 $J \cdot K^{-1}$, according to the manufacturer, C_{PR} was evaluated based on the evolution of chemical composition and temperature [24] and $Cp_{catalyst}$ was found based on the article of Lu et al. [105]. Reaction enthalpies for hydrogenation $\Delta H_{R,Hydrogenation}$ and cyclization $\Delta H_{R,Cyclization}$ were the ones calculated by Wang et al. [46].

3.3. Calibration results (Wilson plot)

In order to verify the thin wall approximation between the heat carrier and reaction mixture and to predict the UA values with reaction temperature, UA value was calculated at different temperatures and rotating speeds in the absence of reaction, i.e., Wilson plot [97]. Fig. 3 shows the linearity between 1/UA and $N^{-2/3}$, confirming the thin wall approximation.

3.4. Gas-liquid mass transfer results

In these experiments, rates of hydrogenation and cyclization are equal to zero, thus one should integrate Eq. (6) to estimate the k_La value. The volumetric mass transfer coefficient was expressed as [57]:

$$k_La = (k_La)_{\text{modified}} \cdot \left(\frac{T_{liq}}{\mu_{liq}}\right)^{0.5} \cdot \left(\frac{\rho_{liq}}{\mu_{liq}}\right)^{0.25} \quad (11)$$

The constant $(k_La)_{modified}$ was calculated from experiments shown in Table 1 as described in Supplementary Material (S1). From Table S1.1, one can notice that the calculated value of $(k_La)_{modified}$ for each run is very similar. The average value of $(k_La)_{modified}$ was found to be $2.25 \cdot 10^{-6}$ $(Pa \cdot s \cdot K^{-1})^{0.5}(Pa \cdot s \cdot kg^{-1} \cdot m^{-3})^{0.25} \cdot s^{-1}$ and the standard deviation was equal to 0.14 $(Pa \cdot s \cdot K^{-1})^{0.5}(Pa \cdot s \cdot kg^{-1} \cdot m^{-3})^{0.25} \cdot s^{-1}$. This value was found to be similar than the one of Wang et al. [57].

3.5. Kinetic modeling

3.5.1. Regression

The five models were tested during the regression (ER1, LH1, LH2, NCLH1 and NCLH2). The Akaike information criterion (AIC) was used to evaluate the most reliable models, and it was calculated as

$$\text{AIC: number of independant event} \cdot ln\left(\frac{\left[Y_{ju} - f_{ju}(\xi)\right]^2}{\text{number of independantevent}}\right) + 2.\text{Numberofestimatedparameters} \quad (12)$$

This criterion penalizes models with numerous parameters to estimate. Table 6 shows the values for each observable.

Table 6 shows that NCLH1 and NCLH2 are the most reliable model by considering the AIC for all observables. Indeed, NCLH1 and NCLH2 models present a good compromise between the lowest AIC values for Tr and medium AIC values for BL, BHP and GVL.

For the sake of clarity, modeling results using NCLH1 model are displayed, and the others are in Supplementary Material (S2). Table 7 shows the value of the estimated parameters and the statistical values. The model can estimate the kinetic constants with low credible intervals. However, the estimation of adsorption constants is more challenging due to the difficulty to estimate such thermodynamic constants.

Correlation between the majority of estimated parameters are lower than 0.90 in absolute value, thus one can consider that the estimated parameters are not correlated [106] (Table 8.). This absence of correlation shows that the parameters are well identified. The parameter $ln\left(k_1\left(T_{ref}\right)\right)$ and $ln(K_H)$ are strongly correlated, due to the difficulty to correctly track the hydrogenation rate.

Figs. 4-6 show the fit of the model to experimental data in different thermal modes for NCLH1 model. Generally, the model fits well the experimental data in these modes as it is confirmed with the parity plot (Fig. 7). In isothermal mode, experimental temperatures were not considered in the objective function, because the reaction temperature is stable along the reaction course. For adiabatic and isoperibolic experiments, we measured concentrations at the beginning and at the end of the reaction.

3.5.2. Validation stage

A holdout validation method was used. The estimated kinetic and thermodynamic constants obtained from the regression stage were used to predict the kinetic profile by using initial experimental conditions from Table 3. Fig. 8 show parity plots for the validation experiments for NCLH1, showing the good prediction capacity of NCLH1. NCLH1 can correctly predict BL and GVL concentrations, as well as reaction temperature. This model is less accurate for BHP concentration.

4. Conclusions

There is a need to develop reliable and robust kinetic models to scaleup, optimize process production, energy consumption and production, cost production and for thermal risk assessment. Traditionally, these types of kinetic models are developed in isothermal conditions without considering the energy balance. Thus, such models are limited for energy optimization or thermal risk assessment.

In this work, we developed and assessed 5 kinetic models in different thermal modes, i.e., isothermal, adiabatic and isoperibolic one. We applied this approach for the production of γ-valerolactone from the hydrogenation of butyl levulinate. To the best of the authors' knowledge, it is the first time that kinetic model are done in different thermal modes. Such models can provide crucial information in process optimization, scaleup, energy recovery for pinch analysis and thermal risk assessment.

Kinetic experiments were performed by using high concentrated solution of BL in the RC1 calorimeter using three thermal modes (isothermal, isoperibolic and adiabatic). For the regression stage, we varied the initial temperature from 383 to 430 K, catalyst loading from 6.5 to 13.5 kg/m^3 and hydrogen pressure from 15 to 35 bar. We were able to estimate kinetic constants for 5 kinetic models: Eley-Rideal with no adsorption of hydrogen (ER1), Langmuir Hinshelwood with molecular adsorption of H_2 (LH1), Langmuir Hinshelwood with hydrogen dissociation (LH2), Non-competitive Langmuir Hinshelwood with no dissociation of hydrogen (NCLH1) and Non-competitive Langmuir Hinshelwood with hydrogen dissociation (NCLH2). From the AIC criterion, we found that NCLH1 and NCLH2 models were the most reliable model. A validation stage was done using a holdout method, and confirmed the reliability of NCLH1 model.

A continuation of this work could be the determination of these constants from quantum mechanics method.

CRediT authorship contribution statement

Wenel Naudy Vásquez Salcedo: Investigation, Methodology. **Mélanie Mignot:** Resources, Investigation. **Bruno Renou:** Investigation, Supervision. **Sébastien Leveneur:** Conceptualization, Investigation, Writing – review & editing, Supervision.

Declaration of Competing Interest

The authors declare that they have no known competing financial interests or personal relationships that could have appeared to influence the work reported in this paper.

Data availability

Data will be made available on request.

Acknowledgments

This investigation was carried out in the framework of the ARBRE project (Risk Analysis to processes valorizing 2nd generation biomass and using Renewable energies). ARBRE is cofounded by European Union through the European Regional Development Fund (agreement n° 00130305) and by Normandy Region (agreement n° 21E05304), via the support of "pôle CTM (Continuum Terre-Mer) and EP2M (Énergies, Propulsion, Matière, Matériaux) de Normandie université". The authors thank the Ministry of High Education, Science and Technology of Dominican Republic (MESCYT).

For the analytical part, this work has been partially supported by University of Rouen Normandy, INSA Rouen Normandy, the Centre National de la Recherche Scientifique (CNRS), European Regional Development Fund (ERDF) N° HN0001343, Labex SynOrg (ANR-11-LABX-0029), Carnot Institute I2C, the graduate school for reasearch XL-Chem (ANR-18-EURE-0020 XL CHEM) and by Region Normandie. GC was financed by FEDER RIN Green Chem 2019NU01FOBC08 Number: 17P04374.

Appendix A. Supplementary data

Supplementary data to this article can be found online at https://doi.org/10.1016/j.fuel.2023.128792.

References

[1] Rapier R. Highlights From The BP Statistical Review Of World Energy 2021 2021. https://sourcezon.com/articles/highlights-from-the-bp-statistical-review-of-world-energy-2021?slug=highlights-from-the-bp-statistical-review-of-world-energy-2021&q= (accessed February 5, 2023).

[2] Manikandan S, Vickram S, Sirohi R, Subbaiya R, Krishnan RY, Karmegam N, et al. Critical review of biochemical pathways to transformation of waste and biomass into bioenergy. Bioresour Technol 2023;372:128679. https://doi.org/10.1016/j.biortech.2023.128679.

[3] Amerit B, Ntayi JM, Ngoma M, Bashir H, Echegu S, Nantongo M. Commercialization of biofuel products: a systematic literature review. Renewable Energy Focus 2023;44:223–36. https://doi.org/10.1016/j.ref.2022.12.008.

[4] Jiang Y, Li Z, Li Y, Chen L, Zhang H, Li Hu, et al. Recent advances in sustainable catalytic production of 5-methyl-2-pyrrolidones from bio-derived levulinate. Fuel 2023;334:126629. https://doi.org/10.1016/j.fuel.2022.126629.

[5] Ashokkumar V, Venkatkarthick R, Jayashree S, Chuetor S, Dharmaraj S, Kumar G, et al. Recent advances in lignocellulosic biomass for biofuels and value-added bioproducts - A critical review. Bioresour Technol 2022;344:126195. https://doi.org/10.1016/j.biortech.2021.126195.

[6] Liu WJ, Yu HQ. Thermochemical conversion of lignocellulosic biomass into mass-producible fuels: emerging technology progress and environmental sustainability evaluation. ACS Environ Au 2022;2:98–114. https://doi.org/10.1021/acsenvironau.1c00025.

[7] Jamil F, Saleem M, Ali Qamar O, Khurram MS, Al-Muhtaseb AH, Inayat A, et al. State-of-the-art catalysts for clean fuel (methyl esters) production—a comprehensive review. JPhys Energy 2023;5(1):014005. https://doi.org/10.1088/2515-7655/aca5b3.

[8] Tomei J, Helliwell R. Food versus fuel? Going beyond biofuels Land Use Policy 2016;56:320–6. https://doi.org/10.1016/j.landusepol.2015.11.015.

[9] Alonso DM, Wettstein SG, Mellmer MA, Gurbuz EI, Dumesic JA. Integrated conversion of hemicellulose and cellulose from lignocellulosic biomass. Energ Environ Sci 2013;6:76–80. https://doi.org/10.1039/c2ee23617f.

[10] Li G, Liu W, Ye C, Li X, Si C-L. Chemocatalytic conversion of cellulose into key platform chemicals. Int J Polym Sci 2018;2018:1–21.

[11] Guo K, Guan Q, Xu J, Tan W. Mechanism of preparation of platform compounds from lignocellulosic biomass liquefaction catalyzed by bronsted acid: a review. J Bioresour Bioprod 2019;4:202–13. https://doi.org/10.12162/jbb.v4i4.009.

[12] Di Menno Di Bucchianico D, Wang Y, Buvat J-C, Pan Y, Casson Moreno V, Leveneur S. Production of levulinic acid and alkyl levulinates: a process insight. Green Chem 2022;24(2):614–46.

[13] Yan K, Yang Y, Chai J, Lu Y. Catalytic reactions of gamma-valerolactone: a platform to fuels and value-added chemicals. Appl Catal B Environ 2015;179:292–304. https://doi.org/10.1016/J.APCATB.2015.04.030.

[14] Kerkel F, Markiewicz M, Stolte S, Müller E, Kunz W. The green platform molecule gamma-valerolactone - ecotoxicity, biodegradability, solvent properties, and potential applications. Green Chem 2021;23:2962–76. https://doi.org/10.1039/d0gc04353b.

[15] Qu R, Junge K, Beller M. Hydrogenation of carboxylic acids, esters, and related compounds over heterogeneous catalysts: a step toward sustainable and carbon-neutral processes. Chem Rev 2023;123(3):1103–65.

[16] Di Menno Di Bucchianico D, Buvat JC, Mignot M, Casson Moreno V, Leveneur S. Role of solvent the production of butyl levulinate from fructose. Fuel 2022;318:123703. https://doi.org/10.1016/j.fuel.2022.123703.

[17] Liu C, Wei M, Wang J, Xu J, Jiang J, Wang K. Facile directional conversion of cellulose and bamboo meal wastes over low-cost sulfate and polar aprotic solvent. ACS Sustain Chem Eng 2020;8:5776–86. https://doi.org/10.1021/acssuschemeng.0c01280.

[18] Wang S, Zhao Y, Lin H, Chen J, Zhu L, Luo Z. Conversion of C5 carbohydrates into furfural catalyzed by a Lewis acidic ionic liquid in renewable γ-valerolactone. Green Chem 2017;19:3869–79. https://doi.org/10.1039/c7gc01298e.

[19] Chew AK, Walker TW, Shen Z, Demir B, Witteman L, Euclide J, et al. Effect of mixed-solvent environments on the selectivity of acid-catalyzed dehydration reactions. ACS Catal 2020;10(3):1679–91.

[20] Kang D, Choi M, Kim D, Han J. Environmental analysis of catalytic adipic acid production strategies from two different lignocellulosic biomasses. ACS Sustain Chem Eng 2022;10(18):5888–94.

[21] Motagamwala AH, Won W, Maravelias CT, Dumesic JA. An engineered solvent system for sugar production from lignocellulosic biomass using biomass derived γ-valerolactone. Green Chem 2016;18:5756–63. https://doi.org/10.1039/c6gc02297a.

[22] Baco S, Klinksiek M, Ismail Bedawi Zakaria R, Antonia Garcia-Hernandez E, Mignot M, Legros J, et al. Solvent effect investigation on the acid-catalyzed esterification of levulinic acid by ethanol aided by a linear solvation energy relationship. Chem Eng Sci 2022;260:117928.

[23] Pokorný V, Štejfa V, Fulem M, Červinka C, Růžička K. Vapor pressures and thermophysical properties of ethylene carbonate, propylene carbonate, γ-valerolactone, and γ-butyrolactone. J Chem Eng Data 2017;62:4174–86. https://doi.org/10.1021/acs.jced.7b00578.

[24] Ariba H, Wang Y, Devouge-Boyer C, Stateva RP, Leveneur S. Physicochemical properties for the reaction systems: levulinic acid, its esters, and γ-valerolactone. J Chem Eng Data 2020;65:3008–20. https://doi.org/10.1021/acs.jced.9b00965.

[25] Horváth IT, Mehdi H, Fábos V, Boda L, Mika LT. γ-Valerolactone—a sustainable liquid for energy and carbon-based chemicals. Green Chem 2008;10:238. https://doi.org/10.1039/b712863k.

[26] Raj T, Chandrasekhar K, Banu R, Yoon JJ, Kumar G, Kim SH. Synthesis of γ-valerolactone (GVL) and their applications for lignocellulosic deconstruction for sustainable green biorefineries. Fuel 2021;303:121333. https://doi.org/10.1016/j.fuel.2021.121333.

[27] Al-Naji M, Puértolas B, Kumru B, Cruz D, Bäumel M, Schmidt BVKJ, et al. Sustainable continuous flow valorization of γ-valerolactone with trioxane to α-methylene-γ-valerolactone over basic beta zeolites. ChemSusChem 2019;12(12):2628–36.

[28] Manzer LE. Catalytic synthesis of α-methylene-γ-valerolactone: a biomass-derived acrylic monomer. Appl Catal A 2004;272:249–56. https://doi.org/10.1016/J.APCATA.2004.05.048.

[29] Choi M, Byun J, Park H, Jeong K, Kim SM, Han J. Economically-feasible, "greener" transformation of gamma-valerolactone to nylon 6,6. Biomass Bioenergy 2022;162:106503. https://doi.org/10.1016/J.BIOMBIOE.2022.106503.

[30] Hayes G, Laurel M, MacKinnon D, Zhao T, Houck HA, Becer CR. Polymers without petrochemicals: sustainable routes to conventional monomers. Chem Rev 2023;123(5):2609–734.

[31] Alonso DM, Bond JQ, Dumesic JA. Catalytic conversion of biomass to biofuels. Green Chem 2010;12:1493–513. https://doi.org/10.1039/c004654j.

[32] Dutta S, Yu IKM, Tsang DCW, Ng YH, Ok YS, Sherwood J, et al. Green synthesis of gamma-valerolactone (GVL) through hydrogenation of biomass-derived levulinic acid using non-noble metal catalysts: A critical review. Chem Eng J 2019;372:992–1006.

[33] Making alternative fuels cheaper | MIT News | Massachusetts Institute of Technology n.d. https://news.mit.edu/2013/making-alternative-fuels-cheaper-0617 (accessed February 5, 2023).

[34] Anagnostopoulou E, Lilas P, Diamantopoulou P, Fakas C, Krithinakis I, Patatsi E, et al. Hydrogenation of the pivotal biorefinery platform molecule levulinic acid into renewable fuel γ-valerolactone catalyzed by unprecedented highly active and stable ruthenium nanoparticles in aqueous media. Renew Energy 2022;192:35–45.

[35] Kasar GB, Date NS, Bhosale PN, Rode CV. Steering the ester and γ-valerolactone selectivities in levulinic acid hydrogenation. Energy Fuel 2018;32:6887–900. https://doi.org/10.1021/acs.energyfuels.8b01263.

[36] Alonso DM, Wettstein SG, Dumesic JA. Gamma-valerolactone, a sustainable platform molecule derived from lignocellulosic biomass. Green Chem 2013;15:584–95. https://doi.org/10.1039/c3gc37065h.

[37] Yan K, Lafleur T, Wu X, Chai J, Wu G, Xie X. Cascade upgrading of γ-valerolactone to biofuels. Chem Commun 2015;51:6984–7. https://doi.org/10.1039/c5cc01463h.

[38] Ayodele OO, Dawodu FA, Yan D, Dong H, Xin J, Zhang S. Production of bio-based gasoline by noble-metal-catalyzed hydrodeoxygenation of α-angelica lactone derived di/trimers. ChemistrySelect 2017;2:4219–25. https://doi.org/10.1002/slct.201700451.

[39] Wang H, Wu Y, Guo S, Dong C, Ding M. γ-Valerolactone converting to butene via ring-opening and decarboxylation steps over amorphous SiO2-Al2O3 catalyst. Mol Catal 2020;497:111218. https://doi.org/10.1016/j.mcat.2020.111218.

[40] Wang H, Wu Y, Li Y, Peng J, Gu XK, Ding M. One-step synthesis of pentane fuel from γ-valerolactone with high selectivity over a Co/HZSM-5 bifunctional catalyst. Green Chem 2021;23:4780–9. https://doi.org/10.1039/d1gc01062j.

[41] Bond JQ, Alonso DM, Wang D, West RM, Dumesic JA. Integrated catalytic conversion of γ-valerolactone to liquid alkenes for transportation fuels. Science 2010;327(5969):1110–4.

[42] Han J. Integrated process for simultaneous production of jet fuel range alkenes and N-methylformanilide using biomass-derived gamma-valerolactone. J Ind Eng Chem 2017;48:173–9. https://doi.org/10.1016/j.jiec.2016.12.036.

[43] He J, Lin Lu, Liu M, Miao C, Wu Z, Chen R, et al. A durable Ni/La-Y catalyst for efficient hydrogenation of γ-valerolactone into pentanoic biofuels. J Energy Chem 2022;70:347–55.

[44] Casson Moreno V, Garbetti AL, Leveneur S, Antonioni G. A consequences-based approach for the selection of relevant accident scenarios in emerging technologies. Saf Sci 2019;112:142–51. https://doi.org/10.1016/j.ssci.2018.10.024.

[45] Wang Y, Vernières-Hassimi L, Casson-Moreno V, Hébert JP, Leveneur S. Thermal risk assessment of levulinic acid hydrogenation to γ-valerolactone. Org Process Res Dev 2018;22:1092–100. https://doi.org/10.1021/acs.oprd.8b00122.

[46] Wang Y, Plazl I, Vernières-Hassimi L, Leveneur S. From calorimetry to thermal risk assessment: γ-Valerolactone production from the hydrogenation of alkyl levulinates. Process Saf Environ Prot 2020;144:32–41. https://doi.org/10.1016/j.psep.2020.07.017.

[47] Karanwal N, Kurniawan RG, Park J, Verma D, Oh S, Kim SM, et al. One-pot, cascade conversion of cellulose to γ-valerolactone over a multifunctional Ru–Cu/zeolite-Y catalyst in supercritical methanol. Appl Catal B Environ 2022;314:121466. https://doi.org/10.1016/j.apcatb.2022.121466.

[48] Siddiqui N, Pendem C, Goyal R, Khatun R, Khan TS, Samanta C, et al. Study of γ-valerolactone production from hydrogenation of levulinic acid over nanostructured Pt-hydrotalcite catalysts at low temperature. Fuel 2022;323:124272. https://doi.org/10.1016/j.fuel.2022.124272.

[49] Mehdi H, Fábos V, Tuba R, Bodor A, Mika LT, Horváth IT. Integration of homogeneous and heterogeneous catalytic processes for a multi-step conversion of biomass: from sucrose to levulinic acid, γ-valerolactone, 1,4-pentanediol, 2-methyl-tetrahydrofuran, and alkanes. Top Catal 2008;48(1-4):49–54.

[50] Luo W, Deka U, Beale AM, Van Eck ERH, Bruijnincx PCA, Weckhuysen BM. Ruthenium-catalyzed hydrogenation of levulinic acid: Influence of the support and solvent on catalyst selectivity and stability. J Catal 2013;301:175–86. https://doi.org/10.1016/j.jcat.2013.02.003.

[51] Hengne AM, Rode CV. Cu–ZrO2 nanocomposite catalyst for selective hydrogenation of levulinic acid and its ester to γ-valerolactone. Green Chem 2012;14:1064–72. https://doi.org/10.1039/c2gc16558a.

[52] Piskun AS, van de Bovenkamp HH, Rasrendra CB, Winkelman JGM, Heeres HJ. Kinetic modeling of levulinic acid hydrogenation to γ-valerolactone in water

using a carbon supported Ru catalyst. Appl Catal A 2016;525:158–67. https://doi.org/10.1016/j.apcata.2016.06.033.
[53] Capecci S, Wang Y, Delgado J, Casson Moreno V, Mignot M, Grénman H, et al. Bayesian statistics to elucidate the kinetics of γ-valerolactone from n-butyl levulinate hydrogenation over Ru/C. Ind Eng Chem Res 2021;60(31):11725–36.
[54] Capecci S, Wang Y, Casson Moreno V, Held C, Leveneur S. Solvent effect on the kinetics of the hydrogenation of n-butyl levulinate to γ-valerolactone. Chem Eng Sci 2021;231:116315. https://doi.org/10.1016/j.ces.2020.116315.
[55] Xu H, Hu Di, Zhang M, Wang Y, Zhao Z, Jiang Z, et al. Bimetallic nicu alloy catalysts for hydrogenation of levulinic acid. ACS Appl Nano Mater 2021;4(4):3989–97.
[56] Al-Shaal MG, Wright WRH, Palkovits R. Exploring the ruthenium catalysed synthesis of γ-valerolactone in alcohols and utilisation of mild solvent-free reaction conditions. Green Chem 2012;14:1260–3. https://doi.org/10.1039/c2gc16631c.
[57] Wang Y, Cipolletta M, Vernières-Hassimi L, Casson-Moreno V, Leveneur S. Application of the concept of Linear Free Energy Relationships to the hydrogenation of levulinic acid and its corresponding esters. Chem Eng J 2019;374:822–31. https://doi.org/10.1016/j.cej.2019.05.218.
[58] Li C, Xu G, Zhai Y, Liu X, Ma Y, Zhang Y. Hydrogenation of biomass-derived ethyl levulinate into Γ-valerolactone by activated carbon supported bimetallic Ni and Fe catalysts. Fuel 2017;203:23–31. https://doi.org/10.1016/j.fuel.2017.04.082.
[59] Yan K, Chen A. Selective hydrogenation of furfural and levulinic acid to biofuels on the ecofriendly Cu–Fe catalyst. Fuel 2014;115:101–8. https://doi.org/10.1016/J.FUEL.2013.06.042.
[60] Li Z, Hao H, Lu J, Wu C, Gao R, Li J, et al. Role of the Cu-ZrO2 interface in the hydrogenation of levulinic acid to γ-valerolactone. J Energy Chem 2021;61:446–58.
[61] Fang S, Cui Z, Zhu Y, Wang C, Bai J, Zhang X, et al. In situ synthesis of biomass-derived Ni/C catalyst by self-reduction for the hydrogenation of levulinic acid to Γ-valerolactone. J Energy Chem 2019;37:204–14.
[62] Orlowski I, Douthwaite M, Iqbal S, Hayward JS, Davies TE, Bartley JK, et al. The hydrogenation of levulinic acid to Γ-valerolactone over Cu–ZrO2 catalysts prepared by a pH-gradient methodology. J Energy Chem 2019;36:15–24.
[63] Shen Q, Zhang Y, Zhang Y, Tan S, Chen J. Transformations of biomass-based levulinate ester into Γ-valerolactone and pyrrolidones using carbon nanotubes-grafted N-heterocyclic carbene ruthenium complexes. J Energy Chem 2019;39:29–38. https://doi.org/10.1016/j.jechem.2019.01.007.
[64] Delgado J, Vasquez Salcedo WN, Bronzetti G, Casson Moreno V, Mignot M, Legros J, et al. Kinetic model assessment for the synthesis of γ-valerolactone from n-butyl levulinate and levulinic acid hydrogenation over the synergy effect of dual catalysts Ru/C and amberlite IR-120. Chem Eng J 2022;430:133053. https://doi.org/10.1016/j.cej.2021.133053.
[65] Shimizu KI, Kanno S, Kon K. Hydrogenation of levulinic acid to γ-valerolactone by Ni and MoO x co-loaded carbon catalysts. Green Chem 2014;16:3899–903. https://doi.org/10.1039/c4gc00735b.
[66] Hengne AM, Malawadkar AV, Biradar NS, Rode CV. Surface synergism of an Ag-Ni/ZrO2 nanocomposite for the catalytic transfer hydrogenation of bio-derived platform molecules. RSC Adv 2014;4:9730–6. https://doi.org/10.1039/c3ra46495d.
[67] Heeres H, Handana R, Chunai D, Borromeus Rasrendra C, Girisuta B, Jan HH. Combined dehydration/(transfer)-hydrogenation of C6-sugars (D-glucose and D-fructose) to γ-valerolactone using ruthenium catalysts. Green Chem 2009;11:1247–55. https://doi.org/10.1039/b904693c.
[68] Fellay C, Dyson PJ, Laurenczy G. A viable hydrogen-storage system based on selective formic acid decomposition with a ruthenium catalyst. Angew Chemie - Int Ed 2008;47:3966–8. https://doi.org/10.1002/anie.200800320.
[69] Fábos V, Mika LT, Horváth IT. Selective conversion of levulinic and formic acids to γ-valerolactone with the shvo catalyst. Organometallics 2014;33:181–7. https://doi.org/10.1021/om400938h.
[70] Deng L, Zhao Y, Li J, Fu Y, Liao B, Guo QX. Conversion of levulinic acid and formic acid into γ-valerolactone over heterogeneous catalysts. ChemSusChem 2010;3:1172–5. https://doi.org/10.1002/cssc.201000163.
[71] Deng L, Li J, Lai DM, Fu Y, Guo QX. Catalytic conversion of biomass-derived carbohydrates into γ-valerolactone without using an external h2 supply. Angew Chemie - Int Ed 2009;48:6529–32. https://doi.org/10.1002/anie.200902281.
[72] Ruppert AM, Jędrzejczyk M, Sneka-Płatek O, Keller N, Dumon AS, Michel C, et al. Ru catalysts for levulinic acid hydrogenation with formic acid as a hydrogen source. Green Chem 2016;18(7):2014–28.
[73] Yuan J, Li S-S, Yu L, Liu Y-M, Cao Y, He H-Y, et al. Copper-based catalysts for the efficient conversion of carbohydrate biomass into γ-valerolactone in the absence of externally added hydrogen. Energ Environ Sci 2013;6(11):3308.
[74] Son PA, Nishimura S, Ebitani K. Production of γ-valerolactone from biomass-derived compounds using formic acid as a hydrogen source over supported metal catalysts in water solvent. RSC Adv 2014;4:10525–30. https://doi.org/10.1039/c3ra47580h.
[75] Li H, Fang Z, Yang S. Direct catalytic transformation of biomass derivatives into biofuel component γ-valerolactone with magnetic nickel-zirconium nanoparticles. ChemPlusChem 2016;81:135–42. https://doi.org/10.1002/cplu.201500492.
[76] Chia M, Dumesic JA. Liquid-phase catalytic transfer hydrogenation and cyclization of levulinic acid and its esters to γ-valerolactone over metal oxide catalysts. Chem Commun 2011;47:12233–5. https://doi.org/10.1039/c1cc14748j.
[77] Li H, Fang Z, Yang S. Direct conversion of sugars and ethyl levulinate into γ-valerolactone with superparamagnetic acid-base bifunctional zrfeox nanocatalysts. ACS Sustain Chem Eng 2016;4:236–46. https://doi.org/10.1021/acssuschemeng.5b01480.
[78] Ju Z, Feng S, Ren L, Lei T, Cheng H, Yu M, et al. Probing the mechanism of the conversion of methyl levulinate into γ-valerolactone catalyzed by Al(OiPr)3in an alcohol solvent: A DFT study. RSC Adv 2022;12(5):2788–97.
[79] Ortuño MA, Rellán-Piñeiro M, Luque R. Computational mechanism of methyl levulinate conversion to γ-valerolactone on UiO-66 metal organic frameworks. ACS Sustain Chem Eng 2022;10:3567–73. https://doi.org/10.1021/acssuschemeng.1c08021.
[80] Chen X, Zhao T, Zhang X, Zhang Y, Yu H, Lyu Q, et al. Synthesis of ternary magnetic nanoparticles for enhanced catalytic conversion of biomass-derived methyl levulinate into γ-valerolactone. J Energy Chem 2021;63:430–41.
[81] Zhang C, Huo Z, Ren D, Song Z, Liu Y, Jin F, et al. Catalytic transfer hydrogenation of levulinate ester into γ-valerolactone over ternary Cu/ZnO/Al 2 O 3 catalyst. J Energy Chem 2019;32:189–97.
[82] Wu J, Zhu Y, Liao P, Xu T, Lu L, Zhang X, et al. Sustainable metal-lignosulfonate catalyst for efficient catalytic transfer hydrogenation of levulinic acid to γ-valerolactone. Appl Catal A 2022;635:118556. https://doi.org/10.1016/j.apcata.2022.118556.
[83] Protsenko II, Nikoshvili LZ, Matveeva VG, Sulman EM. Kinetic modelling of levulinic acid hydrogenation over ru-containing polymeric catalyst. Top Catal 2020;63:243–53. https://doi.org/10.1007/s11244-020-01223-0.
[84] Huang X, Liu K, Vrijburg WL, Ouyang X, Iulian Dugulan A, Liu Y, et al. Hydrogenation of levulinic acid to γ-valerolactone over Fe-Re/TiO2 catalysts. Appl Catal B Environ 2020;278:119314. https://doi.org/10.1016/j.apcatb.2020.119314.
[85] Chalid M, Broekhuis AA, Heeres HJ. Experimental and kinetic modeling studies on the biphasic hydrogenation of levulinic acid to γ-valerolactone using a homogeneous water-soluble Ru-(TPPTS) catalyst. J Mol Catal A Chem 2011;341:14–21. https://doi.org/10.1016/j.molcata.2011.04.004.
[86] Abdelrahman OA, Heyden A, Bond JQ. Analysis of kinetics and reaction pathways in the aqueous-phase hydrogenation of levulinic acid to form γ-Valerolactone over Ru/C. ACS Catal 2014;4:1171–81. https://doi.org/10.1021/cs401177p.
[87] Molleti J, Tiwari MS, Yadav GD. Novel synthesis of Ru/OMS catalyst by solvent-free method: selective hydrogenation of levulinic acid to Γ-valerolactone in aqueous medium and kinetic modelling. Chem Eng J 2018;334:2488–99. https://doi.org/10.1016/j.cej.2017.11.125.
[88] Leveneur S, Pinchard M, Rimbault A, Safdari Shadloo M, Meyer T. Parameters affecting thermal risk through a kinetic model under adiabatic condition: application to liquid-liquid reaction system. Thermochim Acta 2018;666:10–7. https://doi.org/10.1016/j.tca.2018.05.024.
[89] Cao CR, Liu SH. Thermal hazard characteristic evaluation of two low-temperature-reactive azo compounds under adiabatic process conditions. Process Saf Environ Prot 2019;130:231–7. https://doi.org/10.1016/j.psep.2019.08.020.
[90] Bhattacharya A. A general kinetic model framework for the interpretation of adiabatic calorimeter rate data. Chem Eng J 2005;110:67–78. https://doi.org/10.1016/j.cej.2005.05.003.
[91] Stoessel F. Thermal safety of chemical processes: risk assessment and process design. Wiley-VCH 2008. https://doi.org/10.1002/9783527621606.
[92] Zheng JL, Wärnå J, Salmi T, Burel F, Taouk B, Leveneur S. Kinetic modeling strategy for an exothermic multiphase reactor system: application to vegetable oils epoxidation using Prileschajew method. AIChE J 2016;62:726–41. https://doi.org/10.1002/aic.15037.
[93] Xie Q, Zhang Z, Zhang L, Xie Y, Liu W, Chen H. Thermal decomposition behavior and kinetics for nitrolysis solution from the nitration of hexamethylenetetramine. React Kinet Mech Catal 2019;128:645–62. https://doi.org/10.1007/s11144-019-01658-x.
[94] Andreozzi R, Canterino M, Caprio V, Di Somma I, Sanchirico R. Batch salicylic acid nitration by nitric acid/acetic acid mixture under isothermal, isoperibolic and adiabatic conditions. J Hazard Mater 2006;138:452–8. https://doi.org/10.1016/j.jhazmat.2006.05.104.
[95] Alamgir Ahmad K, Haider Siddiqui M, Pant KK, Nigam KDP, Shetti NP, Aminabhavi TM, et al. A critical review on suitability and catalytic production of butyl levulinate as a blending molecule for green diesel. Chem Eng J 2022;447:137550. https://doi.org/10.1016/j.cej.2022.137550.
[96] Delgado J, Vásquez Salcedo WN, Devouge-Boyer C, Hebert J-P, Legros J, Renou B, et al. Reaction enthalpies for the hydrogenation of alkyl levulinates and levulinic acid on Ru/C– influence of experimental conditions and alkyl chain length. Process Saf Environ Prot 2023;171:289–98.
[97] Lavanchy F. Development of reaction calorimetry... - Google Scholar. n.d.
[98] Nasrifar K. Comparative study of eleven equations of state in predicting the thermodynamic properties of hydrogen. Int J Hydrogen Energy 2010;35:3802–11. https://doi.org/10.1016/j.ijhydene.2010.01.032.
[99] Stewart WE, Caracotsios M, editors. Computer-Aided Modeling of Reactive Systems. Wiley; 2008.
[100] Stewart WE, Caracotsios M, Sørensen JP. Parameter estimation from multiresponse data. AIChE J 1992;38(5):641–50.
[101] Kopyscinski J, Choi J, Hill JM. Comprehensive kinetic study for pyridine hydrodenitrogenation on (Ni)WP/SiO2 catalysts. Appl Catal A 2012;445–446:50–60. https://doi.org/10.1016/j.apcata.2012.08.027.
[102] Van Boekel MAJS. Statistical aspects of kinetic modeling for food science problems. J Food Sci 1996;61:477–86. https://doi.org/10.1111/j.1365-2621.1996.tb13138.x.
[103] Caracotsios M, Stewart WE. Sensitivity analysis of initial value problems with mixed odes and algebraic equations. Comput Chem Eng 1985;9:359–65. https://doi.org/10.1016/0098-1354(85)85014-6.

[104] Capecci S, Wang Y, Delgado J, Casson Moreno V, Mignot M, Grénman H, et al. Bayesian statistics to elucidate the kinetics of γ-valerolactone from n-butyl levulinate hydrogenation over Ru/C. Ind Eng Chem Res 2021;60:11725–36. https://doi.org/10.1021/ACS.IECR.1C02107/ASSET/IMAGES/LARGE/IE1C02107_0008.JPEG.

[105] Lu X, Wang Y, Estel L, Kumar N, Grénman H, Leveneur S. Evolution of specific heat capacity with temperature for typical supports used for heterogeneous catalysts. Processes 2020;8:911. https://doi.org/10.3390/PR8080911.

[106] Toch K, Thybaut JW, Marin GB. A systematic methodology for kinetic modeling of chemical reactions applied to n-hexane hydroisomerization. AIChE J 2015;61:880–92. https://doi.org/10.1002/aic.14680.

B.4 Article: Thermal Stability for the Continuous Production of γ-valerolactone from the Hydrogenation of N-Butyl Levulinate in a CSTR

processes

MDPI

Article

Thermal Stability for the Continuous Production of γ-Valerolactone from the Hydrogenation of N-Butyl Levulinate in a CSTR

Wenel Naudy Vásquez Salcedo [1,2], Bruno Renou [2] and Sébastien Leveneur [1,*]

[1] INSA Rouen Normandie, University Rouen Normandie, Normandie Université, LSPC, UR 4704, F-76000 Rouen, France
[2] INSA Rouen-Normandie, UNIROUEN, CNRS, CORIA, Normandie University, F-76000 Rouen, France
* Correspondence: sebastien.leveneur@insa-rouen.fr

Abstract: γ-valerolactone can be a game-changer in the chemical industry because it could substitute fossil feedstocks in different fields. Its production is from the hydrogenation of levulinic acid or alkyl levulinates and can present some risk of thermal runaway. To the best of our knowledge, no studies evaluate the thermal stability of this production in a continuous reactor. We simulated the thermal behavior of the hydrogenation of butyl levulinate over *Ru/C* in a continuous stirred-tank reactor and performed a sensitivity analysis. The kinetic and thermodynamic constants from Wang et al.'s articles were used. We found that the risk of thermal stability is low for this chemical system.

Keywords: simulation; GVL; thermal stability; hydrogenation

Citation: Vásquez Salcedo, W.N.; Renou, B.; Leveneur, S. Thermal Stability for the Continuous Production of γ-Valerolactone from the Hydrogenation of N-Butyl Levulinate in a CSTR. *Processes* **2023**, *11*, 237. https://doi.org/10.3390/pr11010237

Academic Editor: Antoni Sánchez

Received: 7 December 2022
Revised: 8 January 2023
Accepted: 9 January 2023
Published: 11 January 2023

1. Introduction

The shift from fossil raw materials to renewable raw materials in the chemical industry is mandatory to make this industry sustainable and decrease its negative environmental impact. Among renewable raw materials, lignocellulosic biomass (LCB), that is not in competition with the food sector, is an excellent candidate because it could avoid the dilemma of food versus fuel that led to the alimentary crisis in the late 2000s. Even if there is divergence on the role of biofuel production in explaining the food shortage [1,2], non-food-use raw materials for chemical, biofuel, or material production should be favored [3].

LCB is available worldwide and can be obtained from agricultural wastes, such as maize stover, straw, wheat straw, sugarcane bagasse, rice husk, etc.; forestry residues including remaining wood harvestings, such as roots, branches, and leaves; dedicated crops on marginal land that is not suitable for food growth (e.g., miscanthus, switchgrass, eucalyptus, etc.); and the paper industry [4,5].

LCB consists of three main elements: cellulose and hemicellulose, which are polymers of sugars, and lignin, a polymer of aromatic compounds. The percentage of these three elements varies with species, location, and seasons, making it challenging to develop the same pretreatment or valorization process for all LCB raw materials. Nevertheless, these raw materials can lead to the production of fuels, materials, and chemicals.

The sugar fraction valorization can produce valuable platform molecules or building blocks such as levulinic acid/levulinate, furfural, GVL, HMF, etc. [3,6,7]. The potential use of GVL in fuels, materials, and chemicals is enormous [8–13]. GVL was found to be a suitable solvent for the dissolution of lignin, hemicellulose, cellulose, or fructose [14–19]. GVL can reduce CO exhaust, unburned fuel, and smoke [20]. GVL updated to hydrocarbons can be a temporary solution for jet fuels [21]. The valorization of GVL into alpha methylene can lead to an excellent substitute for acrylate [22,23].

GVL is produced from the hydrogenation of levulinic acid or alkyl levulinates. There are three main approaches: molecular hydrogen, catalytic transfer hydrogenation via the use of alcohol, or the in situ decomposition of formic acid [24–26]. The most common approach is using molecular hydrogen over Ru on activated carbon.

There are two types of catalytic systems in GVL production: homogeneous and heterogeneous. The advantage of homogeneous systems is their high catalytic performance [27,28]. However, separation processes need to be implemented to separate the catalyst from the final products, while heterogeneous catalysts are easy to remove and can be recycled [29,30].

In heterogeneous systems, the most common catalysts for GVL production from levulinic acid and alkyl levulinates are ruthenium (Ru), rhodium (Rh), palladium (Pd), platinum (Pt), gold (Au), and rhenium (Re) in which the noble metal Ru exhibits a high selectivity [8]. Manzer studied the hydrogenation of levulinic acid over a series of metal catalysts (Ir, Rh, Pd, Ru, Pt, Re, and Ni) supported on carbon (metal loading was equal to 5%) wherein a 5 wt.% *Ru/C* catalyst had the highest performance in terms of conversion and selectivity [23]. The catalytic activity of *Ru/C* and some other solid catalysts show promising results for the hydrogenation of butyl levulinate [31–34].

We have demonstrated that the hydrogenation of levulinic acid or alkyl levulinates presents some risk of thermal runaway when the thermal mode is adiabatic and in batch conditions [35,36]. One way to decrease the thermal risk is to work in continuous mode in a steady-state regime [37]. Nevertheless, one needs to assess the thermal stability of such continuous reactor [38,39]. In the literature we can find studies about thermal stability, dynamic stability, and sensitivity assessments in continuous reactors for reactions such as the hydrolysis of acetic anhydride, polystyrene production in CSTRs, and light-cycle oil hydrotreatment [40–43]. To the best of our knowledge, such a study has not been conducted for the continuous production of GVL.

In this paper, we focused on evaluating the thermal stability of GVL production from butyl levulinate over *Ru/C* and included a sensitivity approach. We modeled the thermal behavior of an ideal continuous stirred-tank reactor (CSTR) and used the kinetic and thermodynamic constants from Wang et al. [35,44]. A CSTR was chosen because its mixing is more efficient than other continuous reactors, which is vital for a gas–liquid–solid system.

2. Materials and Methods

2.1. Kinetics

Wang et al. showed that the hydrogenation of BL over *Ru/C* is a two-step reaction (Figure 1). BHP stands for butyl 4-hydroxypentanoate, and it is an intermediate. They performed this study by using GVL as a solvent.

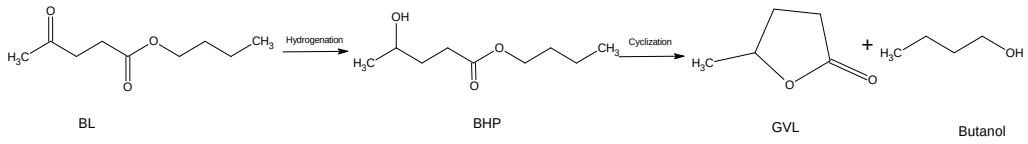

Figure 1. Reaction scheme for BL hydrogenation.

The rate expression for the hydrogenation step is derived as follows:

$$R_1 = k_1 \cdot [BL]_{Liq} \cdot [H_2]_{Liq} \cdot \omega_{Ru/C} \quad (1)$$

The rate expression for the cyclization is:

$$R_2 = k_2 \cdot [BHP]_{Liq} \quad (2)$$

where $\omega_{Ru/C}$ is the catalyst loading in kg/L.

The kinetic and thermodynamic constants from the articles of Wang et al. [35,44] were used (Table 1).

Table 1. Kinetic and thermodynamic constants.

	Values	Units
k_1 (T = 403.15 K)	$3.09 \cdot 10^{-6}$	$m^6 \cdot mol^{-1} \cdot kg^{-1} \cdot s^{-1}$
Ea_1	9.68	$kJ \cdot mol^{-1}$
ΔH_{R1}	−38.66	$kJ \cdot mol^{-1}$
k_2 (T = 403.15 K)	$1.88 \cdot 10^{-4}$	s^{-1}
Ea_2	10.25	$kJ \cdot mol^{-1}$
ΔH_{R2}	6.50	$kJ \cdot mol^{-1}$

2.2. Mass and Energy Balances

In this study, the flow distribution was assumed to be ideal. Thus, the material balance for a compound *j* can be written:

$$\frac{dC_j}{dt} = \frac{C_{j_{in}} - C_{j_{out}}}{\tau} + \sum_i v_{j,i} R_i \tag{3}$$

where *i* represents the reaction index, τ is the space-time, $v_{j,i}$ represents the stoichiometry coefficient of compound *j* in reaction *i*, and *Ri* is the reaction rate.

In a previous study by our group [44], we showed that the kinetics of hydrogen mass transfer from the gas to the liquid phase can be considered fast when GVL is the solvent. Thus, the hydrogen concentration in the liquid phase (reaction mixture) can be assumed to be constant. The solubility of hydrogen in GVL solvent was calculated from the following relationships:

$$C_{H2} = P_{H_2} \cdot He\left(T_{Ref} = 373.15\text{K}\right) \cdot exp\left(\frac{-\Delta H_{Sol.}}{R} \cdot \left(\frac{1}{T_R} - \frac{1}{373.15}\right)\right) \tag{4}$$

where P_{H_2} is the hydrogen pressure in the reactor, $He\left(T_{Ref} = 373.15K\right) = 1.86\ \text{mol} \cdot \text{m}^{-3} \cdot \text{bar}^{-1}$ is Henry's constant at 373.15 K, and $\Delta H_{Sol.} = 5936.8\ \text{J} \cdot \text{mol}^{-1}$ is the enthalpy of solubilization [44].

For an ideal CSTR, the energy balance of the reactionary phase can be written as:

$$\left[\left(\rho \hat{C}_P\right)_{liq} + \left(\rho \hat{C}_P\right)_{ins}\right] \frac{dT_r}{dt} = \frac{\sum C_{j_{in}} \overline{C}_{P_j}}{\tau} (T_{in} - T_r) + Ua(T_c - T_r) - \sum_i R_i \Delta H_i \tag{5}$$

where ρ is the volumic mass, $\hat{C}_P$ is the specific heat capacity, T_r is the reactionary media temperature, T_C is the temperature of the heat carrier in the jacket, Ua is the global heat transfer coefficient, *ins* represents the reactor insert, and ΔH_i is the enthalpy of reaction *i*. Data for heat capacities and volumetric mass were found in the literature [45,46].

The flow distribution of the heat carrier fluid is ideal; thus, the energy balance is:

$$\rho_c \hat{C}_{P_c} \frac{dT_c}{dt} = \frac{\rho_c \hat{C}_{P_c}}{\tau_c} (T_{c_0} - T_c) + Ua(T_r - T_c) \tag{6}$$

where ρ_c and $\hat{C}_{P_c}$ are the volumic mass and heat capacity of the heat carrier, and T_{c_0} is the heat carrier temperature at the inlet.

Figure 2 is a schematic representation of the reactor setup.

In this study, we will consider the steady-state regime; thus, Equations (3), (5), and (6) become:

$$\frac{dT_c}{dt} = \frac{dT_R}{dt} = 0\ \text{K} \cdot \text{s}^{-1} and\ \frac{dC_j}{dt} = 0\ \text{mol} \cdot \text{L}^{-1} \cdot \text{s}^{-1} \tag{7}$$

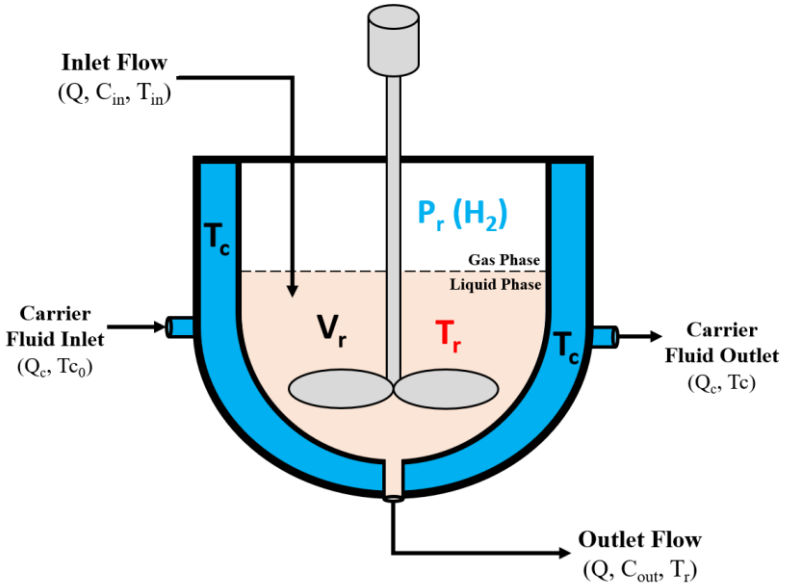

Figure 2. Reactor setup.

2.3. Operating Conditions

The simulation was performed under isobaric conditions within a reaction temperature range of 300–600 K. Table 2 shows the operating conditions used during the simulation. The inlet concentrations, catalyst loading, and temperature were in the same ranges as the ones from Wang et al. [44].

Table 2. Operating conditions used in this study.

Inlet Parameters	Values	Units
C_{BL_0}	4840	$mol \cdot m^{-3}$
C_{BHP_0}	0	$mol \cdot m^{-3}$
C_{GVL_0}	2080	$mol \cdot m^{-3}$
C_{BuOH_0}	0	$mol \cdot m^{-3}$
ω_{Cat}	10	$kg \cdot m^{-3}$
T_r	300 to 600	K
T_{in}	333.15	K
P_{H_2}	25	bar
τ	2000	s
Ua	17,000	$W \cdot m^{-3} \cdot K^{-1}$

2.4. Thermal Stability Criterion

To assess the stationary thermal stability, the van Heerden criterion was calculated during the course of the reaction. The van Heerden criterion is a stability-based criterion defined as [47–49]:

$$\frac{dQ_{Removal}}{dt} > \frac{dQ_{Generated}}{dt} \quad (8)$$

where $Q_{Removal}$ is the amount of energy exchange between the reactionary media and the heat carrier fluid, and $Q_{Generated}$ is the amount of energy released during the reaction.

The van Heerden criterion is necessary to satisfy stationary stability and states that the energy removed from a reactionary system must be higher than the energy generated by the system.

$\frac{dQ_{Removal}}{dt}$ and $\frac{dQ_{Generated}}{dt}$ were calculated from the material and energy balances.

2.5. Simulation and Parametric Sensitivity

MATLAB R2021b software was used to make the simulation and to solve the mathematical equations presented during thermal analysis. The ODE15s routine was used to solve stiff differential equations. The FSOLVE routine was used to solve the system of nonlinear equations and the energy and mass balance in the steady-state regime. The EIG routine was used to calculate the eigenvalues and eigenvectors of the Jacobian matrix.

Parametric sensitivity analysis studies the relationship between the system behavior according to changes in the inlet parameters. As mentioned by Varma et al. [50], if a slight variation in the input parameter values can lead to a significant change, then the chemical system is qualified as sensitive.

The parametric sensitivity is defined as follows:

$$S\left(\vec{y},\phi\right) = \frac{d\vec{y}}{d\phi} \tag{9}$$

For a dynamic system, we have that:

$$\frac{dS\left(\vec{y},\phi\right)}{dt} = J{\cdot}S\left(\vec{y},\phi\right) + \frac{d\vec{f}}{d\phi} \tag{10}$$

Solving the expression above for $S\left(\vec{y},\phi\right)$ in the steady state, we obtain:

$$\frac{dS\left(\vec{y},\phi\right)}{dt} = 0 \tag{11}$$

$$S\left(\vec{y},\phi\right) = -J^{-1}{\cdot}\frac{d\vec{f}}{d\phi} \text{ with } \frac{d\vec{f}}{d\phi} = \begin{pmatrix} \frac{df_1}{d\phi} \\ \vdots \\ \frac{df_n}{d\phi} \end{pmatrix} \tag{12}$$

To compare the sensitivity of one output variable according to different parameters, we can define the normalized parametric sensitivity as follows:

$$S_n\left(y,\phi_j\right) = \frac{\phi_j}{y}\frac{dy}{d\phi_j} \tag{13}$$

3. Results and Discussion

3.1. Effect of Space-Time on Conversion

Figure 3 shows the effect of temperature on BL conversion at different space-times. As the reaction temperature and space-time increase, the BL conversion increases. A space-time value of 2000 s was found to be a good compromise between time and conversion since the space-time increase does not significantly improve the conversion. We can realize from Figure 3, comparing the space-times equal to 2000 s and 10,000 s, that the difference in the BL conversion is less than 15%, while space-time is multiplied by a factor of 5.

3.2. Comparison of Heat Flow Rate Exchange Due to Chemical Reactions

By solving the energy balance in the reactionary medium, one obtains:

$$T_c = T_r + \frac{1}{Ua}\sum_i R_i\Delta H_i - \frac{\sum C_{j_{in}}\overline{C}_{P_j}}{\tau{\cdot}Ua}\left(T_{in} - T_r\right) \tag{14}$$

Figure 4 shows the heat flow rates due to chemical reactions in the temperature range of 300–600 K. We plotted the heat flow rate generated in watts per cubic meters for different space-times from 100 s to 10,000 s. Based on the results presented in Figure 4, we can

conclude that the energy release per unit of time per unit of volume decreases if we increase the space-time. Such results are expected for an ideal CSTR.

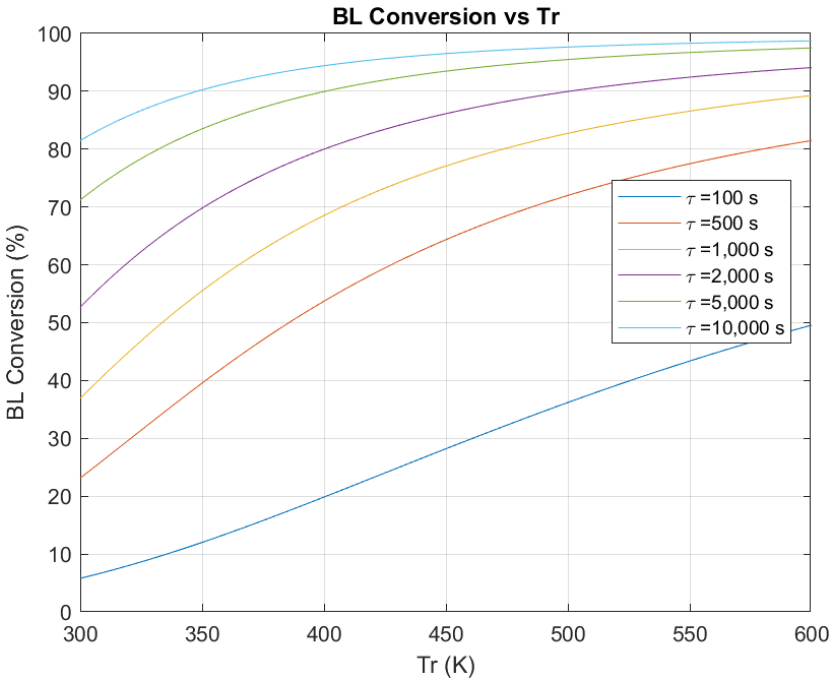

Figure 3. BL conversion as a function of T_r for different space-times.

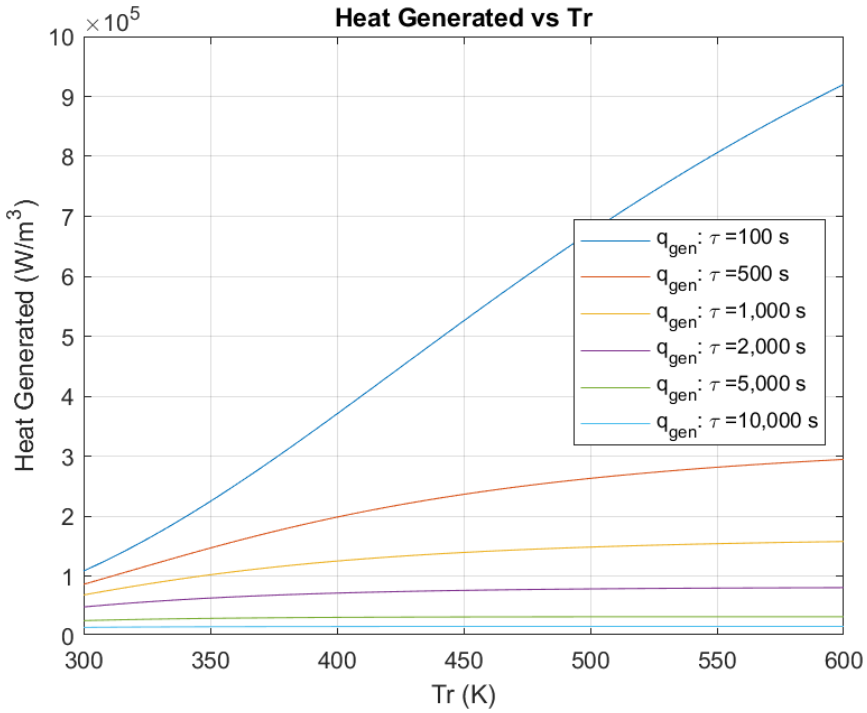

Figure 4. Heat flow as a function of T_r for different space-times.

Figure 5 represents the application of the van Heerden criterion to determine if the reactionary system is stable from the thermal point of view operating at a steady-state regime. This criterion solves the energy balance and determines if T_r is related to T_c by a one-to-one function (injective function). When the one-to-one function relates T_r and T_c, there is no multiplicity of steady states; consequently, the system is stable.

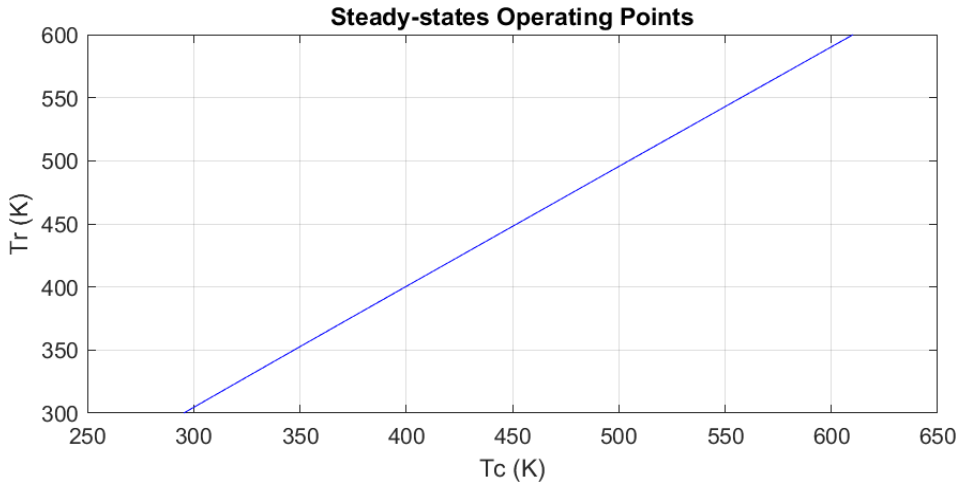

Figure 5. Reactor temperature vs. jacket temperature.

From Figure 5, we can realize that T_r and T_c are related by a one-to-one function in the range 300 K < T_r < 600 K. Thus, we can conclude that there is no multiplicity of steady-states and also that the reactionary system can stably operate in a steady-state regime.

3.3. Parametric Sensitivity

In this part, we evaluate the parametric sensitivity of the BL concentration in the outlet flow, the GVL concentration in the outlet flow, and the reactor temperature. We decided to focus on these three variables since they represent the main reagent, the main product, and the variable linked to thermal stability.

The parameters considered for this evaluation were C_{BL_0}, k_{hyd}, k_{cyc}, Ua, τ, ω_{Cat}, and T_{in}.

Figure 6 shows the normalized parametric sensitivity of the BL concentration in the outlet flow as a function of the reaction temperature. From Figure 6, we can notice that the final BL concentration is more sensitive to the inlet BL concentration, space-time, and catalyst loading. This means that variations in these parameters significantly change the final BL concentration.

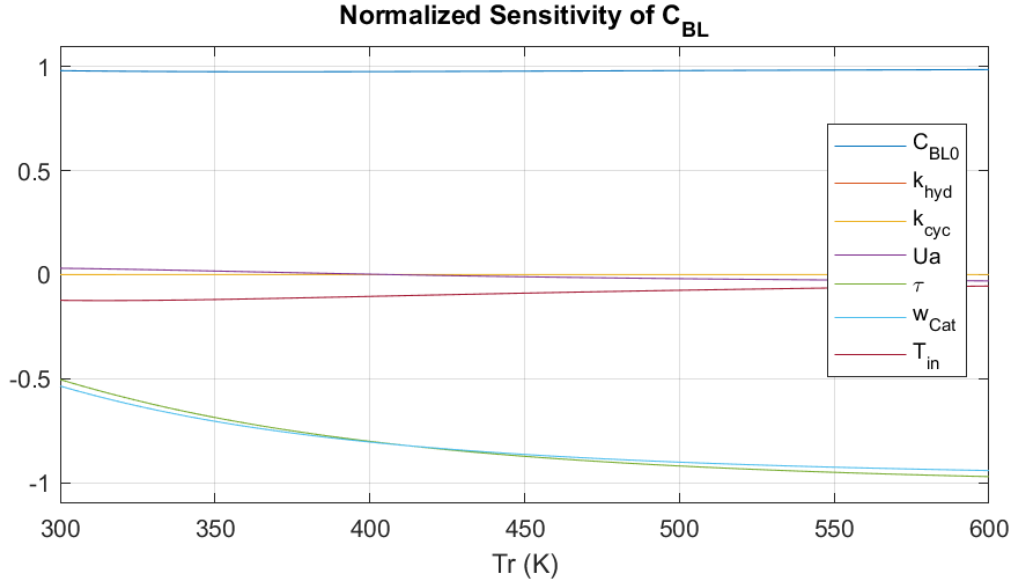

Figure 6. Parametric sensitivity for the outlet BL concentration.

Figure 7 represents the normalized parametric sensitivity of the GVL concentration in the outlet flow as a function of the reaction temperature. Based on the results, we found

that the GVL concentration is more sensitive to variations in the inlet BL concentration, the space-time, and the cyclization rate constant. If any of these parameters increase, then the GVL production also increases. From Figure 7, we can also realize that GVL's sensitivity to these parameters gains importance as we increase the reaction temperature.

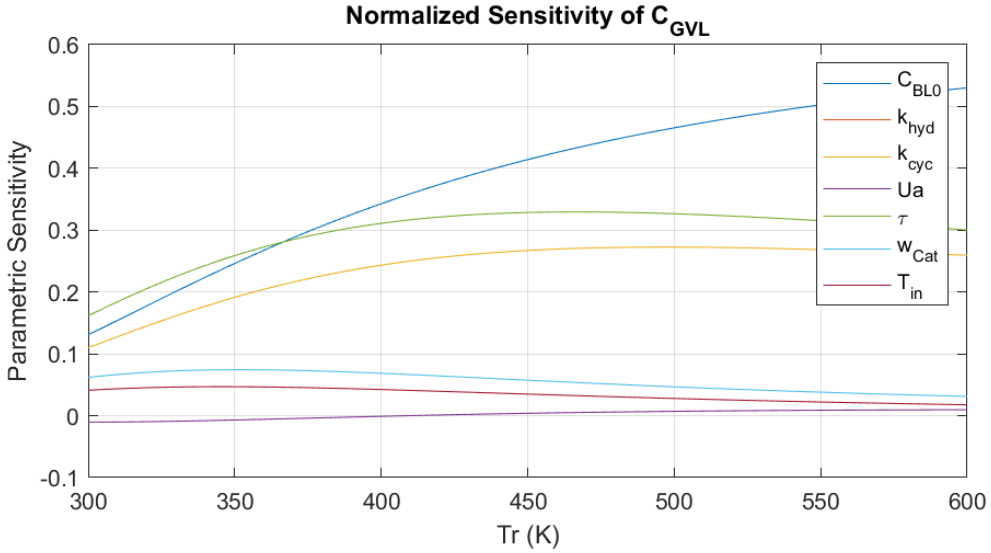

Figure 7. Parametric sensitivity for the outlet GVL concentration.

Figure 8 represents the normalized parametric sensitivity of the reaction temperature in the range of temperatures from 300 K to 600 K. Figure 8 shows how sensitive the reaction temperature is to the operating parameters. We found that reaction temperature is more sensitive to variations in the inlet temperature, the inlet BL concentration, space-time, and the heat transfer coefficient. Based on these results, we can conclude that the inlet BL concentration, the hydrogenation and cyclization rate constants, the heat transfer Ua, the space-time τ, the catalyst loading $\omega_{Ru/C}$, and the inlet temperature T_{in} have a low impact on the reaction temperature within the temperature range of 300–600 K. This low influence explains the low risk of thermal instability for this reaction in a CSTR.

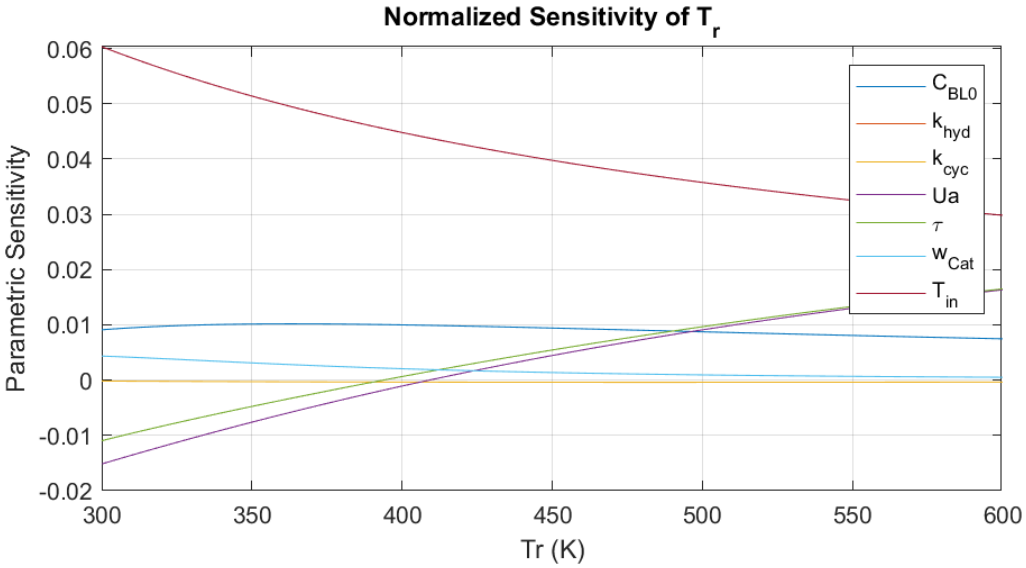

Figure 8. Results: Parametric sensitivity for the reactor temperature (T_r).

3.4. Dynamic Thermal Stability

In this part, we seek to evaluate the dynamic response of the system to perturbations near stationary conditions. For this purpose, we applied the linear dynamic model of perturbation.

Considering our dynamical model:

$$\frac{dy_i}{dt} = f_i(y_1, y_2, \ldots, y_n, \phi, t) \tag{15}$$

where y_i represents the variables of the system, and ϕ represents the other parameters.

$$y_i = C_{BL}, C_{BHP}, C_{GVL}, C_{BuOH}, T_r, T_c \tag{16}$$

Let us define a small perturbation (x_i) on the whole set of variables as follows:

$$x_i = y_i - y_{i,s} \tag{17}$$

Therefore:

$$y_i = y_{i,s} + x_i \tag{18}$$

Now we can define the perturbed dynamical model as follows:

$$\frac{d(y_{i,s} + x_i)}{dt} = f_i(y_{1,s} + x_1, y_{2,s} + x_2, \ldots, y_{n,s} + x_n, \phi, t) \tag{19}$$

As we have an interest in making a linear analysis, we used the 1st-order Taylor expansion of the perturbed dynamical model to obtain:

$$\frac{d(y_{i,s} + x_i)}{dt} = f_i(y_{1,s}, y_{2,s}, \ldots, y_{n,s} + x_n, \phi, t) + \left(\frac{\partial f_i}{\partial y_1}\right) \cdot x_1 + \left(\frac{\partial f_i}{\partial y_2}\right) \cdot x_2 + \cdots + \left(\frac{\partial f_i}{\partial y_n}\right) \cdot x_n \tag{20}$$

Under stationary conditions:

$$\frac{d(y_{i,s} + x_i)}{dt} = 0 \tag{21}$$

$$f_i(y_{1,s}, y_{2,s}, \ldots, y_{n,s} + x_n, \phi, t) = 0 \tag{22}$$

Therefore, the linear model of perturbation under stationary conditions is:

$$\frac{dx_i}{dt} = \left(\frac{\partial f_i}{\partial y_1}\right)_s \cdot x_1 + \left(\frac{\partial f_i}{\partial y_2}\right)_s \cdot x_2 + \cdots + \left(\frac{\partial f_i}{\partial y_n}\right)_s \cdot x_n \tag{23}$$

Developing the linear model of perturbation under stationary conditions for a system with n variables, we have:

$$\begin{cases} \frac{dx_1}{dt} = \left(\frac{\partial f_1}{\partial y_1}\right)_s \cdot x_1 + \left(\frac{\partial f_1}{\partial y_2}\right)_s \cdot x_2 + \cdots + \left(\frac{\partial f_1}{\partial y_n}\right)_s \cdot x_n \\ \vdots \\ \frac{dx_i}{dt} = \left(\frac{\partial f_i}{\partial y_1}\right)_s \cdot x_1 + \left(\frac{\partial f_i}{\partial y_2}\right)_s \cdot x_2 + \cdots + \left(\frac{\partial f_i}{\partial y_n}\right)_s \cdot x_n \\ \vdots \\ \frac{dx_n}{dt} = \left(\frac{\partial f_n}{\partial y_1}\right)_s \cdot x_1 + \left(\frac{\partial f_n}{\partial y_2}\right)_s \cdot x_2 + \cdots + \left(\frac{\partial f_n}{\partial y_n}\right)_s \cdot x_n \end{cases} \tag{24}$$

In a matrix formalism, we can define the linear dynamical model of perturbation as follows:

$$\dot{X} = J \cdot X$$

where

$$X = \begin{pmatrix} x_1 \\ \vdots \\ x_n \end{pmatrix}; \ \dot{X} = \begin{pmatrix} \frac{dx_1}{dt} \\ \vdots \\ \frac{dx_n}{dt} \end{pmatrix}; \ J = \begin{pmatrix} \frac{df_1}{dy_1} & \cdots & \frac{df_1}{dy_n} \\ \vdots & \ddots & \vdots \\ \frac{df_n}{dy_1} & \cdots & \frac{df_n}{dy_n} \end{pmatrix} \tag{25}$$

Solving the linear system leads to these solutions for all the perturbations around the stationary point:

$$\begin{cases} x_1 = \sum_{m=1}^{n} a_m \cdot U_{1,m} \cdot e^{\lambda_m t} \\ \vdots \\ x_i = \sum_{m=1}^{n} a_m \cdot U_{i,m} \cdot e^{\lambda_m t} \\ \vdots \\ x_n = \sum_{m=1}^{n} a_m \cdot U_{n,m} \cdot e^{\lambda_m t} \end{cases} \tag{26}$$

where U_i is the ith eigenvector of J associated to the eigenvalue λ_i. The condition of asymptotic stability is:

$$\forall \, k \lim_{t \to \infty} x_k = 0 \tag{27}$$

This leads to the following:

$$\lambda_i \in \mathbb{C} \cdot \Re e(\lambda_i) < 0 \tag{28}$$

To evaluate the dynamic thermal stability, we defined the Jacobian matrix of the dynamic model in the range of temperature of 300 K to 600 K and calculated the eigenvalues of the Jacobian matrix for each temperature value. The eigenvalues are plotted in Figure 9.

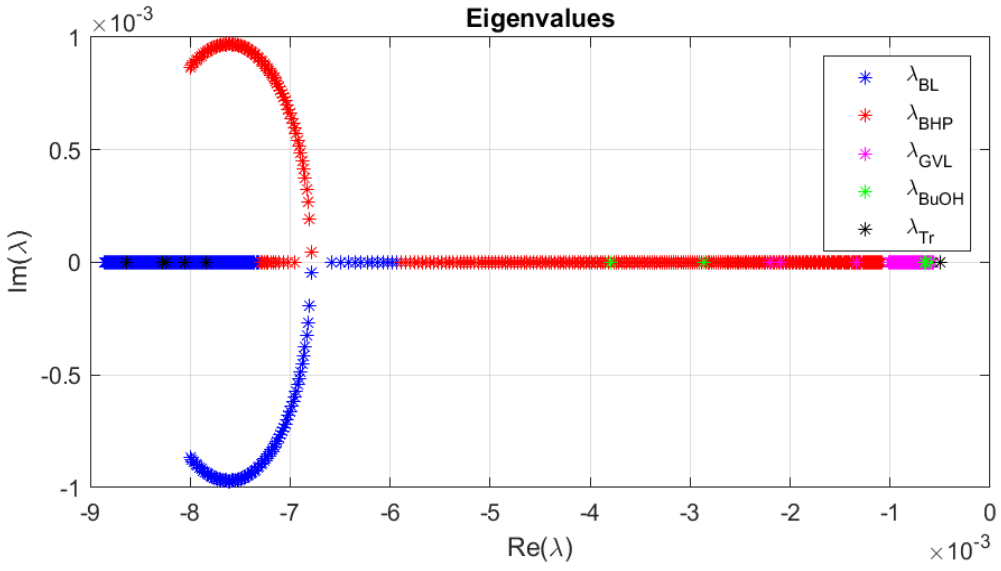

Figure 9. Dynamic Stability—Eigenvalues.

Figure 9 shows the eigenvalues obtained from the Jacobian matrix of the reactionary system in the range of temperature from 300 K to 600 K. This Jacobian matrix was generated from the material and energy balances. It is considered that there are dynamic thermal instabilities in the system when there are eigenvalues whose real parts are positive (Re(λ) > 0). From Figure 9, we can conclude that the CSTR reactor is dynamically stable in the temperature range of 300 K to 600 K since the real parts of all eigenvalues are negative. Visualizing the eigenvalues also helps to identify which variable is responsible for instabilities when the system is not dynamically stable.

4. Conclusions

This article deals with the safety production of GVL from the hydrogenation of butyl levulinate over *Ru/C* in a continuous stirred-tank reactor (CSTR) in a steady-state regime. The kinetic and thermodynamic constants determined from Wang et al.'s articles were used to simulate the thermal behavior in a CSTR. The van Heerden criterion showed that the risk of thermal instability is low for this reaction system with the operating conditions used in this study.

The sensitivity analysis demonstrated that the kinetic constants, global heat transfer, inlet concentrations, space-time, inlet temperature, and catalyst loading have a low impact on the reaction temperature. Nevertheless, the inlet concentration of BL, space-time, and cyclization rate constant have a non-negligible impact on the outlet concentration of GVL.

A continuation of this study could be the study of thermal stability during the transient phase and for non-ideal flow in continuous reactors.

Author Contributions: Conceptualization, W.N.V.S. and S.L.; methodology, W.N.V.S.; formal analysis, W.N.V.S.; investigation, W.N.V.S.; writing—original draft preparation, W.N.V.S., B.R. and S.L.; writing—review and editing, W.N.V.S., B.R. and S.L.; supervision, B.R. and S.L. All authors have read and agreed to the published version of the manuscript.

Funding: This study was conducted in the framework of the PROMETEE project, funded by Rouen Metropole. The authors thank the Ministry of High Education, Science and Technology of Dominican Republic (MESCyT).

Data Availability Statement: Data available on request.

Conflicts of Interest: The authors declare no conflict of interest.

References

1. Filip, O.; Janda, K.; Kristoufek, L.; Zilberman, D. Food versus fuel: An updated and expanded evidence. *Energy Econ.* **2019**, *82*, 152–166. [CrossRef]
2. Timilsina, G.R.; Shrestha, A. How much hope should we have for biofuels? *Energy* **2011**, *36*, 2055–2069. [CrossRef]
3. Isikgor, F.H.; Becer, C.R. Lignocellulosic biomass: A sustainable platform for the production of bio-based chemicals and polymers. *Polym. Chem.* **2015**, *6*, 4497–4559. [CrossRef]
4. Gunasekaran, M.; Kumar, G.; Karthikeyan, O.P.; Varjani, S. Lignocellulosic biomass as an optimistic feedstock for the production of biofuels as valuable energy source: Techno-economic analysis, Environmental Impact Analysis, Breakthrough and Perspectives. *Environ. Technol. Innov.* **2021**, *24*, 102080. [CrossRef]
5. Nahak, B.K.; Preetam, S.; Sharma, D.; Shukla, S.K.; Syväjärvi, M.; Toncu, D.C.; Tiwari, A. Advancements in net-zero pertinency of lignocellulosic biomass for climate neutral energy production. *Renew. Sustain. Energy Rev.* **2022**, *161*, 112393. [CrossRef]
6. Melero, J.A.; Iglesias, J.; Garcia, A. Biomass as renewable feedstock in standard refinery units. Feasibility, opportunities and challenges. *Energy Environ. Sci.* **2012**, *5*, 7393–7420. [CrossRef]
7. Di Menno Di Bucchianico, D.; Wang, Y.; Buvat, J.C.; Pan, Y.; Casson Moreno, V.; Leveneur, S. Production of levulinic acid and alkyl levulinates: A process insight. *Green Chem.* **2022**, *24*, 614–646. [CrossRef]
8. Ye, L.; Han, Y.; Feng, J.; Lu, X. A review about GVL production from lignocellulose: Focusing on the full components utilization. *Ind. Crops Prod.* **2020**, *144*, 112031. [CrossRef]
9. Xu, R.; Liu, K.; Du, H.; Liu, H.; Cao, X.; Zhao, X.; Qu, G.; Li, X.; Li, B.; Si, C. Falling Leaves Return to Their Roots: A Review on the Preparation of γ-Valerolactone from Lignocellulose and Its Application in the Conversion of Lignocellulose. *ChemSusChem* **2020**, *13*, 6461–6476. [CrossRef]
10. Alonso, D.M.; Wettstein, S.G.; Dumesic, J.A. Gamma-valerolactone, a sustainable platform molecule derived from lignocellulosic biomass. *Green Chem.* **2013**, *15*, 584–595. [CrossRef]
11. Tang, X.; Zeng, X.; Li, Z.; Hu, L.; Sun, Y.; Liu, S.; Lei, T.; Lin, L. Production of γ-valerolactone from lignocellulosic biomass for sustainable fuels and chemicals supply. *Renew. Sustain. Energy Rev.* **2014**, *40*, 608–620. [CrossRef]
12. Fábos, V.; Lui, M.Y.; Mui, Y.F.; Wong, Y.Y.; Mika, L.T.; Qi, L.; Cséfalvay, E.; Kovács, V.; Szucs, T.; Horváth, I.T. Use of Gamma-Valerolactone as an Illuminating Liquid and Lighter Fluid. *ACS Sustain. Chem. Eng.* **2015**, *3*, 1899–1904. [CrossRef]
13. Kerkel, F.; Markiewicz, M.; Stolte, S.; Müller, E.; Kunz, W. The green platform molecule gamma-valerolactone—Ecotoxicity, biodegradability, solvent properties, and potential applications. *Green Chem.* **2021**, *23*, 2962–2976. [CrossRef]
14. Di Menno Di Bucchianico, D.; Buvat, J.C.; Mignot, M.; Casson Moreno, V.; Leveneur, S. Role of solvent the production of butyl levulinate from fructose. *Fuel* **2022**, *318*, 123703. [CrossRef]
15. Luo, Y.; Li, Z.; Zuo, Y.; Su, Z.; Hu, C. A Simple Two-Step Method for the Selective Conversion of Hemicellulose in Pubescens to Furfural. *ACS Sustain. Chem. Eng.* **2017**, *5*, 8137–8147. [CrossRef]

16. Yuan, C.; Shi, W.; Chen, P.; Chen, H.; Zhang, L.; Hu, G.; Jin, L.; Xie, H.; Zheng, Q.; Lu, S. Dissolution and transesterification of cellulose in γ-valerolactone promoted by ionic liquids. *New J. Chem.* **2019**, *43*, 330–337. [CrossRef]
17. Xue, Z.; Zhao, X.; Sun, R.C.; Mu, T. Biomass-derived γ-valerolactone-based solvent systems for highly efficient dissolution of various lignins: Dissolution behavior and mechanism study. *ACS Sustain. Chem. Eng.* **2016**, *4*, 3864–3870. [CrossRef]
18. Motagamwala, A.H.; Won, W.; Maravelias, C.T.; Dumesic, J.A. An engineered solvent system for sugar production from lignocellulosic biomass using biomass derived γ-valerolactone. *Green Chem.* **2016**, *18*, 5756–5763. [CrossRef]
19. Di Menno Di Bucchianico, D.; Cipolla, A.; Buvat, J.C.; Mignot, M.; Casson Moreno, V.; Leveneur, S. Kinetic Study and Model Assessment for n-Butyl Levulinate Production from Alcoholysis of 5-(Hydroxymethyl)furfural over Amberlite IR-120. *Ind. Eng. Chem. Res.* **2022**, *61*, 10818–10836. [CrossRef]
20. Yan, K.; Yang, Y.; Chai, J.; Lu, Y. Catalytic reactions of gamma-valerolactone: A platform to fuels and value-added chemicals. *Appl. Catal. B Environ.* **2015**, *179*, 292–304. [CrossRef]
21. Bond, J.Q.; Alonso, D.M.; Wang, D.; West, R.M.; Dumesic, J.A. Integrated catalytic conversion of γ-valerolactone to liquid alkenes for transportation fuels. *Science* **2010**, *327*, 1110–1114. [CrossRef]
22. Al-Naji, M.; Puértolas, B.; Kumru, B.; Cruz, D.; Bäumel, M.; Schmidt, B.V.K.J.; Tarakina, N.V.; Pérez-Ramírez, J. Sustainable Continuous Flow Valorization of γ-Valerolactone with Trioxane to α-Methylene-γ-Valerolactone over Basic Beta Zeolites. *ChemSusChem* **2019**, *12*, 2628–2636. [CrossRef]
23. Manzer, L.E. Catalytic synthesis of α-methylene-γ-valerolactone: A biomass-derived acrylic monomer. *Appl. Catal. A Gen.* **2004**, *272*, 249–256. [CrossRef]
24. Kuwahara, Y.; Kaburagi, W.; Osada, Y.; Fujitani, T.; Yamashita, H. Catalytic transfer hydrogenation of biomass-derived levulinic acid and its esters to γ-valerolactone over ZrO2 catalyst supported on SBA-15 silica. *Catal. Today* **2017**, *281*, 418–428. [CrossRef]
25. Kuwahara, Y.; Kango, H.; Yamashita, H. Catalytic Transfer Hydrogenation of Biomass-Derived Levulinic Acid and Its Esters to γ-Valerolactone over Sulfonic Acid-Functionalized UiO-66. *ACS Sustain. Chem. Eng.* **2017**, *5*, 1141–1152. [CrossRef]
26. Liu, M.; Li, S.; Fan, G.; Yang, L.; Li, F. Hierarchical Flower-like Bimetallic NiCu catalysts for Catalytic Transfer Hydrogenation of Ethyl Levulinate into γ-Valerolactone. *Ind. Eng. Chem. Res.* **2019**, *58*, 10317–10327. [CrossRef]
27. Oklu, N.K.; Makhubela, B.C.E. Highly selective and efficient solvent-free transformation of bio-derived levulinic acid to γ-valerolactone by Ru(II) arene catalyst precursors. *Inorg. Chim. Acta* **2018**, *482*, 460–468. [CrossRef]
28. Chalid, M.; Broekhuis, A.A.; Heeres, H.J. Experimental and kinetic modeling studies on the biphasic hydrogenation of levulinic acid to γ-valerolactone using a homogeneous water-soluble Ru-(TPPTS) catalyst. *J. Mol. Catal. A Chem.* **2011**, *341*, 14–21. [CrossRef]
29. Agirrezabal-Telleria, I.; Hemmann, F.; Jäger, C.; Arias, P.L.; Kemnitz, E. Functionalized partially hydroxylated MgF2 as catalysts for the dehydration of d-xylose to furfural. *J. Catal.* **2013**, *305*, 81–91. [CrossRef]
30. Han, Y.; Ye, L.; Gu, X.; Zhu, P.; Lu, X. Lignin-based solid acid catalyst for the conversion of cellulose to levulinic acid using γ-valerolactone as solvent. *Ind. Crops Prod.* **2019**, *127*, 88–93. [CrossRef]
31. Li, F.; France, L.J.; Cai, Z.; Li, Y.; Liu, S.; Lou, H.; Long, J.; Li, X. Catalytic transfer hydrogenation of butyl levulinate to Γ-valerolactone over zirconium phosphates with adjustable Lewis and Brønsted acid sites. *Appl. Catal. B Environ.* **2017**, *214*, 67–77. [CrossRef]
32. Guo, H.; Ding, S.; Zhang, H.; Wang, C.; Peng, F.; Xiong, L.; Chen, X.; Ouyang, X. Improvement on the catalytic performances of butyl levulinate hydrogenation to γ-valerolactone over self-regenerated CuNiCoB/Palygorskite catalyst. *Mol. Catal.* **2021**, *504*, 111483. [CrossRef]
33. Delgado, J.; Vasquez Salcedo, W.N.; Bronzetti, G.; Casson Moreno, V.; Mignot, M.; Legros, J.; Held, C.; Grénman, H.; Leveneur, S. Kinetic model assessment for the synthesis of γ-valerolactone from n-butyl levulinate and levulinic acid hydrogenation over the synergy effect of dual catalysts Ru/C and Amberlite IR-120. *Chem. Eng. J.* **2022**, *430*, 133053. [CrossRef]
34. Capecci, S.; Wang, Y.; Casson Moreno, V.; Held, C.; Leveneur, S. Solvent effect on the kinetics of the hydrogenation of n-butyl levulinate to γ-valerolactone. *Chem. Eng. Sci.* **2021**, *231*, 116315. [CrossRef]
35. Wang, Y.; Plazl, I.; Vernières-Hassimi, L.; Leveneur, S. From calorimetry to thermal risk assessment: γ-Valerolactone production from the hydrogenation of alkyl levulinates. *Process Saf. Environ. Prot.* **2020**, *144*, 32–41. [CrossRef]
36. Wang, Y.; Vernières-Hassimi, L.; Casson-Moreno, V.; Hébert, J.P.; Leveneur, S. Thermal Risk Assessment of Levulinic Acid Hydrogenation to γ-Valerolactone. *Org. Process Res. Dev.* **2018**, *22*, 1092–1100. [CrossRef]
37. Fei, Y.; Sun, B.; Zhang, F.; Xu, W.; Shi, N.; Jiang, J. Inherently safer reactors and procedures to prevent reaction runaway. *Chin. J. Chem. Eng.* **2018**, *26*, 1252–1263. [CrossRef]
38. Aguilar-López, R.; Mata-Machuca, J.L.; Godinez-Cantillo, V. A tito control strategy to increase productivity in uncertain exothermic continuous chemical reactors. *Processes* **2021**, *9*, 873. [CrossRef]
39. Abusrafa, A.E.; Challiwala, M.S.; Wilhite, B.A.; Elbashir, N.O. Thermal assessment of a micro fibrous fischer tropsch fixed bed reactor using computational fluid dynamics. *Processes* **2020**, *8*, 1213. [CrossRef]
40. Jayakumar, N.S.; Agrawal, A.; Hashim, M.A.; Sahu, J.N. Experimental and theoretical investigation of parametric sensitivity and dynamics of a continuous stirred tank reactor for acid catalyzed hydrolysis of acetic anhydride. *Comput. Chem. Eng.* **2011**, *35*, 1295–1303. [CrossRef]
41. Gómez García, M.Á.; Dobrosz-Gómez, I.; Ojeda Toro, J.C. Thermal stability and dynamic analysis of the acetic anhydride hydrolysis reaction. *Chem. Eng. Sci.* **2016**, *142*, 269–276. [CrossRef]

42. Nguyen, S.T.; Hoang, N.H.; Hussain, M.A. Analysis of the Steady-State Multiplicity Behavior for Polystyrene Production in the CSTR. *Chem. Prod. Process Model.* **2017**, *12*, 20170027. [CrossRef]
43. Schweitzer, J.M.; López-García, C.; Ferré, D. Thermal runaway analysis of a three-phase reactor for LCO hydrotreatment. *Chem. Eng. Sci.* **2010**, *65*, 313–321. [CrossRef]
44. Wang, Y.; Cipolletta, M.; Vernières-Hassimi, L.; Casson-Moreno, V.; Leveneur, S. Application of the concept of Linear Free Energy Relationships to the hydrogenation of levulinic acid and its corresponding esters. *Chem. Eng. J.* **2019**, *374*, 822–831. [CrossRef]
45. Ariba, H.; Wang, Y.; Devouge-Boyer, C.; Stateva, R.P.; Leveneur, S. Physicochemical Properties for the Reaction Systems: Levulinic Acid, Its Esters, and γ-Valerolactone. *J. Chem. Eng. Data* **2020**, *65*, 3008–3020. [CrossRef]
46. Lu, X.; Wang, Y.; Estel, L.; Kumar, N.; Grénman, H.; Leveneur, S. Evolution of specific heat capacity with temperature for typical supports used for heterogeneous catalysts. *Processes* **2020**, *8*, 911. [CrossRef]
47. Aris, R. On stability criteria of chemical reaction engineering. *Chem. Eng. Sci.* **1969**, *24*, 149–169. [CrossRef]
48. Van Heerden, C. Autothermic Processes. *Ind. Eng. Chem.* **1953**, *45*, 1242–1247. [CrossRef]
49. Kummer, A.; Varga, T. What do we know already about reactor runaway?—A review. *Process Saf. Environ. Prot.* **2021**, *147*, 460–476. [CrossRef]
50. Varma, A.; Morbidelli, M.; Wu, H. *Parametric Sensitivity in Chemical Systems*; Cambridge University Press: Cambridge, UK, 1999; ISBN 0521019842.